UNIVERSITY OF Southampton

Faculty of Physical Sciences and Engineering
School of Electronics and Computer Sciences

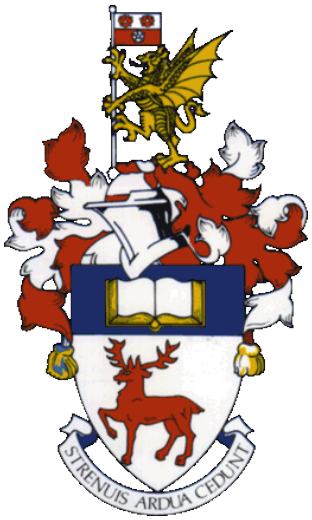

Label-free, microfluidic characterisation and sorting of human skeletal stem cells

Jorge Miguel Queiroz de Almeida Xavier

A thesis for the degree of Doctor of Philosophy
June 2018

Advisors: Professor Hywel Morgan and Professor Richard OC Oreffo
Examiners: Professor Xize Niu and Doctor Mathis Riehle

“An expert is a person who has made all the mistakes that can be made in a very narrow field.”

Niels Bohr

UNIVERSITY OF SOUTHAMPTON

ABSTRACT

FACULTY OF PHYSICAL SCIENCES AND ENGINEERING

Electronics and Computer Sciences

Doctor of Philosophy

LABEL-FREE, MICROFLUIDIC CHARACTERISATION AND SORTING OF HUMAN SKELETAL STEM CELLS

Jorge Miguel Queiroz de Almeida Xavier

Skeletal stem cells (SSCs) are a sub-population of bone marrow (BM) stromal cells with multipotent differentiation potential. SSCs are responsible for the unique regeneration capacity inherent to bone and offer unlimited potential for application in bone regenerative therapies. A current unmet challenge hampering their clinical translation remains the isolation of homogeneous SSC populations with consistent regeneration and differentiation capacities. Factors limiting the efficiency of existing sorting approaches include the scarcity of SSCs in BM, estimated at fewer than 1 in 10,000 nucleated cells, the complexity of BM tissue and, most significantly, the absence of a specific marker that is unique to the SSC.

Microfluidics offers the potential to characterise and sort cells marker-free, based on intrinsic biophysical properties. These include, but are not limited to, cell size, shape, stiffness, and dielectric properties. The work presented herein aimed to provide a comprehensive characterisation of the biophysical fingerprint of SSCs and to build on this new understanding to develop new tools to isolate SSCs, label-free, with significant physiological and therapeutic implications.

In real-time deformability cytometry (RT-DC), cells are deformed by shear and normal stresses as they flow through a narrow constriction at high speed, providing the capability to screen cell mechanical properties at high-throughput. Here, RT-DC was used to relate the mechano-phenotype of expanded SSCs with other cells in BM. Critically, SSCs were found to be significantly stiffer than white blood cells, which are abundant in human BM.

Microfluidic impedance cytometry was coupled to fluorescence optical detection to provide accurate characterisation of the dielectric properties and cell size of SSCs within heterogeneous primary human BM samples. The membrane capacitance of SSCs was found to be indistinct from other cells in BM. Conversely, their average size in suspension, at 9 micrometres, was within the largest BM cell fraction.

Centred on these findings, label-free sorting devices were designed based on the principle of deterministic lateral displacement (DLD). DLD uses arrays of micropillars in a channel to sort cells based on their diameter, at throughputs of thousands per second. Cell deformation, induced by shear and contact with the pillars, can change the effective cell size and affect sorting efficiency. This was demonstrated using two human cells lines of different size and stiffness, and by size fractionation of expanded SSCs. Crucially, SSCs sorted by DLD remained viable and retained their capacity to form clonogenic cultures.

Overall, this work provided a detailed characterisation of relevant biophysical properties of SSCs and paved the way towards the design of a novel label-free sorting approach, potentially based on DLD, to provide purified SSC populations from BM with impactful use in fundamental stem cell research and the clinic.

Table of Contents

Preface and Acknowledgements ..... **xi**

Outline ..... **xiii**

List of Figures ..... **xv**

List of Supplementary Figures ..... **xxiii**

List of Tables ..... **xxv**

List of Supplementary Tables ..... **xxvii**

Author's Declaration ..... **xxix**

Abbreviations ..... **xxxi**

Variables, Constants and Units ..... **xxxiii**

1. **Skeletal Stem Cells** **35**

    1.1. Motivation 35

    1.2. Definition 35

    1.3. Skeletal Stem Cell Applications 37

    1.4. Limitations Hampering Clinical Translation 38

    1.5. Skeletal Stem Cell Enrichment using the Stro-1 antibody 39

    1.6. Summary 43

2. **Microfluidics: Physics and Cell Sorting Applications** **45**

    2.1. Laminar flow 45

    2.2. Navier-Stokes equations and Poiseuille flow 46

    2.3. Label-free Particle Sorting 50

        2.3.1. Affinity-based 50

        2.3.2. Deterministic Lateral Displacement 52

        2.3.3. Magnetophoresis 54

        2.3.4. Inertial Microfluidics 57

        2.3.5. Acoustophoresis 60

        2.3.6. Dielectrophoresis 62

    2.4. Summary and prospects of label-free skeletal stem cell sorting 65

3. **Mechanical Phenotyping** **69**

    3.1. Introduction 69

        3.1.1. Cell Mechanics 69

3.1.2. Real-Time Deformability Cytometry....70
3.2. Results and Discussion....71
3.2.1. HL-60, MG-63 and Mesenchymal and Skeletal Stem Cells....71
3.2.2. Mixed White Blood Cell and Skeletal Stem Cell populations....74
3.3. Conclusions....75
4. **Size and Dielectric Characterisation....77**
4.1. Introduction....77
4.2. Microfluidic Impedance Cytometry....78
4.3. Results and Discussion....80
4.3.1. Cell Size....80
4.3.2. Membrane Capacitance....81
4.3.3. Cell Proliferation, ALP Activity and Gene Expression....84
4.3.4. Tracking Osteogenesis using Microfluidic Impedance Cytometry....84
4.4. Conclusions....87
5. **Size and Mechano-based Cell Sorting....89**
5.1. Introduction....89
5.2. Results and Discussion....91
5.2.1. Size-based sorting of non-deformable polystyrene beads....91
5.2.2. Binary fractionation of MG-63 as a function of cell deformability....92
5.2.3. Size and mechano-based sorting of MG-63 and HL-60....92
5.2.4. Binary fractionation of SSCs as a function of cell deformability....94
5.2.5. Size and mechano-based sorting of SSCs and WBCs....96
5.2.6. Size and mechano-based sorting of SSCs from human BM....98
5.3. Conclusions....99
6. **Discussion and Future Directions....101**
7. **Materials and Methods....105**
7.1. Cell Culture....105
7.1.1. MG-63 and Saos-2....105
7.1.2. GFP^+ MG-63....105
7.1.3. HL-60....105
7.1.4. Human Blood Samples....105
7.1.5. Primary Human Bone Marrow Skeletal Stem Cells....106

7.1.5.1. Osteogenic Differentiation 107
7.2. Fluorescent Cell Labelling 107
7.2.1. Human BMMNCs Labelling of Stro-1 and CD146 107
7.2.2. HL-60 Labelling with CellTracker™ Deep Red Dye 107
7.2.3. Skeletal Stem Cell Labelling with CellTracker™ Green CMFDA Dye 108
7.2.4. White Blood Cell Labelling of CD45 108
7.3. Flow Cytometry 108
7.4. Biochemical Assays 108
7.4.1. Alkaline Phosphatase (ALP) Staining 108
7.4.2. ALP Activity and DNA Quantification 108
7.4.3. CFU-F staining 109
7.5. Molecular Assays 109
7.5.1. RNA Extraction and Complementary DNA Synthesis 109
7.5.2. Quantitative Reverse Transcription Polymerase Chain Reaction 109
7.6. Mechanical Phenotyping 110
7.6.1. Sample Preparation 110
7.6.2. Microfluidic chip and Real-Time Deformability Cytometry Set-up 110
7.7. Size and Dielectric Characterisation 110
7.7.1. Sample Preparation 110
7.7.2. Microfluidic Chip and Impedance Cytometer Set-up 110
7.8. Size and Mechano-based Cell sorting 111
7.8.1. Mask Design for Deterministic Lateral Displacement 111
7.8.2. Microfabrication 114
7.8.3. Soft Lithography 114
7.8.4. Sample Preparation 114
7.8.5. Device Operation 114
7.9. Statistical Analyses 117
7.9.1. Mechanical Phenotyping 117
7.9.2. Size and Dielectric Characterisation 117
7.9.3. Size and Mechano-based cell sorting 117
7.10. Materials 118
7.10.1. List of Buffers 118
References 119

Appendix A.....129
Appendix B.....133
Appendix C.....135

Preface and Acknowledgements

In April 2014 I made the decision to move to the UK to pursue my PhD. It was a hard choice because it meant leaving behind a home that I liked, a loving family, true friends..., and sunny weather! Today though, four years later, I never look back - it was one of the best decisions I have ever made.

I was fortunate to be accompanied in this endeavour by my strongest pillar. And I cannot find a way to put into words how her company has made this journey so much easier and gratifying. That is why my first acknowledgement must go to Catarina, who each day makes me a better person and a better researcher. And what good a time we've had together in the UK...

On the same line of thought I should obviously thank my parents, who I have missed and whom I know have missed me dearly. But who also fill me with pride and have always offered their unconditional support for my little adventure. Similar words must be addressed to my closest family, my sister, my niece and nephews, and my brother-in-law. In particular to my sister, whose resilience, determination, and power of will have for long been a source of great inspiration.

I would not be here today if it were not for my supervisors who granted me this opportunity in the first place. Hywel and Richard have been true mentors and I can certainly say that from both the microfluidics and the stem cell biology arenas I had the rare chance to learn from the very best. This prompts me to also acknowledge my first supervisors, Pedro Granja and Ana Paula Pêgo who believed in me and saw me take my very first steps in the world of scientific research.

I was also lucky to be part of a European consortium, the LAPASO project, which has granted me the possibility to travel and to establish an invaluable network of collaborations that I hope to carry with me through the various stages of my career. I remember my first LAPASO meeting, which took place in Lund in June 2014, and sitting around a table with some of the PIs discussing my PhD project: Hywel Morgan, Thomas Laurell, Jonas Tegenfeldt, Jochen Guck, Gerhard Gompper, Lisa Ranford-Cartwright, Michael Barrett, Birgitta Henriques-Normark... I wasn't aware then but these were some of the leading Professors in theoretic and applied microfluidics, parasitology, and microbiology across Europe. I remember it well because I felt like a fish out of water.

I also insist on mentioning the names of all the other LAPASO fellows that have contributed to make our meetings so scientifically stimulating and so socially enjoyable. In no particular order: Joseph, Neils, Dmitry, Ewan, Zunmin, Jenny, Peter, Vítor, Elisabeth, Anke, Bao, Kush, Jason, Stefan, Guillaume, Walter, Monica, Simone, Ahsan, Laura, Clément and of course my LAPASO partner in crime, Carlos.

Still on the scientific angle, thank you to Philip Rosendahl and Oliver Otto who welcomed me in Dresden and helped make the RT-DC work possible. To bring DLD to Southampton, I

am grateful for the discussions I had with Jason Beech and Stefan Holm, the DLD gurus - they can sort!

One of the biggest challenges of my PhD was its exceptional multidisciplinarity. I could not have done the work with impedance cytometry without the help of Dan Spencer. Thank you Dan for showing me the ways into Engineering and rapid prototyping when I first arrived in Southampton. And thank you May for sharing your expertise in molecular biology.

This thesis would also not have been possible without the technical support teams from the CHB and the Bone&Joint research group. From the CHB, Sarah Helps and Ying Tran, and from the Bone&Joint, Kate White, Stef Inglis, Julia Wells and Janos Kanczler. I am still certain that the lab would fall apart within a few minutes would Janos decide to leave us.

Huge collective thanks to the Bone&Joint research group whose spirit of collegiality has made it a pleasure to work with. We also throw the best parties! Some names should be mentioned, some of them for the second time: Catarina, May, Julia, Edo, Ewa, Gibbs, Inés, Gry, Gianluca, Tsiloon, Anna, Stef, Stuart, Shona, Patrick, Cameron, Rosanna, Roxanna, Juan, Lauren, Mohamed, Leafy, the list could go on...! And Antonio, a friendship I intend to take with me for life. It was also a pleasure to have the visit of a former colleague from INEB, Estrela, for 3 months in our lab. That was by far the most entertaining period of the last 4 years!

I also need to thank my friend Gil for always being a safe haven of true Portuguese friendship in the UK. It seems to me that I cannot think of a better example of someone who has changed so much over the course of a few years and yet remained unchanged. Gil, whenever I visited you in London or Oxford, or when you visited us in Southampton, we all knew what to expect, and we welcomed it warmly.

Finally, thank you to my SRC family, which have helped me keep sane through these years by showing me the thrill of running and active living! I could expect to leave Southampton with a PhD but I surely did not expect to also become a runner, a swimmer, a marathoner, a sailor... who knows what comes next?

I may have been slightly carried away while writing these words of acknowledgement. I am sure I never intended this section to be so long! I just wish I had had the same enthusiasm while writing the bulk of this thesis. It could well have saved me the trouble of paying the £110 fine to the University of Southampton for apparently having taken too long.

On the off chance that someone other than my examiners, my supervisors, and my mum and dad ever happen to read this thesis, I do hope that they enjoy it and find it useful. I regret leaving some questions unanswered. Those who know me will know that I am always driven by a will to do and learn more. But unfortunately time, and funding, eventually run out.

This work was funded by the European Commission through the Label-free particle sorting (LAPASO) ITN project of the European Union's Seventh Framework Programme FP7/2007-2013 under REA grant agreement n° 607350.

Outline

This work aimed to find new solutions to isolate homogenous populations of skeletal stem cells from primary human bone marrow samples, to potentiate their use in fundamental stem cell research and in routine clinical practice. It addressed the hypothesis that skeletal stem cells hold a unique biophysical fingerprint that could be used for cell sorting using innovative label-free microfluidic approaches.

The work was divided into 5 core chapters. The two first chapters are predominantly introductory and present the motivation behind this work and key scientific concepts underlying the topics explored in chapters 3 to 5. In each of the five chapters, any relevant methodology is described in brief to allow the reader to follow the results obtained and their discussion in a logical manner. Detailed descriptions of the methods used throughout this work can be found posteriorly in Chapter 7 the assigned Materials and Methods section.

Chapter 1 defines skeletal stem cells, their applications, and the limitations of the current isolation techniques that hamper the use of skeletal stem cells routinely in the clinic. Chapter 2 introduces microfluidics and provides an overview of the fundamental physics behind handling fluids and particle suspensions at the microscale. A selection of relevant label-free, microfluidic sorting techniques is critically reviewed, offering a perspective of their applicability to skeletal stem cell sorting.

Chapters 3 and 4 exploited microfluidic approaches for the biophysical characterisation of single cells. The former introduces real-time deformability cytometry, an innovative technique developed at the University of Dresden, which was used in this work to provide a mechanical characterisation of primary human skeletal stem cells and a comparison of the mechanical properties of SSCs with other cells in bone marrow. Chapter 4 studied the size and dielectric properties of skeletal stem cells in primary human bone marrow samples, using microfluidic impedance cytometry, a tool that has been developed and optimised in our lab with demonstrated enhanced accuracy and sensitivity.

Chapter 5 built on the findings described in chapters 3 and 4 to design a microfluidic device that uses deterministic lateral displacement to sort cells based on cell size and deformability. Finally, following Chapter 5 a general discussion chapter is presented, which summarises the main results presented throughout this work and suggests design improvements to be included in future research work.

Figure 1.1 – Cell surface antigens of human bone marrow skeletal stem cells. Image adapted from Xavier *et al.*[62] 40

Figure 1.2 – CFU-F staining for alkaline phosphatase (red) and DNA/protein (crystal violet, purple). a) and b) show images of wells from a 6-well plate of unsorted BMSCs after density centrifugation at 14 days *in vitro*. c) shows a higher magnification of a section in b) highlighting the heterogeneous cell phenotype and variation in level of ALP expression in BMSC colonies. d) Colony of Stro-1 enriched BMSCs plated at passage 1 (28 days *in vitro*) 40

Figure 1.3 – Fluorescence flow cytometry of unexpanded human bone marrow mononuclear cells (hBMMNCs). a), b), d) and e) show plots (forward *vs* side scatter) of unexpanded hBMMNCs before (a, d) and after (b, e) enrichment of Stro-1^+ cells by magnetic-activated cell sorting (MACS). The three gates indicate the fraction of cells falling inside the typical FSC and SSC distributions for lymphocytes, granulocytes and monocytes as previously detailed.[65] c) and f) illustrate frequency histograms of the fluorescence intensity of hBMMNCs before and after enrichment by MACS and the respective matched isotype controls. The top and bottom panel images refer to the expression levels detected using the Stro-1 antibody and an anti-CD146 antibody respectively..... 42

Figure 1.4 – Fluorescence flow cytometry of human bone marrow mononuclear cells (hBMMNCs). Frequency of Stro-1^+ (a, c) and $CD146^+$ (b, d) hBMMNCs in the BM, before and after enrichment of the Stro-1^+ population by MACS, and following cell expansion under basal culture conditions (passages 0 to 3). Values represent mean ± SD ($N \geq 4$; *$p < 0.05$; ***$p < 0.001$, with p-values obtained using the one-way analysis of variance (ANOVA) with Tukey's post-hoc test)..... 43

Figure 2.1 – a) Laminar flow within a microfluidic device. Image courtesy of the Folch Lab (albertfolch.wixsite.com). b) Laminar flow of two flowing glaciers (Silverthrone and Klinaklini) from the Heiltskuk Icefield as seen from space. Image courtesy of NASA. c) The author of this thesis investigating the effects of laminar flow at the macroscale while visiting the Vatnajökull glacier, in Iceland. 46

Figure 2.2 – Unidirectional pressure-driven flow between two stationary plates of infinite dimensions separated by h. The Poiseuille solution to the simplified Navier-Stokes equations shows the formation of a flow velocity profile that takes the form of a parabola satisfying the no slip boundary condition that dictates that the flow velocity at the wall is equal to the velocity of the wall itself, which in this case is null. b) The shape of a card deck when the middle card is pulled while holding the top and bottom cards stationary resembles the parabolic flow velocity profile. The cards behave as the fluid laminae exerting shear stress when sliding over each other..... 49

Figure 2.3 – Affinity-based cell sorting. a) Simulation of cell trajectories in the equilateral triangular arrays. Red dots indicate cell-ending positions. b) Scanning electron micrograph of a CTC captured after contact with an EpCAM-functionalised micropost[81]. c) Comparison of cell surface interactions between the herringbone chip and a flat-walled microdevice. The probability of cell-antibody interaction is increased by passive mixing caused by the generation of micro-vortices from the chevrons at the device surface.[82] d) Cell trajectory simulation in GEDI devices predicting the frequency of cell-obstacle collisions[83]. e) Size-dependent trajectories of cells flowing in GEDI devices[85]. Pathlines (various colours) denote trajectories of cells of different diameters (1-25 μm). Cell displacement caused by impact with the obstacles increases the probability of future impacts for larger cells

promoting contact with the antibodies. The array geometry (*e.g.* obstacle diameter, 2r) can be adjusted to address specific size thresholds. Image adapted from Xavier *et al.*[62].....52

Figure 2.4 – Deterministic Lateral Displacement. a) Size-based separation in a DLD device with period N=3. Cylindrical obstacles with diameter D_{POST}, are separated by a gap G and the row shift fraction is given by Δλ. λ equals $G+D_{post}$ and Θ is the angle of the pillar array in relation the main flow direction. The micropost array divides the flow going between two posts in 3 parallel streamlines with identical flow volumes. The width of the streamline closest to the post determines the critical size for separation (R_C). Smaller, red particles, flow in zigzagging mode and suffer no net total displacement. Bigger, green particles, with radii larger than the critical separation size ($R_{EFF} > R_C$) are deflected at each critical decision point flowing in bumping mode and being laterally displaced at the end of the array. b)[103] shows an example of the operation and principle of sheathless DLD devices. d) shows the 128 parallel DLD arrays used in the most recent version of CTC-iChip to debulk whole blood at 15-20 million cells·min^{-1}.[104] Image adapted from Xavier *et al.*[62].....53

Figure 2.5 – Magnetophoresis. a) Representation of the quadrupole magnetic flow sorter with cells flowing in a central channel and separation occurring when a magnetic field actuates on the labelled cells driving them away from the centre of the device into a peripheral channel. b) Monolithic CTC-iChip. Magnetophoresis removed $CD45^+$ and $CD66b^+$ cells from whole blood and detect CTCs.[104] Image adapted from Xavier *et al.*[62] and Fachin *et al.*[104] 57

Figure 2.6 – Inertial microfluidics. a) Representation of particles flowing inside a circular channel with a typical parabolic velocity profile, showing the two dominant inertial lift forces (wall, F_{LW}, and shear gradient, F_{S-G}) acting on the particles and drawing them onto inertial focusing equilibrium positions. b) Examples of inertial focusing are given for circular, square, and rectangular channels. c) Representation of red blood cells flowing in a capillary evidencing the Fårhaeus-Lindqvist effect with RBCs focusing in the centre of the channel and a cell-free layer forming in the periphery. d) Formation of secondary flow Dean Vortices in a curved rectangular channel causing differential equilibrium positions for different particles given the balance of inertial lift and Dean flow. e) Spiral microfluidic channel used to sort CTCs from RBC-lysed clinical samples.[136] Image from Xavier *et al.*[62].....59

Figure 2.7 – Acoustophoresis. a) Formation of a pressure node and two anti-nodes when a fundamental resonance frequency is applied with the width of the channel (w) being equal to half the wavelength of the ultrasound. b) Particles with acoustic contrast factors with opposite signs (*e.g.* red blood cells and lipid particles) are focused respectively on the pressure node and anti-nodes of the channel. c) and d) Examples of separation by acoustophoresis by a density-based, equilibrium method, and a size-based, kinetic method, respectively. e) Sheathless two-stage acoustophoresis device used to sort fixed DU145 CTCs spiked into RBC-lysed whole blood. The first stage pre-aligns the cells near the channel walls. At the second stage, the larger CTCs are focused faster towards the channel centre and collected in outlet 2.[149] Image from Xavier *et al.*[62] 61

Figure 2.8 – Dielectrophoresis. a) Schematic of the deflection of electric field lines by mammalian cells in a low conductivity suspending medium. On the left, the typical response to low-frequency electric fields with field lines bent around the cell creating a negative DEP force that pushes cells away from the high field region. On the right, the opposite scenario is represented with field lines drawn to the surface of the cell, resulting in a force which pulls cells towards high field regions. b) Theoretical model of the Clausius-Mossotti factor (f_{CM}) as a function of frequency for a viable cell in a suspending medium of conductivity 40 mS·m^{-1}. The response curves of three different cells differing in size (20 or 10 μm), membrane capacitance (20 or 10 mF·m^{-2}) or both, are represented. The following

parameters were used: membrane thickness, 5 nm, nuclear envelope thickness, 40 nm, nuclear radius, 5 μm, medium relative permittivity, 78.5, membrane conductivity, 10-5 $S \cdot m^{-1}$, cytoplasm conductivity, 0.6 $S \cdot m^{-1}$, Nuclear envelope conductivity, $5x10^{-3}$, nucleoplasm conductivity, 2 $S \cdot m^{-1}$, cytoplasm relative permittivity, 60, nuclear envelope relative permittivity, 20 and nucleoplasm relative permittivity, 120. c) Schematic of a possible dielectrophoresis sorting device including a region for focusing cells, a sorting region taking advantage of different cell's dielectric properties and a trapping region using positive DEP. Image from Xavier *et al.*[62] 63

Figure 3.1 – Real-time deformability cytometry. (a) Schematic of the RT-DC set-up. (b) shows images of a single cell deforming into the characteristic bullet-like shape in a 20 x 20 μm cross-sectional constriction within the microfluidic chip depicted in (a); scale bar: 50 μm. (c) shows the shear and normal stresses acting on a cell flowing in the constriction channel; black arrows indicate stress directions; surface colour indicates magnitude and blue lines show the flow profile in a co-moving reference frame. (d) shows deformation *vs* projected size (in μm^2) of HL-60 cells, measured at 0.32 $\mu L \cdot s^{-1}$, including isoelasticity lines, which divide a typical deformation scatter plot from a 30 μm x 30 μm constriction channel into areas of identical stiffness for multiples of a given elastic modulus (E_0). Solid black line highlights 50%-density contour. Adapted from Otto *et al.* Nat. Meth. 12, 199-202 (2015).[175] 71

Figure 3.2 – Real-time deformability cytometry. Deformation vs projected size (in μm^2) of HL-60 cells measured in isolation at increasing flow rates (0.12 – 0.32 $\mu L \cdot s^{-1}$). All scatter plots show deformation *vs* cell size (cross-sectional area) and experiments were carried out using the 30 x 30 μm cross-sectional channel; colour indicates density scale and each dot is representative of a single event from a total of 2,000 events. As a control, cells were imaged upstream of the constriction channel (reservoir) where deformation should not occur. The 50 %-density contour plots highlight the increase in cell deformation with no changes in cell size as could be anticipated. 72

Figure 3.3 – Real-time deformability cytometry. (a) MG-63 mixed 1:1 with HL-60; (b) shows deformation vs projected size (in μm^2) of MG-63 and HL-60 combining events from 3 measurements unbiasedly allocated using mixture models, with respective histograms demonstrating cell size and deformation distributions. The p-values were calculated using 1-dimensional linear mixed models. (c) Stro-1^+-enriched skeletal stem cells; (d) Human bone marrow mesenchymal stromal cells and (e) Stro-1^+-enriched skeletal stem cells mixed 1:1 with HL-60; All scatter plots show deformation *vs* cell size (cross-sectional area) and experiments were carried out at 0.32 $\mu L \cdot s^{-1}$ through the 30 x 30 μm cross-sectional channel; colour indicates density scale and each dot is representative of a single event from a total of 2,000 events. Images (f) to (h) show representative captures of the cells from (a, c, e) with the red line representing the contour determined by image analysis in real-time. 73

Figure 3.4 – Real-time deformability cytometry. (a) White blood cells obtained from RBC-lysed human whole blood. Images (b) and (c) show representative captures of WBCs flowing at 0.32 $\mu L \cdot s^{-1}$ through the 30-μm cross-sectional channel. The red line represents the contour determined by image analysis in real-time. (d) MG-63 mixed 1:2 with human WBCs. (e) Stro-1^+-enriched skeletal stem cells mixed 1:2 with human WBCs. Image shows scatter plots of deformation vs cell size (cross-sectional area); colour indicates density scale and each dot is representative of a single event from a total of 5,000 events. (f) Bar chart summarising size and deformation of WBCs, HL-60, MG-63, Stro-1^+-enriched skeletal stem cells and human BMSCs (MSCs) measured by real-time deformability cytometry. Values represent Mean ± SD ($N \geq 3$; *$p<0.05$, **$p<0.01$, ***$p<0.001$) with p-values obtained using 1-dimensional linear mixed models. 75

Figure 4.1 – (a) Diagram of the experimental protocol. Human bone marrow mononuclear cells (hBMMNCs) were obtained by density centrifugation of BM samples and enriched by MACS sorting of the Stro-1$^+$ population. Before expansion and at each passage and corresponding day *in vitro* (DIV), cells were analysed using microfluidic impedance cytometry (MIC), flow cytometry (FC), alkaline phosphatase (ALP) activity, and/or quantitative reverse transcription polymerase chain reaction (qRT-PCR). At passage 1, the same analyses were performed to detect changes in cells following osteogenic differentiation. (b) Shows the impedance cytometry set-up including the confocal-optical detection. Cells flow through the microchannel, passing between pairs of electrodes and the optical detection region. The fluorescence properties of the cell were measured simultaneously with the impedance allowing direct correlation of the electrical and fluorescent properties on a single cell basis. 79

Figure 4.2 – Simulation (in MATLAB™) of impedance response. (a) 7-µm polystyrene reference beads and (b-c) cells using a single-shell model with a suspending medium of conductivity 1.6 S·m^{-1}. The data shows three different cells, which differ in size (8 to 12 µm), or membrane capacitance (10 to 20 mF·m^{-2}). d) and e) Impedance response of the cells normalised to the reference beads. The two frequencies used in the study to calculate cell size (500 kHz) and opacity (2 MHz) are indicated by vertical dashed lines. Coloured full and dashed lines represent the real and imaginary parts of the signal respectively. The following parameters were used: membrane thickness, 5 nm, medium relative permittivity, 78.5, membrane conductivity, 10^{-5} S·m^{-1}, cytoplasm conductivity, 0.8 S·m^{-1} and cytoplasm relative permittivity, 60. 79

Figure 4.3 – Fluorescence-assisted microfluidic impedance cytometry of Stro-1-enriched human bone marrow mononuclear cells (hBMMNCs). a) Scatter plot of cell size (µm) *vs* electrical opacity (normalised to 7-µm diameter reference beads) of Stro-1$^+$-enriched hBMMNCs obtained from one individual patient. Top and bottom histograms demonstrate the cell size and opacity distributions respectively, with colour-coded Gaussian distributions fitted to the data. The dark red line represents the distribution of CD146$^+$ cells. b) and c) show histograms of the distribution of cell size and electrical opacity with increasing cell passage from one individual patient.....81

Figure 4.4 – Size and electrical opacity of cells analysed by microfluidic impedance cytometry. Bar charts summarise the cell size (a) and electrical opacity (b) of hBMMNCs in the bone marrow (BM), after expansion at passages 0 to 3, and following osteogenic differentiation (P1 Osteo). Within the BM, cell size and opacity were measured for Stro-1$^-$ cells, and both the CD146$^-$ and CD146$^+$ populations within the Stro-1$^+$ fraction. Skeletal stem cells (SSCs) are contained within the Stro-1$^+$/CD146$^+$ population. Also shown are data for two adherent (MG-63 and Saos-2) and one suspension (HL-60) human cancer cell lines. c) and d) show the mean ± SD for each individual analysed patient sample. The appended table summarises the statistical analyses of the data with the top-right and bottom-left values showing the p-values for cell size and opacity, respectively. Values represent mean ± SD ($N \geq 3$; *$p < 0.05$; **$p < 0.01$; ***$p < 0.001$; N.S. – not significant, with p-values obtained using the one-way analysis of variance (ANOVA) with Tukey's post-hoc test for samples that followed a normal distribution or the Mann-Whitney U-test for samples that did not follow a normal distribution). 82

Figure 4.5 – Optical microscopy. Images show apparent changes in the size and morphology of unexpanded hBMMNCs after enrichment of the Stro-1$^+$ population by MACS (BM after MACS) and at different passages (P0 to P3) growing under basal expansion conditions. Cells typically appeared to grow larger and were observed to display a spread morphology with increasing passage. Scale bar 500 µm (100 µm in BM) in top panel and 200 µm (50 µm in BM) in lower panel.....83

Figure 4.6 – Proliferation and alkaline phosphatase activity of Stro-1-enriched human bone marrow mononuclear cells (hBMMNCs). a) Total DNA quantification from hBMMNCs grown for 14 days at each passage (P0-P3) determined using the PicoGreen® nucleic acid quantitation assay. b) Specific ALP activity of hBMMNCs grown for 14 days at each passage determined by the colorimetric detection of the dephosphorylation of p-nitrophenyl phosphate. Values represent mean ± SD (N = 4). 84

Figure 4.7 – Quantitative reverse-transcriptase polymerase chain reaction. Relative gene expression of relevant genes of interest of Stro-1$^+$-selected human bone marrow mononuclear cells (hBMMNCs) grown in basal expansion conditions at different passages (P0-P3). *GNL3* is associated with stem cell proliferation, *RUNX2*, *ALPL*, *COL1A1* and *BGLAP* are genes related with the process of osteogenesis and *PPARG* is a regulator of adipocyte differentiation. Values represent mean ± SD normalised to the expression levels of hBMMNCs at passage 0 (N = 4; *p < 0.05, with p-values obtained using the one-way analysis of variance (ANOVA) with Tukey's post-hoc test or the Mann-Whitney U-test for samples that followed or did not follow a normal distribution respectively..... 85

Figure 4.8 – Alkaline phosphatase (ALP) activity. ALP staining of human BM colony forming units-fibroblastic (CFU-F) grown on 6-well plates for 14 days under basal expansion conditions or following osteogenic (osteo) differentiation. Images represent an entire well captured using a dissecting stereoscope. 85

Figure 4.9 – Quantitative reverse-transcriptase polymerase chain reaction. Relative gene expression of relevant genes of interest of passage 1 Stro-1$^+$-selected hBMMNCs after 14 days following osteogenic (osteo) differentiation. *GNL3* and *SOX2* are associated with stem cell proliferation and stem cell maintenance respectively. *RUNX2*, *ALPL*, *COL1A1* and *BGLAP* are genes related with the process of osteogenesis, with *RUNX2* and *BGLAP* being early and late osteogenic markers respectively. *SOX9* and *COL2A1* are genes associated with chondrogenic differentiation, and *PPARG* and *FBAP4* with adipocyte differentiation. Values represent mean ± SD normalised to the expression of hBMMNCs growing under basal expansion conditions (N ≥ 4; *p < 0.05; ***p < 0.001, with p-values obtained using the Student's t-test for independent samples). 86

Figure 5.1 – Particle sorting by deterministic lateral displacement based on differences in particle size (left) and deformation (right). In size-based separation, particles with a radius smaller than Rc (red) are predominantly affected by the streamline flowing closest to the micropillar and are not forced to cross streamlines, zigzagging throw the microarray. In deformation-based cell sorting, particles with similar size but different deformability can be sorted due to an effective change in particle size upon deformation due to gradient shear stresses, acceleration and interaction with the micropillars. Here, the more compliant red particle deforms to an extent that its radius becomes smaller than R_C allowing it to continue along the original streamline..... 90

Figure 5.2 – Predicted cell trajectories in DLD devices from designs 1 and 2. In Design 1 (top), cells are initially focused hydrodynamically in a single flow stream. Larger particles (green) are displaced away from the smaller particles (red) which zigzag through the pillar array maintaining a null net displacement. In Design 2 (bottom), cells introduced from a single inlet are initially displaced towards the outer channel walls in a first section with a small critical separation size (D_{C1}), creating a central cell-free stream. In section 2, the direction of the micropillar array is inverted vertically and the D_C increased to displace only larger particles (green) into the central cell-free stream while smaller particles (red) continue zigzagging near the channel walls. 91

Figure 5.3 – Size and deformation-based particle sorting a) Purity of 16 (red) and 24-µm (green, dotted) beads mixed 1:1 and sorted by DLD at an inlet pressure of 250 mbar. Percentages of the fractions collected in each outlet were calculated from flow cytometry data. Bars show mean ± SD (N=6) and circles show the mean purity of individual experiments. b) Binary fractionation of MG-63 as a function of cell deformation induced by increasing overpressure at the inlet (100-1000 mbar). As the input pressure was increased, the flow rate increased leading to accentuated cell deformation. Green (dotted) and red bars show the percentage of MG-63 collected at the 'larger' and 'smaller' outlets respectively (N=2). As a control, non-deformable 16-µm (closed circles) and 24-µm (open circles) polystyrene beads were flowed in the same conditions with the sorting purity remaining consistent up to 1 bar. 93

Figure 5.4 – Cell deformation in a DLD device. a) to f) show images following the movement of a single MG-63 (red arrow) cell flowing from left to right through a deterministic lateral displacement micropillar array at an inlet pressure of 1,000 mbar (corresponding to an estimated mean flow speed of 10 $cm \cdot s^{-1}$). Images were taken using a high-speed camera (Vision Research, Wayne, NJ, USA) and bespoke software (Phantom Camera Control Software, Vision Research). Cell deformation due to shear stresses and interaction with the micropillars is shown. Cell deformation changes the effective cell size altering its trajectory in the DLD device. 93

Figure 5.5 – Size and deformation-based sorting of MG-63 and HL-60. a) and b) show fluorescence microscopy images (Zeiss Axiovert 200 microscope, 5x objective) of the cell fractions from the 'smaller' and 'larger' outlets respectively. Green and red fluorescence corresponds to GFP^+ MG-63 cells and CellTracker™ deep red-labelled HL-60. c) and d) show the purity of MG-63 (green, dotted) and HL-60 (red) cells collected from the smaller and larger outlets, after separation at varying flow rates (15-200 $\mu L \cdot min^{-1}$). Values show mean ± SD (N=5). 94

Figure 5.6 – Binary fractionation of skeletal stem cells as a function of cell deformability. a) Fraction of SSCs collected at the smaller (red) and larger (green, dotted) outlets *vs* flow rate. b) and c) show the median and mean FSC-A values of the cells collected at the smaller (red) and larger (green, dotted) outlets, respectively. d) CFU-F formation capacity of SSCs after sorting by DLD. Overall, the capacity to form CFU-F was not affected by DLD (dashed line shows the number of CFU-F obtained for unsorted SSCs). At 15 $\mu L \cdot min^{-1}$, where the highest difference in cell size was observed, smaller cells (red) displayed a reduced capacity to form clonogenic cultures when compared with SSCs collected in the larger outlet (green, dotted). Values show mean ± SD (N=3; $*p < 0.05$; $***p < 0.001$ with p-values obtained using the Student's t-test for independent samples). 95

Figure 5.7 – Binary fractionation of skeletal stem cells as a function of cell deformability. Colony forming units-fibroblastic (CFU-F), counterstained with crystal violet, growing in wells of a 6-well plate. SSCs were sorted by DLD at 15 $\mu L \cdot min^{-1}$, collected from the smaller and larger outlets and plated at a cell seeding density of 10 $cells \cdot cm^{-2}$. Cells collected at the smaller outlet appear to display a lower capacity to form clonogenic cultures. 97

Figure 5.8 – Size and deformation-based sorting of white blood cells (WBCs) and expanded skeletal stem cells (SSCs) at passage 0. a) and b) purity of SSCs (green, dotted) and WBCs (red) collected from the smaller and larger outlets respectively, after sorting at varying flow rates (15-100 $\mu L \cdot min^{-1}$). c) CFU-F formation capacity of unsorted SSCs (dashed line) and SSCs collected at the smaller (red) and larger (green, dotted) outlets after sorting by DLD. Values show mean purity and CFU-F number (N=1). 98

Figure 5.9 – Size and deformation-based sorting of white blood cells (WBCs) and expanded skeletal stem cells (SSCs) at passage 0. Forward and side scatter distributions of CD45-labelled WBCs (red) and SSCs (green) labelled with CellTracker™ green, unsorted and collected at the larger outlet after label-free sorting by DLD. Contour levels were set at 5 %. 98

Figure 5.10 – Size and deformation-based sorting of human bone marrow mononuclear cells. Forward and side scatter distributions of hBMMNCs unsorted and collected at the smaller and larger outlets after label-free sorting by DLD. Contour levels were set at 5 %..... 99

Figure 7.1 – Representative images of the skeletal stem cell enrichment protocol. a) cell pellet and fat accumulation resulting from the initial wash; b) use of cell strainers to remove bone debris and soft tissue from the cell suspension; c) cell suspension layered upon lymphoprep™ for density centrifugation; d) formation of the 'buffy coat' at the interface between α-MEM and lymphoprep™; and e) shows the resulting fractions after careful collection of the buffy coat. The tube on the left contains the buffy coat diluted in culture media while the one on the right shows the pelleted erythrocytes and polymorphonuclear cells, and the culture media and platelets in suspension, which are discarded..... 106

Figure 7.2 – Current enrichment process of human bone marrow mononuclear cells. Bone marrow samples are centrifuged across a density gradient and the buffy coat enriched for Stro-1^+ cells by magnetic activated cell sorting (MACS) using a mouse hybridoma monoclonal IgM antibody coupled to superparamagnetic rat anti-mouse microbeads. The sorted fraction is plated in culture flasks and further enrichment is achieved by adhesion to tissue culture plastic. 107

Figure 7.3 – Deterministic lateral displacement device designs. Magnifications of the mask drawings for DLD devices from designs 1 (a) and 2 (b). Close-ups show individual sections elucidating the filter array included at the sample inlet (a-i and b-i); the individual (a-ii) and mirrored (b-ii and iii) displacement arrays from design 1 and 2 respectively; the curved channels with varying width and length connecting the two main channels in design 2 devices (b-iv); and the two channel outlets that allow collection of the sorted cell fractions in each of the device designs (a-iii and b-v). 113

Figure 7.4 – Computational fluid dynamics simulation. 2-D plots of critical sections (a and b, channel outlets; and c, curved connecting channels) from design 2 devices with channels of different length and width. Streamlines demonstrate that the flow is split evenly before entering each channel. This ensures that particles will retain their relative lateral position between the different sections. The 2-D simulations were a courtesy of Stefan Holm from the University of Lund, Sweden and were conducted using COMSOL Multiphysics 5.0. 113

Figure 7.5 – Deterministic lateral displacement. a and b) silicon master moulds of DLD devices from generation 1 and 2 respectively; c and d) final DLD devices from each generation mounted on PDMS-coated microscope glass slides; the channels were filled with blue dye for visualisation; e) and f) show optical microscopy cross-sectional images of a generation 1 DLD device showing the pillar array; g)-j) scanning electron micrographs (SEM) showing different perspectives of the DLD devices on PDMS. SEM images were taken by Dr Stefan Holm (University of Lund, Sweden). 116

List of Supplementary Figures

Figure S1 – Real-time deformability cytometry of HL60 and MG-63 cells. Cells were mixed 1:1 and measured at flow rates of 0.12 μL·s^{-1}, 0.16 μL·s^{-1}, 0.32 μL·s^{-1} and in the reservoir for reference. Measurements were carried out using a 30-μm cross-section microfluidic channel at a frame rate of 2,000 fps..... 129

Figure S2 – Real-time deformability cytometry of skeletal stem cells. Cells were measured at flow rates of 0.16 μL·s^{-1}, 0.32 μL·s^{-1} and in the reservoir for reference. Measurements were carried out using a 30-μm cross-section microfluidic channel at a frame rate of 2,000 fps. 129

Figure S3 – Real-time deformability cytometry of human bone marrow stromal cells. Cells were measured at flow rates of 0.16 μL·s^{-1}, 0.32 μL·s^{-1} and in the reservoir for reference. Measurements were carried out using a 30-μm cross-section microfluidic channel at a frame rate of 2,000 fps. 130

Figure S4 – Real-time deformability cytometry of human skeletal stem cells and HL-60. Cells were mixed 1:1 and measured at flow rates of 0.16 μL·s^{-1}, 0.32 μL·s^{-1} and in the reservoir for reference. Measurements were carried out using a 30-μm cross-section microfluidic channel at a frame rate of 2,000 fps..... 130

Figure S5 – Real-time deformability cytometry of human white blood cells. Cells were measured at flow rates of 0.16 μL·s^{-1}, 0.32 μL·s^{-1} and in the reservoir for reference. Measurements were carried out using a 30-μm cross-section microfluidic channel at a frame rate of 2,000 fps. 131

Figure S6 – Real-time deformability cytometry of human white blood cells and MG-63. Cells were mixed 2:1 and measured at flow rates of 0.16 μL·s^{-1}, 0.32 μL·s^{-1} and in the reservoir for reference. Measurements were carried out using a 30-μm cross-section microfluidic channel at a frame rate of 2,000 fps..... 131

Figure S7 – Real-time deformability cytometry of human white blood cells and skeletal stem cells. Cells were mixed 2:1 and measured at flow rates of 0.16 μL·s^{-1}, 0.32 μL·s^{-1} and in the reservoir for reference. Measurements were carried out using a 30-μm cross-section microfluidic channel at a frame rate of 2,000 fps..... 132

Figure S8 – Fluorescence-assisted microfluidic impedance cytometry of Stro-1-enriched human bone marrow mononuclear cells (hBMMNCs). a–f) Scatter plots of cell size (μm) vs electrical opacity (normalised to 7-μm diameter reference beads) of Stro-1^{+}-enriched hBMMNCs obtained from six individual patients..... 133

Figure S9 – Alkaline phosphatase activity. Alkaline phosphatase staining of human BM CFU-F colonies grown under basal expansion conditions at different passages (passage 0 to passage 3). 133

List of Tables

Table 1.1 – Donor information and number of BMMNC before and after MACS sorting of Stro-1-labelled cells..... 40

Table 1.2 – Donor information and percentage of human BMMNCs in each cell fraction of the scatter plots depicted in Figure 1.3. With MACS sorting of Stro-1^+ cells a consistent enrichment towards the monocyte and lymphocyte fractions is evident accompanied by granulocyte depletion..... 42

Table 2.1 – Summary of the best performance examples of the reviewed microfluidic label-free sorting techniques..... 66

Table 2.2 – Current label-free microfluidic applications to stem and progenitor cell sorting. When not referred in the papers, $5x10^9$ and $5x10^6$ red and white blood cells per millilitre of blood, respectively, were considered as reference values for the performance calculations..... 67

Table 2.3 – Current label-free microfluidic applications to circulating tumour cell (CTC) sorting. When not referred in the papers, $5x10^9$ and $5x10^6$ red and white blood cells per millilitre of blood, respectively, were considered as reference values for the performance calculations..... 68

Table 7.1 – Primers used for qRT-PCR (F: forward and R: reverse)..... 109

Table 7.2 – Specifications of the deterministic lateral displacement devices..... 112

Table 7.3 – Microfabrication specifications..... 115

List of Supplementary Tables

Table S1 – Standard normal distribution. Table values (negative) represent area to the left of the Z-score. 135

Table S2 – Standard normal distribution. Table values (positive) represent area to the left of the Z-score. 136

Author's Declaration

I, Jorge Miguel Queiroz de Almeida Xavier, declare that this thesis entitled "*Label-free, microfluidic characterisation and sorting of human skeletal stem cells*" and the work in it presented are my own and have been generated by me as the result of my own original research, unless when specifically stated otherwise.

I confirm that:

1. This work was done wholly while in candidature for a research degree at this University;
2. Where I have consulted the published work of others, this is always clearly attributed;
3. Where I have quoted from the work of others, the source is always given. With the exception of such quotations, this thesis is entirely my own work;
4. I have acknowledged all main sources of help;
5. Where the thesis is based on work done by myself jointly with others, I have made clear exactly what was done by others and what I have contributed myself;
6. Parts of this work have been published as:
    a. Xavier, M., de Andrés, M. C., Spencer, D., Oreffo, R. O. C., & Morgan, H. Size and Dielectric Properties of Skeletal Stem Cells Change Critically After Enrichment and Expansion from Human Bone Marrow: Consequences for Microfluidic Cell Sorting*. J. R. Soc. Interface* 14, 20170233 (2017
    b. Xavier M., Spencer D., Oreffo R.O.C. & Morgan H. Label-free microfluidic sorting of primary human skeletal stem cells for bone regeneration: a bio-physical characterisation. In: *20th International Conference on Miniaturized Systems for Chemistry and Life Sciences, MicroTAS* (2016) Dublin, Ireland. (Conference proceedings)
    c. Xavier M, Rosendahl P, Herbig M, Spencer D, Otto O, Guck J, Oreffo, R.O.C. & Morgan, H. Primary human skeletal stem cell bio-physical characterisation for high-purity microfluidic cell sorting and enrichment. In: Towards Future regenerative Therapies TERMIS-EU 2016 Conference. Uppsala, Sweden: *European Cells and Materials* (2016) pp378. (Conference proceedings)

d. Xavier, M., Oreffo, R. O. C., & Morgan, H. Skeletal stem cell isolation: A review on the state-of-the-art microfluidic label-free sorting techniques. *Biotechnol. Adv.* 34, 908–923 (2016).

e. Xavier, M., Rosendahl, P., Herbig, M., Kräter, M., Spencer, D., Bornhäuser, M., Oreffo, R. O. C., Morgan, H., Guck, J., & Otto, O. Mechanical phenotyping of primary human skeletal stem cells in heterogeneous populations by real-time deformability cytometry. *Integr. Biol.* 8, 616–623 (2016).

f. Xavier M, Rosendahl P, Herbig M, Spencer D, Otto O, Guck J, Oreffo, R.O.C. & Morgan, H. Skeletal stem cell sorting: characterisation of physical properties for microfluidic separations applications. In: Tissue and Cell Engineering Society (TCES) meeting. Southampton, UK: *European Cells and Materials* (2015) pp109. (Conference proceedings)

Signed:

Date:

α-MEM – alpha minimum essential medium
μTAS – Micro total analysis systems
AFM – Atomic force microscopy
ALP – Alkaline phosphatase
APC – Allophycocyanin
BM – Bone marrow
BMMNC – Bone marrow mononuclear cell
BMP – Bone morphogenetic protein
BMSC – Bone marrow stromal cell
BSA – Bovine serum albumin
CD – Cluster of differentiation
CFU-F – Colony forming unit-fibroblastic
CHB – Centre for hybrid biodevices
CMFDA – 5-chloromethylfluorescein diacetate
CMOS – Complementary metal-oxide semiconductor
CT – Cycle threshold
CTC – Circulating tumour cell
CTG – CellTracker™ Green
DEP – Dielectrophoresis
DEP-FFF – Dielectrophoretic field flow fractionation
DIV – Days *in vitro*
DLD – Deterministic lateral displacement
DMEM – Dulbecco's modified eagle's medium
DNA – Deoxyribonucleic acid
ECACC – European collection of authenticated cell cultures
ECM – Extracellular matrix
EDTA – Ethylenediamine tetraacetic acid
EpCAM – Epithelial cell adhesion molecule
ESC – Embryonic stem cell
EU – European Union
FACS – Fluorescence-activated cell sorting
FC – Flow cytometry
FCS – Foetal calf serum
FSC – Forward scatter
GEDI – Geometrically enhanced differential immunocapture
GFP – Green fluorescent protein
HSC – Haematopoietic stem cell
INEB – Instituto de Engenharia Biomédica
LAPASO – Label-free particle sorting

LED – Light-emitting diode
MACS – Magnetic-activated cell sorting
MASC – Multipotent adult stem cell
MEMS – Microelectromechanical systems
MIC – Microfluidic impedance cytometry
MSC – Mesenchymal stem cell
NASA – National aeronautics and space administration
NSPC –Neural stem and progenitor cells
PBPC – Peripheral blood progenitor cell
PBS – Phosphate buffered saline
PDMS – Polydimethylsiloxane
PhD – Doctor of Philosophy
PI – Principal Investigator
QMS – Quadrupole magnetic flow sorter
qRT-PCR – Quantitative reverse transcription polymerase chain reaction
RBC – Red blood cell
(m)RNA – (messenger) Ribonucleic acid
RPMI – Roswell Park Memorial Institute
RT-DC – Real-time deformability cytometry
SD – Standard deviation
SEM – Scanning electron microscopy *and* standard error of mean
SRC – Sweatshop Running Community
SSC – Skeletal stem cell *and* Side scatter
TE – Tris-EDTA
UK – United Kingdom
US – United States
UV – Ultraviolet
WBC – White blood cell

Variables

- ϵ – Electric permittivity ($F \cdot m^{-1}$)
- η – Dynamic viscosity ($Pa \cdot s$)
- ρ – Mass density ($kg \cdot m^{3}$)
- σ – Electric conductivity ($S \cdot m^{-1}$)
- Φ – Acoustic contrast factor
- ω – Angular frequency ($rad \cdot s^{-1}$)
- a – Acceleration ($m \cdot s^{-2}$)
- A – Area (m^2)
- atm – Atmosphere (1.01325×10^5 Pa)
- B – Magnetic field gradient ($T \cdot m^{-1}$)
- C – Circularity
- c – Speed of sound ($m \cdot s^{-1}$)
- D – Deformability
- d – Particle diameter (m)
- D_C – Critical separation size
- De – Dean Number
- D_h – Hydraulic diameter (m)
- F – Force (N)
- G – Gap (m)
- h – Height (m)
- I – Current (A)
- Kn – Knudsen number
- l – Cell perimeter (m)
- L – Length (m)
- m – Mass (kg)
- P – Pressure (Pa)
- R – Radius (m)
- Re – Reynolds number
- R_h – Hydraulic resistance ($Pa \cdot s^{-1} \cdot m^3$)
- u – Flow velocity ($m \cdot s^{-1}$)
- V – Voltage (V)
- T – Temperature (K)
- w – Width (m)

Constants

- K_B – Boltzmann constant ($m^2 \cdot kg \cdot s^{-2} \cdot K^{-1}$)
- μ_0 – Permeability of free space ($m \cdot kg \cdot s^{-2} \cdot A^{-2}$)

Units

Ω – Ohm

A – Ampere

F – Farad

h – Hour

K – Kelvin

L – Litre

m – Metre

min. – Minute

N – Newton

Pa – Pascal ($N \cdot m^{-2}$)

rad – Radians

s – Second

S – Siemens

T – Tesla

V – Volt

Chapter 1

Skeletal Stem Cells

"I took a good clear piece of cork, and with a Penknife sharpen'd as keen as a Razor, I cut a piece of it off, and thereby left the surface of it exceeding smooth, then examining it very diligently with a Microscope, me thought I could perceive it to appear a little porous. … I no sooner discern'd these (which were indeed the first microscopical pores, (or cells), I ever saw, and perhaps, that were ever seen, for I had not met with any Writer or Person, that had made any mention of them before this)."

Robert Hooke, *Micrographia*, 1665.

1.1. Motivation

The 20th century has brought about a number of game-changing revolutions in medical practice and research. For example, in 1901, Karl Landsteiner introduced the ABO classification system for blood typing leading the way to safe blood transfusion. In 1928, Alexander Fleming accidentally discovered the first antibiotic, penicillin, whilst studying the influenza virus responsible for seasonal flu. 1980 saw the first complete eradication of a disease, smallpox, after a vaccination programme that had started almost 200 years earlier.[1] Since the millennium, medical research continues apace and, in mid-2017, the first gene therapy was approved in the US using genetically modified T cells to fight cancer.

Collectively, medical advances have extended life expectancy in developed countries from an average of just 65 years in 1950 to almost 80 years today.[2] However welcome this rise in longevity might be, it also leads to an increasingly aged population, which is associated with exacerbated health issues and higher demands for personalised, directed and effective regenerative therapies.[3,4] Within the musculoskeletal arena, increased bone and joint trauma as well as metabolic bone disease are associated with advancing years prompting the need to search for innovative strategies for tissue augmentation to aid repair and regeneration.

1.2. Definition

As denoted by the quotation in the epigraph, the first reference to the existence of biological cells can be traced as far back as the second half of the 17th century. While the concept of cells working as building blocks in all biological systems has long been known, the existence of a cell or group of cells that can give rise to the different, specialised cell constituents of any multi-cellular organism is far more recent[5] and was only demonstrated for the first time by Till and McCulloch in 1961 for haematopoietic stem cells (HSCs).[6,7] This finding post-dates even the first successful bone marrow (BM) transplant in 1956.[8,9] Today, the term 'stem cell' defines cells with the capacity to i) self-renew, *i.e.* to establish *in vivo*

a population with the same phenotype which can be serial passaged and transplanted and ii) to differentiate to form specialised cells with a defined function within a tissue.[10,11]

Stem cells can be classified according to their differentiation potential ranging from totipotent, the most potent class of stem cells, to unipotent, which comprises stem cells or progenitors that have the capacity to self-renew but can only differentiate to form one specific kind of specialised cells.[12] A noticeable example of a totipotent stem cell is the fertilised egg or zygote, which is capable of fully generating a new, complex living being including all the extraembryonic structures that support its development such as the placenta.[13] Embryonic stem cells (ESCs) are an example of pluripotent stem cells with the capacity to differentiate into all the different cell types that constitute an organism but without the potential to produce a fertile, adult individual in isolation.[13]

A class of stem cells of particular interest in this programme of research are multipotent adult stem cells (MASCs). MASCs are present in the adult and have limited differentiation capacity being only able to differentiate into the cell types that constitute a certain tissue or organ. HSCs are an example of MASCs resident within the bone marrow, with the capacity to form all the cells found in blood through the process of haematopoiesis.[14] Given MASCs can be obtained from adults, these cells provide an invaluable resource for regenerative medicine applications circumventing the ethical considerations typically associated with the use of pluripotent ESCs (destruction of a human embryo).

Bone has unique regenerative capacity and continually remodels throughout adult life.[15] This suggests the presence within the bone of a MASC, other than the HSC, that contributes to skeletal development and without which bone fractures would not heal. Indeed, over half a century ago a series of events led to the acceptance of a stem cell within bone marrow specifically committed to the bone-bone marrow organ. Alexander Friedenstein and his colleagues were the first to observe that BM cells were capable of ectopic bone formation upon transplantation in mice using diffusion chambers.[16] Later, Tavassoli and Crosby (1968) noted that BM transplantation within an open system led not only to the formation of bone but also of new bone marrow tissue.[17] Friedenstein attributed the osteogenic potential of cells in BM to an adherent, clonogenic and non-haematopoietic stromal fraction capable of forming discrete fibroblastic colonies *ex vivo*, termed colony-forming units-fibroblastic (CFU-F).[18,19] Joint work by Alexander Friedenstein and Maureen Owen in 1988, almost 20 years after Friedenstein's pioneering studies, summarised and delineated the formation of different tissues from single clones of BM stromal cells (BMSCs), including bone, cartilage, marrow adipocytes and haematopoiesis-supportive stroma. This formulated the first hypothesis of the existence within the BM of a multipotent stromal progenitor, or skeletal stem cell (SSC).[20]

However, to satisfy the requirements of a 'stem cell', evidence was required that the SSC was capable of self-renewal. This was only demonstrated in 2007 in seminal studies from the group of Paolo Bianco who demonstrated that SSCs are a perivascular, sub-endothelial cell population that resides over BM sinusoids, with the capacity to establish a functional BM haematopoietic microenvironment when transplanted clonally *in vivo,* and can be re-isolated in culture and serially expanded from the *de novo* formed tissue.[21,22]

It is important to note that the term SSC should be distinguished from mesenchymal stem cells (MSCs). The two terms have been used interchangeably but while the term MSC was first introduced to refer to cultures of BMSCs,[23] which indeed include the SSC, it was later extended to define cells from non-skeletal tissues[24] and has become ambiguous. In summary, the SSC is defined as the multi-potent and self-renewing stromal progenitor, that resides over BM sinusoids, and that can support and regulate haematopoiesis *in vivo* and that retains the ability to differentiate to form the skeletal-specific tissues of bone, cartilage and marrow adipocytes.[11,25]

1.3. Skeletal Stem Cell Applications

Applications of SSCs include i) the fundamental study of stem cells, disease mechanisms, and the developmental processes of musculoskeletal tissue, ii) pharmaceutical studies targeting bone and joint disease, and iii) the use of SSCs for regenerative medicine applications in the clinic including stem cell therapies and tissue engineering targeting non-union fractures, healing of critical-sized defects or articular cartilage regeneration. Together, these applications could offer alternatives to the current gold standards for treating small defects – autografts, and for replacing large volumes of lost tissue – human allografts, both associated with specific disadvantages such as donor site morbidity and, the risk of disease transmission and immunogenic reaction, respectively.[26]

The ability of BMSCs to generate histology-proven bone *in vivo* has been repeatedly demonstrated.[25,27–32] Although intravenous infusion of BMSCs has been exploited,[25,33,34] bone formation *in vivo* has been most successful upon direct transplantation of BMSCs to the defect site. However, the ability to retain the transplanted cells at the site of injury remains a challenge. Other hurdles include the capacity to promote the formation of new vasculature that supports tissue growth and to direct BMSCs towards the differentiation pathways needed to recapitulate the phenotype of the damaged tissue.[25] Typical approaches to bridge this gap include the combination of cells with a number of growth factors and biomaterials, either in the form of injectable hydrogels or solid scaffolds including ceramics (*e.g.* hydroxyapatite, tri-calcium phosphates), polymers (*e.g.* polylactic acid) and metals (*e.g.* titanium, tantalum). These strategies often improve the recapitulation of the natural processes occurring in bone development, by the actuation of chemical and/or mechanical cues.[35–37] Recent multidisciplinary research has generated alternative approaches based for example on the use of advanced 3D-printers to design complex cell-laden tissue engineering constructs.[38]

Despite these challenges, SSCs have been used with success in specific clinical applications (reviewed in Bianco, 2015[25]). For example, SSCs have been shown to improve bone graft integration contributing to the generation of new bone in the femoral heads of human patients.[26,32,39] SSCs in combination with a scaffold and bone morphogenetic protein 7 (BMP7) have also been shown to contribute to the regeneration of a large mandibular defect in a human patient.[40,41] Osteoprogenitor cells from a concentrated buffy coat have been used in the treatment of osteonecrosis and fracture non-unions.[42,43] Union was achieved after injection in the tibia in 53 out of 60 patients.[43] Critically, the seven persistent non-

unions all had significantly lower CFU-F counts, and the study determined that a BM graft needed to contain over 1,000 progenitors per cm^3 for the treatment to be successful. This exceeds the level present in fresh iliac crest aspirates, which average 600 per cm^3, and emphasises the need for the development of cell enrichment strategies.[26,43]

As people live longer, robust and reproducible clinical translation of autologous SSC sources holds great potential to provide vital alternatives to the current therapeutic strategies for bone and cartilage repair. These novel approaches could have an important impact to reduce morbidity and provide simple and safe strategies to improve survival and quality of life.

1.4. Limitations Hampering Clinical Translation

Challenges affecting the translation of SSCs to the clinic include i) the isolation and expansion of SSCs *ex vivo*, ii) the targeting and delivery of SSC populations to the site of repair and iii) the timely and directed differentiation of SSCs towards relevant stromal lineages.[25,28,39] This thesis focuses specifically on the challenge of isolating pure and homogeneous multipotent SSC populations from human BM. This challenge is critical not only to provide sufficient homogeneous SSCs for clinical application but also to provide defined populations as a foundation to study the physiology of SSCs, musculoskeletal development, and to develop appropriate strategies to deliver SSCs efficiently and to promote their functionality *in vivo*.

Current strategies to isolate SSCs from BM employ cell adhesion to tissue culture plastic, as developed from Friedenstein's protocols.[16,18,19,44] This is highly efficient as most of the cells from the BM derive from haematopoietic lineages and are non-adherent.[45] However, plastic adhesion is non-specific (*i.e.* other adherent cells are also selected), time-consuming and can result in the alteration of the original SSC phenotype present in the BM microenvironment.[46] Critically, Friedenstein's work showed that only around 15 % of expanded CFU-F clones were able to differentiate and re-capitulate a functional BM-haematopoietic microenvironment.[44] Furthermore, extensive expansion of CFU-F cultures typically leads to a progressive loss of proliferative capacity and multipotency.[28]

To enhance the specificity of adhesion isolation protocols, antibody-based strategies are often used. Antibodies can target molecules both intracellularly and at the cell surface and, in conjugation with fluorescent dies or magnetic beads, allow cells to be sorted using conventional fluorescence- and/or magnetic-activated cell sorters (FACS and MACS). FACS and MACS are costly, involve lengthy protocols and can affect cell viability but when a specific marker is available high levels of cell enrichment can be achieved typically delivering essentially pure cell populations.[47,48]

Different combinations of SSC markers have been explored to enhance the purity of SSCs. In 2003, Gronthos *et al.* obtained a 950-fold enrichment of CFU-F formation after MACS sorting hBMSCs labelled with the Stro-1 antibody.[49] Subsequent FACS sorting of $CD146^+$ cells further improved the separation efficiency to 2,000-fold.[50] Stro-1, first described by Simmons and Torok-Storb, is relatively widely used for selecting high growth-potential CFU-Fs.[51-54] The identity of Stro-1 remained elusive for over two decades but was

recently described to bind to heat shock cognate 70 (HSC70/*HSPA8*) on the surface of approximately 10 % of human BM mononuclear cells (hBMMNCs).[53,55] CD146 (melanoma cell adhesion molecule) exists on a marginal sub-population of hBMMNCs that contribute to the regulation of haematopoiesis.[21,56,57] However, neither of these markers is specific to SSCs limiting the efficiency of antibody-dependent isolation methods. Critically, the SSC is estimated to represent fewer than 1 in every 10,000 hBMMNCs,[44,45] and even a 2,000-fold enrichment results in a purity of, at best, 1 in every 5 cells. Given the ambiguous definition of the SSC, multiple different markers have been proposed but equally lack unique specificity (Figure 1.1).[28,39,54,58]

There is thus an urgent need to design new methods to provide homogeneous SSC populations. While a selective SSC marker is yet to be identified, alternative strategies will involve sorting mechanisms that do not rely on the use antibodies (label-free), but can sort single cells based on a potentially characteristic biophysical phenotype. The application of microfluidics for the development of label-free sorting approaches is introduced in Chapter 2 of this thesis.

1.5. Skeletal Stem Cell Enrichment using the Stro-1 antibody

Although antibody-based approaches do not provide pure SSC populations, BMSCs require a degree of enrichment to obtain representative SSC populations. Throughout this work BM samples were commonly enriched by density centrifugation followed by MACS sorting using Stro-1, and adhesion of the sorted fraction to tissue culture plastic, in the presence of foetal calf serum. A detailed description of this protocol along with representative illustrations can be found in Materials and Methods, section 1.5.

During the course of this work, 26 BM samples were obtained from patients undergoing total hip replacement surgeries, and processed for SSC characterisation and sorting.

Table 1.1 summarises the donor information of all obtained samples and the number of BMMNCs obtained after density centrifugation (before MACS) and after magnetic separation of Stro-1$^+$ cells. As expected, the majority of samples were obtained from female donors, which is representative of the higher incidence of osteoporotic fractures in women.[59-61] There was a striking variation in the number of cells obtained following density centrifugation ranging from 8 million to 1,400 million cells. This is indicative of the significant sample variability between different patients and reflects also the variation of the amount of tissue collected during surgery. Similarly, the percentage of Stro-1$^+$ selected cells varied between 2.6 and 21.6 %, a difference of almost 10-fold. Nevertheless, the mean percentage of Stro-1 selected cells was 9.7 ± 5.2 %, in agreement with literature reports.[53] After enrichment by MACS the sorted fractions were typically plated and further enrichment achieved by cell adhesion and CFU-F formation. Figure 1.2 shows images of characteristic colonies at different stages of human BMMNC (hBMMNC) selection and expansion.

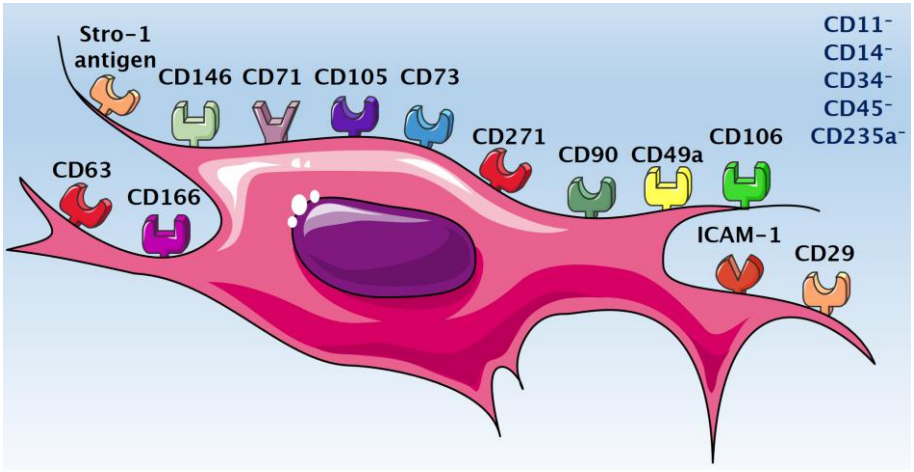

Figure 1.1 – Cell surface antigens of human bone marrow skeletal stem cells. Image adapted from Xavier *et al*.[62]

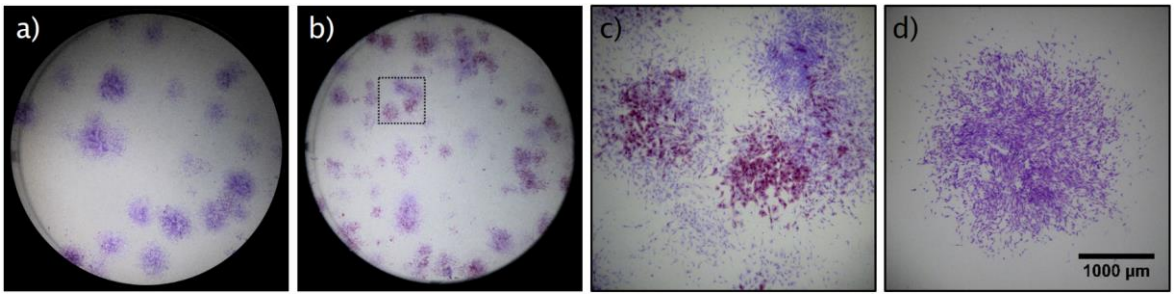

Figure 1.2 – CFU-F staining for alkaline phosphatase (red) and DNA/protein (crystal violet, purple). a) and b) show images of wells from a 6-well plate of unsorted BMSCs after density centrifugation at 14 days *in vitro*. c) shows a higher magnification of a section in b) highlighting the heterogeneous cell phenotype and variation in level of ALP expression in BMSC colonies. d) Colony of Stro-1 enriched BMSCs plated at passage 1 (28 days *in vitro*)

Table 1.1 – Donor information and number of BMMNC before and after MACS sorting of Stro-1-labelled cells.

Donor information			BMMNC number		Sorted fraction
Date of isolation	Gender	Age	Before MACS	After MACS	(%)
23/01/2015	Male	46	27 M	2.5 M	9.3
19/03/2015	Female	71	100 M	21.6 M	21.6
14/05/2015	Male	64	8 M	1.2 M	15.1
14/05/2015	Female	62	120 M	7 M	5.8
21/05/2015	Female	48	80 M	4.9 M	6.1
21/05/2015	Female	57	31 M	3.8 M	12.2
21/05/2015	Female	89	128 M	25 M	19.5
02/12/2015	Male	72	66 M	3.7 M	5.5
20/01/2016	Female	66	32 M	2.5 M	7.7
20/01/2016	Male	69	56 M	3.9 M	6.9
18/02/2016	Male	69	155 M	9.0 M	5.8
09/03/2016	Female	70	500 M	91.4 M	18.3
20/04/2016	Female	69	1,400 M	189 M	13.5
12/05/2016	Male	86	253 M	35 M	13.9
23/05/2016	Female	85	239 M	11.3 M	4.7
09/06/2016	Female	57	215 M	25.8 M	12.0
26/05/2016	Female	80	144 M	16.5 M	11.5
26/08/2016	Female	81	30 M	0.8 M	2.6
07/09/2016	Female	69	955 M	66.9 M	7.0
18/10/2016	Female	80	290 M	14 M	4.8
18/10/2016	Male	79	52 M	2.3 M	4.4
05/01/2017	Female	81	269 M	11.4 M	4.3
05/01/2017	Female	54	268 M	14.8 M	5.5
06/07/2017	Female	55	466 M	76.2 M	16.4
07/07/2017	Male	74	628 M	48.5 M	7.7
19/07/2017	Female	55	287 M	25.8 M	9.0
Mean ± SD		**69 ± 12**	**260 ± 319 M**	**27 ± 41 M**	**9.7 ± 5.2**

The expression of the Stro-1 antigen and CD146 was investigated by flow cytometry before and after enrichment by MACS. A representative scatter plot of forward *vs* side scatter (FSC-A *vs* SSC-A), which relate to cell size and granularity respectively, is presented in Figure 1.3a. The cell populations were noted to fall into three gates (lymphocyte, monocyte and granulocyte fractions) defined according to the similarity with the typical cell distribution of leukocytes. The majority of cells present within the granulocyte fraction were depleted following MACS sorting of Stro-1^+ cells (Figure 1.3b) and the largest enrichment was observed within the lymphocyte and monocyte fractions (Figure 1.3b and Table 1.2). The enrichment in the leukocyte fraction can be partly attributed to nucleated erythroid progenitor cells, which contribute to over 95 % of the Stro-1^+ cells in BM,[63] but typically display lower forward scatter.[64] The Stro-1^+ hBMMNCs were enriched from 13.8 ± 5.9 % in the BM to 76.7 ± 9.0 % after MACS (Figure 1.3a-c and Figure 1.4a, c). MACS enrichment using Stro-1 also increased the frequency of CD146$^+$ cells by more than 2-fold from 1.2 ± 0.4 % in the BM to 2.7 ± 0.9 %, indicating a correlation between CD146 expression and Stro-1^+ cells (Figure 1.3d-f and Figure 1.4b, d). The vast majority of CD146$^+$ cells were localised within the monocyte fraction, as previously reported for putative SSC populations.[65]

The frequency of CD146$^+$ and Stro-1^+ cells was investigated as a function of cell passage. Figure 1.4a illustrates a marked decrease in the Stro-1^+ cell fraction from 76.7 ± 9.0 % following MACS to 28.3 ± 6.3 % ($p<0.001$) after just 14 days in culture (passage 0). The percentage of Stro-1^+ cells continued to decrease significantly with passage to 8.8 ± 8.4 % ($p<0.05$ vs P0) at passage 3, corresponding to 56 days *in vitro* (DIV). These results are in agreement with previous reports. In Simmons *et al.*[63], the percentage of Stro-1^+ cells in adult human BM cells declined to 8.5 % after 6 weeks in culture, and in Gothard *et al.*[66], Stro-1^+ cells were completely absent at passage 7, after 21 to 35 DIV, in human foetal femur-derived BM cell cultures. Stewart and colleagues reported the percentage of Stro-1^+-enriched hBMMNCs to be around 21 ± 6 % (Mean ± SEM) at passage 1 after 28 days in culture which correlates with the current findings of 20.4 ± 14.4 %.[67] Conversely, the frequency of CD146$^+$ cells increased markedly at passage 0 (82.9 ± 5.3 %) compared to straight after MACS isolation (2.7 ± 0.9 %, $p<0.001$). This reflects the efficiency of cell adhesion as part of the current SSC isolation protocol, which removes non-adherent haematopoietic cells that are Stro-1^+ but CD146$^-$, including nucleated erythroid progenitors.[63,64] With cell expansion and passage, the percentage of CD146$^+$ appeared to gradually decline although this did not reach statistical significance. A previous study has shown a marginal decrease in the expression of CD146 after 6 passages.[68]

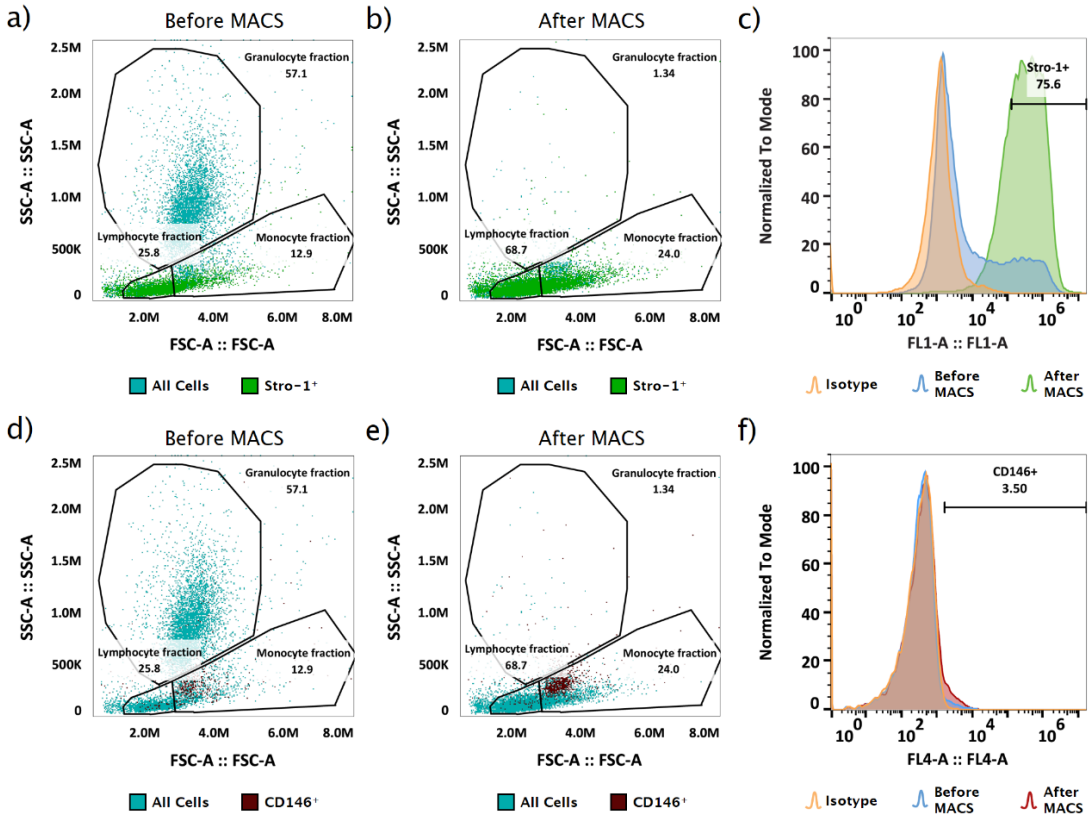

Figure 1.3 – Fluorescence flow cytometry of unexpanded human bone marrow mononuclear cells (hBMMNCs). a), b), d) and e) show plots (forward *vs* side scatter) of unexpanded hBMMNCs before (a, d) and after (b, e) enrichment of Stro-1$^+$ cells by magnetic-activated cell sorting (MACS). The three gates indicate the fraction of cells falling inside the typical FSC and SSC distributions for lymphocytes, granulocytes and monocytes as previously detailed.[65] c) and f) illustrate frequency histograms of the fluorescence intensity of hBMMNCs before and after enrichment by MACS and the respective matched isotype controls. The top and bottom panel images refer to the expression levels detected using the Stro-1 antibody and an anti-CD146 antibody respectively.

Table 1.2 – Donor information and percentage of human BMMNCs in each cell fraction of the scatter plots depicted in Figure 1.3. With MACS sorting of Stro-1$^+$ cells a consistent enrichment towards the monocyte and lymphocyte fractions is evident accompanied by granulocyte depletion.

Donor Information			Granulocyte Fraction		Lymphocyte fraction		Monocyte fraction	
Date of Isolation	Gender	Age	BMMNCs	Stro-1+	BMMNCs	Stro-1+	BMMNCs	Stro-1+
03/12/2015	Male	72	67.7	4.7	13.1	20.2	16.1	70.5
20/01/2016	Male	69	66.2	3.6	15.8	48.5	14.6	40.4
18/02/2016	Male	69	66.5	1.9	14.2	50.3	15.3	41.1
09/03/2016	Female	70	37.0	1.8	36.6	57.2	11.3	23.0
20/04/2016	Female	69	42.1	1.1	43.1	74.3	11.2	22.6
12/05/2016	Male	86	38.0	1.7	32.4	56.1	22.5	29.7
23/05/2016	Female	85	55.6	5.8	24.9	52.4	15.7	34.7
09/06/2016	Female	57	51.8	1.8	25.2	50.7	17.0	40.4
26/08/2016	Female	81	51.9	2.2	30.7	73.0	14.8	20.6
26/08/2016	Female	70	56.7	2.9	21.3	52.3	15.7	30.2
07/09/2016	Female	69	53.0	1.5	28.0	72.1	16.1	22.7
Average		72.5 ± 8.4	53.3 ± 10.9	2.6 ± 1.5	25.9 ± 9.5	55.2 ± 15.2	15.5 ± 3.0	34.2 ± 14.3
Enrichment (fold-increase)			0.05		2.13		2.21	

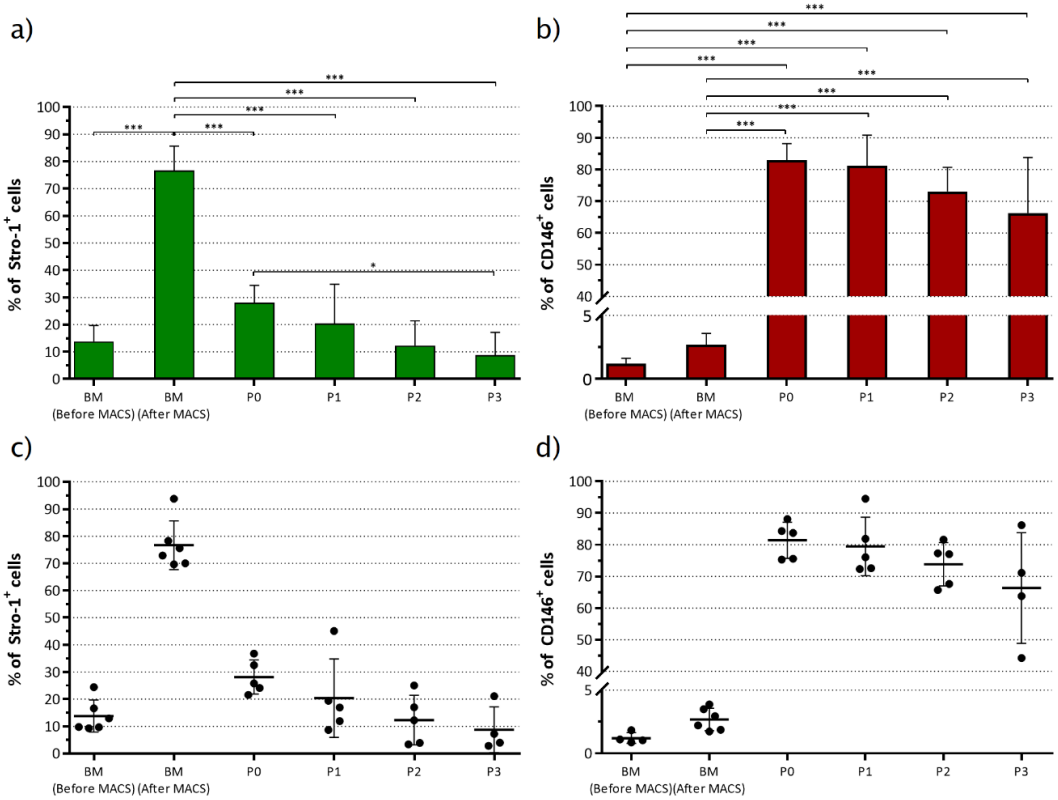

Figure 1.4 – Fluorescence flow cytometry of human bone marrow mononuclear cells (hBMMNCs). Frequency of Stro-1$^+$ (a, c) and CD146$^+$ (b, d) hBMMNCs in the BM, before and after enrichment of the Stro-1$^+$ population by MACS, and following cell expansion under basal culture conditions (passages 0 to 3). Values represent mean ± SD ($N \geq 4$; *$p < 0.05$; ***$p < 0.001$, with p-values obtained using the one-way analysis of variance (ANOVA) with Tukey's post-hoc test).

1.6. Summary

Skeletal stem cells offer great potential for use in tissue engineering and regenerative medicine of bone and cartilage. Indeed, SSCs could pave the way for precision medicine to become common practice in routine clinical procedures in the musculoskeletal arena, with the potential to bridge the gap created by the exacerbated health concerns originating from an aged society.

However, to date, an efficient protocol to achieve homogeneous SSC populations with consistent regenerative and proliferative capacity is yet to be developed. Approaches using for example the Stro-1 antibody have long been tested and optimised but, as revisited in this work, are unspecific or target an antigen that displays transient expression at the cell membrane, in keeping with recent findings from Fitter *et al.*[55] Combinatorial approaches using two or more markers simultaneously have been used[50] but still lack the purity required to guarantee the efficacy of enriched SSC populations in clinical applications.

Solutions to this challenge may include the search for novel markers that are specific to the SSC by means of phage display, DNA libraries, aptamer selection, or by the identification of specific transcriptomic patterns at the single cell level that would allow sorting SSCs based on the expression of particular mRNAs. However, while the search continues, alternative solutions should contemplate approaches that do not depend on antibody selection, but rather on intrinsic biophysical properties of SSCs, and are thus label-free. These

strategies are also attractive as they deliver cells in an unaltered state for further analysis or application.

The following chapters explore the hypothesis that SSCs hold a unique biophysical fingerprint and investigate the potential to use label-free methods based on microfluidics to deliver homogeneous populations of skeletal stem cells from primary human bone marrow tissue.

Chapter 2

Microfluidics: Physics and Cell Sorting Applications

"I am an old man now, and when I die and go to Heaven there are two matters on which I hope for enlightenment. One is quantum electrodynamics, and the other is the turbulent motion of fluids. And about the former I am really rather optimistic."

Sir Horace Lamb, 1932.

2.1. Laminar flow

The famous quote from Sir Horace Lamb in the epigraph highlights the challenge of describing the turbulent motion of fluids. Werner Heisenberg is said to have alluded later to a similar witticism when he compared the mysteries of turbulence to relativity rather than quantum electrodynamics. In fact, turbulence remains today one of the greatest, unsolved problems of Physics, being the subject of extensive modern research[69] and also one of the seven Millennium prize problems for which the first discoverer will be awarded $1,000,000 by the Clay Mathematics Institute.

Turbulent flow is found in the majority of examples of our interaction with fluid dynamics in everyday life, including the stirring of our morning coffee, the flow of water around our bodies during an afternoon swim or smoke rising from a chimney in winter. In turbulent flow, kinetic energy and inertial effects dominate over viscosity. For example, coffee continues to swirl inside its mug long after stirring has stopped and so do our bodies continue to move along the swimming lane after the last stroke. One thing that is representative of turbulent flow is that it is chaotic and unpredictable.

The behaviour of fluids is intimately related with scale. Channels in microfluidics are typically narrower than the width of a human hair, or 0.1 millimetres, which is close to the limit of what our eyes are able to discern. At the microscale, fluid dynamics change and flow is commonly laminar. In laminar flow, inertial effects are generally negligible and viscosity dominates. This prompts the appearance of interesting phenomena, which are often counter-intuitive as they contradict our day-to-day experience. For example, when bacteria stop swimming their movement stops immediately, much like what would happen to a person swimming in molasses. In a microfluidic device, two streams could flow side by side, with no physical separation between them, without ever becoming mixed but by diffusion (Figure 2.1a). At the macroscale, one example of laminar flow is the slow movement of a glacier (Figure 2.1b).[70]

The transition from laminar to turbulent flow can be estimated by a dimensionless number named after Osbourne Reynolds. The Reynolds number (*Re*) compares the magnitude of inertial and viscous effects and is given by Equation 1, with ρ representing the fluid density, u the flow velocity, D_h the hydraulic diameter and η the fluid viscosity.[71]

Figure 2.1 – a) Laminar flow within a microfluidic device. Image courtesy of the Folch Lab (albertfolch.wixsite.com). b) Laminar flow of two flowing glaciers (Silverthrone and Klinaklini) from the Heiltskuk Icefield as seen from space. Image courtesy of NASA. c) The author of this thesis investigating the effects of laminar flow at the macroscale while visiting the Vatnajökull glacier, in Iceland.

$$Re = \frac{\rho u D_h}{\eta} \quad (Equation\ 1)$$

$$D_h = \frac{4 \times cross\ section\ area}{Wetted\ perimeter} = \frac{4A}{P_{wet}} \quad (Equation\ 2)$$

When Re is lower than 1, viscous forces overwhelm inertia and the flow is laminar. Most microfluidic applications work with aqueous solutions, in channels narrower than 0.1 millimetres (100 µm) and at velocities up to 1 centimetre per second. When one applies Equation 1 to these numbers and to the density (~ 1 x 10^3 kg·m^{-3}) and viscosity (~ 1 x 10^{-3} Pa.s) of water at a typical room temperature of 20 ℃, *Re* is kept under 1.

$$Re \leq \frac{1 \times 10^3 \times 1 \times 10^{-2} \times 100 \times 10^{-6}}{1 \times 10^{-3}} \leftrightarrow Re \leq 1$$

Consequently, flow in microfluidic channels is often laminar, and laminar flow is linear, reversible, and predictable. This characteristic flow in microfluidics is the basis of many applications found in 'Lab-on-a-Chip' devices. When *Re* is marginally higher than 1, inertial effects come into play but flow remains laminar. The investigation of the effects of inertia in this regime is the subject of a particular field called 'inertial microfluidics', which is further described in section 2.3.4 of this thesis. Turbulent flow is only fully established at *Re* > 3,000 and the transition from laminar to turbulent flow is usually found between 2,000 < *Re* < 3,000.[72]

2.2. Navier-Stokes equations and Poiseuille flow

The study of fluid mechanics is based on the assumptions that fluids can be treated as being continuous and incompressible. Continuity postulates that the properties of a fluid at the macroscale are the same as if the fluid were perfectly continuous in structure rather than consisting of individual molecules.[71,73] For gases this is often not true, and the Knudsen number (*Kn*) should be used to verify whether the continuity hypothesis holds. When the Knudsen number is significantly smaller than 1, continuity is verified. *Kn* (Equation 3) compares the molecular mean free path length (λ) to a typical physical dimension (*L*), with K_B the Boltzmann constant, *T* the temperature, *d* the particle diameter and *P* the pressure. In a microfluidic device, *L* would be the channel hydraulic diameter.

$$Kn = \frac{mean\ free\ path}{typical\ physical\ length\ scale} = \frac{\lambda}{L} = \frac{K_B T}{\sqrt{2}\pi d^2 P L} \quad (Equation\ 3)$$

For liquids, intermolecular spacing is similar to that found on solids and continuity is typically verified. For example, there would be around 30,000 water molecules spanning the width of a typical 10-µm wide microfluidic channel and over 30 billion molecules in a cubic micrometre.[71] Indeed, microfluidics are at the macroscale to liquid water molecules and microfluidic flow can be generally considered continuous whenever the scale length is larger than 10 nanometres.[71]

Incompressible flow assumes that the mass density of a fluid remains constant. In other words, pressure variations are not large enough to cause changes in the fluid density. Flows with speed much slower than the speed of sound (340 $m \cdot s^{-1}$ in air and 1 484 $m \cdot s^{-1}$ in water) are termed incompressible.[71] For example, for water a hundred-fold increase in pressure leads to less than 0.5 % decrease in volume.[74]

The Navier-Stokes equations (Equation 4) are based on the principles of the conservation of mass, energy and momentum[71] and describe the motion of Newtonian fluids. For Newtonian fluids, viscous stresses are directly proportional to the applied shear rate with the constant of proportionality defining the fluid viscosity.[75] Most liquids comprised of a single type of molecules are Newtonian. Blood is an example of a non-Newtonian fluid as its viscosity decreases with increasing shear rates helping it flow through narrow capillaries.[71]

The Navier-Stokes equations (Equation 4) are analogous to Newton's second law of Physics (Equation 5) with force terms found on the left hand side, including the pressure gradient ($-\nabla P$), viscous effects ($\eta \nabla^2 u$) and body forces (f) like gravity; and inertial acceleration terms falling on the right hand side. Because the equations are applied to fluids, mass and force densities are used rather than discrete dimensions.

$$-\nabla P + \eta \nabla^2 u + f = \rho \left[\frac{\delta u}{\delta t} + (u \cdot \nabla) u \right] \quad (Equation\ 4)$$

$$F = m \cdot a \quad (Equation\ 5)$$

$$\nabla \cdot u = 0 \quad (Equation\ 6)$$

Equation 6 is the continuity equation, which is derived from the assumption that the fluid is incompressible and the mass density is constant in both space and time.[75,76] The non-linear inertial acceleration terms of the Navier-Stokes equations are particularly difficult to resolve, which explains why turbulent flow remains an unsolved mystery. However, when the flow is laminar, as happens in the vast majority of microfluidic applications as seen in section 2.1 of this thesis, the non-linear inertial terms become negligible and the equations can be significantly simplified to the linear Stokes equation (Equation 7).[77]

$$-\nabla P + \eta \nabla^2 u + f = 0 \quad (Equation\ 7)$$

The Poiseuille solution to the linear Stokes equation describes the flow velocity profile of a Newtonian fluid flowing due to a pressure gradient in an infinitely long channel. One important condition for the Poiseuille solution is the no-slip boundary condition, which assumes the velocity of a fluid immediately adjacent to the wall to be the same of the wall

itself.[71,75,77] This assumption is simple and generates results in agreement with macroscopic observations.[71] A simple derivation of the Poiseuille solution is found for flow between two horizontal stationary plates of infinite dimensions separated by h (Figure 2.2a). The plates are parallel to the *xy* plane and a constant pressure difference is maintained over a segment of length *L*. The flow is purely axial and only u_x is non-zero, with u_x a function of *y* and *z* only. Under these assumptions and ignoring body forces, equations 6 and 7 can be further simplified.

$$-\frac{\delta P}{\delta x}+\eta\left(\frac{\delta^2 u_x}{\delta y^2}+\frac{\delta^2 u_x}{\delta z^2}\right)=0 \quad (Equation\ 8)$$

$$\frac{\delta P}{\delta y}=\frac{\delta P}{\delta z}=0 \quad (Equation\ 9)$$

As the plates are infinite in the y direction, the y co-ordinate drops out.[77] Assuming the no-slip boundary condition, the solution to the differential equation of the velocity profile assumes the form of a parabola (Equation 10), and the flow rate (*Q*) is given by the integral over *z* and a section of width *w* (Equation 11).[75,77]

$$u_x(z)=\frac{\Delta P}{2\eta L}(h-z)z \quad (Equation\ 10)$$

$$Q=\frac{h^3 w}{12\eta L}\Delta P \quad (Equation\ 11)$$

$$Q=\frac{\Delta P}{R_h} \quad (Equation\ 12)$$

From Equation 12, the flow rate can be related to the pressure drop by a defined measure that is equal to the hydraulic resistance (R_h) of a channel. R_h is a function of the channel cross-sectional shape and an important consideration in the design of most microfluidic devices. The Hagen-Poiseuille law (Equation 12) is analogous to Ohm's law for electrical circuits.[75] In fact, analogies to electrical circuits can be found to every hydraulic relation and often help in circuit problem solving.[75]

There are solutions to the Navier-Stokes equations for different channel cross-sections. Equations 13 to 15 show the equivalent solutions for a channel of a circular cross-section of radius *R*.[75]

$$v_x(r)=\frac{\Delta P}{4\eta L}(R^2-r^2) \quad (Equation\ 13)$$

$$Q=\frac{\pi R^4}{8\eta L}\Delta P \quad (Equation\ 14)$$

$$R_h=\frac{8\eta L}{\pi R^4} \quad (Equation\ 15)$$

The parabolic flow velocity profile resembles what would happen if one pulled the middle card from a deck while holding the top and bottom cards stationary (Figure 2.2b). The velocity of the fluid is null at the walls and is maximum at the midpoint between the two sheets. In between, the velocity decreases from the centre towards both walls as the fluid moves in parallel thin layers that slide and exert viscous shear stress upon each other.

The behaviour of the fluid as independent thin layers defines laminar flow with the term 'laminar' originating from the Latin 'lamina', which means very thin layer. The imaginary lines between these *laminae* are called streamlines. Laminar flow and the parabolic flow profile are two important notions to understand the fluid behaviour at the microscale.

Laminar flow offers outstanding control over fluid dynamics and its underlying phenomena translate into most advantages of working with microfluidics other than the obvious reduction in costs and sample use. These include the possibility of integrating fluid handling with microelectronics and micromechanical systems (MEMS) in a single device allowing to conduct the steps of sample preparation and analysis in a 'sample in, answer out' fashion, the so-called micro total analysis systems (μTAS), as proposed by Andreas Manz in 1990.[78] Moreover, many phenomena are faster at the microscale as is the example of thermal diffusion, which scales with the square of the layer thickness. Smaller scale also typically leads to an increase in the sensitivity of sensing applications and to an increased magnitude of many applied forces, such as in dielectrophoresis or magnetophoresis.

One application of microfluidics of particular interest to this thesis is label-free particle sorting (LAPASO). As the term suggests, microfluidics offers the possibility of sorting particles without the need for antibody labels but rather relying on the particle biophysical properties which include size, deformability, shape, dielectric and acoustic properties, among others[62]. This is invaluable for the perspective of sorting cells for which a unique marker has not yet been identified, such as the SSC. These methods have been extensively studied to isolate rare circulating tumour cells (CTCs) from the blood of patients with metastatic cancer. However, despite their promise no such approach has been directed to sorting SSCs from human BM. Section 2.3 shows examples of LAPASO approaches focusing on their potential application to SSCs. This work resulted in the publication of a review article[62] in the peer-reviewed journal *Biotechnology Advances* and summarises the best examples found in the field up to the date of submission in early 2016.

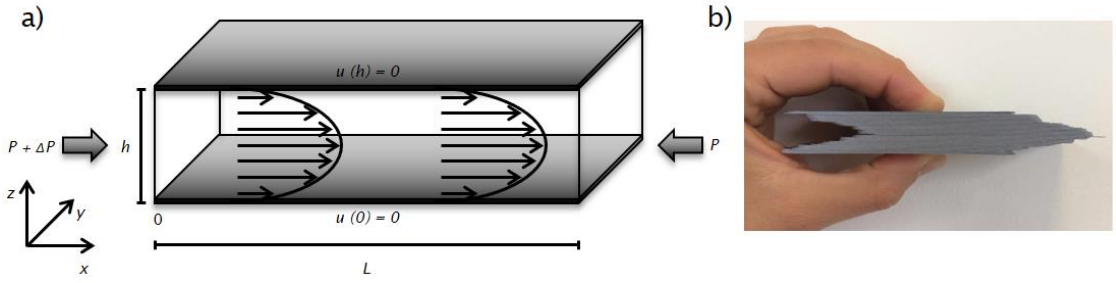

Figure 2.2 – Unidirectional pressure-driven flow between two stationary plates of infinite dimensions separated by h. The Poiseuille solution to the simplified Navier-Stokes equations shows the formation of a flow velocity profile that takes the form of a parabola satisfying the no slip boundary condition that dictates that the flow velocity at the wall is equal to the velocity of the wall itself, which in this case is null. b) The shape of a card deck when the middle card is pulled while holding the top and bottom cards stationary resembles the parabolic flow velocity profile. The cards behave as the fluid laminae exerting shear stress when sliding over each other.

2.3. Label-free Particle Sorting

LAPASO has been the subject of extensive research during the past decade. The advantages of sorting cells label-free are mostly that by evading the use of antibodies the issues associated with cell heterogeneity and the lack of antibody specificity are averted. In addition, sample preparation is typically significantly simplified and systems tend to be easier to use.

Sorting CTCs from the peripheral blood of cancer patients has been the holy grail of LAPASO. This is due to its clinical relevance as much as to its difficulty. Indeed, CTCs can reveal important information about a patient's survival prognosis and can also direct personalised cancer treatment as well as provide a means to understand metastasis and the biology behind cancer development. However, the number of CTCs in 1 millilitre of peripheral blood can be as low as 1, and in the same volume, one can find 4 to 11 million white blood cells (WBCs), 300 million platelets and approximately 5 billion red blood cells (RBCs).[79,80] This makes this quest equivalent to searching for one individual within the entire human population, with the added requirement that it needs to be done fast. For this reason, the literature in the LAPASO field is dominated by examples centred on CTCs and the best examples are summarised in the following sub-sections of this thesis.

Label-free sorting of SSCs is however no easier task. While the frequency of the SSC in the BM is typically higher than of CTCs in whole blood it is still most likely the rarest cell type in BM.[45] Additionally, BM samples are significantly more complex than whole blood comprising over a score of different cells and progenitors as well as fat and potentially soft tissue and bone debris.[45] Because examples of work regarding label-free sorting of SSCs are very limited, the following sub-sections include examples found with different types of stem cells and progenitors. Section 2.4 provides a summary of the best examples in the field and puts them in perspective to the future of the field for the SSC.

2.3.1. Affinity-based

By definition, affinity-based sorting methods are not label-free. However, owing to the phenomena described in section 2.2, microfluidics has contributed to the development of affinity-based methods with enhanced efficiency which significance should not be omitted.

One of the first examples combining microfluidics with immunocapture dates back to 2007 when Sunitha Nagrath developed the CTC-chip.[81] The device was designed with the purpose of capturing CTCs from the peripheral blood of cancer patients. It consisted of 78,000 epithelial cell adhesion molecule (EpCAM) antibody-functionalised microposts that increased the surface area of the device approximately 3-fold and promoted cell-antibody interactions. The posts were arranged in an equilateral triangular array, which was shown by simulation to be the most hydrodynamically efficient geometric arrangement and to create non-linear streamlines promoting cell-antibody contact. Every three rows, the posts were shifted to ensure that cells following streamlines between the microposts were forced to collide with posts located downstream (Figure 2.3a). The device was operated at a flow rate of 1-2 $mL \cdot h^{-1}$ to promote maximum interaction whilst limiting shear forces to maximise the probability of attachment. Under these conditions, more than 60 % of all CTCs spiked

in whole blood could be recovered, and the detection of CTCs in 115 out of 116 cancer patients from disparate cancer backgrounds (lung, prostate, pancreatic, breast and colon cancer) was demonstrated (Figure 2.3b). Applying a different principle, the same group later developed the herringbone-chip, which increased the probability of cell-antibody interaction through passive mixing of blood cells caused by the generation of micro-vortices from the chevrons on the device surface (Figure 2.3c).[82] The device was able to recover over 90 % of CTCs spiked in whole blood and could detect CTCs in 93 % cancer patient samples.

Brian Kirby's group developed devices that used antibody-functionalised silicon microstructures to induce size-dependent collisions.[83] These devices, termed geometrically-enhanced differential immunocapture (GEDI), were designed to distort streamlines so that the cell displacement caused by impact with obstacles increased the probability of future impacts for larger cells, such as CTCs, in detriment of smaller cells, such as WBCs (Fig. 2d, e). The obstacle shape and array geometries can be tuned to address specific cell size thresholds depending on the application (Figure 2.3d, e). GEDI devices were able to recover over 85% of prostate CTCs spiked in whole blood and detected CTCs from the peripheral blood of 18 out of 20 patients, at a processing rate of over ten million cells per minute.[83] GEDI devices have also been shown to isolate breast and gastric cancer cells,[84] and to enable on-chip functional characterisation of CTCs.[85,86] The GEDI principle has also been coupled with dielectrophoresis (DEP) to further increase the probability of antibody interaction by the addition of an external force generated by an electric field.[73,87]

Finally, as an example of an affinity-based approach applied to progenitor cells, one study has reported encapsulation of cells from digested human periosteal tissue into microscale water-in-oil droplets, generated using a T-junction microfluidic flow. The encapsulated cells were analysed on the same device using a micro-FACS system identifying Stro-1^{+}-labelled progenitor cells.[88] Although this was not a sorting device, it showed the potential for developing a novel microfluidic sorting technology for rare stem cell populations.

The examples of affinity-based microfluidic sorting techniques shown above demonstrate encouraging performances in terms of efficiency and throughput. However, some limitations must be accounted for, as for example, when used for positive cell selection, rare cells need to be released after capture. This is done by either applying shear stress or through enzymatic digestion of the coupling ligands but both methods can harm viable cells.[89] However, important advances have recently been made using *e.g.* thermo- and mechano-sensitive smart polymers to increase release efficiency and cell viability.[90,91] Regarding SSC isolation, positive selection would lead to impure populations owing to the absence of selective antibodies. Negative selection using affinity-based microfluidics that capture contaminant cells on chip is generally inefficient for sorting rare cells as the devices can become clogged by the contaminant cells. Consequently, label-free microfluidic sorting techniques or methods offering continuous-flow negative selection for sorting SSCs, are likely to be advantageous over an immunocapture affinity-based approach.

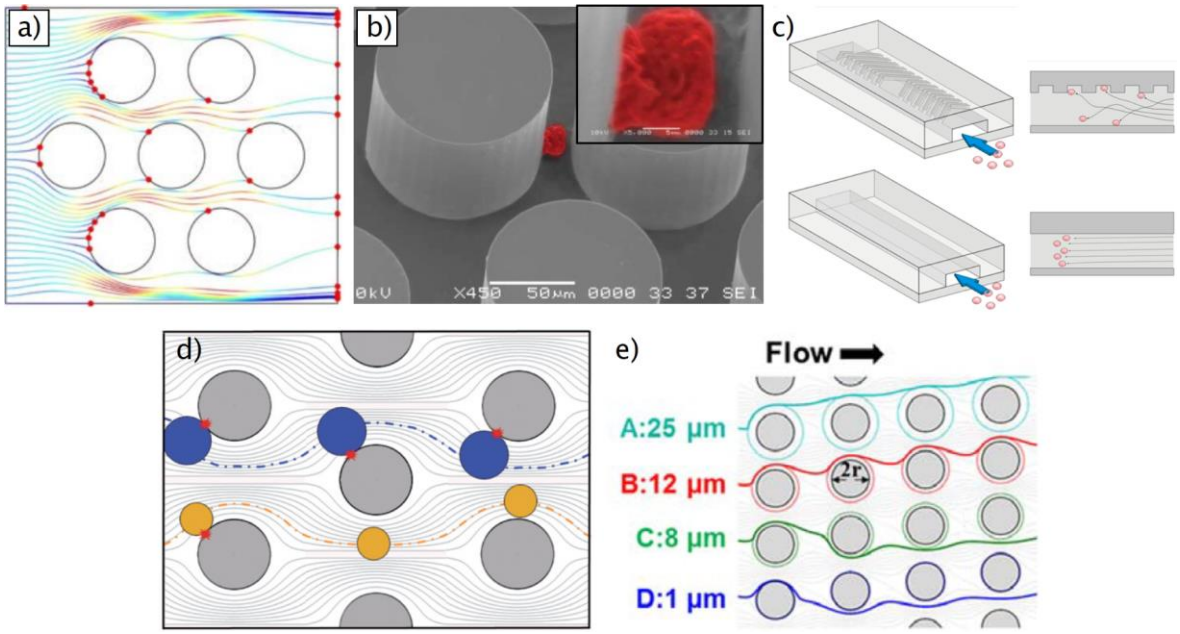

Figure 2.3 – Affinity-based cell sorting. a) Simulation of cell trajectories in the equilateral triangular arrays. Red dots indicate cell-ending positions. b) Scanning electron micrograph of a CTC captured after contact with an EpCAM-functionalised micropost[81]. c) Comparison of cell surface interactions between the herringbone chip and a flat-walled microdevice. The probability of cell-antibody interaction is increased by passive mixing caused by the generation of micro-vortices from the chevrons at the device surface.[82] d) Cell trajectory simulation in GEDI devices predicting the frequency of cell-obstacle collisions[83]. e) Size-dependent trajectories of cells flowing in GEDI devices[85]. Pathlines (various colours) denote trajectories of cells of different diameters (1-25 µm). Cell displacement caused by impact with the obstacles increases the probability of future impacts for larger cells promoting contact with the antibodies. The array geometry (*e.g.* obstacle diameter, 2r) can be adjusted to address specific size thresholds. Image adapted from Xavier *et al.*[62]

2.3.2. Deterministic Lateral Displacement

Deterministic lateral displacement (DLD) is fundamentally a size-based sorting technique. It was first described in 2004[92] and it is capable of high-resolution fractionation, in the order of 2 % in particle size.[92,93] It consists of arrays of micropillars in a microchannel, typically cylindrical in shape, and equally spaced (G), with each row shifted by a small distance horizontally ($\Delta\lambda$) with respect to the previous (Figure 2.4a). After N rows, two pillars are found in the same horizontal position defining the period of the array. The flow is laminar and the main flow stream is split by the pillar array into N parallel laminae with identical flow volumes. Figure 2.4a depicts a hypothetical DLD device with period 3. When cells in a streamline encounter an obstacle, they reach a critical decision point in which their behaviour is determined by the critical separation size of the microarray. The critical size (D_C) corresponds to the width of the streamline found closest to the obstacle and has been empirically determined to be approximated by Equation 16.[92-95]

$$D_C = 1.4G \times N^{-0.48} \quad Equation\ 16$$

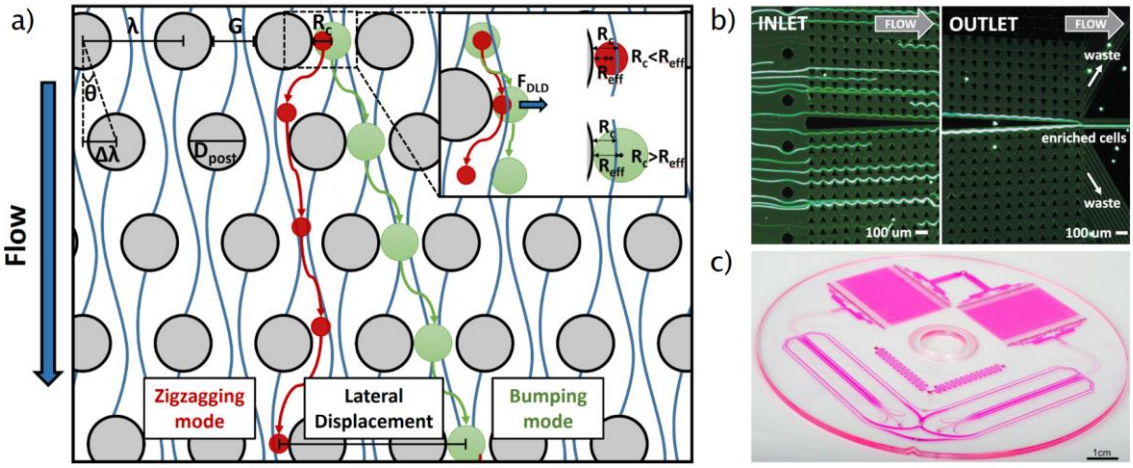

Figure 2.4 – Deterministic Lateral Displacement. a) Size-based separation in a DLD device with period N=3. Cylindrical obstacles with diameter D_{POST}, are separated by a gap G and the row shift fraction is given by Δλ. λ equals $G+D_{post}$ and Θ is the angle of the pillar array in relation the main flow direction. The micropost array divides the flow going between two posts in 3 parallel streamlines with identical flow volumes. The width of the streamline closest to the post determines the critical size for separation (R_C). Smaller, red particles, flow in zigzagging mode and suffer no net total displacement. Bigger, green particles, with radii larger than the critical separation size ($R_{EFF} > R_C$) are deflected at each critical decision point flowing in bumping mode and being laterally displaced at the end of the array. b)[103] shows an example of the operation and principle of sheathless DLD devices. d) shows the 128 parallel DLD arrays used in the most recent version of CTC-iChip to debulk whole blood at 15-20 million cells·min^{-1}.[104] Image adapted from Xavier *et al.*[62]

At each decision point, if the cell diameter is smaller than D_C, the cell is mostly affected by the first streamline and remains unperturbed, zigzagging through the obstacle array. However, if the cell radius is larger than the width of the first streamline ($R_C = D_C/2$) then it will be forced to change streamlines and effectively be 'bumped away', or more correctly, laterally displaced. This phenomenon is repeated upon interaction with every post so that cells larger than D_C will end up completely separated from the initial input flow.[92–95]

Several adaptations to the original DLD principle have been developed, sorting particles according to additional physical properties such as shape,[96] deformability,[96,97] density,[98] and acoustic[99] and dielectric properties.[99,100] The basic rationale is that an additional force changes the apparent radius (and/or trajectory) of the particle. For example, at high pressure, a more deformable particle is squeezed by shear stresses upon interacting with the posts thus appearing smaller.[96] Beech *et al.* explored this effect to show how different red blood cells (discocytes, stomatocytes and echinocytes) had different deformability profiles.[96] More recently, the same principle was applied to sort T-lymphocytes from neutrophils according to differences in their deformability.[97]

To date, DLD has been used to sort different particles including beads, bacteria, parasites, CTCs and blood cells. See McGrath *et al.* for a comprehensive review.[95] There are however no examples of stem cell sorting by DLD. One application regarding tissue engineering purposes was the use of DLD to separate two immortalised cell lines, one fibroblastic and one epithelial, mixed in equal proportions to mimic cardiomyocytes and non-myocytes from a cardiac tissue digest.[101] The same group also demonstrated isolation of cardiomyocytes from primary cardiac tissue digests with a purity of 91 %.[102] However, the

size differences were large, the throughput was relatively low (~20,000 cells·min^{-1}) and the cardiomyocyte recovery efficiency was just 30–35 %. High throughput is most important for sorting rare cell populations such as SSCs from BM, where large sample volumes and cell numbers must be analysed. Likewise, recovery efficiencies need to be maximised to avoid losing rare target cells.

Traditional DLD devices typically operate at flow rates up to a few microlitres per minute and require sheath flow which introduces significant dilution of the sample at the outlets.[95] To improve throughput, devices can be operated in parallel and/or with no sheath flow. Of relevance to SSC sorting, Inglis *et al.*[105] showed a 10-fold enrichment of leukocytes from whole blood, with 98 % recovery efficiency. Blood samples were sorted undiluted and the volumetric throughput was increased to 115 µL·min^{-1} when using 6 parallel arrays.

Sheathless DLD devices have also been developed for sorting rare cells. Two mirrored DLD arrays with triangular posts were used to displace and concentrate target cells. Breast and prostate cancer cell lines spiked (1:300) into diluted blood were separated at flow rates of 10 mL·min^{-1}.[103] A recovery efficiency of 86 % was reported but as many as 5 in every 100 cells in the input were cancer cells and the output was still highly contaminated with blood cells (>80 %) (Figure 2.4b). Despite the high flow velocities achieved (~1.5 m·s^{-1}) the cells were shown to remain viable after separation. Liu *et al.*[106] sorted two breast cancer cell lines spiked at a ratio of 1:10,000 in diluted blood. Isolation efficiencies of 99 and 80 % were achieved at a flow rate of 2 mL·min^{-1} translating into a higher efficiency at a similar throughput as the target rare cells were significantly more diluted.

A high-throughput DLD system used for de-bulking and pre-processing samples used 24 parallel, mirrored arrays. It could process blood to remove RBCs and platelets at flow rates up to 8 mL·h^{-1}.[107–109] Combining DLD with subsequent magnetophoretic sorting based on the intrinsic magnetic susceptibility of the haemoglobin-positive progenitor nucleated RBCs found in the peripheral blood of pregnant women showed over 1,000-fold enrichment.[109] Recently, DLD was combined with magnetic-bead based depletion of CD45$^+$ and CD66b$^+$ WBCs, for CTC isolation, achieving 97 % recovery from patient samples, whilst removing all RBCs and depleting WBCs by a 3.8-log ratio.[108] This device has been further improved to include 128 DLD arrays and debulk blood at 15 to 20 million cells per second (Figure 2.4c).[104]

While the volumetric and cell sorting throughputs reported above are adequate for sorting SSCs from human bone marrow, size differences on their own may not be sufficient to sort SSCs by DLD. Nevertheless, DLD may be used as a passive, efficient and relatively simple procedure to decomplex bone marrow samples prior to further selection by an additional sorting technique.

2.3.3. Magnetophoresis

Magnetophoresis uses magnetic fields to manipulate particles. Cells can be sorted according to their intrinsic magnetic susceptibility or based on superparamagnetic nanoparticles bound to antibodies – a method termed immunomagnetic sorting. This is the principle behind MACS, which is usually not label-free and requires highly specific antibodies.[110]

Nevertheless, like affinity-based methods, magnetophoresis has been miniaturised in microfluidic devices bringing the advantage of scale. Specifically it is much easier to generate well-defined, high magnetic field gradients at the microscale. Furthermore, when used for negative depletion of contaminant cells, magnetophoresis does not depend on the specific expression of a certain antigen by the cells of interest. As mentioned in section 2.3.2, it has been used to improve the purity of target cell populations in continuous-flow in combination with DLD.[107-109] A similar approach could be applied as a sorting strategy for SSCs, where contaminating cells like monocytes, are often found in the final SSC cultures since they are mononuclear, and can adhere to tissue culture polystyrene in the presence of cell adhesion proteins present in foetal calf serum. Monocyte depletion could be achieved by negative depletion with CD14 or CD45 antibodies since neither are expressed by SSCs.

In magnetophoresis, cell movement depends on the different forces acting on it, which in flow comprise magnetic, buoyancy, inertial and drag forces. The magnetic force will depend on the volume of the magnetic particle (V_p), the difference between the magnetic susceptibility of the particle and the suspending medium ($\nabla\chi$), and the square of the magnetic field gradient ($(\vec{B}.\nabla)\vec{B}$), with μ_0 being the permeability of free space.[110]

$$\vec{F}_m = \frac{V_p \nabla\chi}{\mu_0}(\vec{B}\cdot\nabla)\vec{B} \quad (Equation\ 17)$$

As the magnetic susceptibility of the suspending medium is usually several orders of magnitude lower than the magnetic particles used for sorting, $\nabla\chi$ is often determined by the susceptibility of the particles alone.[110] When labelling cells with antibody-coated magnetic beads, the equation can be modified to accommodate the number of magnetic beads on the cell surface that are conjugated to the antibody (β), the number of cell-surface markers targeted (n), the fraction of these which was bound by the antibody (θ) and the number of antibodies which can bind to a single marker (λ).[110]

$$\vec{F}_m = \frac{V_p \nabla\chi\beta n\theta\lambda}{\mu_0}(\vec{B}\cdot\nabla)\vec{B} \quad (Equation\ 18)$$

Applications of magnetophoresis can be grouped into three categories: conventional MACS systems, still the gold standard in magnetic separation, the quadrupole magnetic flow sorter (QMS) and microfluidic-magnetophoretic applications. The concept of QMS was introduced by Zborowski *et al.* in 1999.[111] It uses four permanent magnets to create a quadrupole magnetic field with a centrifugal character deviating magnetic-labelled cells from a central stream into the channel periphery, later separated by a flow splitter (Figure 2.5a).[111] Advantages of the QMS are its high throughput and recovery efficiencies, sorting over 1 million cells per second while retaining 95 % of the target cells.[110]

Important applications of the QMS include those from Chalmers and Zborowski's group in which human $CD34^+$ progenitor cells were sorted from peripheral blood samples by negative selection of leukocytes labelled with a tetrameric antibody cocktail[112] or an anti-CD3 antibody,[113] achieving up to 4-log depletion of leukocytes without the need for labelling the progenitor cells. Yang *et al.* sorted CTCs by negative depletion of $CD45^+$ cells after RBC-lysis. The device achieved a 2.9 log-depletion of leukocytes and a 5.7 log-depletion of total

blood cells from peripheral blood samples of cancer patients while recovering an average of 22 CTCs per millilitre of blood.[114] Another interesting application by the same group concerned blood debulking by depletion of RBCs down to 5 % of their initial value simply relying on their intrinsic magnetic susceptibility, owed to haemoglobin.[115]

Microfluidic magnetophoretic systems have been used for positive selection of labelled-cells for many years, and these devices are commonly referred to as micro-MACS (μMACS). When an antibody with high specificity is used, high recovery efficiencies are possible with excellent depletion of contaminating cells at high throughput. The work of Plouffe *et al.*[116] and Huang *et al.*[117] are two good examples in which the throughput was of the order of hundreds of millions to a billion cells per minute. Plouffe *et al.*[116] reported recovery of spiked CTCs or primary HSCs from whole blood with efficiencies of 88 % and 97 %, whilst Huang *et al.*[117] successfully detected CTCs from cancer patients with recovery efficiencies rounding 60 % to 70 %.

Given the lack of a specific marker for SSC, the magnetophoretic approach by negative depletion is of interest. The work from Toner's lab is notable for achieving a 3.8 log-depletion of WBCs and CTC recovery efficiencies rounding 97% from whole blood.[107,108] The magnetophoretic stage of the system is able to continuously sort over $5x10^5$ cells·min^{-1}. To maximise efficiency, both labelled and unlabelled cells are pre-aligned in the magnetic field by inertial focusing (Figure 2.5b). The magnetically labelled WBCs are deflected from the focused streams in two serial stages. In the first stage, cells travel faster and are exposed to a low magnetic field gradient, which typically deflects 99.9 % of all WBCs. The WBCs are deflected to the centre of the channel rather than onto the channel walls in order to minimise the formation of cell aggregates and the propensity of clogging the device. At the second stage, the cell speed is slower increasing cell residence time, and the magnetic field gradient experienced by the cells is increased. This provides a higher force, deflecting even WBCs labelled with fewer than 6 magnetic beads per cell, ergo increasing purity.

Two publications describe devices that are totally label-free. Taking advantage of the paramagnetic nature of deoxyhaemoglobin RBCs, over 93 % were removed from diluted whole blood whilst retaining 97.4 % of WBCs, resulting in a 15-fold enrichment.[118] Huang *et al.*[109] applied the same principle to sort nucleated RBCs (nRBCs) from the peripheral blood of pregnant women for diagnosis of maternal and foetal health. DLD was used in a first stage to remove RBCs and platelets from diluted blood at $6x10^8$ cells·min^{-1}. The sample, now deprived of 99.99 % of the RBCs, was flowed through a commercial magnetic column, like in a typical MACS application, which removed 99.9 % of all haemoglobin-negative cells while retaining nucleated RBCs, resulting in an over 10^3-fold enrichment. Using this system, nRBCs were sorted from all 58 patients. Note that the nucleated erythroid cells represent 95 % of the Stro-1 expressing cells in the bone marrow,[53] representing the most abundant contaminant population when isolating Stro-1$^+$ SSC by MACS. As the erythroid cells are non-adherent, they can be easily removed after adhesion of the SSCs to tissue culture flasks. However, when SSCs are needed immediately after sample collection, cell adhesion is too slow and magnetophoretic removal of nRBCs could be a viable alternative.

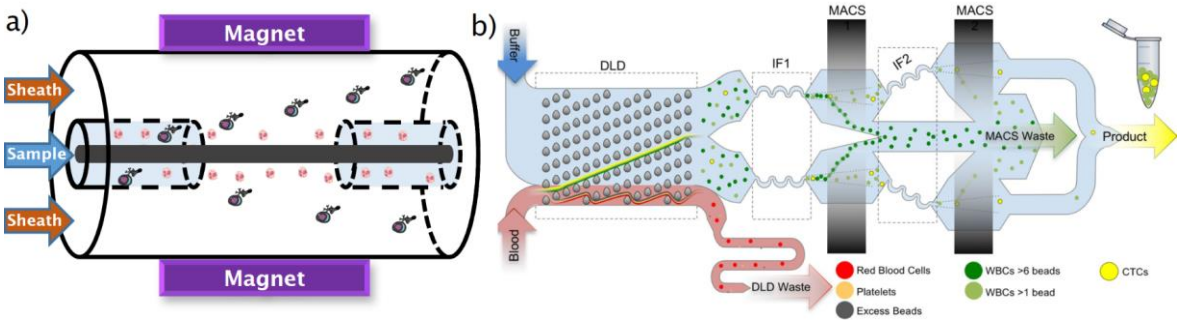

Figure 2.5 – Magnetophoresis. a) Representation of the quadrupole magnetic flow sorter with cells flowing in a central channel and separation occurring when a magnetic field actuates on the labelled cells driving them away from the centre of the device into a peripheral channel. b) Monolithic CTC-iChip. Magnetophoresis removed $CD45^+$ and $CD66b^+$ cells from whole blood and detect CTCs.[104] Image adapted from Xavier *et al.*[62] and Fachin *et al.*[104]

2.3.4. Inertial Microfluidics

For Reynolds numbers in the range of 1 to 100 flow remains laminar but inertial forces begin to play an increasingly important role in determining the behaviour of flowing cells and their suspending medium.[119] The use of inertial effects to manipulate cells has resulted in several applications for cell focusing and sorting, as well as sample decomplexing, which have been previously reviewed.[119–121]

Inertial microfluidics generates forces acting on particles perpendicular to the main direction of flow. In general, two counteracting forces are responsible for inertial effects. The first is exerted by the presence of a boundary, typically the channel wall. The perturbation of the flow field exerted by the cell and the reflection of this perturbation at the closest wall will direct the cell away from it (F_{LW}). In addition, the parabolic velocity profile of Poiseuille flow described in section 2.2 induces a shear gradient lift force ($F_{LS\text{-}G}$), which draws the particle away from the centre of the channel. For a cell of radius R_C flowing in a channel with hydraulic diameter D_h, and when the ratio R_c/Dh is in the range 0.05 and 0.2, the wall and shear gradient lift forces are proportional to equations 19 and 20.[119,121,122]

$$F_{L_W} \propto \frac{\rho u^2 R_c^6}{{D_h}^4} \quad (Equation\ 19)$$

$$F_{L_{S-G}} \propto \frac{\rho u^2 R_c^3}{D_h} \quad (Equation\ 20)$$

Here u and ρ are the average flow velocity and the suspending medium mass density respectively. When these two forces match, the particles are focused to an equilibrium position as shown schematically in Figure 2.6a. Neutrally buoyant spherical particles flowing in a cylindrical channel spontaneously focus at an annulus with a radius of 0.6 times that of the channel (Figure 2.6b). [123] For square or rectangular channels, particles focus into 4 or 2 symmetric equilibrium positions, respectively (Figure 2.6b).[119] Note that inertial focusing is a function of particle to channel size ratio and also particle concentration due to particle-particle hydrodynamic interactions.[119,122] The rheological properties of the fluid, particle shape and also particle deformability can all affect the lift force thereby causing particles to focus at different positions. For example, discoid deformable particles, such as RBCs in whole blood, experience a net lift force towards the centre of the channel, as described by the Fårhaeus-Lindqvist effect (Figure 2.6c).[119,121,124]

Particle manipulation by inertial microfluidics can be further modified by the introduction of different structures into the micro-channels, such as curves, grooves, pillars, herringbones or different cross-sections.[119,120,125–127] Curved channels for instance, introduce additional effects into the system due to the formation of a secondary flow, known as Dean Flow, which arises from the fact that the fluid has to travel different distances along the inner and outer sides of a curved channel resulting in different velocity profiles at different radial positions. A set of secondary flows named Dean vortices are formed, with fluid near the centre of the channel travelling outwards while fluid near the top and bottom walls travels inwards to compensate and conserve mass (Figure 2.6d).[119,120,126,128] This leads to lateral migration of cells by the introduction of Dean Drag resulting in the alteration of the initial inertial equilibrium focusing positions. The magnitude of these forces is estimated through a dimensionless number, the Dean number (*De*, equation 21),[121] and the force experienced by a cell is approximated by the expression in equation 22.[121]

$$De = Re\sqrt{\frac{D_h}{2R_{curve}}} \quad (Equation\ 21)$$

$$F_D = 5.4 \times 10^{-4}\pi\eta De^{1.63}R_c \quad (Equation\ 22)$$

R_{curve} is the radius of the channel curvature and η the suspending medium dynamic viscosity. Particles with different sizes will therefore focus to unique equilibrium positions depending on the ratio of lift and drag forces (Figure 2.6d). The Dean force should not be confused with centrifugal forces, which arise from a density mismatch between particle and fluid, and are often negligible in microfluidics.[119,120,126–128]

Inertial microfluidics has been successfully used to sort progenitor cell populations. Recently, Poon *et al.* designed a microfluidic spiral channel with a trapezoidal cross-section to perform binary size fractionation of human BMSCs at 3 million cells per minute.[129] Despite some overlap between the larger ($2r_c$ = 21.9 ± 5.3 μm) and smaller cell populations ($2r_c$ = 14.8 ± 2.4 μm), there was a correlation between the larger BMSCs and a commitment to osteoprogenitor lineages *in vitro*, as well as an increased survival of lethally irradiated mice after *in vivo* transplantation with the larger BMSC fraction. The same device was used to separate cells by exploiting size differences between cell cycle phases.[130] BMSC biophysical markers such as size, nuclear fluctuation and deformability have been related to the differentiation potency, associating smaller, softer and high nuclear fluctuation phenotypes with increased multipotency.[131]

Dino Di Carlo's group demonstrated label-free separation of adrenal cortical progenitor cells from digestions of murine adrenal glands.[132] The smaller progenitor cells were isolated from the larger somatic cells and large clusters through different magnitudes of inertial lift forces in a long rectangular channel. The progenitor cells were positioned nearest to the channel walls, and sorted at rates of 24,000 cells per minute, though purity and recovery rates were not reported.

In 2011, Bhagat *et al.* described a pinched-flow inertial microfluidic device for sorting MCF-7 cancer cells spiked into diluted whole blood. Over 80 % of the cells were recovered with a 5.5 and 4.1 log-depletion of RBCs and WBCs respectively. However, the purity was

only about 0.025 % owing to the persistence of large numbers of RBCs at the sample outlet.[133] Later, Shen *et al.* combined inertial microfluidics with steric hindrance into a single system achieving a 5.3 log-depletion of all blood cells in a sample diluted 40 times and spiked with fewer than 1,000 CTCs·mL^{-1}, which was comparable to the work of Bhagat *et al.* Recovery of 90 % of the CTCs equated to a purity of 20%.[134]

Finally, two publications used spiral micro-channels (Figure 2.6e) to sort CTCs spiked into diluted[135] or RBC-lysed whole blood.[136] In the first example, 85 % of CTCs were recovered, which along with a 9 and 3 log-depletion of RBCs and WBCs respectively resulted in purities over 95 %.[135] In the second, Warkiani *et al.* introduced an RBC-lysis step and improved WBC depletion up to 4-log, resulting in a CTC purity of 80 %, which is an improvement over the previous example since the starting CTC concentration was 5,000 times less (100 compared to 5 million).[136] Both publications also report the isolation and detection of CTCs from patients with metastatic lung and breast cancer. Detection was achieved for all patients in both cases[135,136]. A detailed protocol of Warkiani's device was published recently[137] showing a multiplexed version that increased the device recovery efficiency to 85 % while retaining its high throughput.[138]

Inertial microfluidic devices are typically associated with high flow rates, of the order of millilitres per minute, and throughputs up to hundreds of millions of cells per minute. As previously discussed, this feature is invaluable for sorting rare cell populations. However, the reported purities are only as high as 80% for relatively rare cell populations (100 CTCs·mL^{-1} RBC-lysed blood).[136] These values are low compared with the required purity for SSC applications. Consequently, inertial microfluidics for sorting SSCs from bone marrow would need to be improved, or again combined with another sorting technique, to deliver enhanced cell purity.

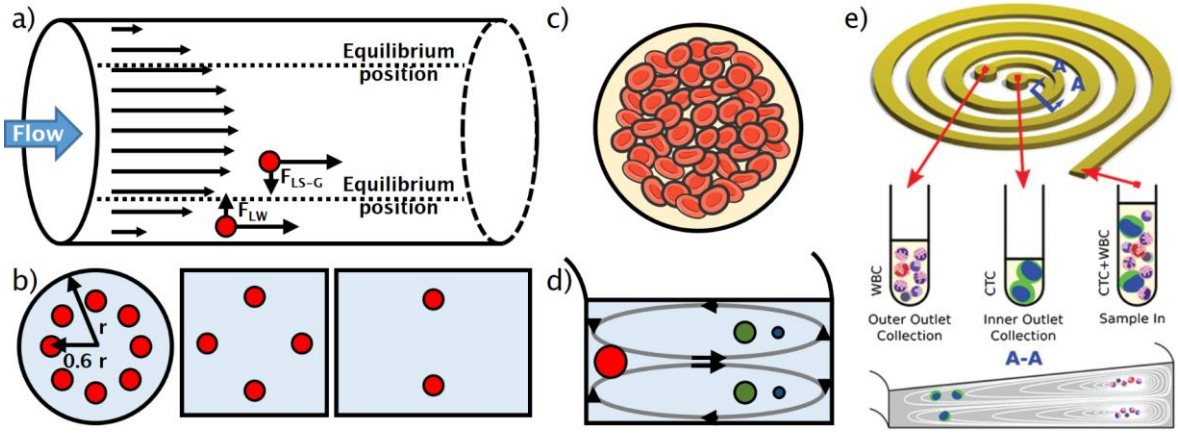

Figure 2.6 – Inertial microfluidics. a) Representation of particles flowing inside a circular channel with a typical parabolic velocity profile, showing the two dominant inertial lift forces (wall, F_{LW}, and shear gradient, F_{S-G}) acting on the particles and drawing them onto inertial focusing equilibrium positions. b) Examples of inertial focusing are given for circular, square, and rectangular channels. c) Representation of red blood cells flowing in a capillary evidencing the Fårhaeus-Lindqvist effect with RBCs focusing in the centre of the channel and a cell-free layer forming in the periphery. d) Formation of secondary flow Dean Vortices in a curved rectangular channel causing differential equilibrium positions for different particles given the balance of inertial lift and Dean flow. e) Spiral microfluidic channel used to sort CTCs from RBC-lysed clinical samples.[136] Image from Xavier *et al.*[62]

2.3.5. Acoustophoresis

The first reports of particle manipulation using ultrasonic waves date as far back as the early 1900's [139] but it was not until recently that acoustic forces started being used on-chip for continuous flow separation, combining small devices with higher resonance frequency transducers to improve performance.[140,141] The principles of acoustophoresis lie in the generation of an acoustic standing wave between two sound sources, commonly a piezoceramic actuator facing a sound reflector. At a given frequency, when half the wavelength of the ultrasound matches the width of the channel where the reflector is located, a standing wave is generated (Figure 2.7a). Cells exposed to the pressure wave experience acoustic radiation forces provided that their acoustic properties differ from that of the surrounding medium. This force is given by the acoustic contrast factor Φ, which depends on both the densities of (ρ_c and ρ_m) and the speed of sound in (c_c and c_m) the cell and suspending medium.[140,142–144]

$$\Phi = \frac{\rho_c + \frac{2}{3}(\rho_c - \rho_m)}{2\rho_c + \rho_m} - \frac{1}{3}\frac{\rho_m c_m^2}{\rho_c c_c^2} \quad (Equation\ 23)$$

These forces can be divided into the primary radiation force (Equation 24) generated from the standing wave, and the secondary Bjerknes forces, which arise from scattered waves due to particle-particle interaction.[145] Secondary Bjerknes forces are inversely proportional to the distance between particles to the power of 4 and therefore become negligible in most applications.[140,146]

$$F_{acoustic} = 4\pi {R_c}^3 E_{ac} k\, sin(2kz)\Phi \quad (Equation\ 24)$$

In equation 24, E_{ac} is the acoustic energy density, k the wavenumber ($2\pi f \cdot cm^{-1}$), and z the distance between cell and pressure anti-node. From equations 23 and 24 it is intuitive that particle sorting by acoustophoresis can be achieved through differences in cell size (R_c), density (ρ_c) or compressibility, which relates directly to the speed of sound inside the cell (c_c).

The sign of the acoustic contrast factor determines whether the cell is pushed towards a pressure node or anti-node.[140,144,146] Cells with opposing contrast factors can be separated by being concentrated in different locations inside the channel. Most commonly, acoustophoretic sorting is achieved using a single pressure node located at the centre of the channel.[143] Therefore, particles with positive contrast factors (most solid particles and cells in aqueous conditions) are drawn to the centre of the channel, whereas particles with negative contrast factors (air bubbles or oil droplets) are drawn to the pressure anti-nodes near the channel walls (Figure 2.7b, c).[143]

When cells have similar contrast factors, separation can be performed based on size. The acoustic force is directly proportional to the cell volume and therefore larger cells will be displaced faster than smaller cells and can be collected in different outlets (Figure 2.7d). Reviews on the detailed physics of acoustophoresis as well as applications can be found elsewhere.[140,143,144,146]

Using acoustophoresis, cancer cell lines have been sorted from RBC-lysed whole blood obtained from healthy volunteers.[147,148] Using tilted-angle standing surface acoustic waves,

MCF-7, spiked at $3x10^5$ cells·mL^{-1}, were sorted with 84 % purity and a recovery of 71 % of the total cell number.[148] Augustsson *et al.* obtained higher purities when sorting prostate cancer cell lines using a bulk acoustic wave but the best results were obtained with fixed cells. DU145 cells could be sorted with a purity of 98 % and very little cell loss (3 %). PC3 cells behaved similarly to DU145 but results with LNCaP cells were disappointing, with recovery rates lower than 80 % and purity in the range of 60 %. The authors speculate that differences in density and/or compressibility of these cells were responsible for the lower efficiency. For live unfixed cells the best results were obtained again with DU145 but with slightly lower purity (93 %) and higher cell loss (16 %). Recently, the same group demonstrated sorting of fixed DU145 from WBCs with similar results but using a single-inlet two-stage bulk acoustophoresis device.[149] The first stage pre-positions all cells near the walls of the device eliminating the need for sheath flow focusing. A second acoustophoretic stage draws all cells into the centre of the channel allowing kinetic separation of the larger CTCs in a central outlet (Figure 2.7e). It should be noted that in all these applications, CTCs were spiked at concentrations of 10^4 to 10^5-fold higher than those found in clinical samples.[150]

With respect to rare progenitor cells, Dykes *et al.* used a bulk acoustophoretic device to deplete platelets from peripheral blood progenitor cell (PBPC) samples obtained by leukapheresis, ultimately for haematopoietic stem cell transplantation.[151] Platelets were depleted by 88 % while almost 98 % of the leukocytes were retained. The authors also demonstrated that the progenitor cells retained viability and maintained their colony-forming ability post-sorting. The same group used immunomagnetic beads to alter the acoustic properties of the cells to achieve improved separation.[152] $CD4^+$ lymphocytes were separated from RBC-depleted PBPC samples with 87 % purity and separation efficiencies of 65 %, comparable to MACS. Cell viability was not affected and both the $CD4^+$ lymphocytes and the non-targeted progenitors function was preserved.

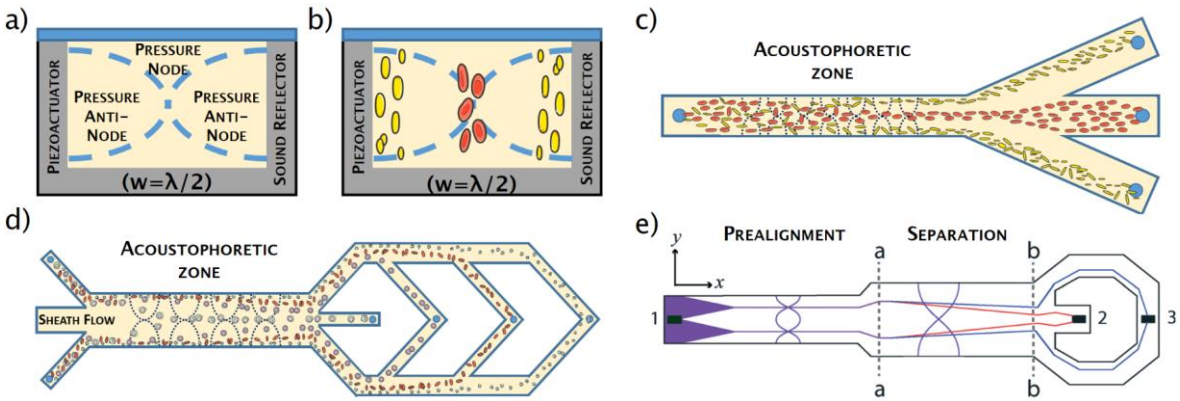

Figure 2.7 – Acoustophoresis. a) Formation of a pressure node and two anti-nodes when a fundamental resonance frequency is applied with the width of the channel (w) being equal to half the wavelength of the ultrasound. b) Particles with acoustic contrast factors with opposite signs (*e.g.* red blood cells and lipid particles) are focused respectively on the pressure node and anti-nodes of the channel. c) and d) Examples of separation by acoustophoresis by a density-based, equilibrium method, and a size-based, kinetic method, respectively. e) Sheathless two-stage acoustophoresis device used to sort fixed DU145 CTCs spiked into RBC-lysed whole blood. The first stage pre-aligns the cells near the channel walls. At the second stage, the larger CTCs are focused faster towards the channel centre and collected in outlet 2.[149] Image from Xavier *et al.*[62]

One aspect that stands out from all these applications is that in all cases separation was achieved based on differences in cell size. In the one case in which cell discrimination by size was not possible, $CD4^+$ lymphocytes were immuno-labelled to alter their acoustic properties and allow separation.[152] Sorting SSCs based solely on size differences is unlikely to discriminate sufficiently, as SSCs are characterised by a broad distribution in size and co-localise mainly with the monocyte population.[65] Additionally, antibody-labelling will not provide an improvement over current SSC sorting techniques while a specific SSC marker is yet to be identified. Most of the publications used samples that had been subjected to some kind of decomplexation and with a high concentration of targeted cells. Given the rarity of SSCs and the complexity of bone marrow tissue, none of these papers described a technology that would be suitable for SSC isolation. Finally, only one publication reports a throughput (300,000 cells/min)[152] of the order of magnitude required for SSC isolation from a bone marrow buffy coat, which can comprise over a billion cells. Thus, acoustophoresis may not demonstrate the throughput required for sorting SSCs from bone marrow harvests. However, like DLD, acoustophoresis could be used for decomplexing and to enrich the SSCs in a bone marrow buffy coat through size fractionation. Further purification could be achieved in a two-stage acoustophoresis approach by immuno-labelling the remaining contaminant cells in order to change their acoustic contrast factor.

2.3.6. Dielectrophoresis

When a biological particle is subjected to an AC electric field, it polarises due to the accumulation of charge at interfaces such as the cell membrane and its surrounding medium, leading to the formation of an induced electrical dipole.[153–156] Provided the electrodes geometry creates a non-homogeneous electric field, this polarisation gives rise to a force on the cell called dielectrophoresis (DEP). The cell can move towards or away from the high-field regions, termed positive (pDEP) or negative (nDEP) DEP, respectively (Figure 2.8a). The magnitude of the DEP force scales with cell volume and with the electric field gradient which depends on the applied voltage and electrode geometry. The DEP force also depends on the cell polarizability, which is frequency-dependent (Figure 2.8b).[153–156] Please not that DEP should be distinguished from electrophoresis, which results from the effect of a homogeneous DC field on a charged particle.

$$F_{DEP} = 2\pi\varepsilon_m {R_c}^3 Re(f_{CM})\nabla|E|^2 \quad (Equation\ 25)$$

$$f_{CM} = \frac{\tilde{\varepsilon}_P - \tilde{\varepsilon}_m}{\tilde{\varepsilon}_P + 2\tilde{\varepsilon}_m} \quad (Equation\ 26) \quad with \quad \tilde{\varepsilon} = \varepsilon - j\sigma/\omega$$

In equation 25, ϵ_m is the absolute permittivity of the suspending medium, R_c is the cell radius, $\nabla|E|^2$ the gradient of the electric field squared, and $Re(f_{CM})$ the real part of the Clausius-Mossotti factor which reflects cell polarizability. The Clausius-Mossotti factor (Equation 26) depends on the frequency of the applied AC field and on both the cell and suspending medium complex permittivity ($\tilde{\varepsilon}$) where $j^2=-1$, ω is the angular frequency and ϵ and σ the permittivity and conductivity respectively. The subscripts 'p' and 'm' refer to particle and medium.

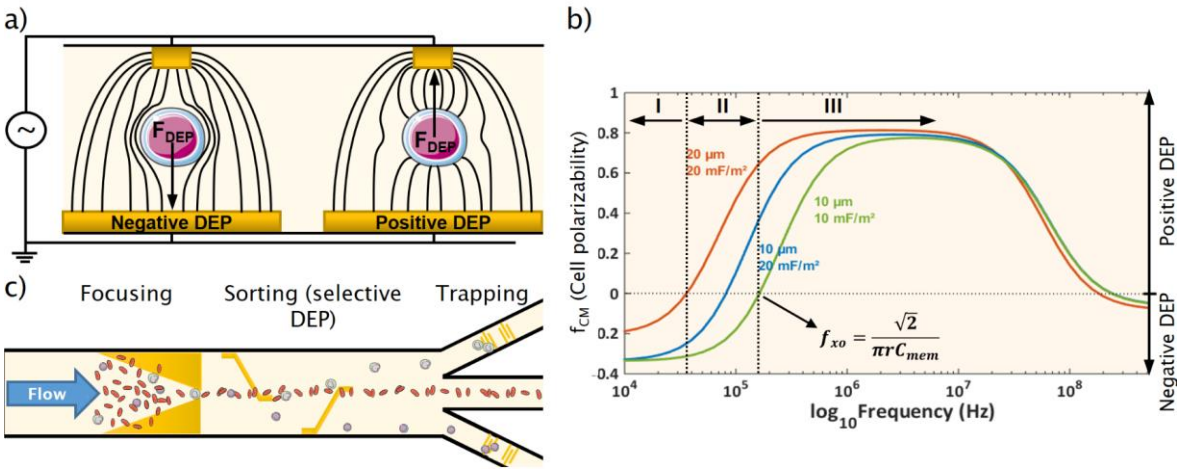

Figure 2.8 – Dielectrophoresis. a) Schematic of the deflection of electric field lines by mammalian cells in a low conductivity suspending medium. On the left, the typical response to low-frequency electric fields with field lines bent around the cell creating a negative DEP force that pushes cells away from the high field region. On the right, the opposite scenario is represented with field lines drawn to the surface of the cell, resulting in a force which pulls cells towards high field regions. b) Theoretical model of the Clausius-Mossotti factor (f_{CM}) as a function of frequency for a viable cell in a suspending medium of conductivity 40 mS·m^{-1}. The response curves of three different cells differing in size (20 or 10 µm), membrane capacitance (20 or 10 mF·m^{-2}) or both, are represented. The following parameters were used: membrane thickness, 5 nm, nuclear envelope thickness, 40 nm, nuclear radius, 5 µm, medium relative permittivity, 78.5, membrane conductivity, 10-5 S·m^{-1}, cytoplasm conductivity, 0.6 S·m^{-1}, Nuclear envelope conductivity, 5x10^{-3}, nucleoplasm conductivity, 2 S·m^{-1}, cytoplasm relative permittivity, 60, nuclear envelope relative permittivity, 20 and nucleoplasm relative permittivity, 120. c) Schematic of a possible dielectrophoresis sorting device including a region for focusing cells, a sorting region taking advantage of different cell's dielectric properties and a trapping region using positive DEP. Image from Xavier *et al.*[62]

For cell sorting, DEP is usually performed using a suspending medium of low conductivity. At lower frequencies, cells typically experience negative DEP. At higher frequencies, cells experience positive DEP and are attracted to electrodes (Figure 2.8a).[153–156] The frequency at which this response changes from nDEP to pDEP is called the cross-over frequency (f_{xo}), and is cell dependent, varying primarily with the cell membrane capacitance (C_{mem}) and size.[155]

$$f_{xo} = \frac{\sqrt{2}}{2\pi R_c C_{mem}} \quad (Equation\ 27)$$

Cell populations with different membrane capacitance or size may therefore experience DEP forces of different magnitudes and/or directions. Figure 2.8b shows a plot of the polarizability of three cell types with different sizes and membrane capacitance. Regions I and III represent frequency ranges in which all cells experience DEP with the same direction but with different magnitudes. Region II represents a frequency window in which cells experience DEP forces with opposite directions, allowing for selective DEP sorting. Many different strategies have been developed to sort cells by DEP, including focusing, trapping, or deflecting cells into different flow streams (Figure 2.8c).[156–161]

An early paper describing cell sorting with DEP used positive DEP to trap and enrich CD34$^+$ human HSCs in leukocyte fractions obtained from the buffy coat of peripheral blood and bone marrow samples.[162] However, the final purity was low (just under 5 % CD34$^+$ cells)

and the enrichment under 6-fold. Five years later, Wang *et al.* sorted $CD34^+$ HSCs (obtained by MACS separation of peripheral blood), from a human breast cancer cell line originally mixed 1:1 at a high throughput ($1.2x10^5$ cells·min^{-1}).[163] The enrichment was almost 2-fold with a final purity of over 99 % HSCs. The study included other separations such as the enrichment of leukocytes in diluted whole blood and the separation of different leukocyte populations. In this setup, a negative DEP force generated by electrodes on the bottom of a microfluidic channel levitated cells to different heights depending on their dielectric properties and buoyancy. This force pushed cells into different equilibrium positions and therefore different flow streams thus leading to kinetic separation under the influence of the parabolic flow velocity profile, in a technique known as field flow fractionation (DEP-FFF).[163] Flanagan *et al.* showed separation of astrogenic and neurogenic progenitors from neural progenitor/stem cell samples obtained from the cerebral cortex of mice brains. In their recent publication,[164] viable astrocyte progenitor-enriched populations were sorted by DEP at a rate of 2,500 cells per minute. In these devices, interdigitated electrode arrays in a microfluidic chamber were actuated with a 7 V_{p-p} signal at 1 MHz trapping all viable cells. Sequentially, under a constant sheath flow, the frequency was lowered in 100 kHz deductions, releasing cells from the array according to their cross-over frequency. As the average cell size was the same for different fractions, separation was based on differences in the membrane capacitance of neuroprogenitors which was higher for astrogenic-committed than neurogenic-committed cells. The dielectric properties of astrocytes, neurons and their progenitors were characterised according to DEP trapping over defined frequency ranges.[165–167] Astrocytes were trapped at lower frequencies (300 kHz) while neurons only achieved over 95% capture at 5,000 kHz. Interestingly, progenitor cells were trapped at intermediate frequencies rounding 1,000 kHz.

Two publications demonstrate sorting of human BMSCs.[168,169] One used a human immortalised MSC cell line that differentiated to form osteoblasts. The two cell populations were separately harvested, mixed together in a 1:1 ratio and processed at 300 cells per minute through a microfluidic chamber with oblique interdigitated electrodes. Osteoblasts experienced stronger positive DEP forces and were deflected laterally into a different outlet. Although sorting efficiencies were not high (86 % and 67 % recovery efficiencies, for MSCs and osteoblasts respectively), this work was an important proof of principle of sorting BMSCs using DEP.[168] Vykoukal *et al.* used DEP-FFF to enrich populations of $NG2^+$ putative adipose-derived stromal stem cells from human samples.[169] A 14-fold enrichment was obtained increasing the amount of $NG2^+$ cells from round 2 % to over 27 %.

The MG-63 cell line is osteoblast-like and commonly used as a Stro-1^+ model for SSCs. Their dielectric properties were measured by DEP and compared to another osteosarcoma cell line, Saos-2, and human primary Stro-1-enriched SSCs.[170] Ling *et al.* took advantage of the much larger size of MG-63 to sort them from erythrocytes by positive DEP using a periodic microelectrode array, obtaining a purity of 83 % (11-fold enrichment),[171] though actual cell collection was not performed.

Apart from the work of Wang *et al.*, in which cells were sorted at over 100,000 per minute,[163] throughput in DEP is generally low. Additionally, most of the examples referred

to above were performed on samples in which the target cells were not rare and with modest enrichment. Although this is true for all the applications shown with progenitor cells, examples with higher throughput and enrichment can be found in DEP approaches to CTC sorting. Moon *et al.* combined inertial microfluidics, using an expansion and contraction array, with DEP to separate MCF-7 cells mixed with WBCs and RBCs in a 1 to 1 to 1,000 ratio.[172] At the end of the two separation stages, up to 75% of the cancer cells were recovered with approximately 16% purity, representing a 160-fold enrichment. The total throughput was higher than 1 million cells per minute, although this was mostly due to the initial inertial microfluidics step. Shim *et al.* used a continuous flow DEP-FFF approach to sort a breast cancer cell line spiked at a low frequency (50-600·mL^{-1}) into the buffy coats of healthy peripheral blood samples.[173] The frequency of the AC electric field was set between the cross-over frequencies of the tumour cells and blood mononuclear cells so that the cells experienced DEP forces of different polarity. The reported throughput was the highest ever achieved for DEP sorting at up to one million cells per minute. Purities of 80 % were achieved with a recovery of about 75 % of the spiked tumour cells.

2.4. Summary and prospects of label-free skeletal stem cell sorting

Microfluidic techniques for stem cell sorting are at an early stage and count with few publications. However, label-free separation technologies exist and have improved over the past two decades as evidenced by the progress in CTC sorting from complex or even clinical samples. When sorting SSCs from BM, high purity is a significant concern with target values of 100 % pure populations. MACS separation of Stro-1$^+$ cells provides a 950-fold enrichment of SSCs over BMSCs,[49] a value which can be further increased to 2,000-fold by further selection of CD146$^+$ cells.[50] Such enrichment values are far above the best examples using microfluidic techniques to sort stem cells.[169] However, they are within the range of enrichment achieved for sorting CTCs[108,134] or nucleated RBCs[109] from whole blood where over 10^4-fold and 10^3-fold enrichment have been achieved respectively. Table 2.1 provides a summary of the best examples found for each technique. Table 2.2 and Table 2.3 show examples of each of the techniques discussed in section 2.3 for sorting stem or progenitor cells and CTCs, respectively.

Given the rarity of SSCs in human BM, a high-throughput separation method is critical to enable a practical number of cells to be sorted for clinical applications. Ideally, a throughput of around one million cells per minute would be desirable for sorting bone marrow buffy coat, or even higher for sorting non-processed bone marrow. With the exception of acoustophoresis and possibly DEP, most microfluidic sorting techniques have now demonstrated very high throughput in the range of millions of cells per minute (Table 2..1). However, owing to the complexity of BM tissue and the heterogeneity of the SSC, sorting SSCs from human BM with high purity and within a reasonable amount of time, will likely require a combination of different sorting techniques rather than one technique in isolation. For example, a decomplexing step based on cell size fractionation followed by a refining step to increase purity.

Also due to the complexity of BM, any sorting approach would likely benefit from initial washes and straining to remove fat and bone debris as this would be hard to achieve on chip without clogging. Further removal of RBCs using either density centrifugation or selective lysis would result in a significant decomplexing of the sample to be processed. Cell lysis is advantageous in terms of rapid processing and simplicity. Density centrifugation is slower and is less than 100 % effective but, in addition to RBC removal, it is able to deplete the sample partially of contaminating platelets and granulocytes.

Label-free separation approaches will depend on identifying unique biophysical features of SSCs that render them distinguishable from other nucleated cells in the BM. High-throughput single-cell characterisation techniques such as microfluidic impedance cytometry (MIC)[174] and real-time deformability cytometry (RT-DC)[175] can provide data on cell dielectric and cell mechanical properties. The next two chapters of this thesis explore these techniques to address the size, dielectric, and mechanical characterisation of SSCs in order to aid in the design of a label-free approach to sort SSCs from human BM with significant physiological and therapeutic implications.

Table 2.1 – Summary of the best performance examples of the reviewed microfluidic label-free sorting techniques.

Technique	Discriminating features	Throughput	Purity	Enrichment	Recovery	Label-free
DLD	Size, shape, deformability	1.8×10^9 cells·min^{-1} [176]	98.7 % [106]	Depletion of platelets & RBCs [107,108] 174-fold [176]	99 % [106]	Yes
Acoustophoresis	Size, density, compressibility	3×10^5 cells·min^{-1} [152]	98 % [147]	8.4-fold [148]	98 % [151]	Yes
Inertial	Size, density, deformability	2.5×10^8 cells·min^{-1} [135]	99 % [177]	10^9-fold over RBCs [135] $10^{3.3}$-fold over RBCs [135]	99 % [178]	Yes
Dielectrophoresis	Size, dielectric properties	1.3×10^6 cells·min^{-1} [172]	99 % [163]	10^4-fold [173]	92 % [179]	Yes
Magnetophoresis	Magnetic susceptibility	4×10^6 cells·min^{-1} [180]	50 % [107]	$10^{3.8}$-fold [107]	97 % [108]	Yes, negative depletion
Affinity-based	Antibody-labelling	1×10^8 cells·min^{-1} [82]	68 % [83]	~ 10^9-fold [81-83]	92 % [82]	No

Table 2.2 – Current label-free microfluidic applications to stem and progenitor cell sorting. When not referred in the papers, $5x10^9$ and $5x10^6$ red and white blood cells per millilitre of blood, respectively, were considered as reference values for the performance calculations.

Ref.	Sorting Method	Cell types / Sample	Throughput	Purity	Enrichment	Recovery Rate
[88]	Affinity-Based (μ-FACS)	Stro-1$^+$ progenitor cells from human periosteal tissue	1 μL·min^{-1} 500-1,000 cells·min^{-1}	N/A	N/A	N/A
[101]	DLD	Cell lines mimicking e cardio-myocytes and nonmyocytes from cardiac tissue	200 μL·min^{-1} 10^5 cells·min^{-1}	97 %	1.9-fold	90 %
[102]	DLD	Diluted rat cardiac tissue digests (3.3×10^5 cells·mL^{-1})	80 μL·min^{-1} 2.6×10^4 cells·min^{-1}	91 %	1.5-fold	30-35 %
[109]	DLD Magnetophoresis	Nucleated-RBCs from peripheral blood (diluted 1:2)	216 μL·min^{-1} $6x10^8$ cells·min^{-1}	<0.01 %	> 10^3-fold	N/A
[129]	Inertial focusing	Larger and smaller MSCs from human BM after plastic adhesion	3 mL·min^{-1} 3×10^6 cells·min^{-1}	N/A	N/A	N/A
[132]	Inertial focusing	Adrenal cortical progenitors from murine adrenal gland di-gests (4×10^5 cells/mL)	60 μL·min^{-1} 2.4×10^4 cells·min^{-1}	N/A	N/A	N/A
[151]	Acoustophoresis	Peripheral blood progenitor cells sorted from platelets in leu-kapheresis samples	20 μL·min^{-1} 3.5×10^4 cells·min^{-1}	< 50 %	3-fold 88 % - platelet depletion	97.8 %
[152]	Acoustophoresis	CD4$^+$ lymphocytes sorted from peripheral blood progenitor cell samples	30 μL·min^{-1} 3×10^5 cells·min^{-1}	87 %	4-fold	65 %
[162]	DEP	HSCs enriched from BM and blood buffy coats	N/A	5 %	~6-fold	N/A
[163]	DEP	Human HSCs mixed 1:1 with a cancer cell line (MDA-435)	100 μL·min^{-1} 1.2×10^5 cells·min^{-1}	99 %	~2-fold	N/A
[164]	DEP	Mouse neural progenitors frac-tionated into viable astrocyte progenitors	0.5 μL·min^{-1} 2.5×10^3 cells·min^{-1}	N/A	2.41-fold	N/A
[181]	DEP	C2C12 progenitor myoblasts separated from their progeny (myotubes) after differentiation	2 μL·min^{-1} <8×10^4 cells·min^{-1}	95 % myoblasts 98.6 % myotubes	~ 2-fold	N/A
[168]	DEP	Immortalized hMSCs mixed 1:1 with differentiated osteoblasts	0.3 μL·min^{-1} 3×10^2 cells·min^{-1}	84 % (hMSCs) 68 % (osteoblast)	1.7-fold 1.3-fold	86 % (hMSCs) 67 % (osteo-blasts)
[169]	DEP	Putative progenitor cells sorted from human enzyme-digested adipose tissue	1.5 mL·min^{-1} ~$2x10^4$ cells·min^{-1}	28 %	14-fold	N/A
[171]	DEP	MG-63 mixed 1:3 with RBCs	2.5 μL·min^{-1} 1.3×10^3 cells·min^{-1}	83 %	~11.4-fold	N/A

Table 2.3 – Current label-free microfluidic applications to circulating tumour cell (CTC) sorting. When not referred in the papers, $5x10^9$ and $5x10^6$ red and white blood cells per millilitre of blood, respectively, were considered as reference values for the performance calculations.

Ref.	Sorting Method	Cell types / Sample	Throughput	Purity	Enrichment	Recovery Rate
[81]	Affinity-based	Human cancer cell lines spiked (100 CTCs·mL^{-1}) in whole blood Cancer patients whole blood	17-34 µL·min^{-1} 9-17 x 10^7 cells·min^{-1}	9.2 % 52-67 %	~10^9-fold	>65 % 115/116 patients
[82]	Affinity-based	PC-3 cells spiked (1,000 CTCs·mL^{-1}) in whole blood Cancer patients whole blood	20 µL·min^{-1} 1 x 10^8 cells·min^{-1}	14 %	~10^9-fold	92 % 13-13,000 CTCs 14/15 patients
[83]	Affinity-based	LNCaP prostate cancer cell line spiked in whole blood Prostate cancer patients whole blood	17 µL·min^{-1} 8.5 x 10^7 cells·min^{-1}	62-68 %	~10^9-fold	85 % 18/20 patients
[103]	DLD	3 cancer cell lines spiked (10^6 CTCs·mL^{-1}) in PBS or (~7 x 10^6 CTCs·mL^{-1}) in diluted blood	10 mL·min^{-1} 3 x 10^8 cells·min^{-1}	16.7 %	3.34-fold	86 %
[106]	DLD	5 cancer cell lines spiked (10^5 CTCs·mL^{-1}) in PBS or (10^4 CTCs·mL^{-1}) in diluted blood	50-2,000 µL·min^{-1} 9 x 10^8 cells·min^{-1} (for 2,000 µL·min^{-1})	98.7 % (at 2 000 µL·min^{-1})	40-fold over WBCs 115-fold over RBCs (at 2 000 µL·min^{-1})	99 % (for MCF-7 in diluted blood run at 2,000 µL·min^{-1})
[107]	DLD Inertial focusing Magnetophoresis	5 cancer cell lines spiked (200-1,000 CTCs·mL^{-1}) in whole blood Prostate and breast cancer patients (~50 CTC·mL^{-1}) whole blood	133 µL·min^{-1} 6 x 10^8 cells·min^{-1}	7.8 % (positive selection)	Total removal of RBCs 3.5 log WBC depletion (99.9%) (positive selection) 2.5 log WBC depletion (99.7%) (negative depletion)	11-99 % (positive selection; cell-line dependent) 97 % (negative depletion)
[108]	DLD Inertial focusing Magnetophoresis	6 cancer cell lines spiked (1,000 CTCs·mL^{-1}) in whole blood	133 µL·min^{-1} 6 x 10^8 cells·min^{-1}	~ 50 %	Total removal of RBCs 3.8 log-depletion (99.9%) of WBCs (negative depletion)	97 %
[133]	Inertial	MCF-7 spiked (500 CTCs·mL^{-1}) in 1:20 diluted blood	400 µL·min^{-1} 10^8 cells·min^{-1}	0.025 %	5.5 log-depletion (RBCs) 4.1 log-depletion (WBCs)	81 %
[134]	Steric Hindrance Inertial	3 cancer cell lines) spiked (100-1,000 CTCs·mL^{-1}) in diluted blood	6 µL·min^{-1} 2.3 x 10^7 cells·min^{-1}	~20 %	<2 x 10^5-fold 5.3 log-depletion of blood cells	>90 %
[135]	Inertial	MCF-7 spiked (10^5 CTCs·mL^{-1}) in diluted blood Lung cancer patients whole blood	100 µL·min^{-1} 2.5 x 10^8 cells·min^{-1}	~95 % ~10 %	9 log-depletion (RBCs) 3-3.3 log-depletion (WBCs)	85 % 5-88 CTCs·mL^{-1} (20/20 patients)
[136]	Inertial	3 cancer cell lines spiked (<100 CTCs·mL^{-1}) in RBC-lysed blood Breast and lung cancer patients whole blood	1.7 mL·min^{-1} 6 x 10^6 cells·min^{-1}	<20 % N/A	~4 log-depletion of WBCs N/A	>80 % 3-125 CTC·mL^{-1} (10/10 patients)
[147]	Acoustophoresis	Fixed/viable cancer cells spiked (2.5 x 10^5 CTCs·mL^{-1}) in diluted RBC-lysed blood	70 µL·min^{-1} ~5 x 10^4 cells·min^{-1}	98 % (fixed) 93 % (viable)	95 % WBC depletion	97 % (fixed) 84 % (viable)
[148]	Acoustophoresis	MCF-7 cancer cell line spiked (3 x 10^5 CTCs·mL^{-1}) in diluted RBC-lysed blood	2 µL·min^{-1} ~10^4 cells·min^{-1}	84 %	8.4-fold	71 %
[149]	Acoustophoresis	DU145 prostate cancer cell line spiked (5 x 10^4 CTCs·mL^{-1}) in diluted RBC-lysed blood	100 µL·min^{-1} ~5 x 10^4 cells·min^{-1}	97.6 % (fixed)	98 % WBC depletion 40-fold	96 %
[172]	DEP	MCF-7 cells mixed with WBCs and RBCS (1:1:1,000)	126 µL·min^{-1} 1.3 x 10^6 cells·min^{-1}	16 %	162-fold 99 % RBC depletion 94 % WBC depletion	76 %
[173]	DEP	2 cancer cell lines spiked (<600 CTCs·mL^{-1}) in blood buffy coat Buffy coats from late stage cancer patients	250 µL·min^{-1} 10^6 cells·min^{-1}	70-80 % 10 % CTCs detected	~10^4-fold N/A	75 % N/A

Chapter 3

Mechanical Phenotyping

"The good thing about Science is that it is true whether or not you believe in it."
Neil deGrasse Tyson

3.1. Introduction

3.1.1. Cell Mechanics

Microfluidic label-free cell sorting techniques, covered in Chapter 2, are able to sort cells based on particular biophysical properties that differentiate the cells of interest from other cells in a heterogeneous mixture. Cell biophysical properties include, but are not limited to, cell size, shape, stiffness, compressibility, density, intrinsic magnetic susceptibility, and dielectric properties.

This chapter focuses on the mechanical phenotyping of SSCs, particularly SSC deformation under flow. Cell stiffness/deformability is a biophysical property that gained significant interest in the past decades and can be used to sort cells using microfluidic methods capable of high-throughput cell sorting, such as DLD or inertial microfluidics. Additionally, it has long been demonstrated that cell mechanical properties are intrinsically related to their cytoskeletal structure which translates to different cell states, function and differentiation paths.[182–187] For example, human BMSCs were shown to stiffen with both passage number and population doubling, with more deformable cells typically displaying an enhanced differentiation potential.[188] A recent study has also correlated the elastic modulus of BMSCs with their differentiation potency.[131]

The elastic modulus, or Young's modulus, is a measure of an object's resistance to elastic (*i.e.* non-permanent) deformation. A stiffer material will have a higher elastic modulus.[189] There is a degree of variation within the elastic moduli reported for hBMSCs.[131,184,188,190,191] These range from just over 0.2 kPa[131] to 8 kPa,[188] with the higher values being typically associated with cells of higher passage numbers or that have passed through several passage doublings.

However, there has been no study of the deformability of SSCs in the context of a label-free biomarker for cell separation. Separation by stiffness is based on the fact that two cells of similar size but with significantly different mechanical properties will have different effective radii. Accordingly, the more deformable or compliant cell will be squeezed by shear forces and therefore appear smaller than its actual size. For example, in 2014 Holmes et al.[97] showed that by deforming cells in a DLD device operated at increasing pressure (flow rates) it is possible to discriminate between sub-populations of leukocytes (T-lymphocytes and neutrophils) through a combination of size and deformation differences. Interestingly,

this effect had already been alluded to in one of the very first publications on DLD by Robert Austin's group in 2006.[192]

Due to the growing interest in cell mechanics, cell compliance, stiffness and deformability have been studied using disparate methods including atomic force microscopy,[188] micropipette aspiration[190] and optical stretchers.[186,188] However, these methods are limited by a low throughput, which is typically between 10 to 100 cells per hour, and are not applicable to study rare and heterogeneous cell populations. Conversely, microfluidics offers alternatives to perform high-throughput single cell mechanical phenotyping at rates of hundreds per second, including the deformability cytometer developed in Dino Di Carlo's group[193] or real-time deformability cytometry (RT-DC) introduced by Oliver Otto in Jochen Guck's lab.[175] Since its introduction in 2015, RT-DC has been included in multiple publications studying diverse biological phenomena including cytoskeleton alterations,[194–196] the BM HSC microenvironment[197] or RBC infection with the malaria parasite.[198] The work presented in this chapter studies the mechanical properties of enriched populations of primary human SSCs while providing a direct comparison with other cell populations present in the BM, including WBCs from human blood and a human myeloid progenitor cell line – HL-60.

This work was performed in collaboration with the Technische Universität Dresden and Professor Jochen Guck's research group. The concept design and device production were carried out by Dr. Oliver Otto and the team of ZellMechanik Dresden, GmbH, a partner of the EU LAPASO project that funded this PhD. The statistical analyses and the analytical model that allowed the introduction of isoelasticity lines to the RT-DC scatter plots were developed by Maik Herbig.[199–201] The work resulted in one of the first original research publications using RT-DC, published in the peer-reviewed journal *Integrative Biology* in early 2016.

3.1.2. Real-Time Deformability Cytometry

RT-DC is a contactless microfluidic technique for high-throughput screening of cell mechanical properties. Cells, suspended in a viscosity-adjusted medium, are hydrodynamically focused and flow through a narrow constriction where they deform from a typical circular shape into a bullet-like shape at steady state, due to shear and normal stresses (Figure 3.a–c). Images are captured and analysed in real-time, at rates of hundreds of cells per second, allowing to determine the cell cross-sectional area and circularity (*C*), given by equation 28, where *A* is the cell projected area and *l* its perimeter.

$$C = \frac{\sqrt{2\pi A}}{l} \quad (Equation\ 28)$$

Cells are characterised by their deformation *(D = 1 – C)*, which defines the deviation of a cell from a perfect circle (*C = 1*). Both cell deformation and size are displayed as scatter plots (Figure 3.d). Because flow is laminar, larger cells are subjected to higher shear stresses for flowing closer to the channel walls where the fluid velocity is slower. Thus, larger cells will deform more than smaller cells with identical mechanical properties. To disentangle both contributions, an analytical model was developed by calculating the hydrodynamic flow profile around a moving cell in confinement and coupling the resulting surface stress

to a linear elastic model.[200] This model was recently further expanded to account for the influence of cell deformation on the fluid flow with good agreement with the analytical model used to date.[199] The model predicts the resulting deformation and introduces isoelasticity lines to the scatter plots (Figure 3.d). The lines divide a typical deformation scatter plot into areas of identical stiffness for multiples of a given elastic modulus E_0 (Figure 3.d).[175,200,202] This enables cell deformation to be determined independently of hydrodynamic stresses thus permitting comparison between cells with significant size differences.

3.2. Results and Discussion

3.2.1. HL-60, MG-63 and Mesenchymal and Skeletal Stem Cells

MG-63, MSCs and SSCs are large cells with considerable size heterogeneity.[170] The constriction in the RT-DC device needed to be wide enough to allow the larger cells to flow through, but not so large that smaller cells would not experience enough shear stress to deform.[175] HL-60 are generally measured using 20 x 20 µm cross-section channels, but for this work 30 x 30 µm channels were used to accommodate the larger MG-63 and SSCs. Consequently, the first experiments were to verify that the deformation of HL-60 (a model for human haematopoietic progenitor cells) could be measured in the larger channels using different flow rates (Figure 3.2). Indeed, the deformation of HL-60 increased with the flow rate indicating that the 20 x 20 cross-section channels could be used. As a control, cells were also imaged upstream of the constriction channel (reservoir) where deformation should not occur. The same control was used for every cell measured in this study with RT-DC.

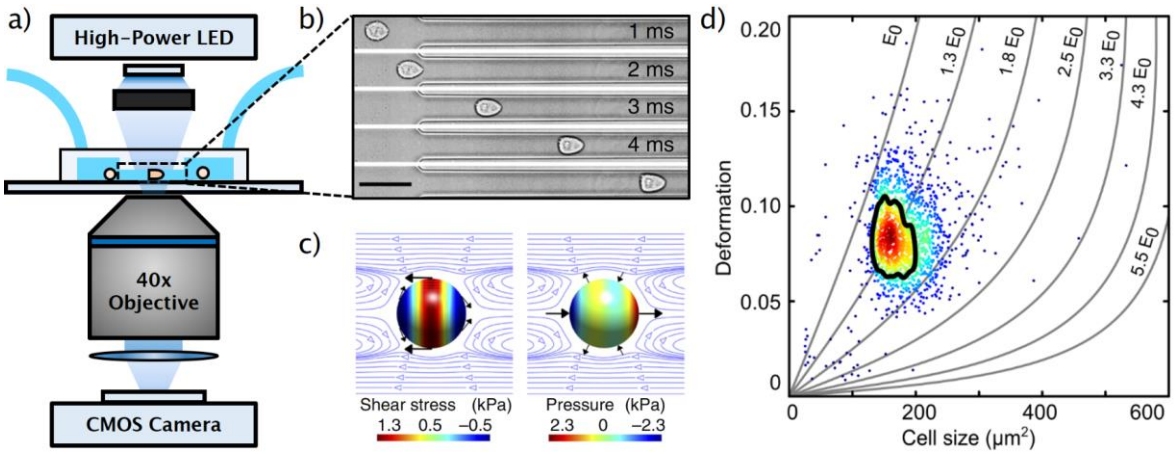

Figure 3.1 – Real-time deformability cytometry. (a) Schematic of the RT-DC set-up. (b) shows images of a single cell deforming into the characteristic bullet-like shape in a 20 x 20 µm cross-sectional constriction within the microfluidic chip depicted in (a); scale bar: 50 µm. (c) shows the shear and normal stresses acting on a cell flowing in the constriction channel; black arrows indicate stress directions; surface colour indicates magnitude and blue lines show the flow profile in a co-moving reference frame. (d) shows deformation *vs* projected size (in µm²) of HL-60 cells, measured at 0.32 µL·s^{-1}, including isoelasticity lines, which divide a typical deformation scatter plot from a 30 µm x 30 µm constriction channel into areas of identical stiffness for multiples of a given elastic modulus (E_0). Solid black line highlights 50%-density contour. Adapted from Otto *et al.* Nat. Meth. 12, 199-202 (2015).[175]

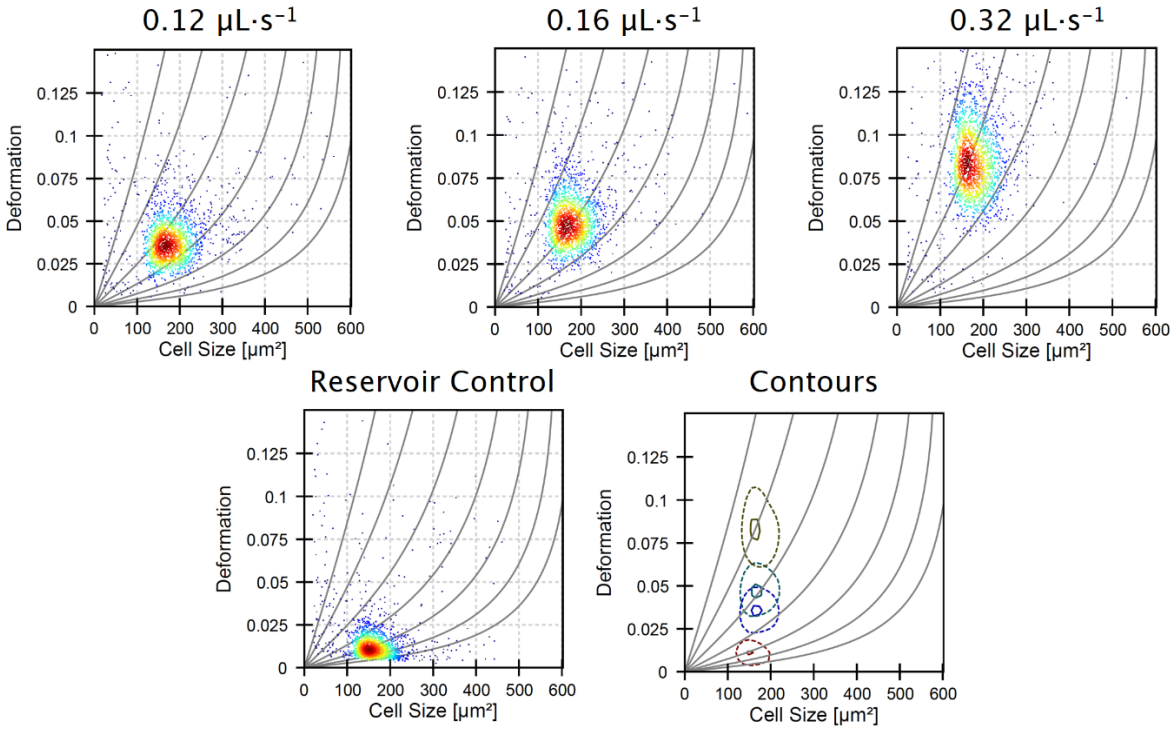

Figure 3.2 – Real-time deformability cytometry. Deformation vs projected size (in µm²) of HL-60 cells measured in isolation at increasing flow rates (0.12 – 0.32 µL·s⁻¹). All scatter plots show deformation *vs* cell size (cross-sectional area) and experiments were carried out using the 30 x 30 µm cross-sectional channel; colour indicates density scale and each dot is representative of a single event from a total of 2,000 events. As a control, cells were imaged upstream of the constriction channel (reservoir) where deformation should not occur. The 50 %-density contour plots highlight the increase in cell deformation with no changes in cell size as could be anticipated.

To compare the deformability of HL-60 and MG-63, both cells were mixed in approximately equal numbers and measured simultaneously. The deformation scatter plot for the two cell populations demonstrated a clear discrimination in size and deformation (Figure 3.3a and Appendix A, Figure S1). Using a two-dimensional mixture model[203–205] and linear mixed models[206], as described in the Materials and Methods chapter of this thesis, MG-63 cells were observed to be larger ($p<0.0001$) and deform less ($p<0.01$) than HL-60 cells (Figure 3.3b). Analysis of captured cell images (Figure 3.3f, g) confirmed that the HL-60 cells were smaller and observed to be more elongated (more deformed) than MG-63. As previously described, larger cells are subject to higher shear gradient stresses as the cells flow closer to the channel walls. The fact that MG-63 are larger and deformed less than HL-60 cells indicates that MG-63 have a higher Young's modulus.

SSC size and deformation were subsequently measured in isolation (Figure 3.3c and Appendix A, Figure S2). The population of small particles on the bottom left corner was debris from the high ECM production of confluent SSCs. SSCs displayed a much broader distribution reflecting the population heterogeneity. This was expected given these are primary cells from human samples enriched via Stro-1 antibody selection, but still represent a heterogeneous population. Despite the greater spread, the SSC population almost matches the MG-63 osteoblast-like cells in terms of size and deformation. This can also be seen for the representative images in Figure 3.3g and h.

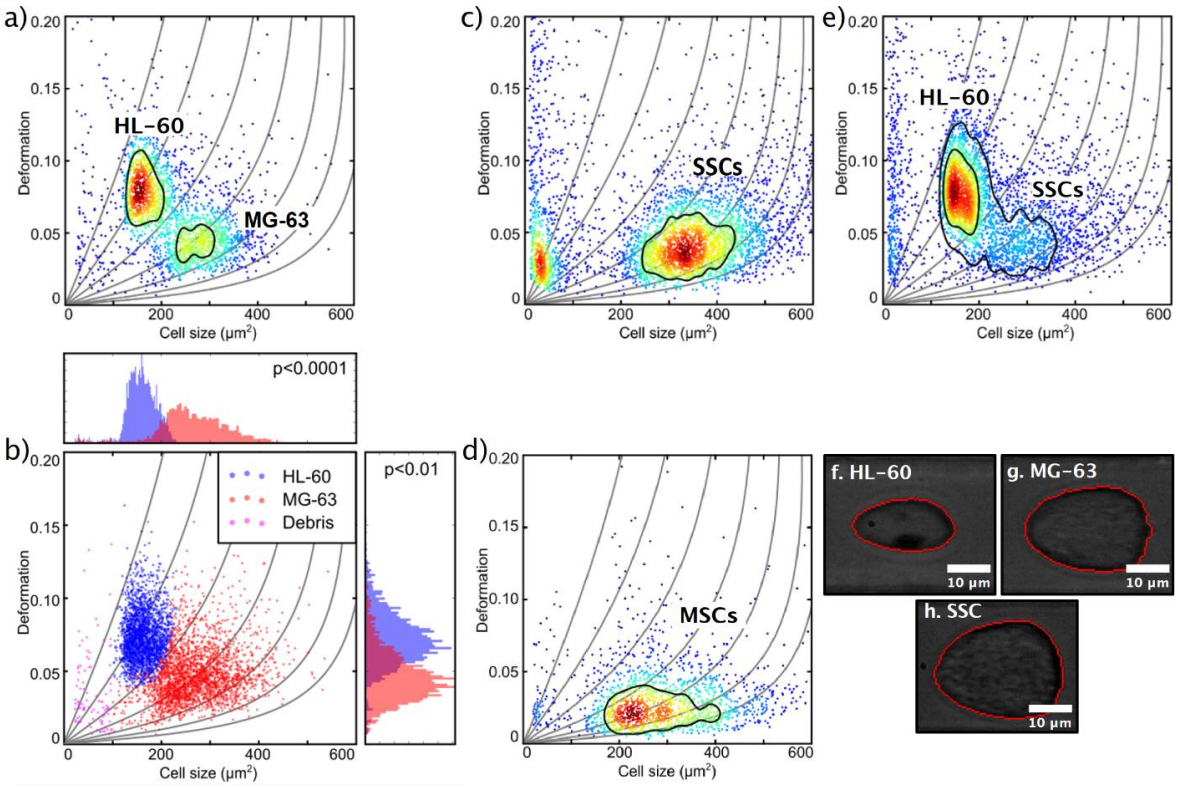

Figure 3.3 – Real-time deformability cytometry. (a) MG-63 mixed 1:1 with HL-60; (b) shows deformation vs projected size (in μm²) of MG-63 and HL-60 combining events from 3 measurements unbiasedly allocated using mixture models, with respective histograms demonstrating cell size and deformation distributions. The p-values were calculated using 1-dimensional linear mixed models. (c) Stro-1⁺-enriched skeletal stem cells; (d) Human bone marrow mesenchymal stromal cells and (e) Stro-1⁺-enriched skeletal stem cells mixed 1:1 with HL-60; All scatter plots show deformation *vs* cell size (cross-sectional area) and experiments were carried out at 0.32 μL·s⁻¹ through the 30 x 30 μm cross-sectional channel; colour indicates density scale and each dot is representative of a single event from a total of 2,000 events. Images (f) to (h) show representative captures of the cells from (a, c, e) with the red line representing the contour determined by image analysis in real-time.

Although it is hard to find agreement in the published values of the Young's modulus of MSCs, probably owing to the ambiguity of their definition and different tissue sources,[207] studies report that MSCs are typically stiffer than their differentiation progenies or similar to osteoblasts.[184,190,191,208] In fact, the measurement of MSCs in isolation (Figure 3.3d and Appendix A, Figure S3) shows a population that is heterogeneous in size and encompasses the SSC population shown in Figure 3.3c. This supports the fact that SSCs are a sub-population found within the group of progenitors that represent the MSCs. Interestingly, Stro-1-enriched SSCs differ significantly in deformation from MSCs ($p<0.05$), highlighting the potential of RT-DC for label-free identification and sorting of stem cells.

Measurement of a mixture of SSCs and HL-60 cells together (Figure 3.3d and Appendix A, Figure S4), displayed distinct populations to be present though with a degree of overlap. SSCs were observed to be larger ($p<0.001$), however, their deformation was generally lower than that of HL-60 ($p<0.01$), indicating higher stiffness. In a previous study it was shown that HSCs derived from human BM are softer than HL-60.[175] Consequently, the current study implies that SSCs are stiffer than human BM-derived HSCs.

3.2.2. Mixed White Blood Cell and Skeletal Stem Cell populations

For label-free isolation of SSCs from human BM to reach successful clinical application, SSCs should be significantly different from white blood cells. WBCs arise from HSCs, which share their stem cell niche with SSCs in the bone marrow. WBCs can be divided into three main populations: lymphocytes, monocytes and granulocytes, with neutrophils representing the vast majority of the latter.[209–211] WBCs were isolated from human blood samples by selective lysis and measured by RT-DC. As shown in Figure 3.4a and Appendix A, Figure S5, it was possible to discriminate between lymphocytes (Figure 3.4b) and granulocytes/monocytes (Figure 3.4c), with lymphocytes being noted to be the smallest cells and deforming less than granulocytes and monocytes ($p<0.001$).[211]

It is broadly accepted that WBCs are highly deformable. Indeed, the inherent ability of leukocytes to deform is important in their immune function and methods for determining impaired WBC deformability have been previously proposed for the diagnostics of certain conditions such as trauma or sepsis.[185,212,213]

The scatter plots in Figure 3.4d (Appendix A, Figure S6) and Figure 3.4e (Appendix A, Figure S7), show RT-DC data of human WBCs mixed with MG-63 or SSCs, respectively. The data were analysed using a two-dimensional mixture model[203–205] and linear mixed models[206] (Figure 3.4f). These models reveal that all cell types could be discriminated based on size and deformation with statistical significance. In fact, although being the largest cells investigated ($p<0.001$), MG-63 ($p<0.01$) and SSCs (not significant) deform less than granulocytes and monocytes. The two WBC sub-populations are difficult to resolve in Figure 3.4d and Figure 3.4e due to scaling, but comparison of these figures with Figure 3.4a shows that the two sub-populations are located within isoelasticity lines (Figure 3.d) of lower Young's modulus indicating that both MG-63 and SSCs have a Young's modulus superior to any sub-population of WBCs.

This provides a possibility for exploiting novel mechanical-based sorting strategies for SSC isolation. The fact that SSCs form a mechanically different sub-population within MSCs of higher deformability clearly points in this direction and is in agreement with current literature indicating that cells of higher potency tend to deform more.[188] Taking advantage of the high-throughput of RT-DC, SSCs could be detected and sorted in real-time using an integrated cell sorting mechanism. Alternatively, passive label-free sorting techniques such as DLD or inertial microfluidics could be used as these have been shown to be sensitive to differences in both cell size and deformation.[96,97,214,215]

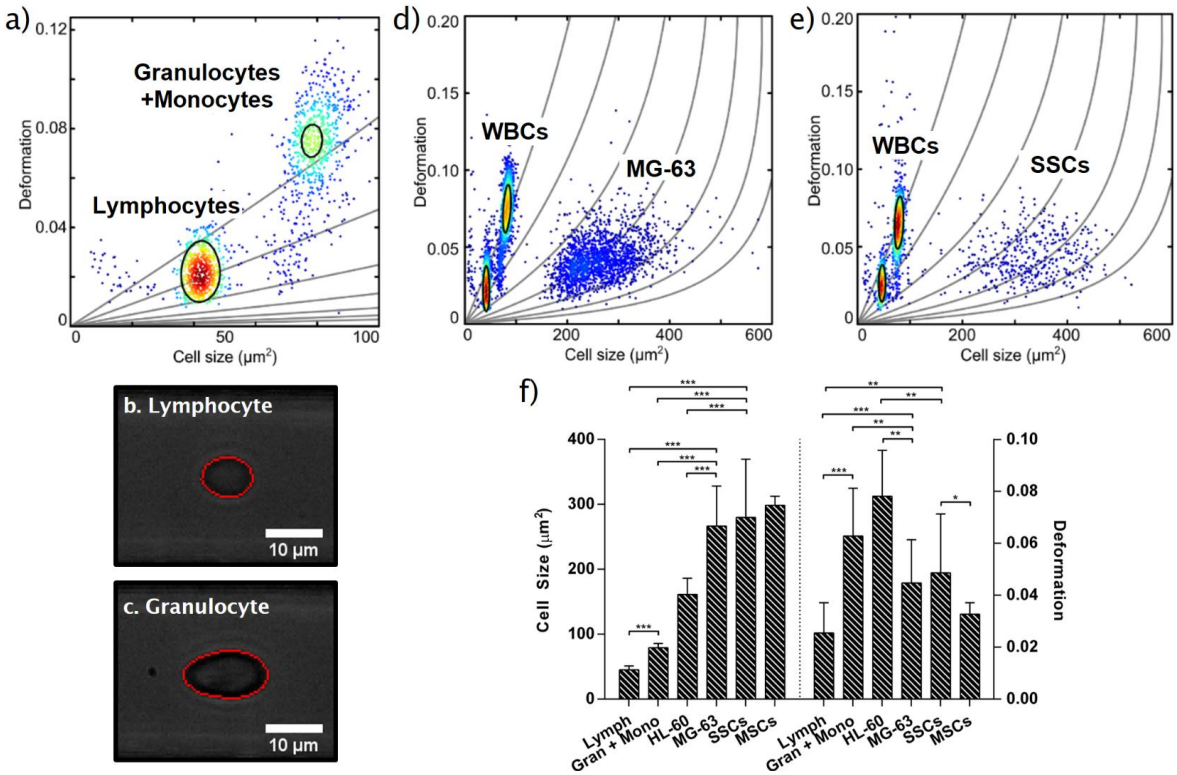

Figure 3.4 – Real-time deformability cytometry. (a) White blood cells obtained from RBC-lysed human whole blood. Images (b) and (c) show representative captures of WBCs flowing at 0.32 μL·s^{-1} through the 30-μm cross-sectional channel. The red line represents the contour determined by image analysis in real-time. (d) MG-63 mixed 1:2 with human WBCs. (e) Stro-1^{+}-enriched skeletal stem cells mixed 1:2 with human WBCs. Image shows scatter plots of deformation vs cell size (cross-sectional area); colour indicates density scale and each dot is representative of a single event from a total of 5,000 events. (f) Bar chart summarising size and deformation of WBCs, HL-60, MG-63, Stro-1^{+}-enriched skeletal stem cells and human BMSCs (MSCs) measured by real-time deformability cytometry. Values represent Mean ± SD (N≥3; *p<0.05, **p<0.01, ***p<0.001) with p-values obtained using 1-dimensional linear mixed models.

3.3. Conclusions

This study has demonstrated significant differences in size and deformability between skeletal stem cells, mesenchymal stromal cells and white blood cells. Critically, primary human SSCs are stiffer when compared to HL-60, a myeloid progenitor cell line, and to all main WBC populations (lymphocytes, monocytes and granulocytes) after RBC-lysis. This suggests the use of cell deformability as a biophysical marker for label-free cell sorting from human BM. However, SSCs were measured after expansion, following adhesion to tissue culture plastic and thus it will be interesting to determine whether such large difference is also observed for freshly harvested cells. At the time of this study, such measurements could not be performed due to the complexity of BM tissue and the scarcity of SSCs, forcing some sort of sample pre-processing and SSC enrichment. Recently, RT-DC has been coupled with simultaneous fluorescence detection.[216] This would allow the identification of rare SSCs within a heterogeneous sample by fluorescently labelling multiple SSC markers. A similar approach is employed in the work presented in Chapter 4 of this thesis using fluorescence and microfluidic impedance cytometry for size and dielectric characterisation of SSCs in freshly isolated bone marrow samples.

Additionally, given the bone marrow is a highly complex tissue with multiple cell types displaying overlapping features, SSC isolation will not depend solely on their separation from cells of the haematopoietic lineage but also from other adherent cell populations such as fibroblasts or endothelial cells.[49,50,217] These cells may be similar in size and/or deformability. Still, the findings here reported do demonstrate the potential of exploiting differences in cell stiffness within a new deformability-based strategy to improve SSC isolation with significant implications and potentiate their clinical translation. Chapter 5 explores the results here obtained in the development of a size and deformation-based cell sorting approach based on deterministic lateral displacement.

Chapter 4

Size and Dielectric Characterisation

"If you can't explain it simply, you don't understand it well enough."
Albert Einstein, 1932.

4.1. Introduction

Skeletal stem cells are rare and are part of a heterogeneous cell population within the BM. For this reason, to date, most work with SSCs has employed pre-enriched cell populations. A crucial step in most protocols to enrich for the skeletal stem and progenitor population is the isolation of cells that adhere to tissue culture plastic, mediated by the presence of adhesion-promoting proteins in serum, *e.g.* fibronectin.[218] However, it is not clear whether plastic adhesion alters the SSC phenotype from its original state in the BM microenvironment. Following adhesion, SSCs are commonly expanded for several weeks before assay, which can further alter their properties. Indeed, there is emerging evidence that human BM stromal cells become i) larger,[129,207] ii) stiffer,[188] iii) less proliferative,[219–222] iv) display increased heterogeneity[207,222] and v) display loss of multipotent differentiation potential[220–222] and surface markers[63,66–68] with passage. The latter has also been investigated within the scope of this thesis, with results (shown in section 1.5) demonstrating a significant loss of expression of the Stro-1-reactive antigen and CD146 with cell passage.

Microfluidic, label-free cell sorting requires *a priori* knowledge of the unique biophysical features that discriminate SSCs from other cells. As described in Chapter 2, most label-free sorting techniques depend on cell size. Obvious examples include inertial microfluidics and DLD, which are fundamentally size-based sorting approaches. Likewise, both the acoustophoretic and dielectrophoretic forces scale proportionally with cell volume. Thus, to design a label-free sorting approach to isolate SSCs it is important to determine the size of the SSC in its original state, *i.e.* before plastic adhesion and expansion.

Dielectrophoresis can also be used to measure the size and dielectric properties of cells by analysing their response to an electric field with varying frequencies.[156,223–225] As mentioned previously in 2.3.6, Flanagan *et al.* showed that mouse neural stem and precursor cells (NSPC) have different dielectric properties compared to neurons and astrocytes.[165] The same authors later showed that NSPCs displayed different DEP responses depending on the population bias towards astrogenic or neurogenic lineages in both human[166] and mouse[226] cells. Using DEP, human embryonic stem cell lines were shown to undergo a significant increase in membrane capacitance following differentiation into a MSC-like phenotype.[225] DEP was also used to characterise the dielectric properties of expanded SSCs and of MG-63 and Saos-2 cell lines, representative of early and mature bone cell populations respectively.[170] However, DEP typically analyses cells in bulk and with relatively low throughput.

4.2. Microfluidic Impedance Cytometry

Microfluidic impedance cytometry (MIC) is a non-invasive, high-throughput single cell characterisation technique that provides an accurate measurement of the size and dielectric properties of cells in flow.[174] High throughput is particularly valuable as it allows rare cell populations to be studied. MIC was recently used to study the differentiation of rat neural stem cells[227] and mouse embryonic stem cells (mESC).[228,229] The differentiation process of mESC was associated with an increase in the cells membrane capacitance indicating the potential of MIC to monitor stem cell differentiation.

In this thesis, MIC was used to characterise the size and dielectric properties of primary SSCs derived from unexpanded BM samples. Cells flow through a microfluidic channel with top and bottom electrodes connected to AC voltages at fixed frequencies (Figure 4.1a). When a particle moves between the electrode pairs, a differential current flows in the system. One pair of electrodes measures the electrical signal from the particle whilst the other pair acts as reference. The change in electric current reflects the dielectric response of the system and depends on the size, shape and dielectric properties of the flowing particle. Impedance was measured simultaneously at two frequencies (500 kHz and 2 MHz). At a low frequency (500 kHz), cells are insulating and for viable cells electrical impedance scales linearly with cell volume. Thus, MIC provides accurate data of cell size. For absolute size determination, and to eliminate drift and experiment-to-experiment variability, polymer beads with a known size are mixed with the cells for reference. At 2MHz, it is possible to detect changes in cell membrane capacitance, which reflects differences in the composition and morphology of the cell plasma membrane (Figure 4.2), and can be used to sort cells using DEP. However, to consider the influence of cell size at 2MHz, the measurement must be normalised to the cell volume to give the so-called electrical opacity: the impedance ratio at a higher to a lower frequency (2 MHz/500 kHz). Lower electrical opacity values translate into higher membrane capacitance.

In this work, SSCs were pre-enriched using magnetic isolation of Stro-1^+ cells and progenitor and SSC populations found within hBMMNCs were further identified with simultaneous $CD146^+$ fluorescent detection. The size and membrane capacitance of SSCs was compared with other hBMMNCs, and analysed as a function of cell expansion and passage. Changes in cell proliferation, alkaline phosphatase (ALP) activity, and the expression of relevant genes of interest were also investigated. In addition, the dielectric properties of SSCs were measured following osteogenic differentiation, thus assessing the potential of MIC as a label-free method to track SSC differentiation. A diagram of this study with time-points of analysis is shown in Figure 4.1b. This work aimed to emphasise the importance of using unexpanded SSC cultures and to generate critical information on the biophysical properties of SSCs in the human BM.

The fluorescence microfluidic cytometer was set up with the assistance of Daniel C. Spencer, PhD, and the molecular laboratory work was coordinated by María C. de Andrés, PhD. The work resulted in a publication in the peer-reviewed *Journal of the Royal Society Interface* in mid-2017.[46]

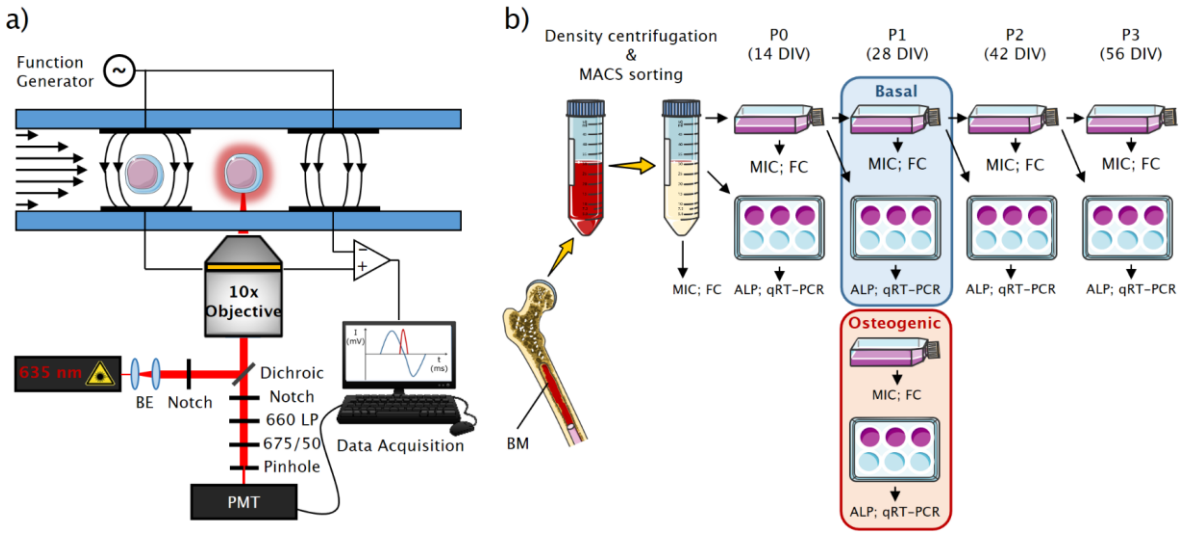

Figure 4.1 – (a) Diagram of the experimental protocol. Human bone marrow mononuclear cells (hBMMNCs) were obtained by density centrifugation of BM samples and enriched by MACS sorting of the Stro-1$^+$ population. Before expansion and at each passage and corresponding day *in vitro* (DIV), cells were analysed using microfluidic impedance cytometry (MIC), flow cytometry (FC), alkaline phosphatase (ALP) activity, and/or quantitative reverse transcription polymerase chain reaction (qRT-PCR). At passage 1, the same analyses were performed to detect changes in cells following osteogenic differentiation. (b) Shows the impedance cytometry set-up including the confocal-optical detection. Cells flow through the microchannel, passing between pairs of electrodes and the optical detection region. The fluorescence properties of the cell were measured simultaneously with the impedance allowing direct correlation of the electrical and fluorescent properties on a single cell basis.

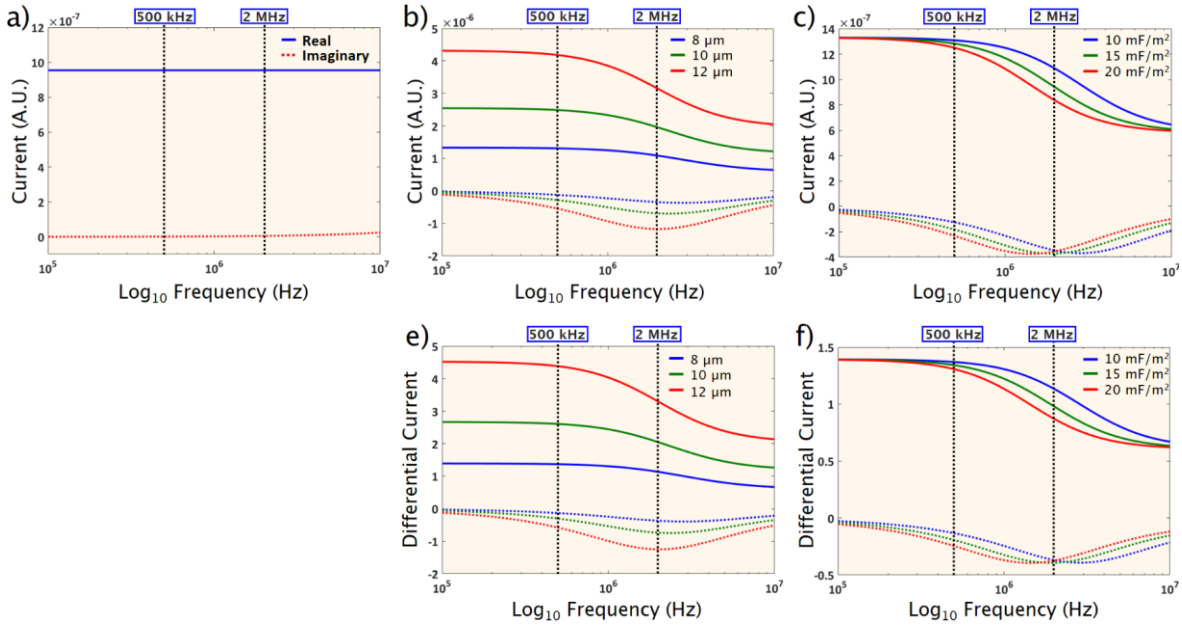

Figure 4.2 – Simulation (in MATLAB™) of impedance response. (a) 7-µm polystyrene reference beads and (b-c) cells using a single-shell model with a suspending medium of conductivity 1.6 S·m^{-1}. The data shows three different cells, which differ in size (8 to 12 µm), or membrane capacitance (10 to 20 mF·m^{-2}). d) and e) Impedance response of the cells normalised to the reference beads. The two frequencies used in the study to calculate cell size (500 kHz) and opacity (2 MHz) are indicated by vertical dashed lines. Coloured full and dashed lines represent the real and imaginary parts of the signal respectively. The following parameters were used: membrane thickness, 5 nm, medium relative permittivity, 78.5, membrane conductivity, 10^{-5} S·m^{-1}, cytoplasm conductivity, 0.8 S·m^{-1} and cytoplasm relative permittivity, 60.

4.3. Results and Discussion

4.3.1. Cell Size

In this work, a custom-made impedance cytometer was coupled with simultaneous fluorescence detection to provide an accurate size measurement of fluorescently labelled SSCs (Figure 4.1a). Figure 4.3a shows an impedance scatter plot of Stro-1^+ unexpanded hBMMNCs obtained from one individual patient. For individual impedance scatter plots of six patient BM samples see Appendix B Figure S8. Fluorescence detection uniquely identified the $CD146^+$ cells (dark red). Enrichment of the Stro-1^+ hBMMNCs using MACS and restriction of subsequent analyses to the $CD146^+$ fraction increased the frequency of SSCs in the samples from 1 in 10,000 to around 1 in every 40 hBMMNCs, a significant sub-population.

In Figure 4.3a, histograms illustrate the distribution of size and opacity of the cells along with a Gaussian fit for the size distribution of $CD146^+$ (dark red line) and $CD146^-$ cells (blue and green). Given the comparable size distributions, these can be associated with the lymphocyte and monocyte fractions from typical flow cytometry scatter plots. The mean cell size and opacity values calculated from a minimum of three independent measurements for each analysed group of cells are presented in Figure 4.4a-d.

The size of the $CD146^+$ cells in the Stro-1-enriched unexpanded hBMMNCs was observed to overlap significantly with other ($CD146^-$) hBMMNCs (Figure 4.3a) indicating that cell size is not a unique marker for SSCs and suggesting that these cells cannot be isolated based solely on size. The SSCs were found within the largest cell fraction in the BM (Figure 5a), with a measured diameter of 9.0 ± 0.4 µm, compared to 7.4 ± 0.2 µm and 8.3 ± 0.9 µm for Stro-1^+/$CD146^-$ and Stro-1^- cells respectively. The size of the SSCs was significantly larger following adhesion and expansion (Figure 4.3b). As early as passage 0 (14 DIV), the average cell size was noted to more than double, increasing to 18.2 ± 1.3 µm (Figure 4.4a, c, $p<0.001$). The cell size continued to increase gradually to an average of 21.7 ± 0.3 µm at passage 3, significantly larger than at passage 0 ($p<0.001$). The average size range observed for expanded cells (18.2 – 21.7 µm) is in agreement with the sizes reported for expanded hBMMNCs estimated using microscopy[129,131,170,207] or deformability cytometry.[230] These results also support previous findings that hBMMNCs increase in size with expansion,[129,207,231] associated with a loss of both self-replicative[207] and differentiation capacity.[131,231] The substantial size difference found between unexpanded and expanded SSCs highlights the phenotypic changes that SSCs undergo during expansion, and emphasise the need to study SSCs in their unaltered state. Indeed, if the size of expanded SSCs were observed in the BM, size-based SSC isolation would become trivial.

Nevertheless, the average cell size found for SSCs in the BM was the largest of the cell populations analysed. These results indicate that cell size could be used in combination with another biophysical parameter, for example cell stiffness, for SSC purification from human BM. However, given the phenotypic changes reported here for SSCs following adhesion and expansion it would be important to determine whether the higher SSC stiffness at passage 0 described in Chapter 3 could be verified in unexpanded samples.

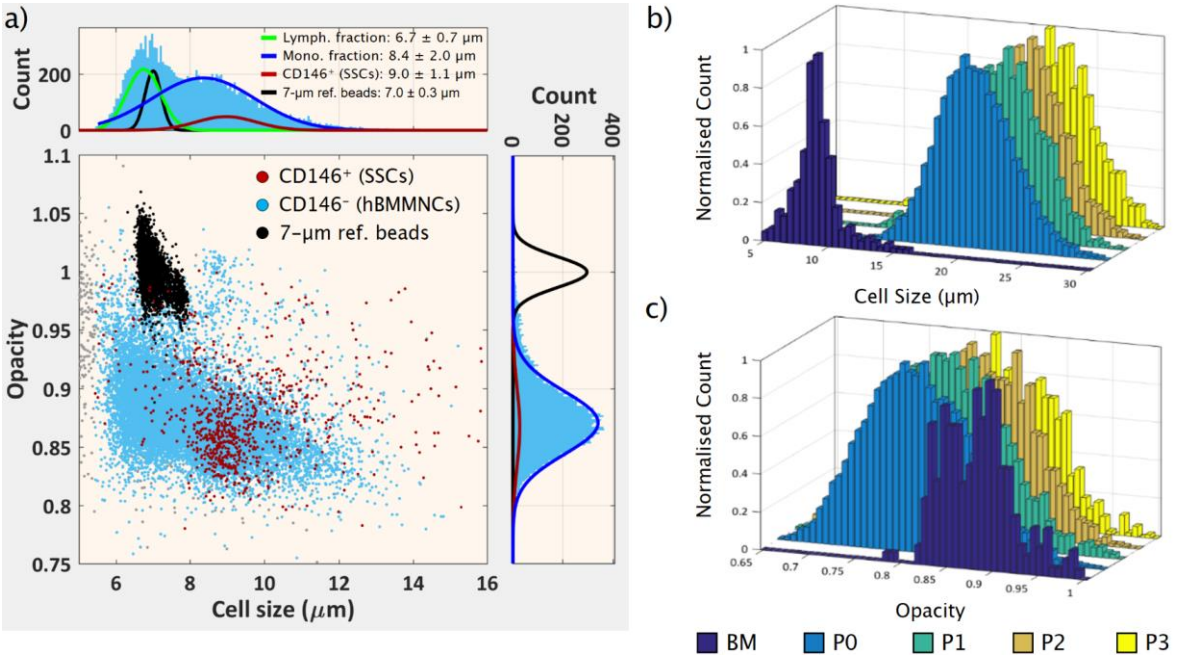

Figure 4.3 – Fluorescence-assisted microfluidic impedance cytometry of Stro-1-enriched human bone marrow mononuclear cells (hBMMNCs). a) Scatter plot of cell size (µm) *vs* electrical opacity (normalised to 7-µm diameter reference beads) of Stro-1⁺-enriched hBMMNCs obtained from one individual patient. Top and bottom histograms demonstrate the cell size and opacity distributions respectively, with colour-coded Gaussian distributions fitted to the data. The dark red line represents the distribution of CD146⁺ cells. b) and c) show histograms of the distribution of cell size and electrical opacity with increasing cell passage from one individual patient.

4.3.2. Membrane Capacitance

Figure 4.3a shows that the opacity of CD146⁺ and CD146⁻ cells completely overlap, with no significant differences between the average opacity of Stro-1⁻ (0.87 ± 0.01), Stro-1⁺/CD146⁻ (0.88 ± 0.01) and Stro-1⁺/CD146⁺ (0.88 ± 0.01) cells. This indicates that opacity cannot be used as a label-free marker for the SSC contained within the Stro-1⁺/CD146⁺ sub-population. It also shows that the membrane capacitance of unexpanded SSCs is indistinct from other cells in the BM indicating that sorting SSCs from human BM using DEP is unlikely to yield pure sub-populations.

The opacity of the SSC was observed to decrease after adhesion in culture (Figure 4.3c), *i.e.* a significant increase in membrane capacitance. At passage 0, the average opacity values were observed to fall to 0.82 ± 0.02 ($p<0.001$) with no further changes up to passage 3 when cells were kept in basal expansion conditions that do not promote cell differentiation (Figure 4.4b, d). This is in keeping with significant phenotypical changes between expanded and unexpanded SSCs. Although not quantitative, optical microscopy images of SSCs following expansion indicate morphological changes such as an increase in cell size and spreading with increasing passage (Figure 4.5), which is consistent with previous observations.[207] Higher membrane capacitance may arise from an increase in the membrane surface area and morphology, including the presence of microvilli, blebs, folds or ruffles,[153,155,156,232] some of which may affect cell adhesion.

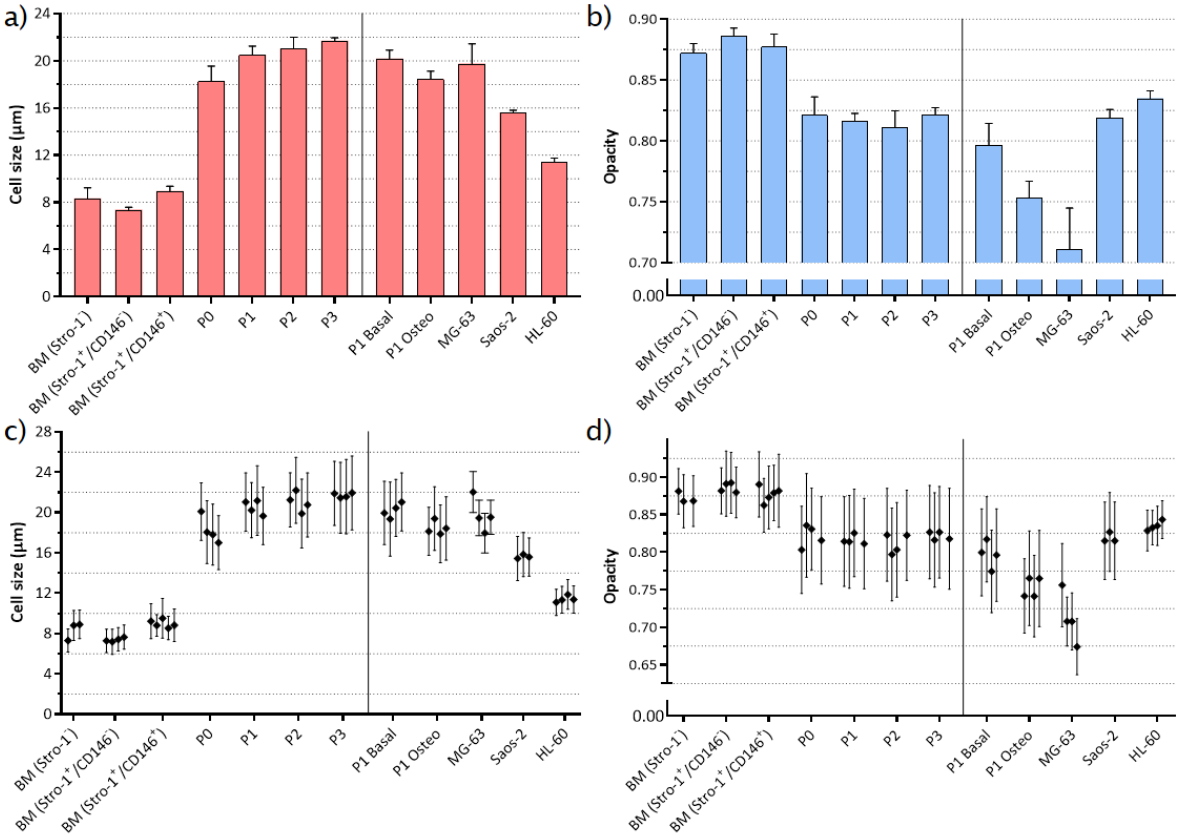

Size / Opacity	BM (Stro-1⁻)	BM (Stro-1⁺/CD146⁻)	BM (Stro-1⁺/CD146⁺)	Passage 0	Passage 1	Passage 2	Passage 3	Passage 1 Basal	Passage1 Osteo	MG-63	Saos-2	HL-60
BM (Stro-1⁻)		N.S.	N.S.	***	***	***	***	***	***	***	***	***
BM (Stro-1⁺/CD146⁻)	N.S.		N.S.	***	***	***	***	***	***	***	***	***
BM (Stro-1⁺/CD146⁺)	N.S.	N.S.		***	***	***	***	***	***	***	***	**
Passage 0	*	**	**		*	**	***	N.S.	N.S.	N.S.	***	***
Passage 1	*	**	**	N.S.		N.S.	N.S.	N.S.	*	N.S.	***	***
Passage 2	*	**	**	N.S.	N.S.		N.S.	N.S.	***	*	***	***
Passage 3	*	**	**	N.S.	N.S.	N.S.		N.S.	***	*	***	***
Passage 1 Basal	***	***	***	N.S.	N.S.	N.S.	N.S.		N.S.	N.S.	***	***
Passage 1 Osteo	*	*	*	*	*	*	*	*		N.S.	***	***
MG-63	***	***	***	***	***	***	***	**	N.S.		***	***
Saos-2	*	*	*	N.S.	N.S.	N.S.	N.S.	N.S.	*	*		***
HL-60	N.S.	*	N.S.	N.S.	N.S.	N.S.	N.S.	N.S.	*	***	*	

Figure 4.4 – Size and electrical opacity of cells analysed by microfluidic impedance cytometry. Bar charts summarise the cell size (a) and electrical opacity (b) of hBMMNCs in the bone marrow (BM), after expansion at passages 0 to 3, and following osteogenic differentiation (P1 Osteo). Within the BM, cell size and opacity were measured for Stro-1⁻ cells, and both the CD146⁻ and CD146⁺ populations within the Stro-1⁺ fraction. Skeletal stem cells (SSCs) are contained within the Stro-1⁺/CD146⁺ population. Also shown are data for two adherent (MG-63 and Saos-2) and one suspension (HL-60) human cancer cell lines. c) and d) show the mean ± SD for each individual analysed patient sample. The appended table summarises the statistical analyses of the data with the top-right and bottom-left values showing the p-values for cell size and opacity, respectively. Values represent mean ± SD (N ≥ 3; *p < 0.05; **p < 0.01; ***p < 0.001; N.S. – not significant, with p-values obtained using the one-way analysis of variance (ANOVA) with Tukey's post-hoc test for samples that followed a normal distribution or the Mann-Whitney U-test for samples that did not follow a normal distribution).

To assess the connection between cell adhesion and membrane capacitance we also analysed the dielectric properties of cancer cell lines that grow either as adherent (MG-63 and Saos-2) or as suspension (HL-60) cultures (Figure 4.4b). It is well known that cancer cells have high membrane capacitance associated with increasing structural disorder at the original tumour site and the capacity to invade neighbouring healthy tissue.[153] Higher membrane capacitance is also seen in tumour cells that originate from solid tumours. Although

both MG-63 and Saos-2 cells are adherent, the membrane capacitance of MG-63 was significantly higher ($p<0.01$) than Saos-2 (opacity values of 0.71 ± 0.03 and 0.82 ± 0.01 respectively). Conversely, although maintained under different culture methods (adherent *vs* suspension), Saos-2 and HL-60 showed similar opacity values with the HL-60 slightly higher ($p<0.05$). This indicates that factors other than cell adhesion govern cells membrane capacitance. The membrane capacitance of MG-63 was also higher than that of expanded SSCs ($p<0.001$) confirming previous values obtained using dielectrophoresis.[170]

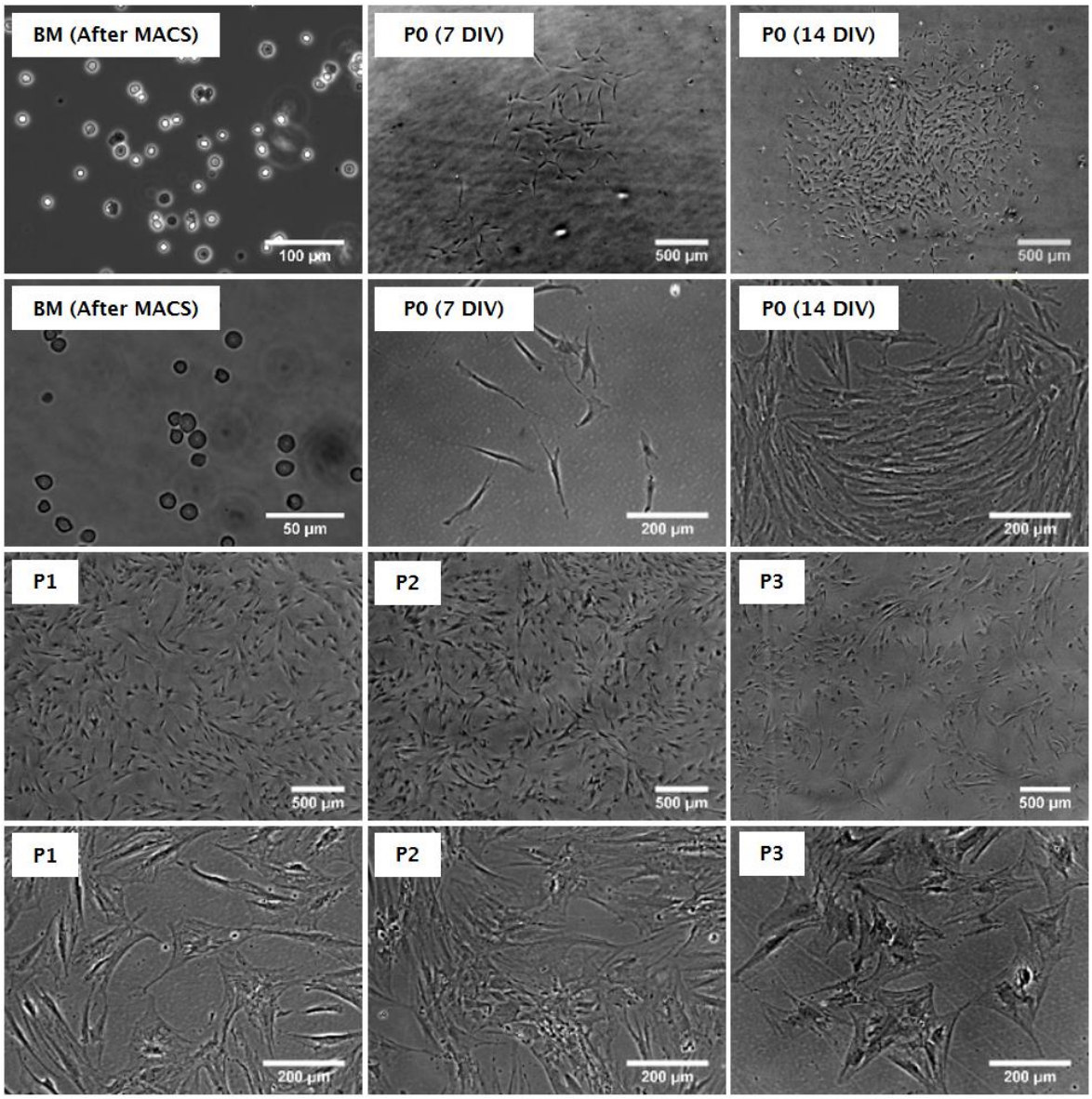

Figure 4.5 – Optical microscopy. Images show apparent changes in the size and morphology of unexpanded hBMMNCs after enrichment of the Stro-1$^+$ population by MACS (BM after MACS) and at different passages (P0 to P3) growing under basal expansion conditions. Cells typically appeared to grow larger and were observed to display a spread morphology with increasing passage. Scale bar 500 µm (100 µm in BM) in top panel and 200 µm (50 µm in BM) in lower panel.

4.3.3. Cell Proliferation, ALP Activity and Gene Expression

To investigate whether there were changes in the proliferation capacity or the osteogenic potential of SSC, total DNA (Figure 4.6a) and specific ALP activity were quantified at each passage (Figure 4.6b and Appendix B Figure S9). There were no statistical differences in the total DNA amount or ALP activity, though both were observed to be higher at passage 1. However, note that it is difficult to draw any conclusions from cell proliferation and ALP activity at passage 0, as following isolation cells are plated at a significantly higher cell density to compensate for the presence of non-adherent haematopoietic cells.

The relative expression of stem and osteogenic genes of interest was assessed using qRT-PCR for all passages (Figure 4.7). No differences were observed in the expression levels of *GNL3* (nucleostemin), a gene associated with stem cell proliferation. The expression of the osteogenic genes (*RUNX2, ALPL, COL1A1* and *BGLAP*) was also measured. No significant differences in *ALPL* and *RUNX2* were observed, although there was an increase in the expression of *ALPL* at passage 1 (2.6 ± 1.7 fold-increase *vs* P0) with expression levels correlating well with the specific ALP activity shown in Figure 4.6b. The expression of *COL1A1* (2.2 ± 1.5 fold-increase *vs* P0) and *BGLAP* (1.8 ± 0.4 fold-increase *vs* P0) was also higher at passage 1 suggesting an enhanced osteogenic phenotype at this passage before dedifferentiation on passage. The expression levels of other genes associated with stem cell maintenance (*SOX2*), chondrogenesis (*SOX9* and *COL2A1*) and adipogenesis (*FABP2* and *PPARG*) were negligible (CT values over 30).

4.3.4. Tracking Osteogenesis using Microfluidic Impedance Cytometry

Microfluidic impedance cytometry and AC electrokinetic methods have demonstrated differences in the dielectric properties of stem cells and their progeny.[165,227-229,233] Exploiting these differences DEP was used to sort osteoblasts (differentiated from a human mesenchymal stem cell line for 21 days) from their progenitor cells with moderate efficiency.[234] To investigate whether impedance cytometry could be used to track osteogenic differentiation of SSCs, Stro-1$^+$-enriched SSCs at passage 1 were cultured under osteogenic conditions for 14 days and the osteogenic phenotype of the cells was initially confirmed.

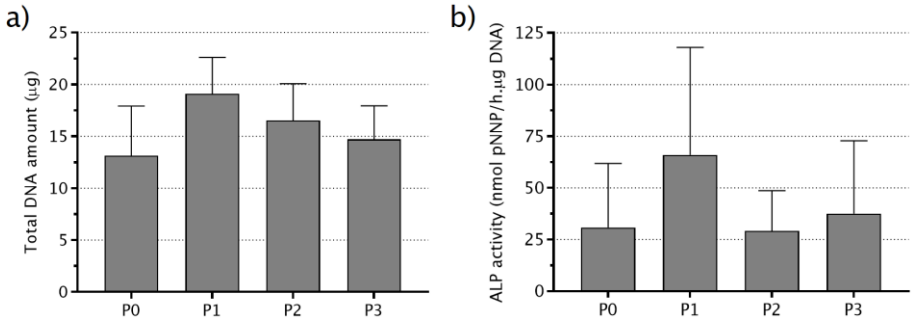

Figure 4.6 – Proliferation and alkaline phosphatase activity of Stro-1-enriched human bone marrow mononuclear cells (hBMMNCs). a) Total DNA quantification from hBMMNCs grown for 14 days at each passage (P0-P3) determined using the PicoGreen® nucleic acid quantitation assay. b) Specific ALP activity of hBMMNCs grown for 14 days at each passage determined by the colorimetric detection of the dephosphorylation of p-nitrophenyl phosphate. Values represent mean ± SD (N = 4).

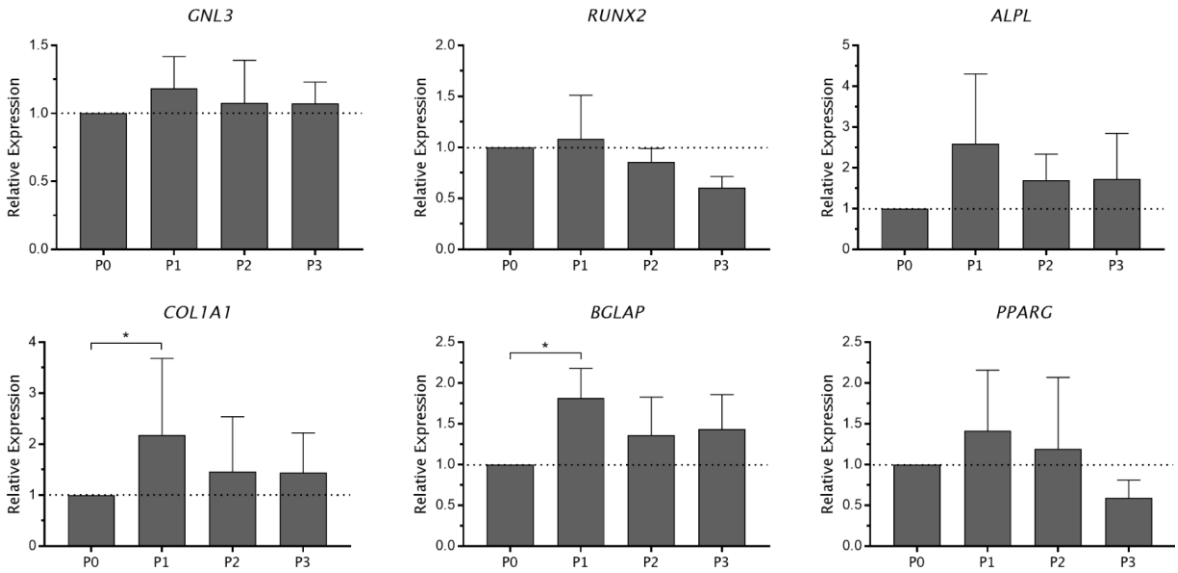

Figure 4.7 – Quantitative reverse-transcriptase polymerase chain reaction. Relative gene expression of relevant genes of interest of Stro-1^{+}-selected human bone marrow mononuclear cells (hBMMNCs) grown in basal expansion conditions at different passages (P0-P3). *GNL3* is associated with stem cell proliferation, *RUNX2*, *ALPL*, *COL1A1* and *BGLAP* are genes related with the process of osteogenesis and *PPARG* is a regulator of adipocyte differentiation. Values represent mean ± SD normalised to the expression levels of hBMMNCs at passage 0 (N = 4; *p < 0.05, with p-values obtained using the one-way analysis of variance (ANOVA) with Tukey's post-hoc test or the Mann-Whitney U-test for samples that followed or did not follow a normal distribution respectively.

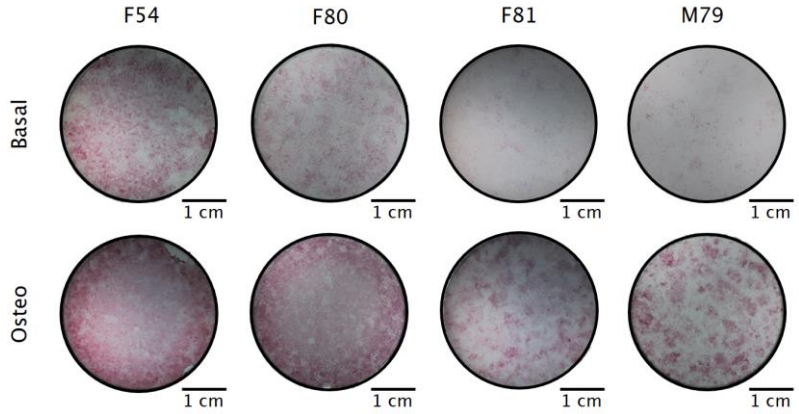

Figure 4.8 – Alkaline phosphatase (ALP) activity. ALP staining of human BM colony forming units-fibroblastic (CFU-F) grown on 6-well plates for 14 days under basal expansion conditions or following osteogenic (osteo) differentiation. Images represent an entire well captured using a dissecting stereoscope.

Osteogenic induction was evidenced by an increase in ALP staining of cells grown in osteogenic conditions compared to basal expansion conditions (Figure 4.8). This was verified by up-regulation of *ALPL* (2.8 ± 1.4 fold-increase, $p < 0.05$) and *COL1A1* (1.2 ± 0.1 fold-increase, $p < 0.05$) in cells following osteogenic differentiation (Figure 4.9). There were no differences in the expression levels of *RUNX2* and *BGLAP*, which are early and late osteogenic markers respectively.[235-237] The expression of *GNL3*, associated with cell proliferation, was unchanged. *SOX2* was significantly downregulated (0.06 ± 0.06 fold-change, $p < 0.001$) although *SOX2* expression was already minimal in basal conditions. *SOX9* (0.5 ± 0.5 fold-change), *COL2A1* (0.5 ± 0.5 fold-change) and *FABP2* (0.8 ± 0.2 fold-change *vs*

Basal), associated with chondrogenesis and adipogenesis respectively, were downregulated despite the high CT values at basal expansion conditions. A significant unexpected upregulation of *PPARG* (4.0 ± 0.5 fold-increase) in cells following osteogenic differentiation was observed, which may be due to the nature of the samples used, which typically originate from older patients undergoing total hip replacement surgery, and the increase in marrow adipogenesis associated with osteoporosis and age-related osteopenia has long been known.[238,239]

Although slightly lower, the average cell size of SSCs following osteogenic differentiation (Figure 4.4a, P1 Osteo, 18.5 ± 0.7 µm) was not statistically distinct from SSCs following expansion (P1 Basal, 20.2 ± 0.7 µm). In contrast, there was a significant increase (Figure 4.4b, $p < 0.05$) in the membrane capacitance of SSCs following osteogenic differentiation reflecting a marked change in opacity, from 0.80 ± 0.02 to 0.75 ± 0.01. Previous studies using impedance cytometry have shown a decrease in opacity (increase in membrane capacitance) of mouse embryonic stem cells following differentiation.[229] Our results show the potential of MIC as a non-invasive and non-destructive technique to track the differentiation of SSCs without the need for any sample pre-processing. For example, using MIC it would be possible to assess the efficiency of the osteogenic differentiation of SSCs while allowing cell subculture, further biological analysis, or their use for *in vivo* implantation.

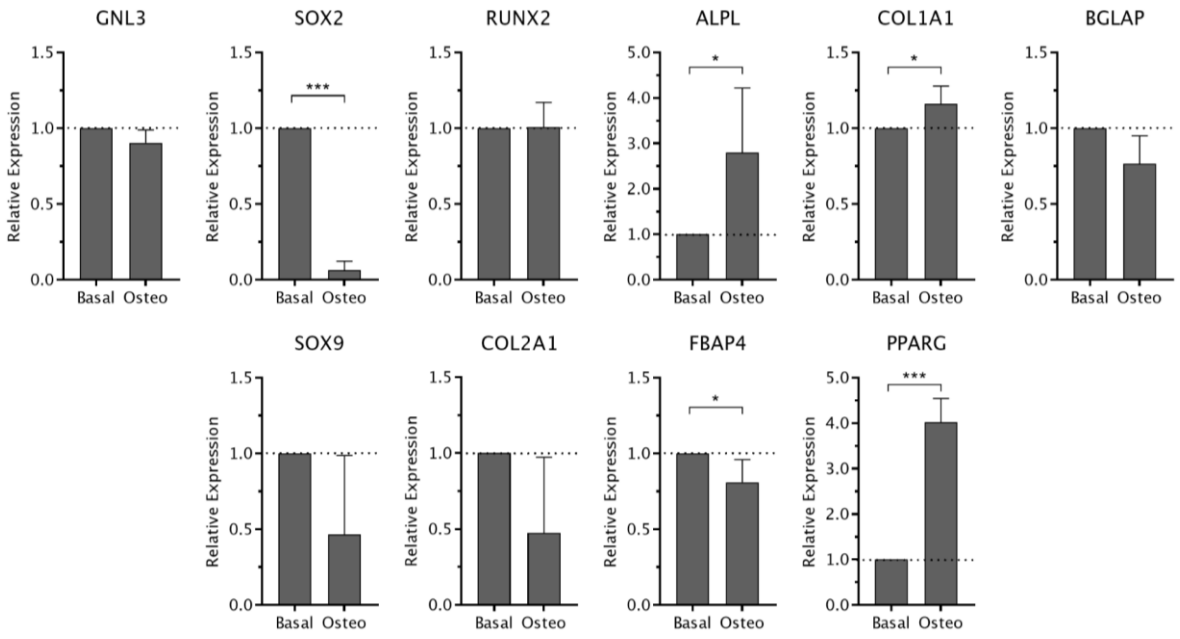

Figure 4.9 – Quantitative reverse-transcriptase polymerase chain reaction. Relative gene expression of relevant genes of interest of passage 1 Stro-1$^+$-selected hBMMNCs after 14 days following osteogenic (osteo) differentiation. *GNL3* and *SOX2* are associated with stem cell proliferation and stem cell maintenance respectively. *RUNX2*, *ALPL*, *COL1A1* and *BGLAP* are genes related with the process of osteogenesis, with *RUNX2* and *BGLAP* being early and late osteogenic markers respectively. *SOX9* and *COL2A1* are genes associated with chondrogenic differentiation, and *PPARG* and *FBAP4* with adipocyte differentiation. Values represent mean ± SD normalised to the expression of hBMMNCs growing under basal expansion conditions (N ≥ 4; *p < 0.05; ***p < 0.001, with p-values obtained using the Student's t-test for independent samples).

4.4. Conclusions

The biophysical properties of enriched human SSC populations (Stro-1$^+$/CD146$^+$) obtained from human BM change significantly under adherent expansion conditions. Specifically, this study demonstrates that both cell size and membrane capacitance of unexpanded SSCs differed from expanded cells as early as passage 0. The average cell size increased over 2-fold to 18.2 ± 1.3 µm while the membrane capacitance increased as determined from the decrease in electrical opacity. These results highlight the importance of studying unaltered SSCs isolated from the original tissue as the primary cell population provides a unique biophysical signature. Critically, if the size and membrane capacitance differences observed between expanded SSCs and other BM cells were verified for unexpanded SSCs, SSC isolation from human BM using microfluidic label-free sorting techniques could be easily achieved.

Nevertheless, although the membrane capacitance of the SSC did not differ from other BM cells, the size of the SSC in the BM was found within the largest cell fraction at 9.0 ± 0.4 µm. This was the first time that the size of the SSC was estimated from unexpanded human BM samples – a crucial step towards the design of a microfluidic device for SSC isolation. When compared to the size distribution of other BM cells (7.4 ± 0.2 µm and 8.3 ± 0.9 µm for Stro-1$^+$/CD146$^-$ and Stro-1$^-$ cells respectively), the data indicates that SSCs could be significantly enriched using a size-based sorting approach to fractionate cells smaller and larger than (*e.g.*) 8.5 µm removing the vast majority of non-relevant cells in the BM. It is important to note that due to the overlapping size distribution, complete SSC isolation cannot be achieved based solely on size. One possible solution would be to design a label-free sorting system that exploits both differences in cell size with another biophysical parameter, which would lead to significant SSC enrichment. Cell stiffness could be used to enhance the SSC sorting purity using a sorting device that is both sensitive to size and deformation. For this, it would be important to confirm if the higher stiffness of SSCs at passage 0 is verified in unexpanded samples. This is the subject of the work presented in Chapter 5 of this thesis, which explores the use of DLD as a size and deformation-based sorting approach and its potential application to SSCs.

Finally, this study demonstrated that impedance cytometry can be used to track osteogenic differentiation of SSCs, verified by quantitative reverse transcription polymerase chain reaction of relevant genes of interest associated with stem cell maintenance and proliferation, and with the osteogenic, chondrogenic and adipogenic differentiation processes. This indicates the potential of MIC as a non-invasive and non-destructive technique to monitor stem cell differentiation in a label-free manner without the need for sample pre-processing.

Chapter 5

Size and Mechano-based Cell Sorting

"Success is stumbling from failure to failure without loss of enthusiasm."
Attributed to Winston Churchill.

5.1. Introduction

The findings described in chapters 3 and 4 point towards the development of a microfluidic sorting device that is sensitive to differences in both cell size and deformation. Deterministic lateral displacement (DLD) is fundamentally a size-based sorting technique but DLD has also been shown to be capable of cell fractionation based on cell deformability.[97] While chapter 4 showed that SSCs are contained within the largest cell fraction in bone marrow, it also showed that selection based solely on cell size is unlikely to generate a pure SSC population for research and clinical evaluation. However, given the greater stiffness of SSCs (as measured by RT-DC) it may be possible to use DLD to enhance differences in cell size and improve separation efficiency.

The principle of DLD was described in section 2.3.2. In brief, DLD flow is typically laminar and particles remain in their streamlines unless external forces are applied. DLD devices consist of arrays of micropillars within a large microchannel set at an angle to the main direction of flow. When the particle suspension flows between two pillars, the cross-sectional area decreases causing acceleration and pushing the streamlines together. The width of the streamline closest to the pillars determines what is called the critical separation size of the array ($D_C = 2R_C$). When the particle radius is larger than R_C, it is forced to cross streamlines and is laterally displaced (Figure 5.1, left).

Similar to the RT-DC (described in chapter 3), particles flowing in a DLD device are exposed to viscous gradient shear forces originating from the parabolic flow profile and from the acceleration caused by the flow contracting between two posts. Additionally, particles interact with the micropillars resulting in further forces. The combination of these effects causes the particle to deform, which may change its effective radius to an extent that a particle originally larger than D_C is no longer forced to cross streamlines when flowing between two microposts (Figure 4., right). It is this principle that makes DLD devices sensitive to differences in cell deformability. This was illustrated in the work of Holmes *et al.*[97] where neutrophils and T-lymphocytes were sorted using DLD based on differences in cell deformability.

In this work, DLD was used to investigate the potential to sort SSCs from human BM using a size and mechano-based sorting approach. Two designs were tested in order to address different questions. Devices from design 1 (Figure 5.2, top) follow the traditional DLD design originally proposed by Huang *et al.*[92], in which sheath flow is used to focus the

sample inlet in a narrow flow stream and away from the channel walls. Particles larger than D_C are bumped away from the inlet position and become separated from smaller particles, which continuously zig zag through the obstacle array. Devices based on design 2 are sheathless and use a mirrored micropillar array as proposed by Loutherback *et al.*[103] (Figure 5.2, bottom). As there is a single inlet, particles initially occupy the entire width of the microchannel. To allow separation, two sections are built with different separation sizes. Section 1 is designed with a D_C smaller than the smallest expected particle diameter allowing the sample to focus towards the channel sidewalls and to create a central cell-free stream. In the second section, the direction of the mirrored array is inverted and the D_C increased to bump the larger particles back to the centre of the device allowing separation.

Consisting of two consecutive sections, devices from design 2 depend on the efficiency of both separation stages to provide pure cell populations. These devices are considerably longer than design 1, complicating fabrication and increasing the risk of cell blockage during long separation experiments. The above may result in a reduction in the separation resolution and sample purity. However, using sheathless DLD devices is advantageous as the device operation is simplified and the cell throughput is significantly increased given that the sample is not diluted by the sheath flow. As mentioned previously, high throughput is paramount for sorting rare cell populations, as in the case of SSCs. The design specifications of the devices from designs 1 and 2 and a list of the available critical separation sizes are provided in section 7.8.1 in Materials and Methods.

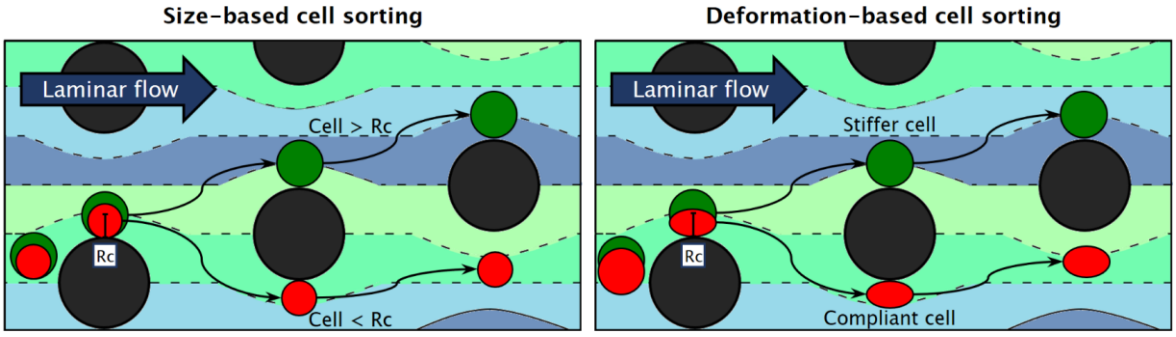

Figure 5.1 – Particle sorting by deterministic lateral displacement based on differences in particle size (left) and deformation (right). In size-based separation, particles with a radius smaller than Rc (red) are predominantly affected by the streamline flowing closest to the micropillar and are not forced to cross streamlines, zigzagging throw the microarray. In deformation-based cell sorting, particles with similar size but different deformability can be sorted due to an effective change in particle size upon deformation due to gradient shear stresses, acceleration and interaction with the micropillars. Here, the more compliant red particle deforms to an extent that its radius becomes smaller than R_C allowing it to continue along the original streamline.

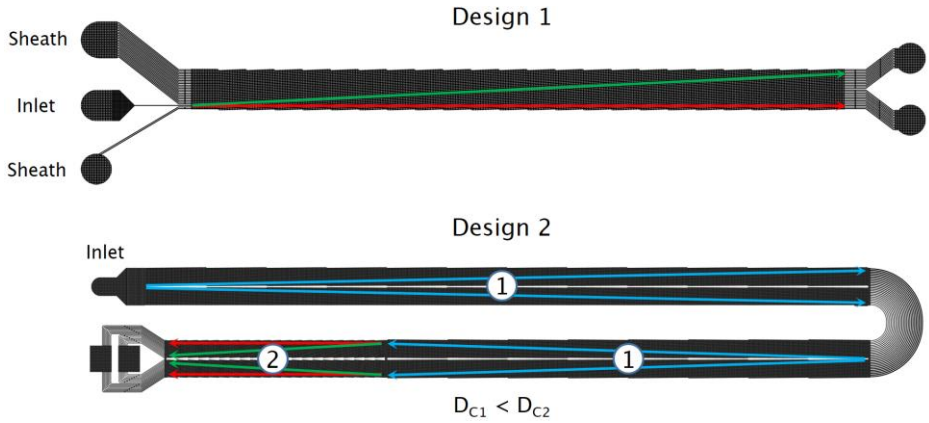

Figure 5.2 – Predicted cell trajectories in DLD devices from designs 1 and 2. In Design 1 (top), cells are initially focused hydrodynamically in a single flow stream. Larger particles (green) are displaced away from the smaller particles (red) which zigzag through the pillar array maintaining a null net displacement. In Design 2 (bottom), cells introduced from a single inlet are initially displaced towards the outer channel walls in a first section with a small critical separation size (D_{C1}), creating a central cell-free stream. In section 2, the direction of the micropillar array is inverted vertically and the D_C increased to displace only larger particles (green) into the central cell-free stream while smaller particles (red) continue zigzagging near the channel walls.

Using design 1, non-deformable polystyrene microbeads of different sizes were separated illustrating the efficiency of size-based particle sorting by DLD. Furthermore, design 1 was used to demonstrate how cell deformation could affect the outcome of cell sorting by DLD using the human osteosarcoma cell line MG-63 as a model. The higher throughput of design 2, with D_C tailored to the mean size of the SSC in BM, allowed efficient sorting of a mixture of two cell lines (MG-63 and HL-60) as a function of differences in cell size and deformability. SSCs at Passage 0 were fractionated in isolation to investigate whether cell size was related with the capacity to form CFU-F. Furthermore, SSCs were sorted from human WBCs verifying the higher stiffness and size of the SSC as determined by RT-DC. Finally, design 2 devices were used to sort SSCs directly from human BM samples. The results indicated the need for important design adjustments to allow efficient removal of the smaller and more deformable cells from the haematopoietic lineage at the first separation.

5.2. Results and Discussion

5.2.1. Size-based sorting of non-deformable polystyrene beads

To test the efficiency of size-based particle sorting by DLD, different sized non-deformable polystyrene beads were mixed in approximately equal numbers and flowed by the action of a pressure-controller through design 1 DLD devices (D_C = 17.48 µm). Beads with sizes of 16 µm (15.66 ± 1.43, Mean ± SD) and 24 µm (23.74 ± 1.41) diameter were used aiming to obtain two populations with high purity at each outlet. It should be noted that considering the mean size and standard deviation of the particles, the size distribution of the 16-µm beads partially overlaps with the device critical separation size. Assuming the size of the beads is normally distributed, it is possible to estimate the fraction of beads that will be larger than 17.48 µm using the standardised Z-score equation (equation 29). According to the normal distribution table (Appendix C, Table S1 and Table S2), it was

estimated that around 10.2 % of the 16-µm beads were larger than the separation size of 17.48 µm.

$$Z = \frac{x - \mu}{\sigma} \quad (Equation\ 29) \quad where\ \mu\ and\ \sigma\ are\ the\ mean\ and\ standard\ deviation$$

The particle suspension was pumped through the device for several minutes, at throughputs up to 10,000 beads per minute at an inlet pressure of 250 mbar. The separation efficiency was quantified by analysing the fractions collected at each of the outlets by flow cytometry (Figure 5.3a). The larger and smaller beads were collected at purities of 88.5 ± 7.6 % and 98.3 ± 2.1 % from the larger and smaller outlets respectively (N=6). This was in line with the expected percentages (given the standard deviation of the 16-µm particles) demonstrating the efficiency of DLD for size-based sorting delivering purities as high as 99.8 %, and typically over 99 % (N=4) for the smaller beads.

To validate that sorting by DLD is independent of flow rate for non-deformable particles, the same bead mixture was separated with an increased inlet pressure (100-1,000 mbar). Figure 5.3b shows that the separation efficiency of the smaller beads (closed circles) and larger beads (open circles) remained constant throughout the range of input pressures even up to 1 bar. This experiment was conducted only once as a negative control for deformability-based particle sorting using DLD, and intra-experimental variability explains the slight inconsistency of the purity values between tested input pressures.

5.2.2. Binary fractionation of MG-63 as a function of cell deformability

To demonstrate that cell deformation affects the outcome of cell sorting by DLD, a human osteosarcoma cell line, MG-63, was pumped through Design 1 devices (D_C = 17.48 µm) at different pressures. In Chapter 4, the diameter of MG-63 cells in suspension was estimated at 19.1 ± 1.9 µm. Therefore, it was expected that at lower flow rates, when cell deformation is less prominent, the majority of MG-63 would be displaced and appear at the larger outlet. Indeed, Figure 5.3 shows that at 100 mbar, greater than 65 % of the MG-63 cells were displaced by the micropillar array and exited at the larger outlet (green bar, N=2). Higher input pressure translates into faster flow rates and shear stresses that lead to more pronounced cell deformation. As a result, the apparent size of the MG-63 is reduced and the fraction of cells displaced by the microarray fell consistently to under 20 % at 1,000 mbar. Note that the same increase in input pressure did not lead to a change in the purity of 16 and 24-µm polystyrene beads, which do not deform. Figure 5.4 shows sequential images of a single MG-63 cell deforming upon interaction with a DLD micropillar at 1,000 mbar. By deforming (Figure 5.4 b-d), the cell becomes smaller than Dc allowing it to remain in its streamline and flow in zigzag mode past the micropillars (Figure 5.4f).

5.2.3. Size and mechano-based sorting of MG-63 and HL-60

As proof-of-concept that cell deformation can lead to improved cell sorting by DLD, MG-63 and HL-60 cells were mixed in approximately equal numbers and sorted using a DLD device (design 2) with a critical separation size of 12.18 µm. As design 2 devices have a single inlet, the flow could be driven using a syringe pump. To facilitate cell discrimination, GFP-transfected MG-63 were used whilst the HL-60 were fluorescently labelled with

CellTracker™ deep red dye. The size of the HL-60 was measured to be 11.4 ± 1.4 µm, whereas MG-63 were estimated to be 19.1 ± 1.9 µm. Additionally, the mechanical phenotyping shown in Chapter 3 revealed that MG-63 are significantly stiffer than HL-60, with a Young's modulus approximately two-fold higher. Given the large difference in size between the two cell types, a high sorting efficiency could be anticipated. Indeed, the purity of HL-60 and MG-63 in the smaller and larger outlet was in excess of 90 % with a flow rate of 15 µL·min^{-1} (Figure 5.5 a-d).

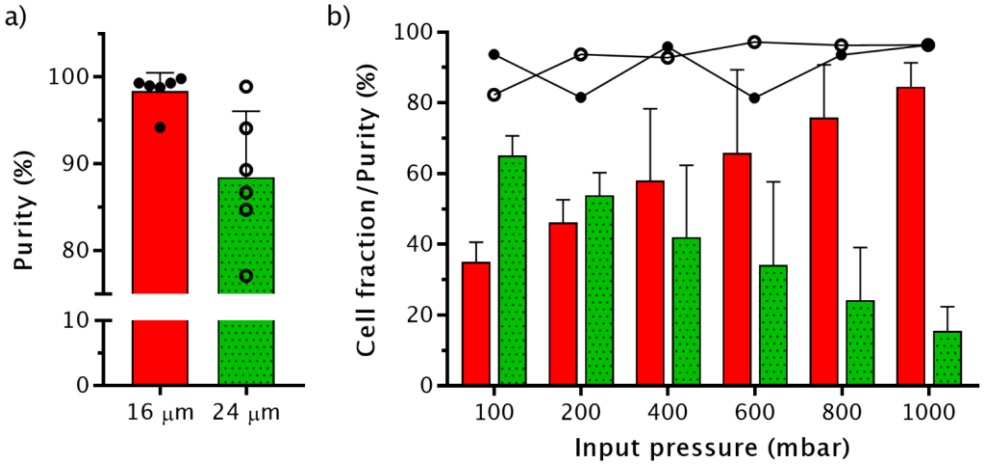

Figure 5.3 – Size and deformation-based particle sorting a) Purity of 16 (red) and 24-µm (green, dotted) beads mixed 1:1 and sorted by DLD at an inlet pressure of 250 mbar. Percentages of the fractions collected in each outlet were calculated from flow cytometry data. Bars show mean ± SD (N=6) and circles show the mean purity of individual experiments. b) Binary fractionation of MG-63 as a function of cell deformation induced by increasing overpressure at the inlet (100-1000 mbar). As the input pressure was increased, the flow rate increased leading to accentuated cell deformation. Green (dotted) and red bars show the percentage of MG-63 collected at the 'larger' and 'smaller' outlets respectively (N=2). As a control, non-deformable 16-µm (closed circles) and 24-µm (open circles) polystyrene beads were flowed in the same conditions with the sorting purity remaining consistent up to 1 bar.

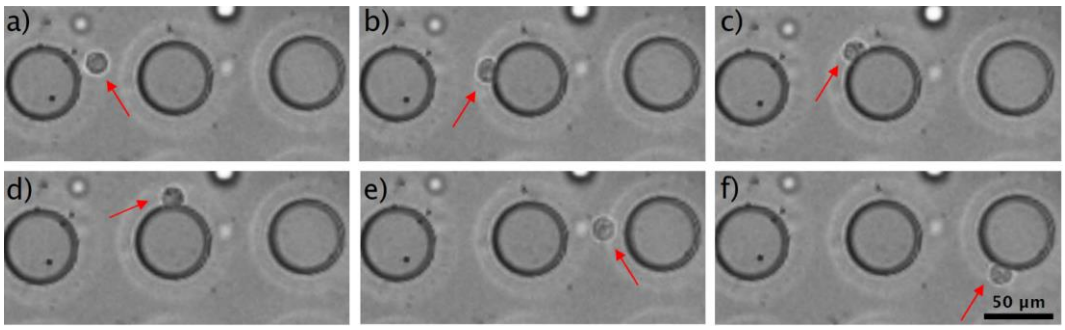

Figure 5.4 – Cell deformation in a DLD device. a) to f) show images following the movement of a single MG-63 (red arrow) cell flowing from left to right through a deterministic lateral displacement micropillar array at an inlet pressure of 1,000 mbar (corresponding to an estimated mean flow speed of 10 cm·s^{-1}). Images were taken using a high-speed camera (Vision Research, Wayne, NJ, USA) and bespoke software (Phantom Camera Control Software, Vision Research). Cell deformation due to shear stresses and interaction with the micropillars is shown. Cell deformation changes the effective cell size altering its trajectory in the DLD device.

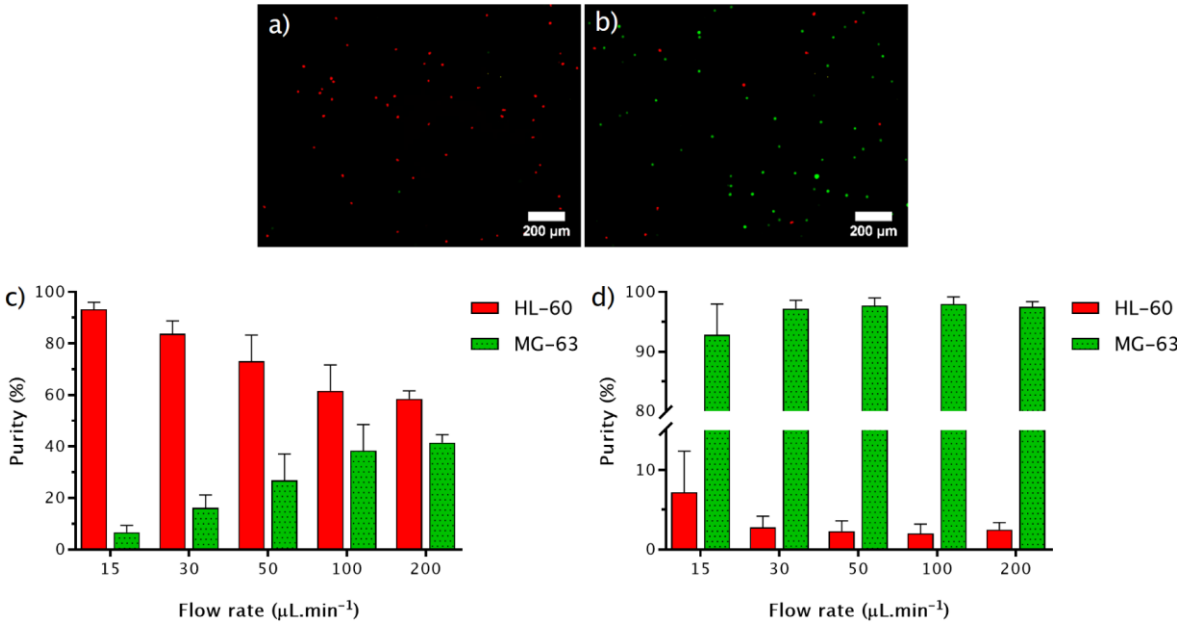

Figure 5.5 – Size and deformation-based sorting of MG-63 and HL-60. a) and b) show fluorescence microscopy images (Zeiss Axiovert 200 microscope, 5x objective) of the cell fractions from the 'smaller' and 'larger' outlets respectively. Green and red fluorescence corresponds to GFP⁺ MG-63 cells and CellTracker™ deep red-labelled HL-60. c) and d) show the purity of MG-63 (green, dotted) and HL-60 (red) cells collected from the smaller and larger outlets, after separation at varying flow rates (15-200 µL·min^{-1}). Values show mean ± SD (N=5).

Increasing the flow rate in DLD leads to larger cell deformation that can affect sorting efficiency. Figure 5.5d shows that at 30 µL·min^{-1}, the deformation of HL-60 resulted in smaller percentages of HL-60 cells being collected in the larger outlet which leads to an increase in the purity of MG-63 cells of up to 98 %. Increasing the flow rate up to 200 µL·min^{-1} did not further increase the purity of MG-63 suggesting that the more compliant HL-60 cells had neared their maximum deformation at 30 µL·min^{-1}. In contrast, the stiffer MG-63 cells had increasing deformation up to 200 µL·min^{-1} (Figure 5.5c). This led to a higher percentage of MG-63 cells collecting in the 'smaller' outlet at higher flow rates indicating that significant cell deformation changes the effective size of MG-63 cells below the D_C of section 2.

These data highlight the potential of DLD for passive label-free sorting based on both size and deformation. The sorting efficiency can be controlled by varying the flow rate, which should be adjusted according to specific cell properties and anticipated outcome. Potentially, a combination of the greater stiffness of SSCs together with any size differences could lead to significant enrichment of BM using DLD.

5.2.4. Binary fractionation of SSCs as a function of cell deformability

Expanded human skeletal stem cell populations at passage 0 (P0) were sorted into two fractions of different size. SSCs were sorted using the sheathless DLD device with a critical separation size of 12.18 µm and at flow rates varying from 15 to 100 µL·min^{-1}. The sorted cell fractions were analysed by flow cytometry to determine changes in the mean cell size of the fractions collected at each outlet from the forward scatter signal (FSC-A). After sorting, 100 cells from each of the sorted fractions were plated into wells of 6-well plates in

triplicate and allowed to adhere and expand to assess their capacity to form colony-forming units-fibroblastic (CFU-F).

At 15 μL·min^{-1} the vast majority of SSCs (95 %) were collected at the larger outlet (Figure 5.6a). This was expected given that the mean size of expanded SSCs at P0 was estimated at 18.2 ± 1.3 μm (by microfluidic impedance cytometry), which is significantly larger than the D_C of the DLD device. With increasing flow rate, cell deformation led to a higher fraction of SSCs collected at the smaller outlet, up to nearly 25 % at 100 μL·min^{-1}.

The mean and median size of cells collected at each outlet is shown in Figure 5.6b and c, with the dashed lines corresponding to unsorted SSCs. At the lowest flow rate, the biggest difference in cell size between the two fractions was achieved. As the flow rate increased, the mean and median FSC-A values generally increased for both fractions. In the smaller outlet, this was the result of larger cells starting to flow in zigzag mode due to greater deformation. In the larger outlet, the increased FSC-A values resulted from a reduction in the number of medium-sized cells collecting at the larger outlet, which are the first to change their displacement mode, effectively skewing the cell size distribution towards larger cells.

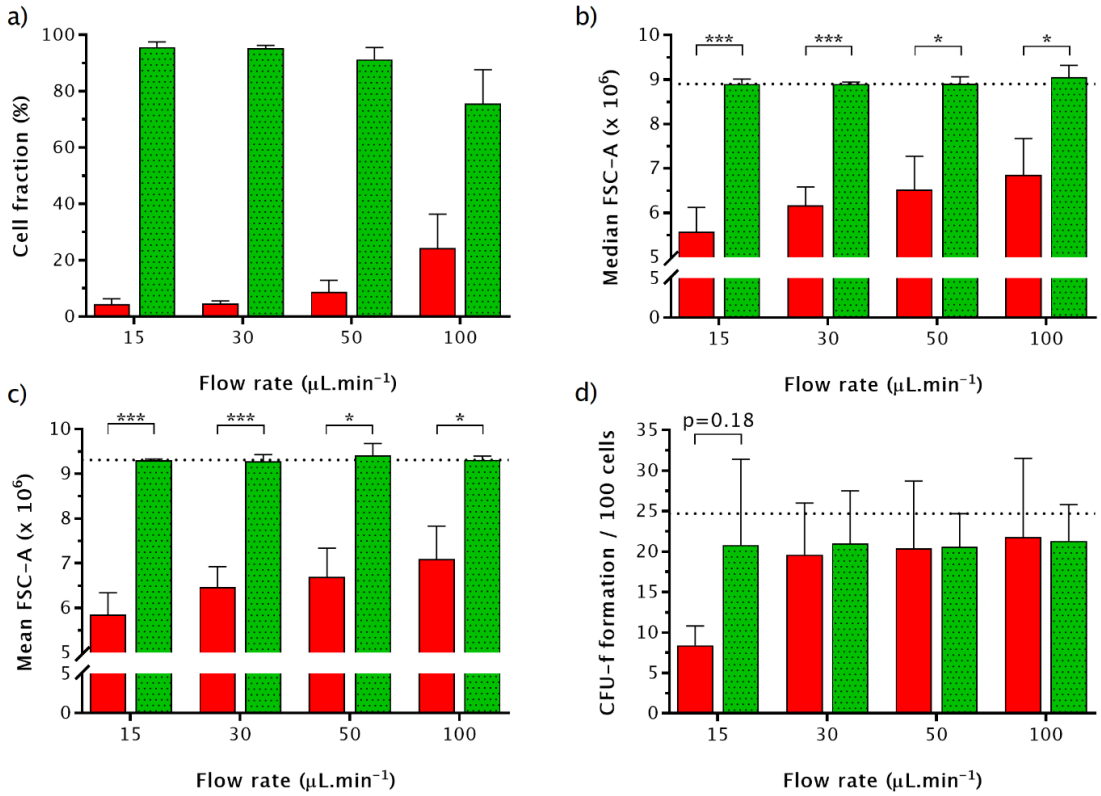

Figure 5.6 – Binary fractionation of skeletal stem cells as a function of cell deformability. a) Fraction of SSCs collected at the smaller (red) and larger (green, dotted) outlets *vs* flow rate. b) and c) show the median and mean FSC-A values of the cells collected at the smaller (red) and larger (green, dotted) outlets, respectively. d) CFU-F formation capacity of SSCs after sorting by DLD. Overall, the capacity to form CFU-F was not affected by DLD (dashed line shows the number of CFU-F obtained for unsorted SSCs). At 15 μL·min^{-1}, where the highest difference in cell size was observed, smaller cells (red) displayed a reduced capacity to form clonogenic cultures when compared with SSCs collected in the larger outlet (green, dotted). Values show mean ± SD (N=3; *p < 0.05; ***p < 0.001 with p-values obtained using the Student's t-test for independent samples).

The capacity to form clonogenic cultures was not significantly affected by DLD, when compared to unsorted SSCs (Figure 5.6d). This indicated that exposure to shear in DLD did not affect basic cell function, even at the highest flow rate tested (100 $\mu L \cdot min^{-1}$), where cells were flowed at faster than 4 centimetres per second. This supports previous studies that found no significant reduction in cell viability of cancer cell lines sorted by DLD at 10 $mL \cdot min^{-1}$, which corresponded to cells flowing at a speed of 35 $cm \cdot s^{-1}$.[103] In this study, the data suggested that shear-induced damage is an integral effect over time, which means that although cells flowing faster are exposed to higher shear rates, viability is not affected because the exposure time is reduced.

Cells collected at both smaller and larger outlets displayed equivalent CFU-F formation capacity, when sorted at 30, 50 and 100 $\mu L \cdot min^{-1}$. The number of CFU-F was around 20 per 100 plated cells, *versus* 24.7 for unsorted SSCs). Interestingly, at 15 $\mu L \cdot min^{-1}$, where the largest difference in the mean cell size was observed, cells collected at the smaller outlet displayed reduced CFU-F formation capacity (Figure 5.6d and Figure 5.7), though this was not statistically significant ($p=0.18$, $N=3$). This suggested that larger SSCs may have a higher capacity to form colonies, in keeping with the observations by Poon et al.[129] who have correlated larger MSCs with higher osteogenic potential and capacity to promote bone marrow regeneration *in vivo,* in preclinical murine BM injury models.

5.2.5. Size and mechano-based sorting of SSCs and WBCs

The sheathless DLD devices used in this work were designed to achieve efficient SSC enrichment from human BM at high throughput. Based on the data obtained by microfluidic impedance cytometry of primary human BM samples, the D_C of section 1 was set at 5.3 µm. This was anticipated to be small enough to displace all the different cell populations present in human BM to create a central cell-free stream, eliminating the need for sheath flow and increasing throughput (Figure 5.2).

To test this design concept, expanded SSCs at P0 were sorted from white blood cells (WBCs) obtained from healthy volunteers. Briefly, RBCs were lysed, WBCs were fluorescently labelled for CD45 using an allophycocyanin (APC) fluorophore and mixed 2:1 with SSCs, also fluorescently tagged with CellTracker™ green (CTG). This allowed unequivocal identification and counting of both cell types. As in section 5.2.4, after sorting, 100 cells from each outlet were plated to assess CFU-F formation capacity.

The trend observed for cells collected at the smaller outlet (Figure 5.8a) was theoretically anticipated. At 15 $\mu L \cdot min^{-1}$, the purity of WBCs in the small outlet reached 99.6 %. With increasing flow rate, the fraction of SSCs collected at the smaller outlet increased due to cell deformation, up to 4.7 % at 100 $\mu L \cdot min^{-1}$. Following cell plating, the diminutive number of SSCs collected at the smaller outlet explains the absence of CFU-F formation, with the exception of cells sorted at 100 $\mu L \cdot min^{-1}$, where a significant number of SSCs (approximately 1 in every 20 cells) were collected (Figure 5.8c). Note that even for unsorted SSCs (Figure 5.8c, dashed line), less than 1 in every 3 cells were capable of forming clonogenic cultures.

At the larger outlet (Figure 5.8b), when cells flowed at 15 μL·min^{-1}, the SSC fraction was enriched by 5.4 fold to 73 %. Low purities could be expected at reduced flow rates despite the larger size of expanded SSCs, as WBCs are a heterogeneous cell mixture covering a wide range of cell sizes, with some populations (*e.g.* monocytes)[240] typically larger than the D_C of section 2 (12.18 μm). With increasing flow rate and cell deformation, a reduction in the number of WBCs collected at the larger outlet was to be anticipated. However, the fraction of WBCs collected at the larger outlet was larger at higher flow rates. Because of the low SSC purity obtained in all conditions, the number of CFU-F ranged from just 6 to 12 CFU-F per every 100 plated cells (Figure 5.8c).

To understand why sorting at increased flow rates led to larger numbers of WBCs in the larger outlet, it was necessary to analyse the forward and side scatter distributions of both cell populations. As SSCs and WBCs were fluorescently labelled it was possible to clearly discriminate the two populations. Figure 5.9 shows contours of the distribution of WBCs (red) and SSCs (green) unsorted and collected from the larger outlet at 15-100 μL·min^{-1}. Interestingly, at 15 μL·min^{-1} it was the smallest fraction of WBCs that appeared in the larger outlet. With increasing flow rate, the size distribution spread to gradually include larger cells but still excluded the largest WBCs.

This leads to the conclusion that cell deformation resulted in the smallest WBC sub-populations to change their effective size to diameters below the D_C of section 1 (5.3 μm). This effect was exacerbated at highest flow rates, when cell deformation became more significant. These data, though precluding the use of sheathless DLD devices for efficient SSC sorting from human BM, provided important information for the design of a new generation of DLD devices. These should include either a smaller D_C in section 1 or re-introduce sheath flow to create a cell-free stream towards which the larger and stiffer SSCs can be sorted with high purity.

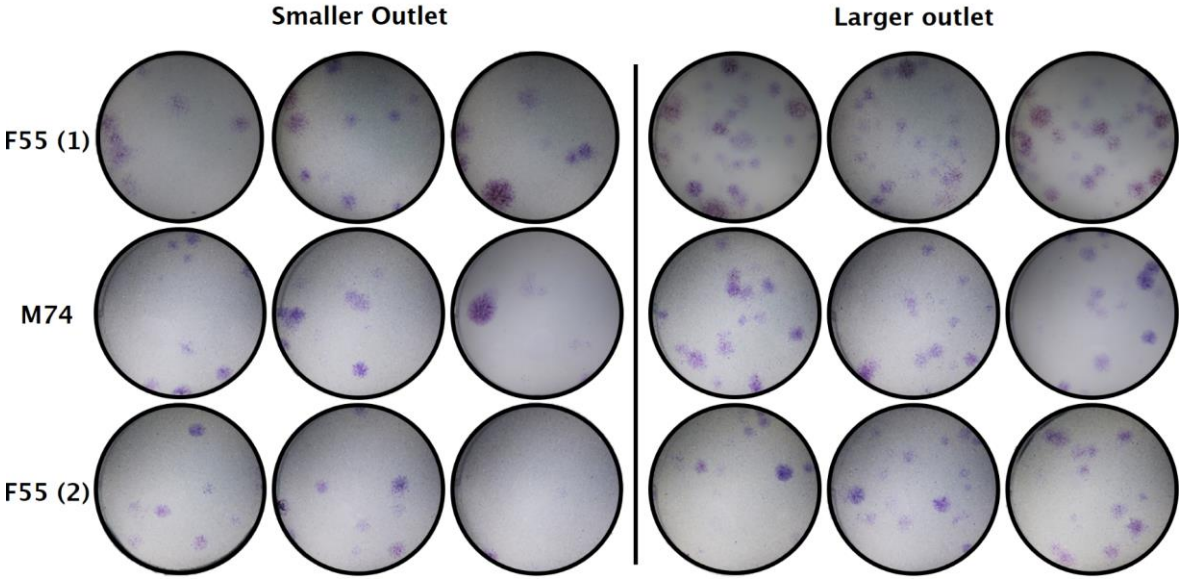

Figure 5.7 – Binary fractionation of skeletal stem cells as a function of cell deformability. Colony forming units-fibroblastic (CFU-F), counterstained with crystal violet, growing in wells of a 6-well plate. SSCs were sorted by DLD at 15 μL·min^{-1}, collected from the smaller and larger outlets and plated at a cell seeding density of 10 cells·cm^{-2}. Cells collected at the smaller outlet appear to display a lower capacity to form clonogenic cultures.

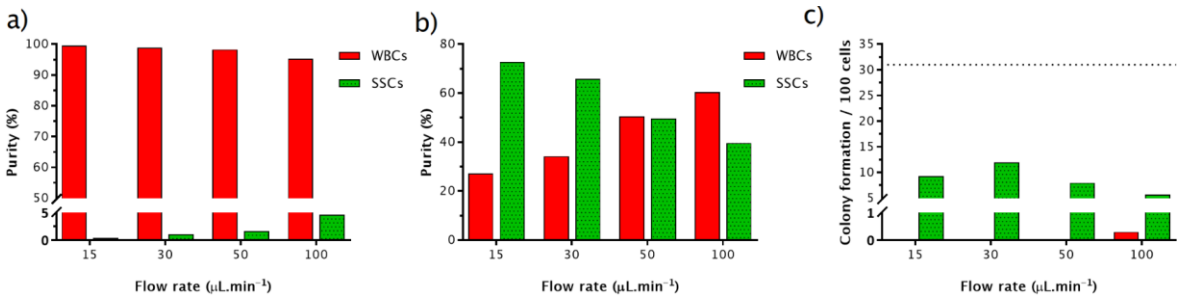

Figure 5.8 – Size and deformation-based sorting of white blood cells (WBCs) and expanded skeletal stem cells (SSCs) at passage 0. a) and b) purity of SSCs (green, dotted) and WBCs (red) collected from the smaller and larger outlets respectively, after sorting at varying flow rates (15–100 µL·min^{-1}). c) CFU-F formation capacity of unsorted SSCs (dashed line) and SSCs collected at the smaller (red) and larger (green, dotted) outlets after sorting by DLD. Values show mean purity and CFU-F number (N=1).

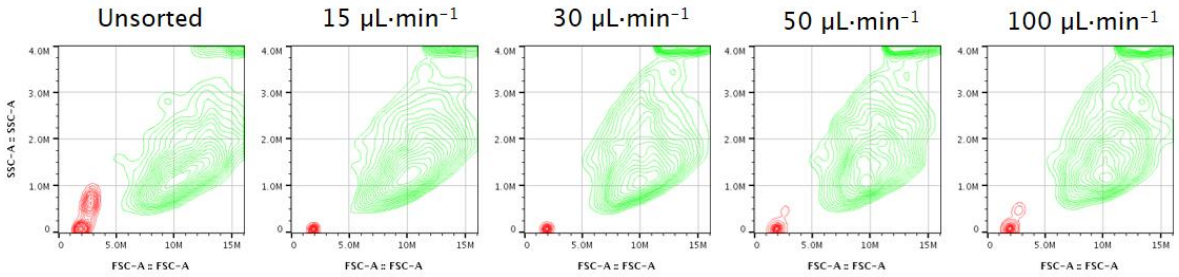

Figure 5.9 – Size and deformation-based sorting of white blood cells (WBCs) and expanded skeletal stem cells (SSCs) at passage 0. Forward and side scatter distributions of CD45-labelled WBCs (red) and SSCs (green) labelled with CellTracker™ green, unsorted and collected at the larger outlet after label-free sorting by DLD. Contour levels were set at 5 %.

5.2.6. Size and mechano-based sorting of SSCs from human BM

To confirm the indications provided by the work in section 5.2.5, the same DLD device was used to sort cells from a primary human BM sample. While the human BM comprises abundant white blood cell populations, BM offers added complexity as a heterogeneous sample containing many different cell types.[45] In this experiment, human BM mononuclear cells (hBMMNCs) were obtained from a BM buffy coat following density centrifugation. The mononuclear cell fraction was washed and re-suspended at a density of 0.5 million cells·mL^{-1} and flowed through the sheathless DLD device with a critical separation size of 12.18 µm at flow rates varying from 15 to 100 µL·min^{-1}. The collected cell fractions were analysed by flow cytometry.

Figure 5.10 shows density contours of FSC-A *vs* SSC-A scatter plots for hBMMNCs unsorted and collected at the smaller and larger outlets after sorting by DLD. The distribution of cells collected at the smaller outlet did not differ significantly from unsorted cells, except for a slight reduction of cells with largest FSC-A and SSC-A values. This was unsurprising given that the size measurements obtained from primary human BM samples in Chapter 4 indicated the diameter of the majority of cells in human BM to be under 12 µm.

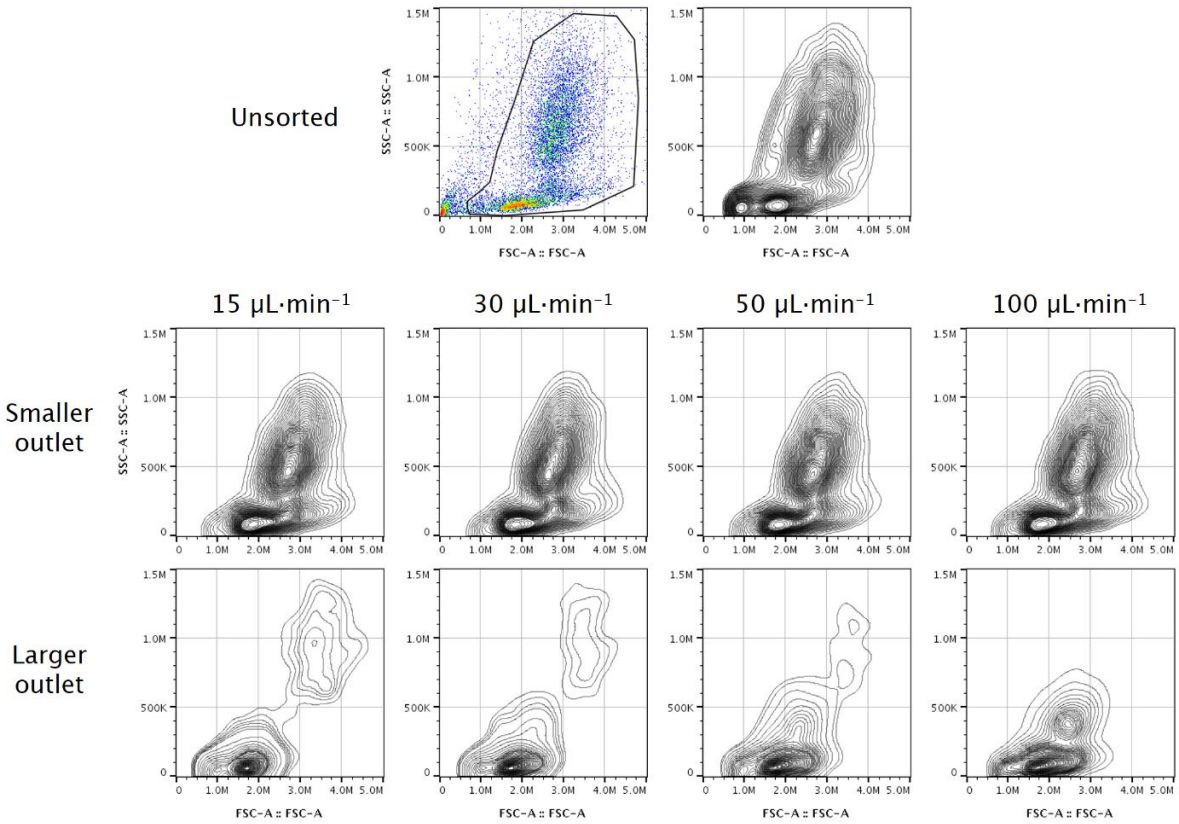

Figure 5.10 – Size and deformation-based sorting of human bone marrow mononuclear cells. Forward and side scatter distributions of hBMMNCs unsorted and collected at the smaller and larger outlets after label-free sorting by DLD. Contour levels were set at 5 %.

At reduced flow rates, there was an enrichment of cells with the largest FSC-A/SSC-A distributions in the larger outlet. This reduced at increased flow rates as cell deformation reduced the effective diameter of the largest hBMMNCs below 12.18 µm. These data highlighted the potential of DLD as a label-free approach to sort SSCs from BM based on size and deformation.

However, as anticipated by the results shown in 5.2.5, the cell fraction collected in the larger outlet was heavily contaminated by the smallest hBMMNCs that deformed to diameters below the critical separation size of section 1 (5.3 µm), and resulted in impaired separation efficiency. As the flow rate increased to 100 µL·min^{-1}, the distribution of cell sizes of the smallest cell fraction collected at the larger outlet increased to include larger cells. This further supported the hypothesis that cell deformation led to a complete bypass of section 1 and pointed to the need of design adjustments to allow a significant enrichment of skeletal stem cell populations from bone marrow by DLD.

5.3. Conclusions

This study demonstrated the potential of DLD for high-throughput method to sort human cell populations as a function of cell size and deformation. Size-based sorting of non-deformable polystyrene beads demonstrated the potential for isolating populations with high purity, reaching as high as 99.8 %. The sorting efficiency of non-deformable particles was not affected by increasing flow rate. This indicated that sorting by DLD is independent

of the flow rate, as long as the laminar flow regime is maintained, and provided a negative control for the deformation-based studies.

The potential to exploit cell deformation as a method of improving sorting by DLD was demonstrated using human cell lines, MG-63 and HL-60. By adjusting the flow rate, the deformation of HL-60 was enhanced because of increased shear forces. This resulted in superior separation efficiencies, up to 98 %.

Expanded human skeletal stem cells were fractionated by DLD into two sub-populations of different mean cell size. The largest difference in cell size was achieved at 15 $\mu L \cdot min^{-1}$. At this flow rate, SSCs collected at the smaller outlet displayed a reduced capacity to form clonogenic cultures when compared with unsorted SSCs, and with SSCs collected at the larger outlet. Although this did not reach statistical significance, the results were in keeping with previous observations that correlated larger MSCs with higher osteogenic potential.[129] Critically, the potential of SSCs to form CFU-F was not affected by processing by DLD, even at the highest flow rate tested (100 $\mu L.min^{-1}$). These results indicated that exposure to shear in DLD was not detrimental to basic skeletal stem cell function.

Finally, DLD was used to sort expanded SSCs from WBCs and to fractionate a primary human bone marrow sample. The results highlighted the potential of DLD as a label-free approach for sorting SSCs from BM based on both cell size and deformation. However, in both studies, deformation of the smallest cell populations reduced the capability of the first section of the DLD device to generate a cell-free central stream towards which the larger cells could be displaced. This significantly impaired the separation efficiency but provided critical data that will lead to an improved design, either by significantly reducing the critical separation size of section 1, or by re-introduction of sheath flow (to remove the need for two consecutive displacement sections of different critical separation sizes). With the proposed design modifications, DLD could offer the potential to exploit the higher stiffness of SSCs in combination with their larger size to allow significant enrichment from human bone marrow, with substantial physiological and therapeutic impact.

Chapter 6

Discussion and Future Directions

"Stay away from negative people. They have a problem to every solution."
Albert Einstein.

The 20th century saw a remarkable gain in mean life expectancy of about 30 years. If the current yearly growth continues, the majority of babies born after the millennium in countries with access to advanced health care will live to become centenarians.[3] While this constitutes a milestone for better lifestyles and medical progress, together with the current reduced birth rates, it contributes to the generation of an aged population in most developed countries. In Europe today, over 17 % of the population is aged 65 or over, a value that is predicted to increase to over 27 % by 2050.[241]

In the musculoskeletal arena, an aged population has implications in the health of the bones and joints and is associated with complications including the onset of osteoporosis, osteomyelitis, osteoarthritis, inflammatory arthritis, or cancer.[4,26] Worldwide, osteoporosis alone is responsible for about 9 million fractures every year, or one fracture every 3 seconds.[59] Major trauma injuries also contribute to bone fractures and non-union may follow any fracture. Furthermore, with longer lives, more people will outlive their prostheses and revision surgery often incurs extensive bone loss.[26] These challenges emphasize the need for innovative approaches to augment and repair tissue lost through trauma or disease.

Bone marrow stromal cells have the capacity to generate bone *in vivo*. Specifically, this capacity has been attributed to a multipotent stem cell population that exists as perivascular cells residing at the outer endothelial lining of bone marrow sinusoids, the so-called skeletal stem cells (SSCs).[242] SSCs have been used with success in the clinic to induce the formation of new cartilage and bone.[26,39,242] Notably, in one of these approaches, the concentration of progenitor cells used in the treatment of non-union fractures of the tibia was correlated with the success rate of the procedure.[43] Critically, it was found that the level of progenitor cells present in bone marrow aspirates was significantly below the concentration needed for the treatment to be successful. This highlighted the need for the development of cell enrichment strategies.[43]

Given the frequency of SSCs *in vivo*, estimated to be lower than 1 in 10,000 bone marrow mononuclear cells, enrichment remains a challenge. Typical approaches are based on density centrifugation, on the ability of SSCs to adhere to culture plastic and on selective culture media. However, these result in heterogeneous populations and are significantly time-consuming.[28] Fluorescence and magnetic-activated cell sorters typically provide high

levels of cell enrichment when a specific marker and a robust antibody are available. However, in the absence of a molecular marker that is unique to the SSC, these fail to provide the purity needed for routine clinical translation.[28,39,43]

Microfluidics offers outstanding control over fluid dynamics and provides the possibility of sorting cell suspensions at the single cell level without using antibodies but rather relying on cell biophysical properties. This work explored the hypothesis that SSCs hold a unique biophysical fingerprint and investigated the potential to use label-free methods based on microfluidics to deliver homogeneous populations of skeletal stem cells from primary human bone marrow tissue.

Real-time deformability cytometry (RT-DC) is a contactless microfluidic technique for high-throughput screening of cell mechanical properties.[175] In this work, RT-DC was used to compare the stiffness of SSCs, after expansion in normal culture conditions, with white blood cells (WBCs). Critically, expanded SSCs were shown to be stiffer than all main WBC populations.[230] This is significant because WBCs are abundant in bone marrow and suggests the use of cell stiffness as a biophysical marker to provide SSC enrichment from human bone marrow. However, it should be noted that cell stiffness could be altered by culture expansion and it would be interesting to determine whether such difference is observed for freshly harvested cells.

Work within this thesis exploited microfluidic impedance cytometry to assess the biophysical properties of unexpanded human SSCs, enriched by means of dual antibody labelling (Stro-1 and CD146).[46] It was observed that both cell size and membrane capacitance of unexpanded SSCs differed from expanded cells as early as after the first passage. These findings highlighted the importance of studying unaltered SSCs isolated from the original bone marrow tissue. Critically, the membrane capacitance of SSCs did not differ from other cells in bone marrow precluding the use of sorting approaches based on AC electrokinetics, such as dielectrophoresis. However, the membrane capacitance of SSCs changed significantly following induced osteogenic differentiation, indicating the potential of impedance cytometry to be used as a non-destructive means to track cell differentiation, as an alternative to the current approaches, which require cell fixation.

Significantly, the size of the SSC in bone marrow was found to be within the largest cell fraction at 9.0 ± 0.4 µm. This was the first time that the size of the SSC was estimated from unexpanded human BM samples and provided crucial information towards the design of a microfluidic device for SSC isolation.

Building on these findings, a microfluidic device based on the principle of deterministic lateral displacement (DLD) was designed to achieve significant enrichment of SSCs from human bone marrow. DLD uses micropillar arrays in a channel to sort cells based on size and deformability, with a throughput of thousands per second.[92,95,97] This work demonstrated the potential to exploit cell deformation within DLD to enhance sorting efficiency. By adjusting the flow rate, two human cell lines were sorted achieving purities up to 98 %. Expanded skeletal stem cell populations were fractionated by size and larger SSCs were correlated with a higher capacity to form clonogenic cultures, indicative of the presence of

progenitor cells. Importantly, using DLD it was possible to sort SSCs in a sterile environment and processing by DLD did not negatively affect the clonogenic capacity of SSCs.

In the current DLD designs, cells were sorted in two consecutive sections with different size thresholds (5.3 and 12.2 µm). When DLD was used to sort primary human bone marrow samples, WBC deformation below 5.3 µm compromised the separation efficiency of the current designs, resulting in cell fractions with no significant SSC enrichment. Despite the unfavourable outcome, the data provided important information that will lead to an improved device design. Specific improvements will include either a significant reduction of the size threshold of the first section, or the use of sheath flow, which allows sorting by DLD using only one section with a larger threshold. Each has their own specific advantages. On the one hand, using sheath flow typically leads to higher sorting efficiencies and purer populations. It also allows using shorter devices, which facilitates fabrication. On the other hand, DLD devices with two consecutive sections are typically very long, particularly when small size thresholds are used. But because there is no sheath flow, device operation is significantly simpler and the throughput is increased.

Overall, this work provided a detailed characterisation of relevant biophysical properties of SSCs and paved the way towards the design of a novel label-free sorting approach, potentially based on DLD. This will, ultimately, provide purified SSC populations from BM with potential application in fundamental stem cell research and the clinic. The ultimate goal is to harness science for therapy, to replace lost or damaged bone and cartilage with autogenous material harvested with minimal morbidity, providing robust, safe and efficient procedures that will drive the future of precision medicine in the 21st century.

Chapter 7

Materials and Methods

"However, not everything that can be counted counts, and not everything that counts can be counted"

William Bruce Cameron, 1963.

7.1. Cell Culture

Cells were maintained in media supplemented with 10 % foetal calf serum (FCS) and 100 U·mL^{-1} penicillin and 100 µg·mL^{-1} streptomycin (1 % Pen/Strep). Supplemented media is referred to as complete media unless otherwise indicated as plain media. Cells were maintained in a humidified chamber at 37 °C and 5 % CO_2. To detach adherent cells, a 0.025 % (w/v) trypsin-EDTA solution with 0.05 % glucose was used for 5-10 minutes unless stated otherwise.

7.1.1. MG-63 and Saos-2

MG-63 human osteosarcoma cells (passages 24 to 30) and Saos-2 human osteosarcoma cells (passages 26 to 28), were obtained from the European Collection of Authenticated Cell Cultures (ECACC, UK) and cultured in complete DMEM and α-MEM respectively. Media was replenished every 2-3 days and cells were routinely sub-cultured at a maximum confluency of 70-80 % and re-plated at a cell seeding density of 2-4 x 10^4 cells·cm^{-2}.

7.1.2. GFP$^+$ MG-63

GFP$^+$ MG-63 cells were established in previous work by transduction with a retroviral pMX-GFP vector (Cell Biolabs, Inc., VPK-302)[243] containing a green fluorescent protein (GFP) insert and using polybrene as a transduction enhancer.[243] Culture of GFP$^+$ MG-63 cells was under the same conditions as the original MG-63.

7.1.3. HL-60

HL-60, human peripheral blood promyelocytic leukaemia cells were obtained from the European Collection of Authenticated Cell Cultures (ECACC, UK) and cultured in complete RPMI-1640 media. Cells were split every other day to maintain a concentration of 1-10 x 10^5 cells·mL^{-1}.

7.1.4. Human Blood Samples

Ethical approval was given by the Isle of Wight, Portsmouth and South East Hampshire Local Research Ethics Committee (Ref no. 06/Q1701/137) and written consent was obtained from all participants for blood sample collection. Blood samples were collected from

healthy volunteers through a finger prick punctured using a safety lancet into blood collection tubes coated with sodium citrate to prevent the coagulation cascade. The tubes were kept on a roller at room temperature and subsequent experimental work was carried out within 2 to 3 hours after collection. Erythrocyte lysis was achieved by addition of a lysis solution in a 12:1 ratio. After constant mixing for 6 seconds the reaction was halted by the addition of 5.3 µL of an isosmotic quencher per microliter of whole blood.

7.1.5. Primary Human Bone Marrow Skeletal Stem Cells

Human BM samples were obtained from patients undergoing total hip replacement surgeries at the Spire Southampton Hospital or the Southampton General Hospital, with full patient consent. Only tissue that would have been discarded was used, with approval of the Southampton and South West Hampshire Research Ethics Committee (Ref no. 194/99/1 & 210/01). Cells were extracted from BM samples through multiples washes with plain α-MEM. After centrifugation to remove fat and soft tissue, the cell suspension was filtered through a 70-µm cell strainer and layered upon Lymphoprep™ to remove red blood cells and the majority of granulocytes by density centrifugation (Figure 7.1 a-c). The BMMNC fraction was collected from the 'buffy coat' and incubated for 30 minutes in blocking buffer to reduce non-specific antibody binding (Figure 7.1d, e). All cell incubations were at 4 ℃ and under agitation and washes between incubations were in MACS buffer. The Stro-1^{+} fraction was enriched by magnetic separation of cells labelled with the Stro-1 monoclonal antibody (IgM) derived from mouse hybridoma produced *in loco* and rat anti-mouse IgM microbeads, as previously detailed (Figure 7.2).[244,245]

The enriched SSC population was plated at a cell density of $1x10^{4}$ cells·cm^{-2} in complete α-MEM (passage 0). After one week of culture, the non-adherent cells were washed away, the media was replenished and subsequently changed every other day. For passage, cells were pre-treated with collagenase IV (200 µg·mL^{-1}) in plain α-MEM for 40 to 60 minutes before being lifted with Trypsin-EDTA. Cells were typically re-plated at a density of 2×10^{2} cells·cm^{-2}.

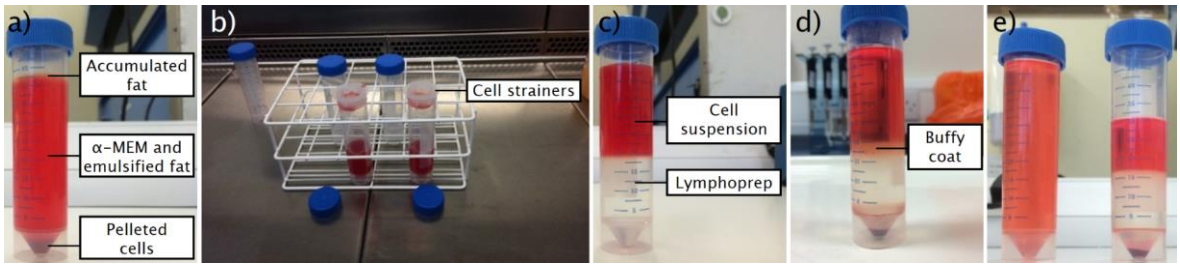

Figure 7.1 – Representative images of the skeletal stem cell enrichment protocol. a) cell pellet and fat accumulation resulting from the initial wash; b) use of cell strainers to remove bone debris and soft tissue from the cell suspension; c) cell suspension layered upon lymphoprep™ for density centrifugation; d) formation of the 'buffy coat' at the interface between α-MEM and lymphoprep™; and e) shows the resulting fractions after careful collection of the buffy coat. The tube on the left contains the buffy coat diluted in culture media while the one on the right shows the pelleted erythrocytes and polymorphonuclear cells, and the culture media and platelets in suspension, which are discarded.

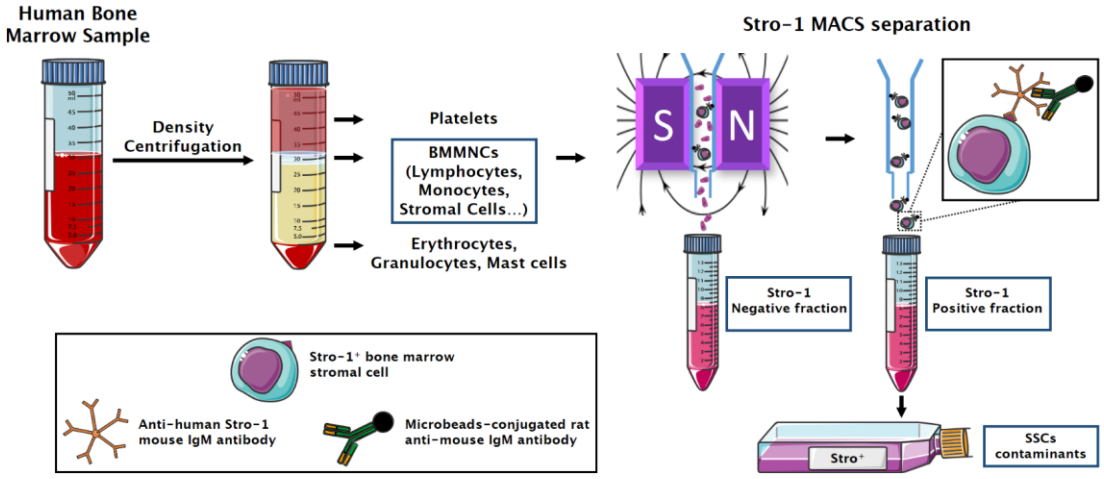

Figure 7.2 – Current enrichment process of human bone marrow mononuclear cells. Bone marrow samples are centrifuged across a density gradient and the buffy coat enriched for Stro-1⁺ cells by magnetic activated cell sorting (MACS) using a mouse hybridoma monoclonal IgM antibody coupled to superparamagnetic rat anti-mouse microbeads. The sorted fraction is plated in culture flasks and further enrichment is achieved by adhesion to tissue culture plastic.

7.1.5.1. Osteogenic Differentiation

After expansion for 14 days, SSCs were passaged, seeded at a cell density of 2 x 10^2 cells·cm^{-2} and cultured in osteogenic media consisting of complete α-MEM media supplemented with dexamethasone (10 nM) and ascorbate-2-phosphate (100 μM). The media was replenished every other day and the cells were analysed after 14 days.[246]

7.2. Fluorescent Cell Labelling

7.2.1. Human BMMNCs Labelling of Stro-1 and CD146

Cells in suspension were incubated with blocking buffer to minimise non-specific antibody bonding. After blocking, cells were incubated with Alexa Fluor® 647-conjugated mouse anti-human CD146 antibody (563619 BD Pharmingen™) diluted 1:50, for 30 minutes at 4 ℃ under agitation. The cells were then incubated with the Stro-1 antibody followed by incubation with Alexa Fluor® 488-conjugated goat anti-mouse IgM antibody (A-21042 from Invitrogen™) at 1:200 dilution. Non-specific binding was controlled using Alexa Fluor® 647-conjugated Mouse IgG1 κ Isotype Control (557714 BD Pharmingen™) and an IgM Isotype Control from a murine myeloma (M5909 SIGMA).

7.2.2. HL-60 Labelling with CellTracker™ Deep Red Dye

HL-60 cells were centrifuged and washed twice with PBS. Cells were suspended in 1μM CellTracker™ deep red dye (C34565 from Invitrogen™) in pre-warmed plain RPMI and incubated for 45 minutes in a humidified chamber at 37 ℃ and 5 % CO_2. After incubation, the dye was removed by centrifugation and the cells washed two more times with PBS before analysis.

7.2.3. Skeletal Stem Cell Labelling with CellTracker™ Green CMFDA Dye

Enriched skeletal stem cells were washed with PBS and pre-treated with collagenase IV (200 $\mu g \cdot mL^{-1}$) in plain α-MEM for 40 to 60 minutes to digest the extensive extracellular matrix produced by SSCs. Cells were incubated with 10μM CellTracker™ green CMFDA (C7025 from Invitrogen™) in pre-warmed plain α-MEM for 45 minutes in a humidified chamber at 37 °C and 5 % CO_2. After incubation, the dye was removed and the cells were further cultured in complete α-MEM for 60 minutes to encourage the conversion of the chloromethyl group into cell-impermeable products by cytosolic esterases. Cells were finally washed with PBS and lifted using Trypsin-EDTA as detailed above in section 7.1.5 of Materials and Methods.

7.2.4. White Blood Cell Labelling of CD45

White blood cells from whole blood were fluorescently labelled for CD45 by incubation with an APC-conjugated anti-human CD45 antibody (Miltenyi Biotec 130-098-143) for 20 minutes under agitation, in the dark. RBC lysis was performed as previously indicated in section 7.1.4 of Materials and Methods. WBCs were then centrifuged twice and re-suspended in PBS before analysis.

7.3. Flow Cytometry

Cells and particles were suspended in running buffer, filtered through a 100-μm cell strainer and analysed using a BD® Accuri C6 flow cytometer (Becton, Dickinson and Company, Franklin Lakes, NJ, USA). Data analysis was performed using FlowJo V10 software (FlowJo LLC, Ashland, OR, USA). Single events were gated for linearity in the forward scatter (FSC-H vs FSC-A) plot and typically, 25,000 events were acquired for each measurement inside the single event gate. Events were considered fluorescently positive above the threshold at which less than 1 % were positive for the matched isotype control.

7.4. Biochemical Assays

7.4.1. Alkaline Phosphatase (ALP) Staining

Cells cultured in 6-well plates were washed with PBS and fixed with 95 % ethanol in dH_2O for 10-15 minutes. Fixed cultures were incubated with a Fast Violet B salt (0.24 $mg \cdot mL^{-1}$) and Naphtol AS-MX solution (4% v/v) in dH_2O for 40 minutes at 37 °C in a humidified atmosphere protected from light. Cultures were washed with dH_2O and imaged using a dissecting stereoscope.[247]

7.4.2. ALP Activity and DNA Quantification

Cells cultured in 6-well plates were washed with PBS and fixed with 95 % (v/v) ethanol in dH_2O for 10-15 minutes. Cells were lysed using 0.05% (v/v) Triton™ X-100 solution in dH_2O followed by three freeze-thaw cycles. Total DNA was quantified against a standard curve (ssDNA from salmon testes) by addition of Quant-iT™ PicoGreen® dsDNA diluted in TE buffer and measurement of the emitted fluorescence (λex = 480nm; λem =520nm) using a FLx800™ fluorescence reader (BioTek, Winooski, VT, US). ALP activity was quantified

against a standard curve (p-nitrophenol) by incubation of the cell lysate with a phosphatase substrate solution (1.33 mg/mL p-nitrophenyl phosphate in 0.5M Alkaline buffer solution) at 37 ℃ in the dark, under gentle agitation. The reaction was terminated by addition of 1M NaOH in dH_2O after 40 minutes and absorbance was measured at 410nm using an ELx800™ absorbance reader (BioTek).[66,244]

7.4.3. CFU-F staining

SSCs cultured in 6-well plates were washed with PBS and fixed with 95 % (v/v) ethanol in dH_2O for 10-15 minutes. Fixed cultures were incubated with a 0.05% crystal violet solution in dH_2O for 5 minutes and washed extensively before imaging. Stained colonies were counted and imaged using a dissecting stereoscope.

7.5. Molecular Assays

7.5.1. RNA Extraction and Complementary DNA Synthesis

Total RNA was extracted from cultured cells using an RNeasy Mini Kit (Qiagen, Hilden, Germany). RNA concentration was measured using a NanoDrop 1000 spectrophotometer (Thermo Fisher Scientific, Waltham, MA, USA) and the RNA was reverse-transcribed using TaqMan Reverse Transcription Reagents (Applied Biosystems, Foster City, CA, USA).

7.5.2. Quantitative Reverse Transcription Polymerase Chain Reaction

Quantification of gene expression was performed as reported previously[248] using an ABI Prism 7500 system and primers, shown in Table 7.1, designed using Primer Express 3.0 (Applied Biosystems). A 20-µL reaction mixture was prepared in duplicate, containing 1 µL of complementary DNA, 10 µL of GoTaq qPCR Master Mix (Promega, WI, USA) and 1 µM of each primer. Thermal cycler conditions included an activation step at 95 ℃ for 10 minutes, followed by a 2-step PCR programme of 95 °C for 15 seconds and 60 ℃ for 60 seconds for 40 cycles. The $2^{-\Delta\Delta Ct}$ method was used for relative quantification of gene expression, and data was normalised to the expression of β-actin, the selected housekeeping gene.[65]

Table 7.1 – Primers used for qRT-PCR (F: forward and R: reverse).

Transcript	Abbreviation (name, length)	Primer sequence (5'-3')	Designed by
Beta-actin	*ACTB* (82)	F: GGCATCCTCACCCTGAAGTA R: AGGTGTGGTGCCAGATTTTC	Dr. Rahul Tare
Alkaline Phosphatase	*ALPL* (86)	F: GGAACTCCTGACCCTTGACC R: TCCTGTTCAGCTCGTACTGC	Dr. Rahul Tare
Runt-related Transcription Factor 2	*RUNX2* (78)	F: GTAGATGGACCTCGGGAACC R: GAGGCGGTCAGAGAACAAAC	Dr. Rahul Tare
Osteocalcin	*BGLAP* (110)	F: AAGAGACCCAGGCGCTACCT R: AACTCGTCACAGTCCGGATTG	Dr. Ewa Czekanska
Transcription Factor SOX2	*SOX2* (95)	F: CAAGATGCACAACTCGGAGA R: GCTTAGCCTCGTCGATGAAC	Dr. Fay Chinnery
Alpha-1 Type I Collagen	*COL1A1* (52)	F: GAGTGCTGTCCCGTCTGC R: TTTCTTGGTCGGTGGGTG	Dr. Rahul Tare
Alpha-1 Type II Collagen	*COL2A1* (58)	F: CCTGGTCCCCCTGGTCTTGG R: CATCAAATCCTCCAGCCATC	Dr. Rahul Tare
Nucleostemin	*GNL3* (98)	F: GGGAAGATAACCAAGCGTGTG R: CCTCCAAGAAGTTTCCAAAGG	Dr. Emmajayne Kingham
Peroxisome Proliferator Activated Receptor Gamma	*PPARG* (108)	F: GGGCGATCTTGACAGGAAAG R: GGGGGGTGATGTGTTTGAACTTG	Dr. Rahul Tare
Fatty Acid Binding Protein 4	*FABP4* (108)	F: TAGATGGGGGTGTCCTGGTA R: CGCATTCCACCACCAGTT	Dr. Rahul Tare
Transcription Factor SOX9	*SOX9* (74)	F: CCCTTCAACCTCCCACACTA R: TGGTGGTCGGTGTAGTCGTA	Dr. Rahul Tare

7.6. Mechanical Phenotyping

7.6.1. Sample Preparation

Cells were harvested, mixed appropriately, centrifuged and re-suspended in a 0.5 % methylcellulose solution in PBS at a concentration of 1-2 x 10^6 cells·mL^{-1}. For measurements of SSCs, cells were first filtered through a 70-µm cell strainer. The cell suspension was drawn into 1 mL syringes, connected to the chip using polymer tubing, and pumped with a syringe pump at a constant flow rate for 2 minutes before collecting data, to stabilise flow.

7.6.2. Microfluidic chip and Real-Time Deformability Cytometry Set-up

RT-DC measurements were performed as previously described.[175,202] Briefly, a microfluidic chip was manufactured from PDMS using soft-lithography and sealed with a glass cover-slip after plasma surface activation. The microfluidic chip consisted of two reservoirs connected by a 300 µm long constriction channel with a 30 by 30 µm cross-section. A row of filter posts at the inlet prevents channel blockage due to cell clumps and debris.

Data was acquired in real-time using a high-speed CMOS camera (MC1362; Mikrotron, Unterschleissheim, Germany), operating at 2,000 fps, and illuminated by a high-power LED (CBT-120, 462 nm; Luminus devices, Woburn, MA, USA). Cells were imaged through a 40x objective from an inverted microscope (Axiovert 200M, Carl Zeiss, Oberkochen, Germany) at the end of the 300-µm long constriction channel where the cell shape has reached steady state (Figure 3.1 a, b). An image processing algorithm implemented on C/LabVIEW was used to determine the cell cross-sectional area and circularity, defined as $c = 2\sqrt{\pi A}/l$, where A is the projected area of the cells and l its perimeter. Typically, a minimum of 2,000 or 5,000 (for measurements with leukocytes) events was acquired at flow rates of 0.16 µL·s^{-1} (0.04 µL·s^{-1} sample + 0.12 µL·s^{-1} sheath) and 0.32 µL·s^{-1} (0.08 µL·s^{-1} sample + 0.24 µL·s^{-1} sheath). Measurements of all samples were repeated at least three times. As a reference, cell circularity was obtained in a section of the microfluidic chip with large cross section where deformation does not occur (Appendix A).

7.7. Size and Dielectric Characterisation

7.7.1. Sample Preparation

The MIC chips were cleaned using 1M NaOH and dH_2O, and primed with MIC running buffer (0.5 % BSA (w/v), 2mM EDTA in 1x PBS.) before each experiment. Cells were suspended in running buffer at a concentration of 2-2.5 x 10^5 cells·mL^{-1} and mixed with 7-µm polystyrene (PS) beads (in PBS, 0.01% Tween-20) at 0.5-1x10^5 particles·mL^{-1}. Polystyrene beads have constant dielectric properties and were used to normalise the MIC results. The cell/bead suspension was pumped through the impedance cytometer at 40 µL·min^{-1}.

7.7.2. Microfluidic Chip and Impedance Cytometer Set-up

The microfluidic chip was fabricated from glass with a microfluidic channel (30 x 40 µm), defined in SU8 photoresist, through which cells flow. A detailed fabrication protocol of the MIC chips can be found elsewhere.[249] Platinum micro-electrodes were lithographically

patterned onto the glass and connected to AC sinusoidal voltages (4Vpp) at fixed frequencies. Single cell impedance was measured using a custom trans-impedance amplifier and an impedance spectroscope (HF2IS, Zurich Instruments AG, Zurich, Switzerland). Simultaneously, when applicable cells were illuminated by a focused 100 mW 635nm laser beam (LRD-0635-PF, Laserglow Technologies, Toronto, ON, Canada) exciting fluorescence from fluorescently labelled $CD146^+$ cells. The fluorescence emission was captured by the objective lens (10x, N.A. 0.30), passed through dichroic and band pass filter sets, spatially filtered using a pinhole and could be detected in the wavelength window from 660 to 700 nm using a photomultiplier (Hamamatsu Photonics, Hamamatsu, Japan).[250] The simultaneous collection of both fluorescence and impedance allows independent identification and verification of cell phenotype. The data was processed and analysed using custom software written in MATLAB™ (Mathworks, Inc. Natick, MA, USA).[251] The impedance data was used to trigger the data acquisition and a peak detection algorithm was used to detect the fluorescence signals.

7.8. Size and Mechano-based Cell sorting

7.8.1. Mask Design for Deterministic Lateral Displacement

CleWin4 from WieWeb Software (Hengelo, The Netherlands) was used to draw the device designs. Two independent masks were designed for the fabrication of DLD devices and photolithographic chrome masks in soda lime were manufactured by JD Photodata (Herts, UK). Devices from design 1 follow the original DLD design proposed by Huang *et al.*[92] and use sheath flow to hydrodynamically focus the sample at the inlet in a narrow stream and to keep cells from flowing close to the channel walls where wall effects may affect sorting efficiency (Figure 7.3a).

Devices from design 2 have a single inlet and are sheathless, which leads to higher throughput and allow device operation using just a syringe pump (Figure 7.3b) or simply a syringe and a valve to compress air as detailed in Holm *et al.*[252]. To allow particle fractionation with high purity, design 2 devices consist of two consecutive sections with different critical separation sizes (Dc). Section 1 is designed with a smaller Dc to displace all particles in flow towards the main channel outer walls in a mirrored micropost array creating a cell-free stream in the centre. The second section, with a larger Dc, inverts the microarray direction to displace only the larger particles back to the centre of the device where they are collected in one of two outlets. Given the two outlets in design 2 are connected by rectangular channels with varying lengths, the channel width was adjusted accordingly to guarantee an identical hydraulic resistance across the device span, which was estimated for each channel using equation 30[77], where w, h and L are the channel dimensions and η the fluid viscosity. Computational fluid dynamics simulations in COMSOL Multiphysics 5.0 (COMSOL AB, Stockholm, Sweden) were conducted, courtesy of Stefan Holm, to verify that both flow and particle profiles were preserved (Figure 7.4 a and b). These steps were also crucial to

assure that particles maintained their relative positions before and after the curved channels that were used to fit the long design 2 devices in single microscope glass slides (Figure 7.4c).

$$R = \frac{12\eta L}{wh^3}\left[1 - \frac{h}{w}\left(\frac{192}{\pi^5}\sum_{n=1}^{\infty}\frac{1}{(2n-1)^5}tanh\left(\frac{(2n-1)\pi w}{2h}\right)\right)\right]^{-1} \quad (Equation\ 30)$$

Both designs are preceded by a filter array (Figure 7.3 a-i and b-i) consisting of smaller pillars separated by narrower gaps to capture impurities and cell agglomerates and prevent particle clogging downstream of the device inlet. The gap size was kept constant to accommodate the largest particles in flow and avoid particle clogging. Devices from design 1 were intended to sort larger cells and non-deformable polystyrene beads, thus the gap size was kept at 50 µm. Devices from design 2, with smaller Dc's have a gap of 30 µm. The gap size, post diameter and the period of the array were chosen with the aim of obtaining a row shifts that were multiples of 0.2 µm in all devices as this was the maximum resolution provided for mask fabrication. The full array specifications for each device can be found in Table 7.2.

A parabolic flow profile is verified between the micropost arrays in DLD and is key for efficient particle separation. However, this profile holds only for infinitely wide arrays and becomes perturbed at the interface between the array and the sidewall flow significantly degrading sorting efficiency. To minimise this effect, Inglis[253] proposed a method for edge correction that assures that 1/N of the total fluid will flow over each post at all times, with N the period of the array. The solution was to adjust the gap size between the pillar rows closest to the walls of the device. The gap between each post and the wall of the zigzagging and the bumping sides is given by Equations 31 and 32 respectively, where n is the column number in a displacement array assuming values from 1 to N, G the gap size and ψ the tangent of the particle migration angle.

$$G_{zigzag}(n) = G\sqrt{n\psi} \quad (Equation\ 31)$$

$$G_{bumping}(n) = G\sqrt{2 - n\psi} \quad (Equation\ 32)$$

Table 7.2 – Specifications of the deterministic lateral displacement devices.

Device No.	Gap size (G)	Post diameter (Dpost)	Period (N)	Migration Angle (θ)	Row shift	Vertical Displacement (µm/mm)	Critical size (Dc)
1.1	50 µm	50 µm	25	2.29°	4 µm	40	14.93 µm
1.2	50 µm	50.8 µm	18	3.18°	5.6 µm	55.6	17.48 µm
1.3	50 µm	50.8 µm	14	4.09°	7.2 µm	71.4	19.72 µm
2.1/2.2/2.3 section 1	30 µm	30 µm	75	0.76°	0.8 µm	13.3	5.29 µm
2.1	30 µm	32 µm	31	1.85°	2 µm	32.3	8.08 µm
2.2	30 µm	30.8 µm	19	3.01°	3.2 µm	54.5	10.22 µm
2.3	30 µm	29.8 µm	13	4.40°	4.6 µm	76.9	12.18 µm

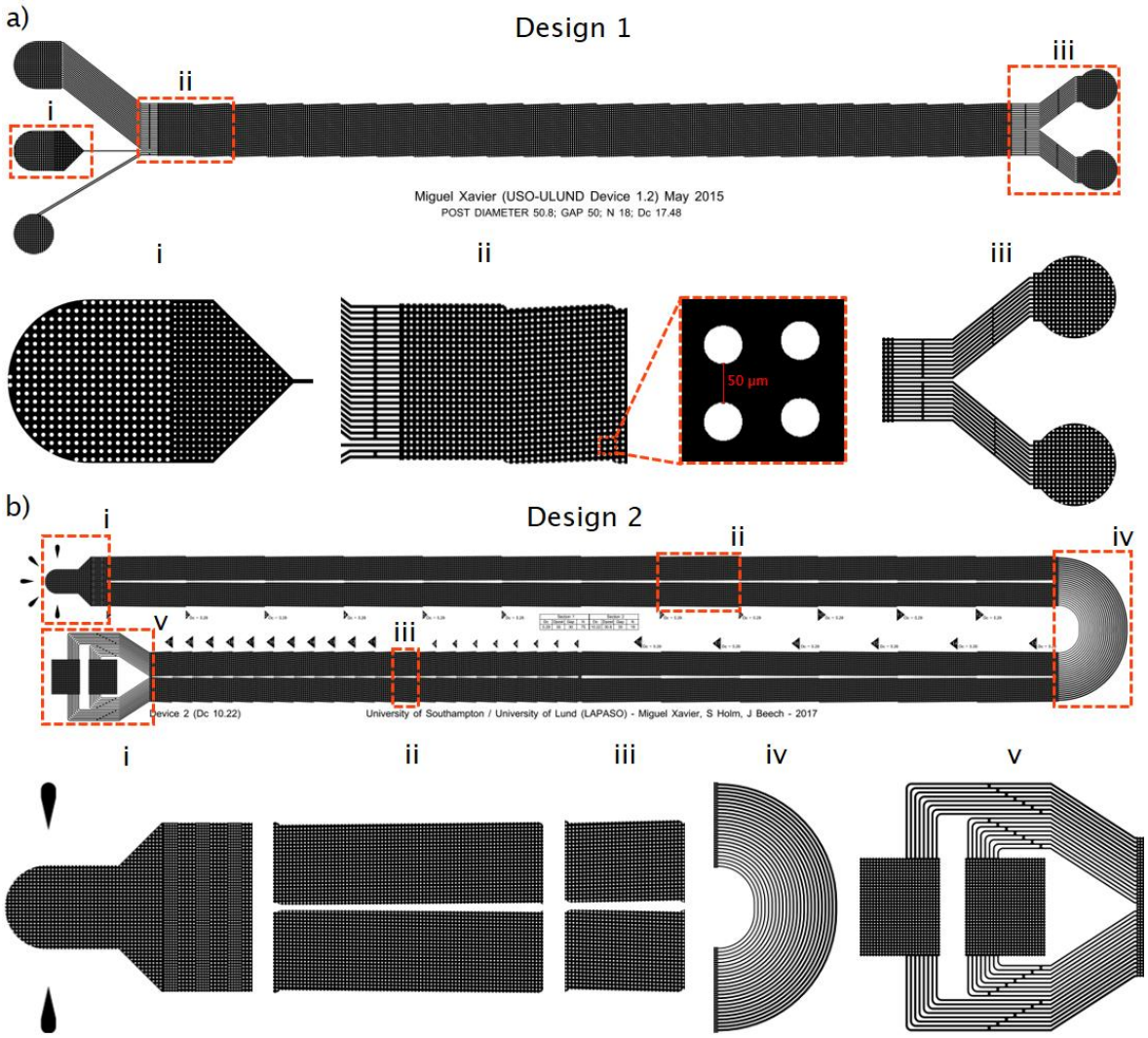

Figure 7.3 – Deterministic lateral displacement device designs. Magnifications of the mask drawings for DLD devices from designs 1 (a) and 2 (b). Close-ups show individual sections elucidating the filter array included at the sample inlet (a-i and b-i); the individual (a-ii) and mirrored (b-ii and iii) displacement arrays from design 1 and 2 respectively; the curved channels with varying width and length connecting the two main channels in design 2 devices (b-iv); and the two channel outlets that allow collection of the sorted cell fractions in each of the device designs (a-iii and b-v).

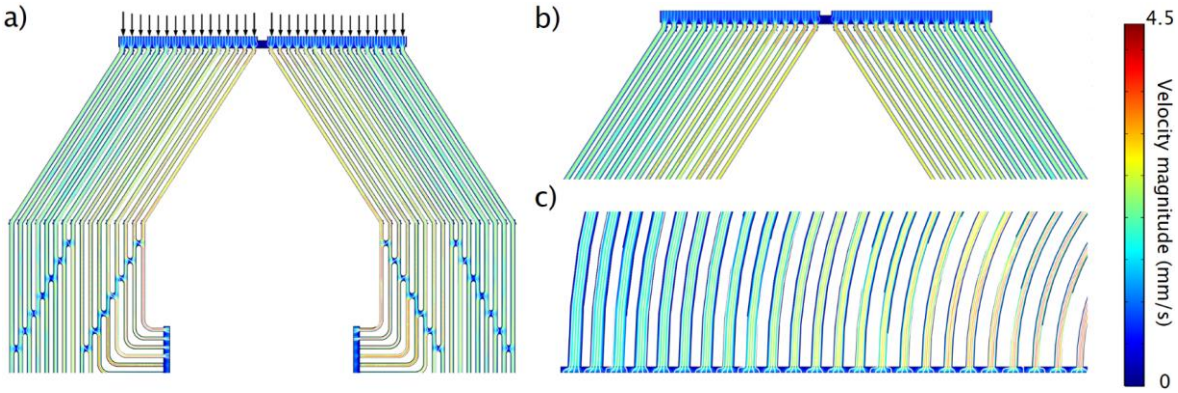

Figure 7.4 – Computational fluid dynamics simulation. 2-D plots of critical sections (a and b, channel outlets; and c, curved connecting channels) from design 2 devices with channels of different length and width. Streamlines demonstrate that the flow is split evenly before entering each channel. This ensures that particles will retain their relative lateral position between the different sections. The 2-D simulations were a courtesy of Stefan Holm from the University of Lund, Sweden and were conducted using COMSOL Multiphysics 5.0.

7.8.2. Microfabrication

Master moulds (Figure 7.5a and b) were fabricated on 4-inch glass or silicon wafers using SU-8 photoresist following standard photolithography techniques. Briefly, wafers were cleaned thoroughly in nitric acid, dehydrated overnight at 210 ℃ and spin-coated (3,000 rpm for 30 seconds) with TI Prime to promote adhesion of the photo-resist. An adequate SU-8 formulation was chosen according to the projected feature height, spin-coated for 30 seconds and soft baked before UV exposure using an EVG® 620T mask aligner (EV Group, St. Florian am Inn, Austria). Wafers were finally post-exposure baked, developed in EC solvent and hard baked. The feature height was verified using a KLA-Tencor surface profiler (CA, USA). Details of the process specifications are detailed in Table 7.3.

7.8.3. Soft Lithography

Master moulds were pre-treated with an anti-adhesion layer of hydrophobic 1H,1H,2H,2H-per-fluorooctyl-trichlorosilane under vacuum to facilitate de-moulding. Sylgard® 184 PDMS elastomer was prepared by mixing the elastomer base with curing agent (10:1, w/w), degassed, poured over the mould, and cured at 80 ℃ for one hour. Once cured, the PDMS was peeled away from the mould and inlets and outlets were opened using a 1.5 mm biopsy punch (Kai Europe GmbH, Solingen, Germany). The PDMS stamp and a PDMS-coated glass-slide were oxygen plasma-treated for 30 seconds in a Femto Plasma Asher (Diener electronic GmbH + Co. KG, Germany) and brought into contact forming an irreversible Si-O-Si covalent bond by condensation. The device was hydrated with a 0.5% (w/v) Pluronic® F-127 solution in PBS to prevent particle adhesion during experiments. Figure 7.5 e and d show images of final DLD devices mounted on PDMS-coated glass slides. Figure 7.5 e-j show different perspectives of the pillar array by optical microscopy and scanning electron microscopy.

7.8.4. Sample Preparation

Polystyrene bead samples were suspended in a 14 % sucrose (w/v), 0.1% Tween® 20 (v/v) solution in 1x PBS. Cell samples were suspended in a 15 % (w/v) Ficoll® PM400, 0.5 % (w/v) BSA and 2 mM EDTA solution in 1x PBS. Sucrose and Ficoll® PM400 were used to increase the suspending medium density to 1.05 $g \cdot mL^{-1}$ and prevent particle sedimentation inside the tubing and reservoirs. Tween® 20 was used to prevent bead aggregation and BSA and EDTA were used to prevent cell aggregation and adhesion to the device walls. The ample concentration was kept between 0.4 and 1 x $10^6 \cdot mL^{-1}$.

7.8.5. Device Operation

DLD devices were mounted on a portable USB microscope to allow imaging particles in flow and monitor the flow stability. Sample reservoirs were connected to the device using 1.6 mm outer diameter polymer tubing and flow was driven by action of a pressure gradient or a syringe pump for devices from generation 1 and 2 respectively. For generation 1 devices, the two outlets were kept at atmospheric pressure and the overpressure at the three inlets was controlled individually using an OB1 MK3 multi-channel flow controller (Elvesys, Paris, France). When deemed necessary, to guarantee sample sterility fluidic tubing and

connections were autoclaved and the DLD devices were exposed to UV light for 20 minutes, primed with 70 % ethanol for 20 minutes and the experiments were run in a laminar flow hood. After passivation with Pluronic® F-127, the devices were primed with DLD running buffer for 20 minutes before samples were flowed through. The flow was always allowed to stabilise prior to any fraction collection to assure the best separation efficiency.

Table 7.3 – Microfabrication specifications

Feature height	**30 µm**	**50 µm**
SU-8	SU-8 3025	SU-8 50
Spin-coating speed	2,500 rpm	2,000 rpm
Pre-exposure bake	65 °C, 2 minutes	65 °C, for 6 minutes
	95 °C, 12 minutes	95 °C, for 20 minutes
Exposure dose	180 mJ·cm^{-2}	200 mJ·cm^{-2}
Post-exposure bake	65 °C, 1 minute	65 °C, for 1 minute
	95 °C, 3 minutes 40 seconds	95 °C, for 5 minutes
Development	6 minutes	6 minutes
Hard bake	150 °C, for 20 minutes	150 °C, for 20 minutes

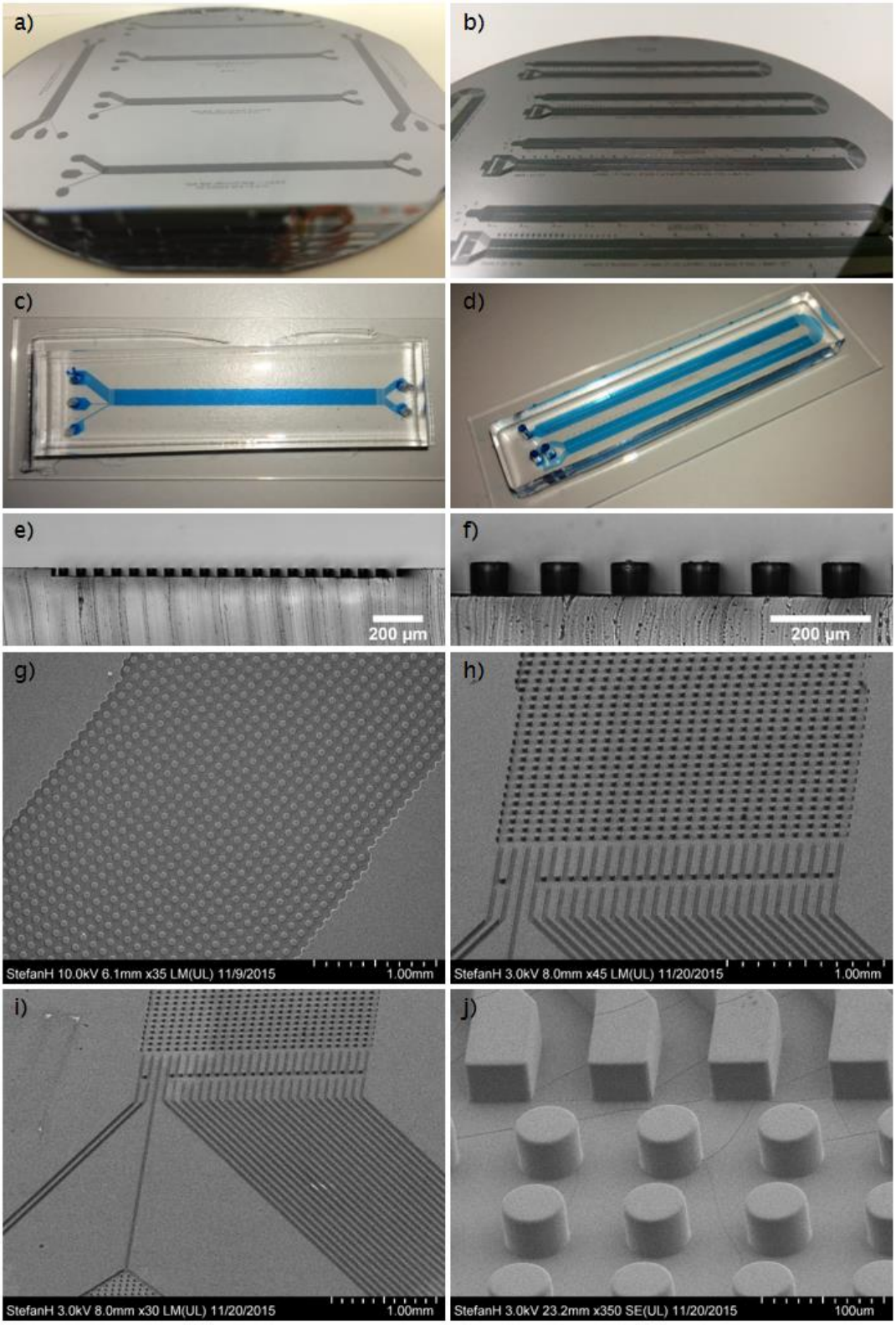

Figure 7.5 – Deterministic lateral displacement. a and b) silicon master moulds of DLD devices from generation 1 and 2 respectively; c and d) final DLD devices from each generation mounted on PDMS-coated microscope glass slides; the channels were filled with blue dye for visualisation; e) and f) show optical microscopy cross-sectional images of a generation 1 DLD device showing the pillar array; g)-j) scanning electron micrographs (SEM) showing different perspectives of the DLD devices on PDMS. SEM images were taken by Dr Stefan Holm (University of Lund, Sweden).

7.9. Statistical Analyses

Statistical analyses were performed using the IBM SPSS software package version 24 (IBM, NY, USA) unless stated otherwise. All data distributions were tested for normality using the Shapiro-Wilk test with a chosen alpha-level of 0.05.[254] To compare two means of independent samples that followed a normal distribution, the Student's t-test was used. To compare differences between three or more group means in samples that followed a normal distribution, p-values were calculated using one-way analysis of variance (ANOVA) with Tukey's post-hoc test. When samples did not follow a Gaussian distribution, the Mann-Whitney U-test was used.[255–257] A different analysis was done for the mechanical phenotyping data obtained by RT-DC, which is detailed below.

7.9.1. Mechanical Phenotyping

A two-dimensional mixture model using a normal distribution for cell size and a log-normal distribution for deformation was applied using R and rebmix.[201,203,205] These assumptions are justified since the lower boundary (D=0) skews the probability density function towards larger deformation values. The algorithm allowed the unbiased assignment of measurement events into clusters that represent different cell populations. Subsequent 1-dimensional linear mixed model analysis based on the R-package lme4 enabled a statistical comparison with respect to cell size and cell deformation.[201,206] To represent the experimental situation, one fixed and one random effect were taken into account to model the difference between sub-populations of cells and to consider the variation of biological replicates, respectively. The random effect was allowed to lead to random intercepts and slopes. P-values were calculated by a likelihood ratio test comparing the full model with a model lacking the fixed effect term. The results obtained were from at least 3 independent measurements and all data analysis was treated equally.

7.9.2. Size and Dielectric Characterisation

All results were obtained from at least four independent measurements from different patients. Results are represented as Mean ± SD unless stated otherwise, with graphs prepared using GraphPad Prism 7 (San Diego, CA, USA). Data distributions were tested for normality using the Shapiro-Wilk test and statistical significance was tested using one-way analysis of variance (ANOVA) with Tukey's post-hoc test for samples following a normal distribution or the Mann-Whitney U-test for samples not following a normal distribution. The statistical significance of the differences in gene expression between basal and osteogenic conditions was assessed using the Student's t-test for independent samples.

7.9.3. Size and Mechano-based cell sorting

Results are represented as Mean ± SD unless stated otherwise, with graphs prepared using GraphPad Prism 7 (San Diego, CA, USA). Data distributions were tested for normality using the Shapiro-Wilk test and statistical significance was tested using the Student's t-test for independent samples. The standardised Z-score was used to calculate the percentage of a particle population (which size follows a normal distribution with known mean and standard deviation), which fell under the critical separation size of a given DLD device. The

standardised Z-score was calculated using equation 29 introduced in Chapter 5 and percentages according to the calculated Z-score were obtained from the normal distribution table (Appendix C, Table S1 and Table S2).

7.10. Materials

BioWhittaker® Dulbecco's modified Eagle medium with glucose and L-glutamine (DMEM), alpha minimum essential medium with deoxyribonucleotides, ribonucleotides and ultra-glutamine (α-MEM), RPMI-1640, Dulbecco's phosphate buffered saline (PBS), foetal calf serum (FCS) and trypsin/EDTA with glucose were obtained from Lonza (Basel, Switzerland). Penicillin-streptomycin 100x, AB human serum, collagenase IV, ethylenediamine tetra-acetic acid (EDTA), methylcellulose, Naphtol AS-MX, fast violet salt B, crystal violet, Triton™ X-100, Tween®20, ssDNA from Salmon testes, Igepal® CA-630, alkaline buffer solution 1.5M, phosphatase substrate, 4-nitrophenol, 7-µm polystyrene beads, Ficoll® PM400, Trichloro(1*H*,1*H*,2*H*,2*H*-perfluorooctyl)silane and Pluronic® F-127 were purchased from Sigma-Aldrich (St. Louis, MO, USA). Non-deformable polystyrene beads for size-based sorting were from Polysciences Europe GmbH (Germany). Quant-iT™ PicoGreen® dsDNA Reagent was from Thermo Fisher Scientific (Waltham, MA, USA). Bovine serum albumin (BSA) was obtained from GE Healthcare (Chicago, IL, USA). Lymphoprep™ was bought from Stem Cell Technologies (Vancouver, Canada). Anti-mouse IgM microbeads, LS MACS™ columns and the QuadroMACS™ separator were purchased from Miltenyi Biotec (Bergisch Gladbach, Germany). TI Prime, SU-8 50 and SU-8 3025 were from Microchem Corp. (Westborough, MA, USA). The EC solvent was from Dow® Microposit® (MicroResist Technology GmbH, Germany). S-Monovette® 9NC tri-sodium citrate tubes were obtained from Sarstedt (Nümbrecht, Germany) and Sylgard® 184 polydimethylsiloxane (PDMS) was purchased from VWR (Darmstadt, Germany).

All reagents were used as received and according to the manufacturer's recommendations.

7.10.1. List of Buffers

- **Blocking buffer:** 10 % AB human serum (v/v), 5 % FCS (v/v) and 1 % BSA (w/v) in α-MEM.
- **MACS buffer:** 0.5 % BSA (w/v), 2mM EDTA in 1x PBS.
- **Antibody-diluting buffer**: 0.5 % BSA (w/v), 2mM EDTA in 1x PBS.
- **MIC running buffer:** 0.5 % BSA (w/v), 2mM EDTA in 1x PBS.
- **DLD running buffer (for polystyrene bead suspensions)**: 14 % sucrose (w/v), 0.1 % Tween® 20 (v/v) solution in 1x PBS.
- **DLD running buffer (for cell suspensions)**: 15 % ficoll PM400® (w/v), 0.5 % BSA (w/v), 2mM EDTA in 1x PBS.
- **RBC lysis solution**: 0.12 % (v/v) formic acid, 0.05 % saponin (w/v) in distilled water.
- **Isosmotic quencher**: 0.6 % w/v sodium carbonate, 3 % w/v sodium chloride solution in distilled water.

References

1. Hajar, R. History of medicine timeline. *Heart Views* **16,** 43–5 (2015).
2. United Nations World Population Prospects: The 2015 Revision. (2015).
3. Christensen, K., Doblhammer, G., Rau, R., & Vaupel, J. W. Ageing populations: the challenges ahead. *Lancet* **374,** 1196–1208 (2009).
4. Rachner, T. D., Khosla, S., & Hofbauer, L. C. Osteoporosis: Now and the future. *Lancet* **377,** 1276–1287 (2011).
5. Ramalho-Santos, M., Willenbring, H., Siminovitch, L., & Weissman, I. L. On the origin of the term stem cell. *Cell Stem Cell* **1,** 35–8 (2007).
6. Till, J. E., & McCulloch, E. A. A Direct Measurement of the Radiation Sensitivity of Normal Mouse Bone Marrow Cells. *Radiat. Res.* **14,** 213 (1961).
7. Becker, A. J., McCulloch, E. A., & Till, J. E. Cytological Demonstration of the Clonal Nature of Spleen Colonies Derived from Transplanted Mouse Marrow Cells. *Nature* **197,** 452–454 (1963).
8. Blume, K. G., & Thomas, E. D. A History of Allogeneic and Autologous Hematopoietic Cell Transplantation. in *Thomas' Hematopoietic Cell Transplantation* 1–11 (John Wiley & Sons, Ltd, 2016).
9. Thomas, E. D., Lochte, H. L., Lu, W. C., & Ferrebee, J. W. Intravenous Infusion of Bone Marrow in Patients Receiving Radiation and Chemotherapy. *N. Engl. J. Med.* **257,** 491–496 (1957).
10. Reya, T., Morrison, S. J., Clarke, M. F., & Weissman, I. L. Stem cells, cancer, and cancer stem cells. *Nature* **414,** 105–111 (2001).
11. Bianco, P., & Robey, P. G. Skeletal stem cells. *Development* **142,** 1023–1027 (2015).
12. Jaenisch, R., & Young, R. Stem Cells, the Molecular Circuitry of Pluripotency and Nuclear Reprogramming. *Cell* **132,** 567–582 (2008).
13. Condic, M. L. Totipotency: what it is and what it is not. *Stem Cells Dev.* **23,** 796–812 (2014).
14. Orkin, S. H., & Zon, L. I. Hematopoiesis: An Evolving Paradigm for Stem Cell Biology. *Cell* **132,** 631–644 (2008).
15. Dimitriou, R., Jones, E., McGonagle, D., & Giannoudis, P. V. Bone regeneration: current concepts and future directions. *BMC Med.* **9,** 66 (2011).
16. Friedenstein, A. J., Piatetzky-Shapiro, I. I., & Petrakova, K. V. Osteogenesis in transplants of bone marrow cells. *Development* **16,** (1966).
17. Tavassoli, M., & Crosby, W. H. Transplantation of Marrow to Extramedullary Sites. *Science (80-.).* **161,** 54–56 (1968).
18. Friedenstein, A. J., Chailakhjan, R. K., & Lalykina, K. S. The development of fibroblast colonies in monolayer cultures of guinea-pig bone marrow and spleen cells. *Cell Prolif.* **3,** 393–403 (1970).
19. Friedenstein, A. J., Chailakhyan, R. K., Latsinik, N. V, Panasyuk, A. F., & Keiliss-Borok, I. V. Stromal cells responsible for transferring the microenvironment of the hemopoietic tissues. Cloning in vitro and retransplantation in vivo. *Transplantation* **17,** 331–40 (1974).
20. Owen, M., & Friedenstein, A. J. Stromal stem cells: marrow-derived osteogenic precursors. *Ciba Found. Symp.* **136,** 42–60 (1988).
21. Sacchetti, B., Funari, A., Michienzi, S. *et al.* Self-Renewing Osteoprogenitors in Bone Marrow Sinusoids Can Organize a Hematopoietic Microenvironment. *Cell* **131,** 324–336 (2007).
22. Méndez-Ferrer, S., Michurina, T. V, Ferraro, F., Mazloom, A. R., Macarthur, B. D., Lira, S. A., Scadden, D. T., Ma'ayan, A., Enikolopov, G. N., & Frenette, P. S. Mesenchymal and haematopoietic stem cells form a unique bone marrow niche. *Nature* **466,** 829–34 (2010).
23. Caplan, A. I. Mesenchymal stem cells. *J. Orthop. Res.* **9,** 641–650 (1991).
24. Meirelles, L. da S., Chagastelles, P. C., & Nardi, N. B. Mesenchymal stem cells reside in virtually all post-natal organs and tissues. *J. Cell Sci.* **119,** (2006).
25. Bianco, P. Stem cells and bone: A historical perspective. *Bone* **70,** 2–9 (2015).
26. Tare, R. S., Kanczler, J., Aarvold, a, Jones, a M. H., Dunlop, D. G., & Oreffo, R. O. C. Skeletal stem cells and bone regeneration: translational strategies from bench to clinic. *Proc. Inst. Mech. Eng. H.* **224,** 1455–1470 (2010).
27. Bianco, P., Robey, P. G., & Simmons, P. J. Mesenchymal stem cells: revisiting history, concepts, and assays. *Cell Stem Cell* **2,** 313–9 (2008).
28. Gothard, D., Tare, R. S., Mitchell, P. D., Dawson, J. I., & Oreffo, R. O. C. In search of the skeletal stem cell: isolation and separation strategies at the macro/micro scale for skeletal regeneration. *Lab Chip* **11,** 1206–1220 (2011).
29. Quarto, R., Mastrogiacomo, M., Cancedda, R., Kutepov, S. M., Mukhachev, V., Lavroukov, A., Kon, E., & Marcacci, M. Repair of Large Bone Defects with the Use of Autologous Bone Marrow Stromal Cells. *N. Engl. J. Med.* **344,** 385–386 (2001).
30. Petite, H., Viateau, V., Bensaïd, W., Meunier, A., De Pollak, C., Bourguignon, M., Oudina, K., Sedel, L., & Guillemin, G. Tissue-engineered bone regeneration. *Nat. Biotechnol.* **18,** 959–963 (2000).

31. Tilley, S., Bolland, B. J., Partridge, K., New, A. M., Latham, J. M., Dunlop, D. G., & Oreffo, R. O. Taking tissue-engineering principles into theater: augmentation of impacted allograft with human bone marrow stromal cells. *Regen. Med.* **1,** 685–692 (2006).

32. Aarvold, A., Smith, J. O., Tayton, E. R., Jones, A. M. H., Dawson, J. I., Lanham, S., Briscoe, A., Dunlop, D. G., & Oreffo, R. O. C. From bench to clinic and back: skeletal stem cells and impaction bone grafting for regeneration of bone defects. *J. Tissue Eng. Regen. Med.* **8,** 779–786 (2014).

33. Sarkar, D., Spencer, J. A., Phillips, J. A., Zhao, W., Schafer, S., Spelke, D. P., Mortensen, L. J., Ruiz, J. P., Vemula, P. K., Sridharan, R., Kumar, S., Karnik, R., Lin, C. P., & Karp, J. M. Engineered cell homing. *Blood* **118,** e184–91 (2011).

34. Schrepfer, S., Deuse, T., Reichenspurner, H., Fischbein, M. P., Robbins, R. C., & Pelletier, M. P. Stem cell transplantation: the lung barrier. *Transplant. Proc.* **39,** 573–6 (2007).

35. Mousa, M., Evans, N. D., Oreffo, R. O. C., & Dawson, J. I. Clay nanoparticles for regenerative medicine and biomaterial design: A review of clay bioactivity. *Biomaterials* **159,** 204–214 (2018).

36. Dalby, M. J., Gadegaard, N., Tare, R., Andar, A., Riehle, M. O., Herzyk, P., Wilkinson, C. D. W., & Oreffo, R. O. C. The control of human mesenchymal cell differentiation using nanoscale symmetry and disorder. *Nat. Mater.* **6,** 997–1003 (2007).

37. Alakpa, E. V., Burgess, K. E. V., Chung, P., Riehle, M. O., Gadegaard, N., Dalby, M. J., & Cusack, M. Nacre Topography Produces Higher Crystallinity in Bone than Chemically Induced Osteogenesis. *ACS Nano* **11,** 6717–6727 (2017).

38. Ahlfeld, T., Cidonio, G., Kilian, D., Duin, S., Akkineni, A. R., Dawson, J. I., Yang, S., Lode, A., Oreffo, R. O. C., & Gelinsky, M. Development of a clay based bioink for 3D cell printing for skeletal application. *Biofabrication* **9,** 034103 (2017).

39. Dawson, J. I., Kanczler, J., Tare, R., Kassem, M., & Oreffo, R. O. C. Concise review: bridging the gap: bone regeneration using skeletal stem cell-based strategies – where are we now? *Stem Cells* **32,** 35–44 (2014).

40. Robey, P. G., & Bianco, P. The use of adult stem cells in rebuilding the human face. *J. Am. Dent. Assoc.* **137,** 961–72 (2006).

41. Warnke, P., Springer, I., Wiltfang, J., Acil, Y., Eufinger, H., Wehmöller, M., Russo, P., Bolte, H., Sherry, E., Behrens, E., & Terheyden, H. Growth and transplantation of a custom vascularised bone graft in a man. *Lancet* **364,** 766–770 (2004).

42. Hernigou, P., Poignard, A., Zilber, S., & Rouard, H. Cell therapy of hip osteonecrosis with autologous bone marrow grafting. *Indian J. Orthop.* **43,** 40–5 (2009).

43. Hernigou, P., Poignard, A., Beaujean, F., & Rouard, A. H. Percutaneous Autologous Bone-Marrow Grafting for Nonunions: Influence of the Number and Concentration of Progenitor Cells. *J. None Jt. Surg.* (2005).

44. Gronthos, S., & Simmons, P. J. The Biology and Application of Human Bone Marrow Stromal Cell Precursors. *J. Hematother.* **5,** 15–23 (1996).

45. Jones, E., & McGonagle, D. Human bone marrow mesenchymal stem cells in vivo. *Rheumatology* **47,** 126–131 (2008).

46. Xavier, M., de Andrés, M. C., Spencer, D., Oreffo, R. O. C., & Morgan, H. Size and Dielectric Properties of Skeletal Stem Cells Change Critically After Enrichment and Expansion from Human Bone Marrow: Consequences for Microfluidic Cell Sorting. *J. R. Soc. Interface* **14,** 20170233 (2017).

47. Grützkau, A., & Radbruch, A. Small but mighty: How the MACS®-technology based on nanosized superparamagnetic particles has helped to analyze the immune system within the last 20 years. *Cytom. Part A* **77A,** 643–647 (2010).

48. Basu, S., Campbell, H. M., Dittel, B. N., & Ray, A. Purification of Specific Cell Population by Fluorescence Activated Cell Sorting (FACS). *J. Vis. Exp* 15463791–1546 (2010). doi:10.3791/1546

49. Gronthos, S., Zannettino, A. C. W., Hay, S. J., Shi, S., Graves, S. E., Kortesidis, A., & Simmons, P. J. Molecular and cellular characterisation of highly purified stromal stem cells derived from human bone marrow. *J. Cell Sci.* **116,** 1827–1835 (2003).

50. Shi, S., & Gronthos, S. Perivascular niche of postnatal mesenchymal stem cells in human bone marrow and dental pulp. *J. Bone Miner. Res.* **18,** 696–704 (2003).

51. Kolf, C. M., Cho, E., & Tuan, R. S. Mesenchymal stromal cells. Biology of adult mesenchymal stem cells: regulation of niche, self-renewal and differentiation. *Arthritis Res. Ther.* **9,** 204 (2007).

52. Lin, G., Liu, G., Banie, L., Wang, G., Ning, H., Lue, T. F., & Lin, C.-S. Tissue distribution of mesenchymal stem cell marker Stro-1. *Stem Cells Dev.* **20,** 1747–52 (2011).

53. Simmons, P. J., & Torok-Storb, B. Identification of stromal cell precursors in human bone marrow by a novel monoclonal antibody, STRO-1. *Blood* **78,** 55–62 (1991).

54. Tare, R. S., Babister, J. C., Kanczler, J., & Oreffo, R. O. C. Skeletal stem cells: Phenotype, biology and environmental niches informing tissue regeneration. *Mol. Cell. Endocrinol.* **288,** 11–21 (2008).

55. Fitter, S., Gronthos, S., Ooi, S. S., & Zannettino, A. C. W. The Mesenchymal Precursor Cell Marker Antibody STRO-1 Binds to Cell Surface Heat Shock Cognate 70. *Stem Cells* **35,** 940–951 (2017).

56. Ramakrishnan, A., Torok-Storb, B., & Pillai, M. M. Primary marrow-derived stromal cells: isolation and manipulation. *Methods Mol. Biol.* **1035,** 75–101 (2013).

57. Bianco, P. Bone and the hematopoietic niche: a tale of two stem cells. *Blood* **117,** 5281–5289 (2011).

58. Zannettino, A. C. W., Paton, S., Kortesidis, A., Khor, F., Itescu, S., & Gronthos, S. Human mulipotential mesenchymal/stromal stem cells are derived from a discrete subpopulation of STRO-1bright/CD34/CD45(-)/glycophorin-A-bone marrow cells. *Haematologica* **92,** 1707–8 (2007).

59. Johnell, O., & Kanis, J. A. An estimate of the worldwide prevalence and disability associated with osteoporotic fractures. *Osteoporos. Int.* **17,** 1726–1733 (2006).

60. van Staa, T., Dennison, E., Leufkens, H., & Cooper, C. Epidemiology of fractures in England and Wales. *Bone* **29,** 517–522 (2001).

61. Svedbom, A., Hernlund, E., Ivergård, M., Compston, J., Cooper, C., Stenmark, J., McCloskey, E. V., Jönsson, B., Kanis, J. A., & IOF, the E. review panel of the. Osteoporosis in the European Union: a compendium of country-specific reports. *Arch. Osteoporos.* **8,** 137 (2013).

62. Xavier, M., Oreffo, R. O. C., & Morgan, H. Skeletal stem cell isolation: A review on the state-of-the-art microfluidic label-free sorting techniques. *Biotechnol. Adv.* **34,** 908–923 (2016).

63. Simmons, P. J., & Torok-Storb, B. Identification of stromal cell precursors in human bone marrow by a novel monoclonal antibody, STRO-1. 55–62 (1991).

64. Janeczek, A. A. Wnt Protein Delivery to Skeletal Stem Cells for Bone Tissue Regeneration. (University of Southampton, 2015).

65. Janeczek, A. A., Tare, R. S., Scarpa, E., Moreno-Jimenez, I., Rowland, C. A., Jenner, D., Newman, T. A., Oreffo, R. O. C., & Evans, N. D. Transient Canonical Wnt Stimulation Enriches Human Bone Marrow Mononuclear Cell Isolates for Osteoprogenitors. *Stem Cells* **34,** 418–430 (2016).

66. Gothard, D., Cheung, K., Kanczler, J. M., Wilson, D. I., & Oreffo, R. O. C. Regionally-derived cell populations and skeletal stem cells from human foetal femora exhibit specific osteochondral and multi-lineage differentiation capacity in vitro and ex vivo. *Stem Cell Res. Ther.* **6,** (2015).

67. Stewart, K., Walsh, S., Screen, J., Jefferiss, C. M., Chainey, J., Jordan, G. R., & Beresford, J. N. Further Characterization of Cells Expressing STRO-1 in Cultures of Adult Human Bone Marrow Stromal Cells. *J. Bone Miner. Res.* **14,** 1345–1356 (1999).

68. Halfon, S., Abramov, N., Grinblat, B., & Ginis, I. Markers Distinguishing Mesenchymal Stem Cells from Fibroblasts Are Downregulated with Passaging. *Stem Cells Dev.* **20,** 53–66 (2011).

69. Cardesa, J. I., Vela-Martín, A., & Jiménez, J. The turbulent cascade in five dimensions. *Science (80-.).* (2017).

70. Purcell, E. M. Life at low Reynolds number. *Am. J. Phys. Appl. Phys. Lett. Fluids Fluids Proc* **45,** 54102–1211 (1977).

71. Nguyen, N.-T., & Wereley, S. T. *Fundamentals and applications of microfluidics*. (Artech House, 2002).

72. Squires, T. M., & Quake, S. R. Microfluidics: Fluid physics at the nanoliter scale. *Rev. Mod. Phys.* **77,** 977–1026 (2005).

73. Huang, C., Liu, H., Bander, N. H., & Kirby, B. J. Enrichment of prostate cancer cells from blood cells with a hybrid dielectrophoresis and immunocapture microfluidic system. *Biomed. Microdevices* **15,** 941–948 (2013).

74. Gad-El-Hak, M. Differences between liquid and gas transport at the microscale. *Bull. POLISH Acad. Sci. Tech. Sci.* **53,** (2005).

75. Kirby, B. J. *Micro and nanoscale fluid mechanics: transport in microfluidic devices*. (Cambridge University Press, 2010).

76. Beech, J. Microfluidics Separation and Analysis of Biological Particles. (Lund University, 2011).

77. Bruus, H. *Theoretical microfluidics*. (Oxford University Press, 2008).

78. Manz, A., Graber, N., & Widmer, H. M. Miniaturized total chemical analysis systems: A novel concept for chemical sensing. *Sensors Actuators B Chem.* **1,** 244–248 (1990).

79. Ganong, W. F., Barman, S. M., Barrett, K. E., Brooks, H. L., & Boitano, S. *Ganong's review of medical physiology*. (McGraw Hill Medical, 2012).

80. Rawal, S., Yang, Y.-P., Cote, R., & Agarwal, A. Identification and Quantitation of Circulating Tumor Cells. *Annu. Rev. Anal. Chem* **10,** 321–43 (2017).

81. Nagrath, S., Sequist, L. V, Maheswaran, S., Bell, D. W., Irimia, D., Ulkus, L., Smith, M. R., Kwak, E. L., Digumarthy, S., Muzikansky, A., Ryan, P., Balis, U. J., Tompkins, R. G., Haber, D. a, & Toner, M. Isolation of rare circulating tumour cells in cancer patients by microchip technology. *Nature* **450,** 1235–9 (2007).

82. Stott, S. L., Hsu, C.-H., Tsukrov, D. I. *et al.* Isolation of circulating tumor cells using a microvortex-generating herringbone-chip. *Proc. Natl. Acad. Sci. U. S. A.* **107,** 18392–18397 (2010).

83. Gleghorn, J. P., Pratt, E. D., Denning, D., Liu, H., Bander, N. H., Tagawa, S. T., Nanus, D. M., Giannakakou, P. a, & Kirby, B. J. Capture of circulating tumor cells from whole blood of prostate cancer patients using geometrically enhanced differential immunocapture (GEDI) and a prostate-specific antibody. *Lab Chip* **10,** 27–29 (2010).

84. Galletti, G., Sung, M. S., Vahdat, L. T., Shah, M. a., Santana, S. M., Altavilla, G., Kirby, B. J., & Giannakakou, P. Isolation of breast cancer and gastric cancer circulating tumor cells by use of an anti HER2-based microfluidic device. *Lab Chip* **14,** 147–56 (2013).

85. Kirby, B. J., Jodari, M., Loftus, M. S., Gakhar, G., Pratt, E. D., Chanel-Vos, C., Gleghorn, J. P., Santana, S. M., Liu, H., Smith, J. P., Navarro, V. N., Tagawa, S. T., Bander, N. H., Nanus, D. M., & Giannakakou, P. Functional characterization of circulating tumor cells with a prostate-cancer-specific microfluidic device. *PLoS One* **7,** 1–10 (2012).

86. Thege, F. I., Lannin, T. B., Saha, T. N., Tsai, S., Kochman, M. L., Hollingsworth, M. a, Rhim, A. D., & Kirby, B. J. Microfluidic immunocapture of circulating pancreatic cells using parallel EpCAM and MUC1 capture: characterization, optimization and downstream analysis. *Lab Chip* **14,** 1775–84 (2014).

87. Smith, J. P., Huang, C., & Kirby, B. J. Enhancing sensitivity and specificity in rare cell capture microdevices with dielectrophoresis. *Biomicrofluidics* **9,** 014116 (2015).

88. Srisa-Art, M., Bonzani, I. C., Williams, A., Stevens, M. M., deMello, A. J., & Edel, J. B. Identification of rare progenitor cells from human periosteal tissue using droplet microfluidics. *Analyst* **134,** 2239–45 (2009).

89. Chen, Y., Li, P., Huang, P.-H., Xie, Y., Mai, J. D., Wang, L., Nguyen, N.-T., & Huang, T. J. Rare cell isolation and analysis in microfluidics. *Lab Chip* **14,** 626–45 (2014).

90. Reátegui, E., Aceto, N., Lim, E. J., Sullivan, J. P., Jensen, A. E., Zeinali, M., Martel, J. M., Aranyosi, A. J., Li, W., Castleberry, S., Bardia, A., Sequist, L. V., Haber, D. A., Maheswaran, S., Hammond, P. T., Toner, M., & Stott, S. L. Tunable nanostructured coating for the capture and selective release of viable circulating tumor cells. *Adv. Mater.* **27,** 1593–1599 (2015).

91. Yoon, H. J., Shanker, A., Wang, Y., Kozminsky, M., Jin, Q., Palanisamy, N., Burness, M. L., Azizi, E., Simeone, D. M., Wicha, M. S., Kim, J., & Nagrath, S. Tunable Thermal-Sensitive Polymer–Graphene Oxide Composite for Efficient Capture and Release of Viable Circulating Tumor Cells. *Adv. Mater.* **28,** 4891–4897 (2016).

92. Huang, L. R., Cox, E. C., Austin, R. H., & Sturm, J. C. Continuous Particle Separation Through Deterministic Lateral Displacement. *Science (80-.).* **304,** 987–990 (2004).

93. Morton, K. J., Loutherback, K., Inglis, D. W., Tsui, O. K., Sturm, J. C., Chou, S. Y., & Austin, R. H. Crossing microfluidic streamlines to lyse, label and wash cells. *Lab Chip* **8,** 1448–1453 (2008).

94. Holm, S. H., Beech, J. P., Barrett, M. P., & Tegenfeldt, J. O. Separation of parasites from human blood using deterministic lateral displacement. *Lab Chip* **11,** 1326–1332 (2011).

95. McGrath, J., Jimenez, M., & Bridle, H. Deterministic lateral displacement for particle separation: a review. *Lab Chip* **14,** 4139–58 (2014).

96. Beech, J. P., Holm, S. H., Adolfsson, K., & Tegenfeldt, J. O. Sorting cells by size, shape and deformability. *Lab Chip* **12,** 1048 (2012).

97. Holmes, D., Whyte, G., Bailey, J., Vergara-Irigaray, N., Ekpenyong, A., Guck, J., & Duke, T. Separation of blood cells with differing deformability using deterministic lateral displacement. *Interface Focus* **4,** 20140011 (2014).

98. Holm, S. H., Beech, J. P., & Tegenfeldt, J. O. Combined Density and Size-based Sorting in Deterministic Lateral Displacement Devices. in *17th International Conference on Miniaturized Systems for Chemistry and Life Sciences* 1224–1226 (2013).

99. Collins, D. J., Alan, T., & Neild, A. Particle separation using virtual deterministic lateral displacement (vDLD). *Lab Chip* **14,** 1595–603 (2014).

100. Beech, J. P., Jönsson, P., & Tegenfeldt, J. O. Tipping the balance of deterministic lateral displacement devices using dielectrophoresis. *Lab Chip* **9,** 2698–2706 (2009).

101. Green, J. V., Radisic, M., & Murthy, S. K. Deterministic lateral displacement as a means to enrich large cells for tissue engineering. *Anal. Chem.* **81,** 9178–9182 (2009).

102. Zhang, B., Green, J. V., Murthy, S. K., & Radisic, M. Label-free enrichment of functional cardiomyocytes using microfluidic deterministic lateral flow displacement. *PLoS One* **7,** 1–9 (2012).

103. Loutherback, K., D'Silva, J., Liu, L., Wu, A., Austin, R. H., & Sturm, J. C. Deterministic separation of cancer cells from blood at 10 mL/min. *AIP Adv.* **2,** 0–7 (2012).

104. Fachin, F., Spuhler, P., Martel-Foley, J. M. *et al.* Monolithic Chip for High- throughput Blood Cell Depletion to Sort Rare Circulating Tumor Cells. *Sci. Rep.* **7,** 10936 (2017).

105. Inglis, D. W., Lord, M., & Nordon, R. E. Scaling deterministic lateral displacement arrays for high throughput and dilution-free enrichment of leukocytes. *J. Micromechanics Microengineering* **21,** 054024 (2011).

106. Liu, Z., Huang, F., Du, J., Shu, W., Feng, H., Xu, X., & Chen, Y. Rapid isolation of cancer cells using microfluidic deterministic lateral displacement structure. *Biomicrofluidics* **7,** (2013).

107. Ozkumur, E., Shah, A. M., Ciciliano, J. C. *et al.* Inertial Focusing for Tumor Antigen-Dependent and -Independent Sorting of Rare Circulating Tumor Cells. *Sci. Transl. Med.* **5,** (2013).

108. Karabacak, N. M., Spuhler, P. S., Fachin, F. *et al.* Microfluidic, marker-free isolation of circulating tumor cells from blood samples. *Nat. Protoc.* **9,** 694–710 (2014).

109. Huang, R., Barber, T. A., Schmidt, M. A., Tompkins, R. G., Toner, M., Bianchi, D. W., Kapur, R., & Flejter, W. L. A microfluidics approach for the isolation of nucleated red blood cells (NRBCs) from the peripheral blood of pregnant women. *Prenat. Diagn.* **28,** 892–899 (2008).

110. Plouffe, B. D., Murthy, S. K., & Lewis, L. H. Fundamentals and application of magnetic particles in cell isolation and enrichment: a review. *Rep. Prog. Phys.* **78,** 016601 (2014).

111. Zborowski, M., Sun, L., Moore, L. R., Stephen Williams, P., & Chalmers, J. J. Continuous cell separation using novel magnetic quadrupole flow sorter. *J. Magn. Magn. Mater.* **194,** 224–230 (1999).

112. Jing, Y., Moore, L. R., Schneider, T., Williams, P. S., Chalmers, J. J., Farag, S. S., Bolwell, B., & Zborowski, M. Negative selection of hematopoietic progenitor cells by continuous magnetophoresis. *Exp. Hematol.* **35,** 662–672 (2007).

113. Tong, X., Xiong, Y., Zborowski, M., Farag, S. S., & Chalmers, J. J. A novel high throughput immunomagnetic cell sorting system for potential clinical scale depletion of T cells for allogeneic stem cell transplantation. *Exp. Hematol.* **35,** 1613–1622 (2007).

114. Yang, L., Lang, J. C., Balasubramanian, P., Jatana, K. R., Schuller, D., Agrawal, A., Zborowski, M., & Chalmers, J. J. Optimization of an Enrichment Process for Circulating Tumor Cells From the Blood of Head and Neck Cancer Patients Through Depletion of Normal Cells. **102,** 521–534 (2009).

115. Moore, L. R., Nehl, F., Dorn, J., Chalmers, J. J., & Zborowski, M. Open Gradient Magnetic Red Blood Cell Sorter Evaluation on Model Cell Mixtures. *IEEE Trans. Magn.* **49,** 309–315 (2013).

116. Plouffe, B. D., Mahalanabis, M., Lewis, L. H., Klapperich, C. M., & Murthy, S. K. Clinically Relevant Microfluidic Magnetophoretic Isolation of Rare- Cell Populations for Diagnostic and Therapeutic Monitoring Applications. *Anal. Chem.* **84,** 1336–1344 (2012).

117. Huang, Y. Y., Hoshino, K., Chen, P., Wu, C. H., Lane, N., Huebschman, M., Liu, H., Sokolov, K., Uhr, J. W., Frenkel, E. P., & Zhang, J. X. J. Immunomagnetic nanoscreening of circulating tumor cells with a motion controlled microfluidic system. *Biomed. Microdevices* **15,** 673–681 (2013).

118. Han, K.-H., & Frazier, A. B. Paramagnetic capture mode magnetophoretic microseparator for high efficiency blood cell separations. *Lab Chip* **6,** 265–273 (2006).

119. Amini, H., Lee, W., & Carlo, D. Di. Inertial microfluidic physics. *Lab Chip* **14,** 2739–2761 (2014).

120. Di Carlo, D. Inertial microfluidics. *Lab Chip* **9,** 3038–3046 (2009).

121. Geislinger, T. M., & Franke, T. Hydrodynamic lift of vesicles and red blood cells in flow – From Fåhræus & Lindqvist to microfluidic cell sorting. *Adv. Colloid Interface Sci.* **208,** 161–176 (2014).

122. Di Carlo, D., Edd, J. F., Humphry, K. J., Stone, H. A., & Toner, M. Particle segregation and dynamics in confined flows. *Phys. Rev. Lett.* **102,** 1–4 (2009).

123. Segré, G., & Silberberg, A. Radial Particle Displacements in Poiseuille Flow of Suspensions. *Nature* **189,** 209–210 (1961).

124. Fåhræus, R., & Lindqvist, T. The viscosity of the blood in narrow capillary tubes. *Am. J. Physiol.* **96,** 562–568 (1931).

125. Stroock, A. D., Dertinger, S. K. W., Ajdari, A., Mezic, I., Stone, H. A., & Whitesides, G. M. Chaotic mixer for microchannels. *Science* **295,** 647–651 (2002).

126. Martel, J. M., & Toner, M. Particle Focusing in Curved Microfluidic Channels. *Sci. Rep.* **3,** 1–8 (2013).

127. Di Carlo, D., Irimia, D., Tompkins, R. G., & Toner, M. Continuous inertial focusing, ordering, and separation of particles in microchannels. *Proc. Natl. Acad. Sci. U. S. A.* **104,** 18892–7 (2007).

128. Kuntaegowdanahalli, S. S., Bhagat, A. A. S., Kumar, G., & Papautsky, I. Inertial microfluidics for continuous particle separation in spiral microchannels. *Lab Chip* **9,** 2973–2980 (2009).

129. Poon, Z., Lee, W. C., Guan, G., Nyan, L. M., Lim, C. T., Han, J., Vliet, K. J. Van, & Van Vliet, K. J. Bone Marrow Regeneration Promoted by Biophysically Sorted Osteoprogenitors From Mesenchymal Stromal Cells. *Stem Cells Transl. Med.* **4,** 56–65 (2015).

130. Lee, W. C., Bhagat, A. A. S., Huang, S., Van Vliet, K. J., Han, J., & Lim, C. T. High-throughput cell cycle synchronization using inertial forces in spiral microchannels. *Lab Chip* **11,** 1359–1367 (2011).

131. Lee, W. C., Shi, H., Poon, Z., Nyan, L. M., Kaushik, T., Shivashankar, G. V, Chan, J. K. Y., Lim, C. T., Han, J., & Van Vliet, K. J. Multivariate biophysical markers predictive of mesenchymal stromal cell multipotency. *Proc. Natl. Acad. Sci. U. S. A.* **111,** 4409–18 (2014).

132. Hur, S. C., Brinckerhoff, T. Z., Walthers, C. M., Dunn, J. C. Y., & Di Carlo, D. Label-Free Enrichment of Adrenal Cortical Progenitor Cells Using Inertial Microfluidics. *PLoS One* **7,** (2012).

133. Bhagat, A. A. S., Hou, H. W., Li, L. D., Lim, C. T., & Han, J. Pinched flow coupled shear-modulated inertial microfluidics for high-throughput rare blood cell separation. *Lab Chip* **11,** 1870–1878 (2011).

134. Shen, S., Ma, C., Zhao, L., Wang, Y., Wang, J.-C., Xu, J., Li, T., Pang, L., & Wang, J. High-throughput rare cell separation from blood samples using steric hindrance and inertial microfluidics. *Lab Chip* **14,** 2525–38 (2014).

135. Hou, H. W., Warkiani, M. E., Khoo, B. L., Li, Z. R., Soo, R. A., Tan, D. S.-W., Lim, W.-T., Han, J., Bhagat, A. A. S., & Lim, C. T. Isolation and retrieval of circulating tumor cells using centrifugal forces. *Sci. Rep.* **3,** 1259 (2013).

136. Warkiani, M. E., Guan, G., Luan, K. B., Lee, W. C., Bhagat, A. A. S., Chaudhuri, P. K., Tan, D. S.-W., Lim, W. T., Lee, S. C., Chen, P. C. Y., Lim, C. T., & Han, J. Slanted spiral microfluidics for the ultra-fast, label-free isolation of circulating tumor cells. *Lab Chip* **14,** 128–37 (2014).

137. Warkiani, M. E., Khoo, B. L., Wu, L., Tay, A. K. P., Bhagat, A. A. S., Han, J., & Lim, C. T. Ultra-fast, label-free isolation of circulating tumor cells from blood using spiral microfluidics. *Nat. Protoc.* **11,** 134–48 (2016).

138. Warkiani, M. E., Khoo, B. L., Tan, D. S.-W., Bhagat, A. A. S., Lim, W.-T., Yap, Y. S., Lee, S. C., Soo, R. a, Han, J., & Lim, C. T. An ultra-high-throughput spiral microfluidic biochip for the enrichment of circulating tumor cells. *Analyst* **139,** 3245–55 (2014).

139. King, L., & Macdonald, F. On the Acoustic Radiation Pressure on Spheres. **A147,** 212–240 (1934).

140. Laurell, T., Petersson, F., & Nilsson, A. Chip integrated strategies for acoustic separation and manipulation of cells and particles. *Chem. Soc. Rev.* **36,** 492–506 (2007).

141. Hawkes, J. J., & Coakley, W. T. Force field particle filter, combining ultrasound standing waves and laminar flow. *Sensors Actuators B Chem.* **75,** 213–222 (2001).

142. Petersson, F., Åberg, L., Swärd-Nilsson, A.-M., & Laurell, T. Free Flow Acoustophoresis: Microfluidic-Based Mode of Particle and Cell Separation. *Anal. Chem.* **79,** 5117–5123 (2007).

143. Lenshof, A., & Laurell, T. Emerging Clinical Applications of Microchip-Based Acoustophoresis. *J. Lab. Autom.* **16,** 443–449 (2011).

144. Lenshof, A., Magnusson, C., & Laurell, T. Acoustofluidics 8: Applications of acoustophoresis in continuous flow microsystems. *Lab Chip* **12,** 1210 (2012).

145. Gröschl, M. Ultrasonic Separation of Suspended Particles - Part I: Fundamentals. *Acta Acust. united with Acust.* **84,** 432–447 (1998).

146. Kapishnikov, S., Kantsler, V., & Steinberg, V. Continuous particle size separation and size sorting using ultrasound in a microchannel. *J. Stat. Mech. Theory Exp.* **2006,** P01012 (2006).

147. Augustsson, P., Magnusson, C., Nordin, M., Lilja, H., & Laurell, T. Microfluidic, Label-Free Enrichment of Prostate Cancer Cells in Blood Based on Acoustophoresis. *Anal. Chem.* **84,** 7954–4962 (2012).

148. Ding, X., Peng, Z., Lin, S.-C. S., Geri, M., Li, S., Li, P., Chen, Y., Dao, M., Suresh, S., & Huang, T. J. Cell separation using tilted-angle standing surface acoustic waves. *Proc. Natl. Acad. Sci.* **111,** 12992–12997 (2014).

149. Antfolk, M., Antfolk, C., Lilja, H., Laurell, T., & Augustsson, P. A single inlet two-stage acoustophoresis chip enabling tumor cell enrichment from white blood cells. *Lab Chip* **15,** 2102–2109 (2015).

150. Miller, M. C., Doyle, G. V, & Terstappen, L. W. M. M. Significance of Circulating Tumor Cells Detected by the CellSearch System in Patients with Metastatic Breast Colorectal and Prostate Cancer. *J. Oncol.* **2010,** 617421 (2010).

151. Dykes, J., Lenshof, A., Åstrand-Grundström, I. B., Laurell, T., & Scheding, S. Efficient removal of platelets from peripheral blood progenitor cell products using a novel micro-chip based acoustophoretic platform. *PLoS One* **6,** (2011).

152. Lenshof, A., Jamal, A., Dykes, J., Urbansky, A., Astrand-Grundstrom, I., Laurell, T., & Scheding, S. Efficient purification of CD4+ lymphocytes from peripheral blood progenitor cell products using affinity bead acoustophoresis. *Cytom. Part A* **85,** 933–941 (2014).

153. Gascoyne, P. R. C., & Shim, S. Isolation of circulating tumor cells by dielectrophoresis. *Cancers (Basel).* **6,** 545–579 (2014).

154. Morgan, H., & Green, N. G. *AC electrokinetics: colloids and nanoparticles.* (Research Studies Press, 2003).

155. Pethig, R., Menachery, A., Pells, S., & Sousa, P. De. Dielectrophoresis: A Review of Applications for Stem Cell Research. **2010,** (2010).

156. Pethig, R. Dielectrophoresis: Status of the theory, technology, and applications. *Biomicrofluidics* **4,** 022811 (2010).

157. Cheng, I.-F., Chang, H.-C., Hou, D., & Chang, H.-C. An integrated dielectrophoretic chip for continuous bioparticle filtering, focusing, sorting, trapping, and detecting. *Biomicrofluidics* **1,** 021503 (2007).

158. Hughes, M. P. Strategies for dielectrophoretic separation in laboratory-on-a-chip systems. *Electrophoresis* **23,** 2569–2582 (2002).

159. Khoshmanesh, K., Nahavandi, S., Baratchi, S., Mitchell, A., & Kalantar-zadeh, K. Dielectrophoretic platforms for bio-microfluidic systems. *Biosens. Bioelectron.* **26,** 1800–1814 (2011).

160. Gagnon, Z. R. Cellular dielectrophoresis : Applications to the characterization, manipulation, separation and patterning of cells. *Elec* **32,** 2466–2487 (2011).

161. Gascoyne, P. R. C., & Vykoukal, J. Particle separation by dielectrophoresis. *Electrophoresis* **23,** 1973–1983 (2002).

162. Talary, M. S., Mills, K. I., Hoy, T., Burnett, A. K., & Pethig, R. Dielectrophoretic separation and enrichment of CD34+ cell subpopulation from bone marrow and peripheral blood stem cells. *Med. Biol. Eng. Comput.* **33,** 235–7 (1995).

163. Wang, X. B., Yang, J., Huang, Y., Vykoukal, J., Becker, F. F., & Gascoyne, P. R. Cell separation by dielectrophoretic field-flow-fractionation. *Anal. Chem.* **72,** 832–839 (2000).

164. Simon, M. G., Li, Y., Arulmoli, J., McDonnell, L. P., Akil, A., Nourse, J. L., Lee, A. P., & Flanagan, L. A. Increasing label-free stem cell sorting capacity to reach transplantation-scale throughput. *Biomicrofluidics* **8,** 064106 (2014).

165. Flanagan, L. A., Lu, J., Wang, L., Marchenko, S. A., Jeon, N. L., Lee, A. P., & Monuki, E. S. Unique Dielectric Properties Distinguish Stem Cells and Their Differentiated Progeny. *Stem Cells* **26,** 656–665 (2008).

166. Labeed, F. H., Lu, J., Mulhall, H. J., Marchenko, S. A., Hoettges, K. F., Estrada, L. C., Lee, A. P., Hughes, M. P., & Flanagan, L. A. Biophysical characteristics reveal neural stem cell differentiation potential. *PLoS One* **6,** 1–11 (2011).

167. Lu, J., Barrios, C. A., Dickson, A. R., Nourse, J. L., Lee, A. P., & Flanagan, L. A. Advancing practical usage of microtechnology: a study of the functional consequences of dielectrophoresis on neural stem cells. *Integr. Biol. (Camb).* **4,** 1223–36 (2012).

168. Song, H., Rosano, J. M., Wang, Y., Garson, C. J., Prabhakarpandian, B., Pant, K., Klarmann, G. J., Perantoni, A., Alvarez, L. M., & Lai, E. Continuous-flow sorting of stem cells and differentiation products based on dielectrophoresis. *Lab Chip* **15,** 1320–1328 (2015).

169. Vykoukal, J., Vykoukal, D. M., Freyberg, S., Alt, U., & Gascoyne, P. R. C. Enrichment of putative stem cells from adipose tissue using dielectrophoretic field-flow fractionation. *Lab Chip* **8,** 1386–1393 (2008).

170. Ismail, A., Hughes, M., Mulhall, H., Oreffo, R., & Labeed, F. Characterization of human skeletal stem and bone cell populations using dielectrophoresis. *J. Tissue Eng. Regen. Med.* **9,** 162–168 (2015).

171. Ling, S. H., Lam, Y. C., & Chian, K. S. Continuous Cell Separation Using Dielectrophoresis through Asymmetric and Periodic Microelectrode Array Table of Contents : 1–7 (2012).

172. Moon, H.-S., Kwon, K., Kim, S.-I., Han, H., Sohn, J., Lee, S., & Jung, H.-I. Continuous separation of breast cancer cells from blood samples using multi-orifice flow fractionation (MOFF) and dielectrophoresis (DEP). *Lab Chip* **11,** 1118–1125 (2011).

173. Shim, S., Stemke-Hale, K., Tsimberidou, A. M., Noshari, J., Anderson, T. E., & Gascoyne, P. R. C. Antibody-independent isolation of circulating tumor cells by continuous-flow dielectrophoresis. *Biomicrofluidics* **7,** (2013).

174. Sun, T., & Morgan, H. Single-cell microfluidic Impedance cytometry: A review. *Microfluid. Nanofluidics* **8,** 423–443 (2010).

175. Otto, O., Rosendahl, P., Mietke, A., Golfier, S., Herold, C., Klaue, D., Girardo, S., Pagliara, S., Ekpenyong, A., Jacobi, A., Wobus, M., Töpfner, N., Keyser, U. F., Mansfeld, J., Fischer-Friedrich, E., & Guck, J. Real-time deformability cytometry: on-the-fly cell mechanical phenotyping. *Nat. Methods* **12,** 199–202, 4 p following 202 (2015).

176. D'Silva, J., Austin, R. H., & Sturm, J. C. Inhibition of clot formation in deterministic lateral displacement arrays for processing large volumes of blood for rare cell capture. *Lab Chip* **15,** 2240–2247 (2015).

177. Didar, T. F., Li, K., Veres, T., & Tabrizian, M. Separation of rare oligodendrocyte progenitor cells from brain using a high-throughput multilayer thermoplastic-based microfluidic device. *Biomaterials* **34,** 5588–5593 (2013).

178. Lee, M. G., Shin, J. H., Bae, C. Y., Choi, S., & Park, J. Label-Free Cancer Cell Separation from Human Whole Blood Using Inertial Microfluidics at Low Shear Stress. *Anal. Chem.* **85,** 6213–6218 (2013).

179. Gascoyne, P. R. C., Noshari, J., Anderson, T. J., & Becker, F. F. Isolation of rare cells from cell mixtures by dielectrophoresis. *Electrophoresis* **30,** 1388–1398 (2009).

180. Chung, J., Issadore, D., Ullal, A., Lee, K., Weissleder, R., & Lee, H. Rare cell isolation and profiling on a hybrid magnetic/size-sorting chip. *Biomicrofluidics* **7,** (2013).

181. Muratore, M., Srsen, V., Waterfall, M., Downes, A., & Pethig, R. Biomarker-free dielectrophoretic sorting of differentiating myoblast multipotent progenitor cells and their membrane analysis by Raman spectroscopy. *Biomicrofluidics* **6,** (2012).

182. Elson, E. L. Cellular mechanics as an indicator of cytoskeletal structure and function. *Annu. Rev. Biophys. Biophys. Chem.* **17,** 397–430 (1988).

183. González-Cruz, R. D., Fonseca, V. C., & Darling, E. M. Cellular mechanical properties reflect the differentiation potential of adipose-derived mesenchymal stem cells. *Proc. Natl. Acad. Sci.* **109,** E1523–E1529 (2012).

184. Bongiorno, T., Kazlow, J., Mezencev, R., Griffiths, S., Olivares-Navarrete, R., McDonald, J. F., Schwartz, Z., Boyan, B. D., McDevitt, T. C., & Sulchek, T. Mechanical stiffness as an improved single-cell indicator of osteoblastic human mesenchymal stem cell differentiation. *J. Biomech.* **47,** 2197–2204 (2014).

185. Di Carlo, D. A mechanical biomarker of cell state in medicine. *J. Lab. Autom.* **17,** 32–42 (2012).

186. Lautenschläger, F., Paschke, S., Schinkinger, S., Bruel, A., Beil, M., & Guck, J. The regulatory role of cell mechanics for migration of differentiating myeloid cells. *Proc. Natl. Acad. Sci.* **106,** 15696–15701 (2009).

187. Tse, H. T. K., Gossett, D. R., Moon, Y. S., Masaeli, M., Sohsman, M., Ying, Y., Mislick, K., Adams, R. P., Rao, J., & Carlo, D. Di. Quantitative Diagnosis of Malignant Pleural Effusions by Single-Cell Mechanophenotyping. *Sci. Transl. Med.* **5,** (2013).

188. Maloney, J. M., Nikova, D., Lautenschl??ger, F., Clarke, E., Langer, R., Guck, J., & Van Vliet, K. J. Mesenchymal stem cell mechanics from the attached to the suspended state. *Biophys. J.* **99,** 2479–2487 (2010).

189. Askeland, D. R., & Fulay, P. P. *The science and engineering of materials*. (Thomson, 2006).

190. Tan, S. C., Pan, W. X., Ma, G., Cai, N., Leong, K. W., & Liao, K. Viscoelastic behaviour of human mesenchymal stem cells. *BMC Cell Biol.* **9,** 40 (2008).

191. Titushkin, I., & Cho, M. Modulation of cellular mechanics during osteogenic differentiation of human mesenchymal stem cells. *Biophys. J.* **93,** 3693–702 (2007).

192. Davis, J. a, Inglis, D. W., Morton, K. J., Lawrence, D. a, Huang, L. R., Chou, S. Y., Sturm, J. C., & Austin, R. H. Deterministic hydrodynamics: taking blood apart. *Proc. Natl. Acad. Sci. U. S. A.* **103,** 14779–14784 (2006).

193. Gossett, D. R., Tse, H. T. K., Lee, S. A., Ying, Y., Lindgren, A. G., Yang, O. O., Rao, J., Clark, A. T., & Di Carlo, D. Hydrodynamic stretching of single cells for large population mechanical phenotyping. *Proc. Natl. Acad. Sci. U. S. A.* **109,** 7630–5 (2012).

194. Chan, C. J., Ekpenyong, A. E., Golfier, S., Li, W., Chalut, K. J., Otto, O., Elgeti, J., Guck, J., & Lautenschl??ger, F. Myosin II activity softens cells in suspension. *Biophys. J.* **108,** 1856–1869 (2015).

195. Golfier, S., Rosendahl, P., Mietke, A., Herbig, M., Guck, J., & Otto, O. High-throughput cell mechanical phenotyping for label-free titration assays of cytoskeletal modifications. *Cytoskeleton* **74,** 283–296 (2017).

196. The F-actin modifier villin regulates insulin granule dynamics and exocytosis downstream of islet cell autoantigen 512. *Mol. Metab.* **5,** 656–668 (2016).

197. Kräter, M., Jacobi, A., Otto, O., Tietze, S., Müller, K., Poitz, D. M., Palm, S., Zinna, V. M., Biehain, U., Wobus, M., Chavakis, T., Werner, C., Guck, J., & Bornhauser, M. Bone marrow niche-mimetics modulate HSPC function via integrin signaling. *Sci. Rep.* **7,** (2017).

198. Koch, M., Wright, K. E., Otto, O., Herbig, M., Salinas, N. D., Tolia, N. H., Satchwell, T. J., Guck, J., Brooks, N. J., & Baum, J. Plasmodium falciparum erythrocyte-binding antigen 175 triggers a biophysical change in the red blood cell that facilitates invasion. *Proc. Natl. Acad. Sci.* **114,** 4225–4230 (2017).

199. Mokbel, M., Mokbel, D., Mietke, A., Träber, N., Girardo, S., Otto, O., Guck, J., & Aland, S. Numerical Simulation of Real-Time Deformability Cytometry To Extract Cell Mechanical Properties. *ACS Biomater. Sci. Eng.* **3,** 2962–2973 (2017).

200. Mietke, A., Otto, O., Girardo, S., Rosendahl, P., Taubenberger, A., Golfier, S., Ulbricht, E., Aland, S., Guck, J., & Fischer-Friedrich, E. Extracting Cell Stiffness from Real-Time Deformability Cytometry: Theory and Experiment. *Biophys. J.* **109,** 2023–2036 (2015).

201. Herbig, M., Mietke, A., Müller, P., & Otto, O. Statistics for real-time deformability cytometry: Clustering, dimensionality reduction, and significance testing. *Biomicrofluidics* **12,** 042214 (2018).

202. Chan, C. J., Ekpenyong, A. E., Golfier, S., Li, W., Chalut, K. J., Otto, O., Elgeti, J., Guck, J., & Lautenschläger, F. Myosin II Activity Softens Cells in Suspension. *Biophys. J.* **108,** 1856–1869 (2015).

203. Nagode, M. Finite Mixture Modeling via REBMIX. *J. Algorithms Optim.* **3,** 14–28 (2015).

204. Nagode, M., & Fajdiga, M. The REBMIX Algorithm for the Multivariate Finite Mixture Estimation. *Commun. Stat. - Theory Methods* **40,** 2022–2034 (2011).

205. Nagode, M., & Fajdiga, M. The REBMIX Algorithm and the Univariate Finite Mixture Estimation. *Commun. Stat. - Theory Methods* **40,** 876–892 (2011).

206. Bates, D., Mächler, M., Bolker, B. M., & Walker, S. C. Fitting linear mixed-effects models using lme4. *J. Stat. Softw.* **67,** (2015).

207. Whitfield, M. J., Lee, W. C. J., & Van Vliet, K. J. Onset of heterogeneity in culture-expanded bone marrow stromal cells. *Stem Cell Res.* **11,** 1365–1377 (2013).

208. Darling, E. M., Topel, M., Zauscher, S., Vail, T. P., & Guilak, F. Viscoelastic properties of human mesenchymally-derived stem cells and primary osteoblasts, chondrocytes, and adipocytes. *J. Biomech.* **41,** 454–464 (2008).

209. Alberts, B., Johnson, A., Lewis, J., Raff, M., Roberts, K., & Walter, P. *Molecular Biology of the Cell*. (Garland Science, 2002).

210. Méndez-Ferrer, S., Michurina, T. V., Ferraro, F., Mazloom, A. R., MacArthur, B. D., Lira, S. A., Scadden, D. T., Ma'ayan, A., Enikolopov, G. N., & Frenette, P. S. Mesenchymal and haematopoietic stem cells form a unique bone marrow niche. *Nature* **466,** 829–834 (2010).

211. Lewis, S. M. Chapter 2 - Reference ranges and normal values. in *Dacie and Lewis Practical Haematology (Tenth Edition)* (ed. Bates, S. M. L. J. B.) 11–24 (Churchill Livingstone, 2006).

212. Khismatullin, D. B. Chapter 3 The Cytoskeleton and Deformability of White Blood Cells. in *Current Topics in Membranes* (ed. Ley, K.) **64,** 47–111 (Academic Press, 2009).

213. Moazzam, F., DeLano, F. A., Zweifach, B. W., & Schmid-Schönbein, G. W. The leukocyte response to fluid stress. *Proc. Natl. Acad. Sci.* **94,** 5338–5343 (1997).

214. Hur, S. C., Henderson-MacLennan, N. K., McCabe, E. R. B., & Di Carlo, D. Deformability-based cell classification and enrichment using inertial microfluidics. *Lab Chip* **11,** 912–920 (2011).

215. Wang, G., Mao, W., Byler, R., Patel, K., Henegar, C., Alexeev, A., & Sulchek, T. Stiffness Dependent Separation of Cells in a Microfluidic Device. *PLoS One* **8,** (2013).

216. Rosendahl, P., Plak, K., Jacobi, A., Kraeter, M., Toepfner, N., Otto, O., Herold, C., Winzi, M., Herbig, M., Ge, Y., Girardo, S., Wagner, K., Baum, B., & Guck, J. Real-time fluorescence and deformability cytometry. *Nat. Methods* **15,** 355–358 (2018).

217. Fawcett, D., & Bloom, W. Bone Marrow and Blood Cell Formation. in *A Textbook of Histology* (Chapman & Hall, 1994).

218. Nelson, L., McCarthy, H. E., Fairclough, J., Williams, R., & Archer, C. W. Evidence of a Viable Pool of Stem Cells within Human Osteoarthritic Cartilage. *Cartilage* **5,** 203–14 (2014).

219. Bruder, S. P., Jaiswal, N., & Haynesworth, S. E. Growth kinetics, self-renewal, and the osteogenic potential of purified human mesenchymal stem cells during extensive subcultivation and following cryopreservation. *J. Cell. Biochem.* **64,** 278–94 (1997).

220. Banfi, A., Muraglia, A., Dozin, B., Mastrogiacomo, M., Cancedda, R., & Quarto, R. Proliferation kinetics and differentiation potential of ex vivo expanded human bone marrow stromal cells: Implications for their use in cell therapy. *Exp. Hematol.* **28,** 707–715 (2000).

221. Bonab, M. M., Alimoghaddam, K., Talebian, F., Ghaffari, S. H., Ghavamzadeh, A., & Nikbin, B. Aging of mesenchymal stem cell in vitro. *BMC Cell Biol.* **7,** (2006).

222. Kim, J., Kang, J. W., Park, J. H., Choi, Y., Choi, K. S., Park, K. D., Baek, D. H., Seong, S. K., Min, H.-K., & Kim, H. S. Biological characterization of long-term cultured human mesenchymal stem cells. *Arch. Pharm. Res.* **32,** 117–126 (2009).

223. Su, H. W., Prieto, J. L., & Voldman, J. Rapid dielectrophoretic characterization of single cells using the dielectrophoretic spring. *Lab a Chip - Miniaturisation Chem. Biol.* **13,** 4109–4117 (2013).

224. Pethig, R., & Talary, M. S. Dielectrophoretic detection of membrane morphology changes in Jurkat T-cells undergoing etoposide-induced apoptosis. *IET Nanobiotechnology* **1,** 2 (2007).

225. Velugotla, S., Pells, S., Mjoseng, H. K., Duffy, C. R. E., Smith, S., De Sousa, P., & Pethig, R. Dielectrophoresis based discrimination of human embryonic stem cells from differentiating derivatives. *Biomicrofluidics* **6,** 044113 (2012).

226. Nourse, J. L., Prieto, J. L., Dickson, A. R., Lu, J., Pathak, M. M., Tombola, F., Demetriou, M., Lee, A. P., & Flanagan, L. A. Membrane biophysics define neuron and astrocyte progenitors in the neural lineage. *Stem Cells* **32,** 706–716 (2014).

227. Zhao, Y., Liu, Q., Sun, H., Chen, D., Li, Z., Fan, B., George, J., Xue, C., Cui, Z., Wang, J., & Chen, J. Electrical Property Characterization of Neural Stem Cells in Differentiation. *PLoS One* **11,** e0158044 (2016).

228. Song, H., Wang, Y., Rosano, J. M., Prabhakarpandian, B., Pant, K., & Lai, E. A microfluidic impedance flow cytometer for identification of differentiation state of stem cells. *Lab Chip* **13,** 2300–2310 (2013).

229. Zhou, Y., Basu, S., Laue, E., & Seshia, A. A. Single cell studies of mouse embryonic stem cell (mESC) differentiation by electrical impedance measurements in a microfluidic device. *Biosens. Bioelectron.* **81,** 249–258 (2016).

230. Xavier, M., Rosendahl, P., Herbig, M., Kräter, M., Spencer, D., Bornhäuser, M., Oreffo, R. O. C., Morgan, H., Guck, J., & Otto, O. Mechanical phenotyping of primary human skeletal stem cells in heterogeneous populations by real-time deformability cytometry. *Integr. Biol. (Camb).* **8,** 616–623 (2016).

231. Lo Surdo, J., & Bauer, S. R. Quantitative Approaches to Detect Donor and Passage Differences in Adipogenic Potential and Clonogenicity in Human Bone Marrow-Derived Mesenchymal Stem Cells. *Tissue Eng. Part C Methods* **18,** 877–889 (2012).

232. Gascoyne, P. R. C., Shim, S., Noshari, J., Becker, F. F., & Stemke-Hale, K. Correlations between the dielectric properties and exterior morphology of cells revealed by dielectrophoretic field-flow fractionation. *Electrophoresis* **34,** 1042–1050 (2013).

233. Bagnaninchi, P. O., & Drummond, N. Real-time label-free monitoring of adipose-derived stem cell differentiation with electric cell-substrate impedance sensing. *Proc. Natl. Acad. Sci. U. S. A.* **108,** 6462–7 (2011).

234. Song, H., Rosano, J. M., Wang, Y. *et al.* Continuous-flow sorting of stem cells and differentiation products based on dielectrophoresis. *Lab Chip* **15,** 1320–1328 (2015).

235. Bruderer, M., Richards, R., Alini, M., & Stoddart, M. Role and regulation of RUNX2 in osteogenesis. *Eur. Cells Mater.* **28,** 269–286 (2014).

236. Granéli, C., Thorfve, A., Ruetschi, U., Brisby, H., Thomsen, P., Lindahl, A., & Karlsson, C. Novel markers of osteogenic and adipogenic differentiation of human bone marrow stromal cells identified using a quantitative proteomics approach. *Stem Cell Res.* **12,** 153–165 (2014).

237. Baek, W.-Y., Lee, M.-A., Jung, J. W., Kim, S.-Y., Akiyama, H., de Crombrugghe, B., & Kim, J.-E. Positive Regulation of Adult Bone Formation by Osteoblast-Specific Transcription Factor Osterix. *J. Bone Miner. Res.* **24,** 1055–1065 (2009).

238. Nuttall, M., & Gimble, J. Controlling the balance between osteoblastogenesis and adipogenesis and the consequent therapeutic implications. (2004).

239. Akune, T., Ohba, S., Kamekura, S., Yamaguchi, M., Chung, U.-I., Kubota, N., Terauchi, Y., Harada, Y., Azuma, Y., Nakamura, K., Kadowaki, T., & Kawaguchi, H. PPARgamma insufficiency enhances osteogenesis through osteoblast formation from bone marrow progenitors. *J. Clin. Invest.* **113,** 846–55 (2004).

240. Handin, R. I., Lux, S. E., & Stossel, T. P. *Blood : principles and practice of hematology*.

241. He, W., Goodkind, D., & Kowal, P. An Aging World: 2015. (2016).

242. Bianco, P., & Robey, P. G. Skeletal stem cells. *Development* **142,** (2015).

243. Czekańska, E. M. In vitro cell and culture models for osteoblasts and their progenitors. (Cardiff University, 2014).

244. Tare, R. S., Mitchell, P. D., Kanczler, J., & Oreffo, R. O. C. Bone Research Protocols. **816,** 643 (2012).

245. Williams, E. L., White, K., & Oreffo, R. O. C. Isolation and Enrichment of Stro-1 Immunoselected Mesenchymal Stem Cells from Adult Human Bone Marrow. in *Methods in molecular biology* 67–73 (Humana Press, 2013).

246. Dawson, J. I., Smith, J. O., Aarvold, A., Ridgway, J. N., Curran, S. J., Dunlop, D. G., & Oreffo, R. O. C. Enhancing the osteogenic efficacy of human bone marrow aspirate: concentrating osteoprogenitors using wave-assisted filtration. *Cytotherapy* **15,** 242–252 (2013).

247. Gothard, D., Greenhough, J., Ralph, E., & Oreffo, R. O. Prospective isolation of human bone marrow stromal cell subsets: A comparative study between Stro-1-, CD146- and CD105-enriched populations. *J. Tissue Eng.* **5,** (2014).

248. de Andrés, M. C., Imagawa, K., Hashimoto, K., Gonzalez, A., Roach, H. I., Goldring, M. B., & Oreffo, R. O. C. Loss of methylation in CpG sites in the NF-κB enhancer elements of inducible nitric oxide synthase is responsible for gene induction in human articular chondrocytes. *Arthritis Rheum.* **65,** 732–42 (2013).

249. Holmes, D., She, J. K., Roach, P. L., & Morgan, H. Bead-based immunoassays using a micro-chip flow cytometer. *Lab Chip* **7,** 1048–1056 (2007).

250. Morgan, H., Holmes, D., & Green, N. G. High speed simultaneous single particle impedance and fluorescence analysis on a chip. *Curr. Appl. Phys.* **6,** 367–370 (2006).

251. Spencer, D., Hollis, V., & Morgan, H. Microfluidic impedance cytometry of tumour cells in blood. *Biomicrofluidics* **8,** (2014).

252. Holm, S. H., Beech, J. P., Barrett, M. P., & Tegenfeldt, J. O. Simplifying microfluidic separation devices towards field-detection of blood parasites. *Anal. Methods* **8,** 3291–3300 (2016).

253. Inglis, D. W. Efficient microfluidic particle separation arrays. *Appl. Phys. Lett.* **94,** 013510 (2009).

254. Shapiro, S. S., & Wilk, M. B. An analysis of variance test for normality (complete samples). *Biometrika* **52,** 591–611 (1965).

255. Rosner, B. *Fundamentals of biostatistics*. (Thomson Brooks/Cole, 2011).

256. Lehmann, E. L., & D'Abrera, H. J. M. *Nonparametrics: statistical methods based on ranks*. (Springer, 2006).

257. Kutner, M. H., Nachtsheim, C., Neter, J., & Li, W. *Applied linear statistical models*. (McGraw-Hill/Irwin, 2005).

Supplementary Material to Chapter 3: Mechanical Phenotyping

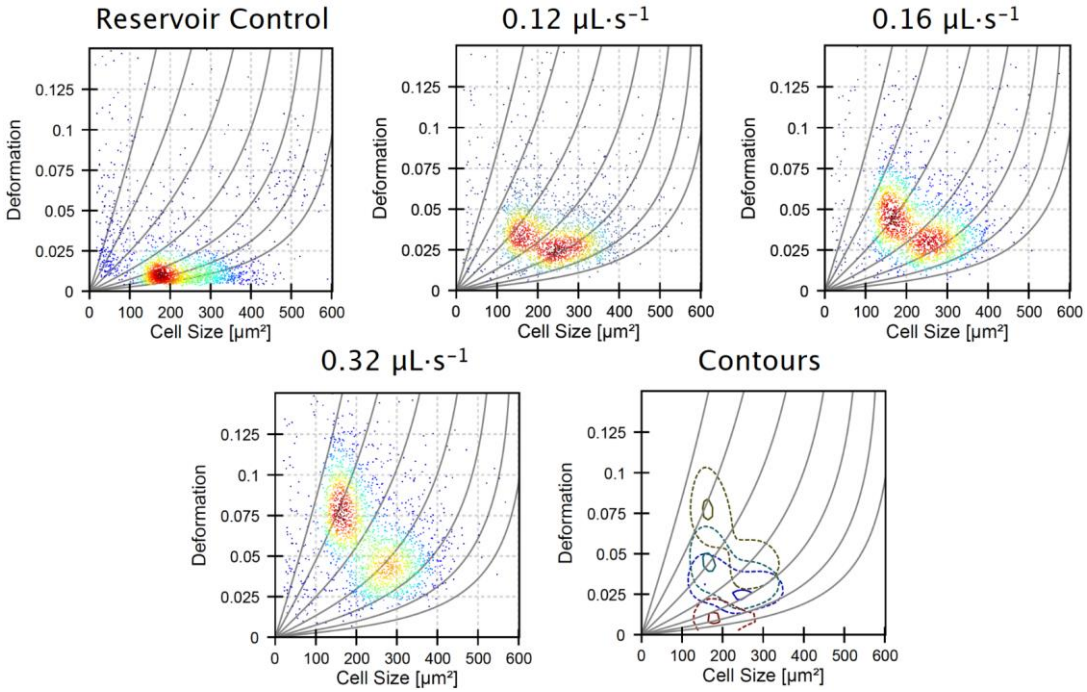

Figure S1 – Real-time deformability cytometry of HL60 and MG-63 cells. Cells were mixed 1:1 and measured at flow rates of 0.12 µL·s^{-1}, 0.16 µL·s^{-1}, 0.32 µL·s^{-1} and in the reservoir for reference. Measurements were carried out using a 30-µm cross-section microfluidic channel at a frame rate of 2,000 fps.

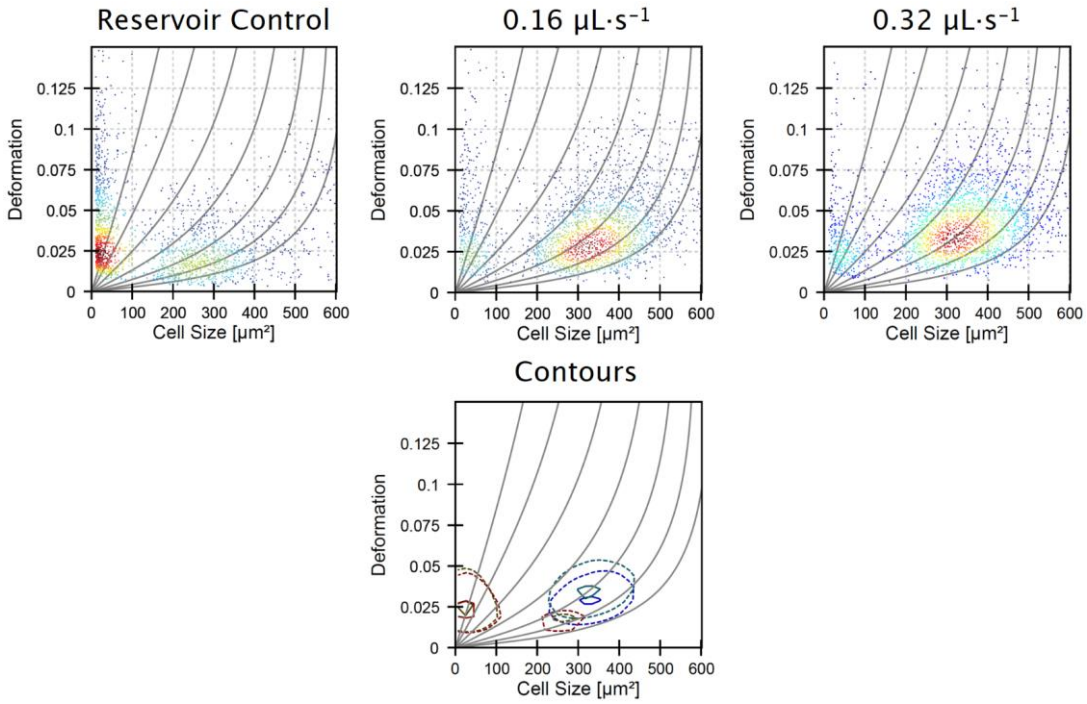

Figure S2 – Real-time deformability cytometry of skeletal stem cells. Cells were measured at flow rates of 0.16 µL·s^{-1}, 0.32 µL·s^{-1} and in the reservoir for reference. Measurements were carried out using a 30-µm cross-section microfluidic channel at a frame rate of 2,000 fps.

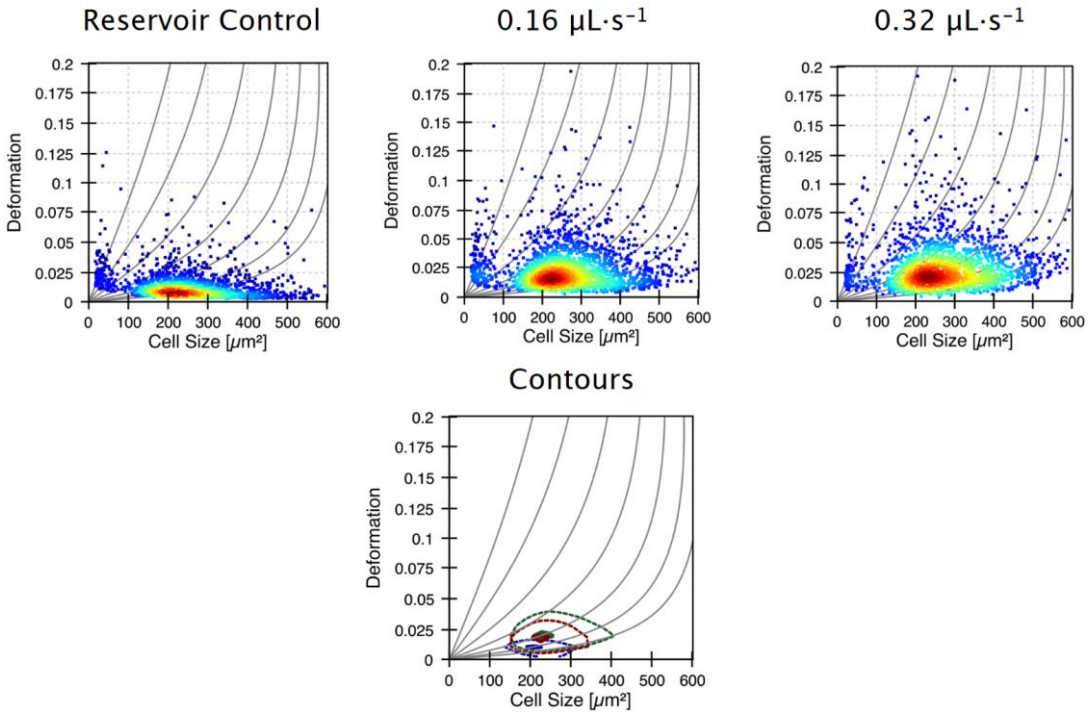

Figure S3 – Real-time deformability cytometry of human bone marrow stromal cells. Cells were measured at flow rates of 0.16 µL·s^{-1}, 0.32 µL·s^{-1} and in the reservoir for reference. Measurements were carried out using a 30-µm cross-section microfluidic channel at a frame rate of 2,000 fps.

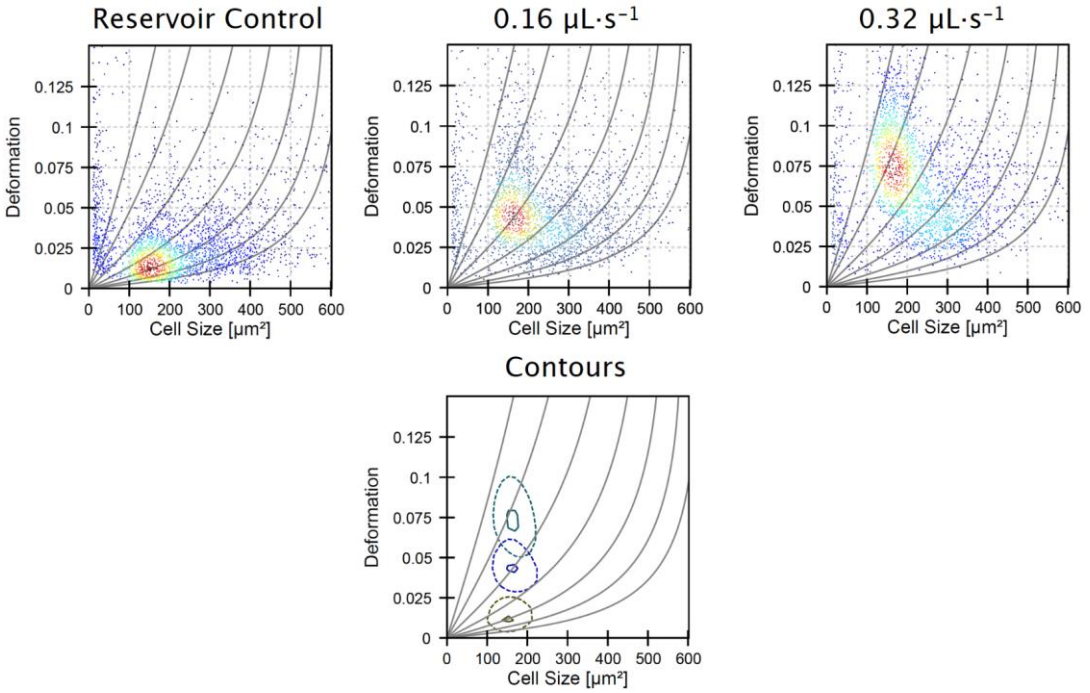

Figure S4 – Real-time deformability cytometry of human skeletal stem cells and HL-60. Cells were mixed 1:1 and measured at flow rates of 0.16 µL·s^{-1}, 0.32 µL·s^{-1} and in the reservoir for reference. Measurements were carried out using a 30-µm cross-section microfluidic channel at a frame rate of 2,000 fps.

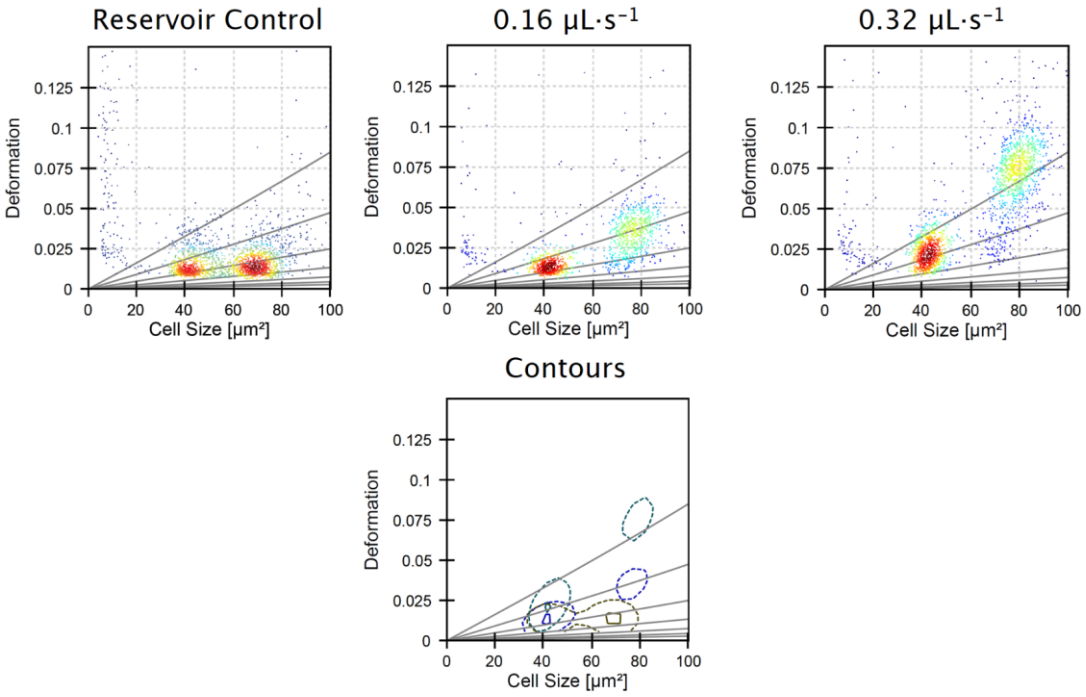

Figure S5 – Real-time deformability cytometry of human white blood cells. Cells were measured at flow rates of 0.16 µL·s^{-1}, 0.32 µL·s^{-1} and in the reservoir for reference. Measurements were carried out using a 30-µm cross-section microfluidic channel at a frame rate of 2,000 fps.

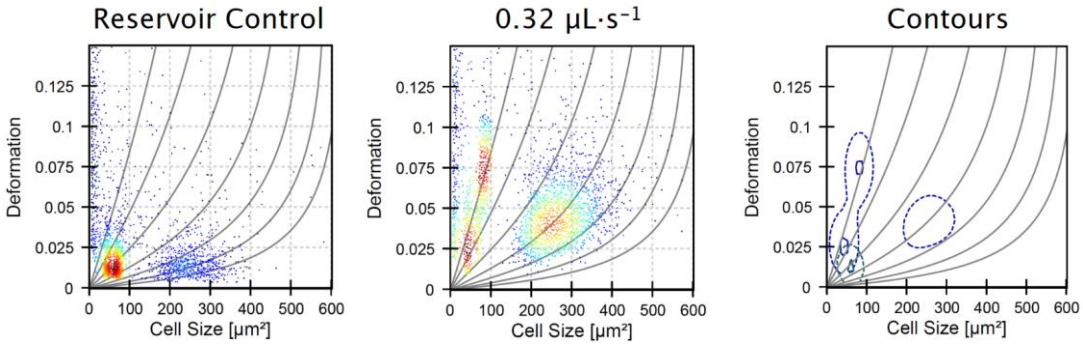

Figure S6 – Real-time deformability cytometry of human white blood cells and MG-63. Cells were mixed 2:1 and measured at flow rates of 0.16 µL·s^{-1}, 0.32 µL·s^{-1} and in the reservoir for reference. Measurements were carried out using a 30-µm cross-section microfluidic channel at a frame rate of 2,000 fps.

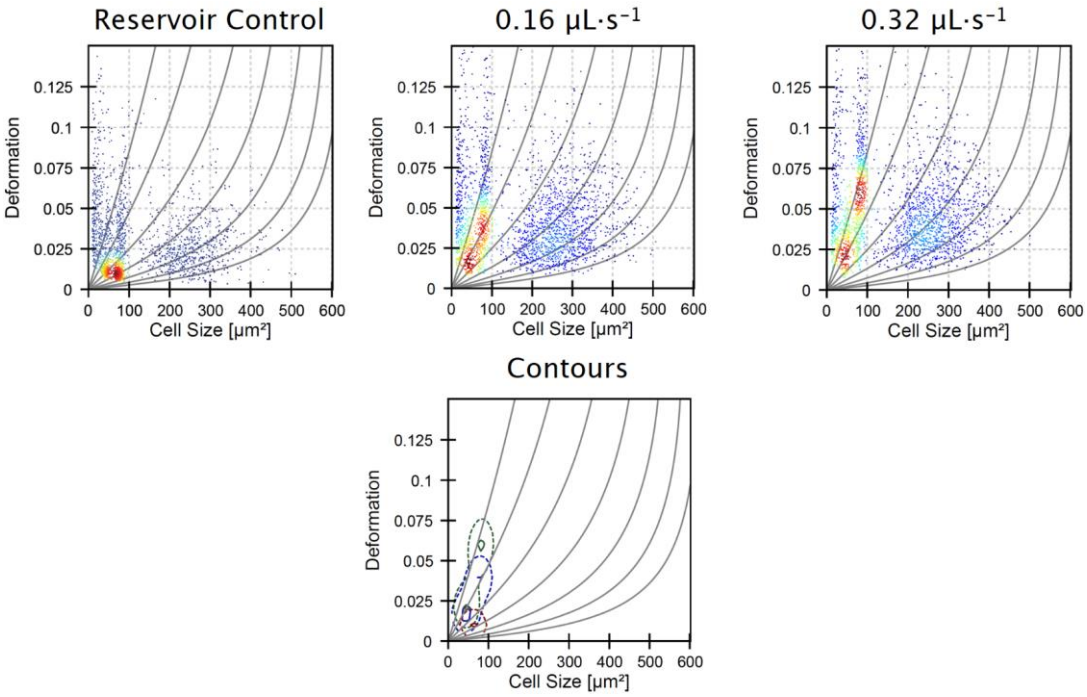

Figure S7 – Real-time deformability cytometry of human white blood cells and skeletal stem cells. Cells were mixed 2:1 and measured at flow rates of 0.16 µL·s^{-1}, 0.32 µL·s^{-1} and in the reservoir for reference. Measurements were carried out using a 30-µm cross-section microfluidic channel at a frame rate of 2,000 fps.

Supplementary Material to Chapter 4: Size and Dielectric Characterisation

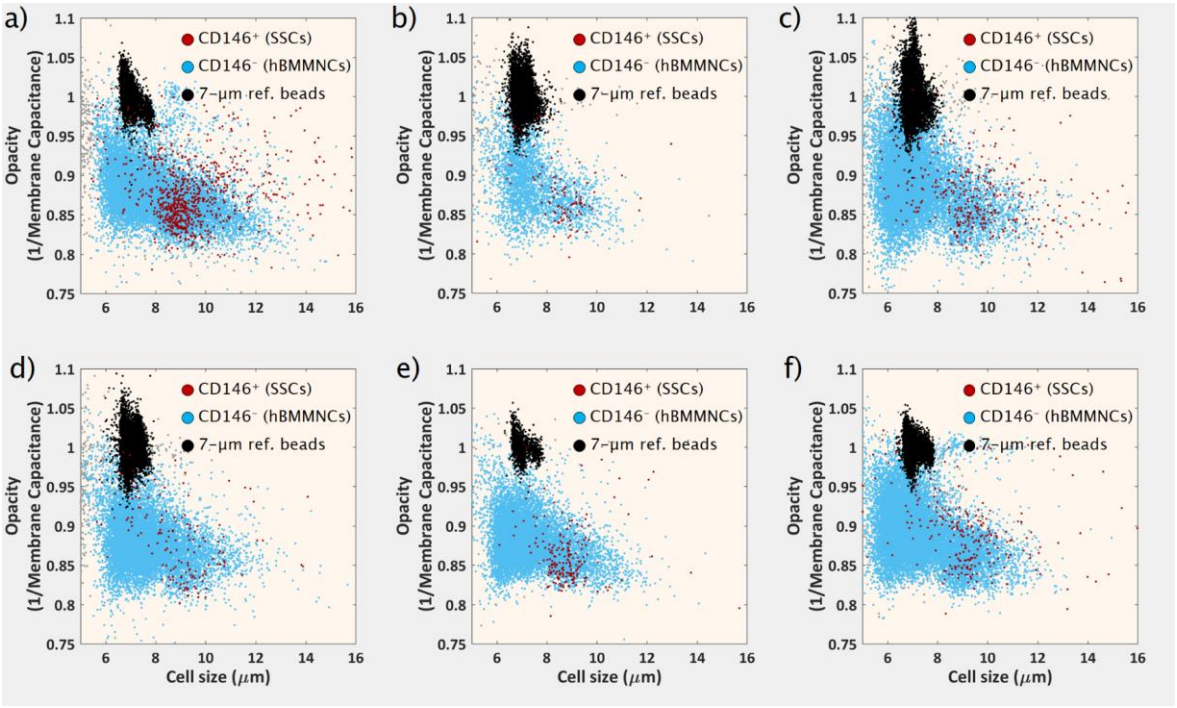

Figure S8 – Fluorescence-assisted microfluidic impedance cytometry of Stro-1-enriched human bone marrow mononuclear cells (hBMMNCs). a–f) Scatter plots of cell size (µm) vs electrical opacity (normalised to 7-µm diameter reference beads) of Stro-1⁺-enriched hBMMNCs obtained from six individual patients.

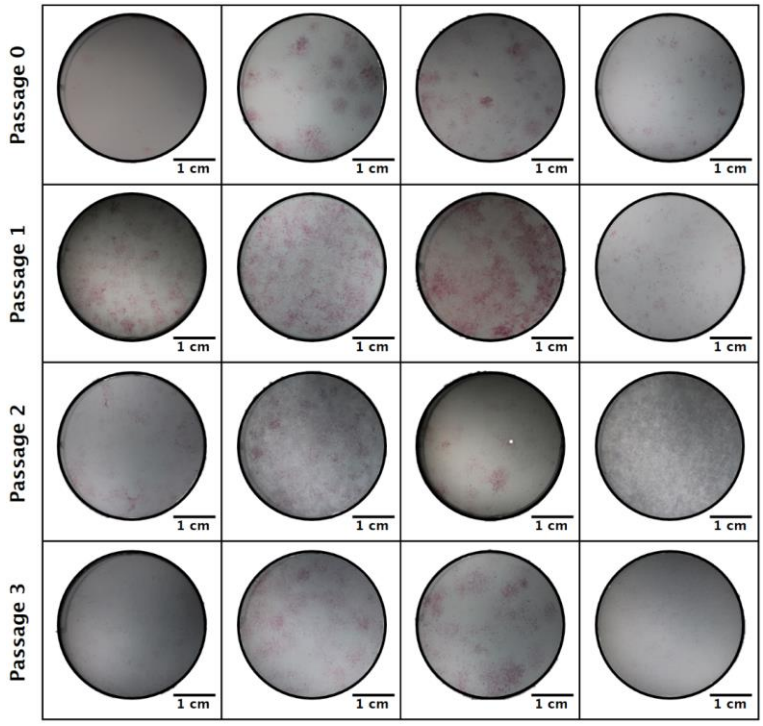

Figure S9 – Alkaline phosphatase activity. Alkaline phosphatase staining of human BM CFU-F colonies grown under basal expansion conditions at different passages (passage 0 to passage 3).

Supplementary Material to Chapter 5: Size and Mechano-based cell sorting

Table S1 – Standard normal distribution. Table values (negative) represent area to the left of the Z-score.

Z	0	0.01	0.02	0.03	0.04	0.05	0.06	0.07	0.08	0.09
-4.0	0.00003	0.00003	0.00003	0.00003	0.00003	0.00003	0.00002	0.00002	0.00002	0.00002
-3.9	0.00005	0.00005	0.00005	0.00005	0.00006	0.00006	0.00006	0.00006	0.00007	0.00007
-3.8	0.00007	0.00008	0.00008	0.00008	0.00008	0.00009	0.00009	0.00010	0.00010	0.00010
-3.7	0.00011	0.00010	0.00010	0.00010	0.00009	0.00009	0.00008	0.00008	0.00008	0.00008
-3.6	0.00016	0.00015	0.00015	0.00014	0.00014	0.00013	0.00013	0.00012	0.00012	0.00011
-3.5	0.00023	0.00022	0.00022	0.00021	0.00020	0.00019	0.00019	0.00018	0.00017	0.00017
-3.4	0.00034	0.00032	0.00031	0.00030	0.00029	0.00028	0.00027	0.00026	0.00025	0.00024
-3.3	0.00048	0.00047	0.00045	0.00043	0.00042	0.00040	0.00039	0.00038	0.00036	0.00035
-3.2	0.00069	0.00066	0.00064	0.00062	0.00060	0.00058	0.00056	0.00054	0.00052	0.00050
-3.1	0.00097	0.00094	0.00090	0.00087	0.00084	0.00082	0.00079	0.00076	0.00074	0.00071
-3.0	0.00135	0.00131	0.00126	0.00122	0.00118	0.00114	0.00111	0.00107	0.00104	0.00100
-2.9	0.00187	0.00181	0.00175	0.00169	0.00164	0.00159	0.00154	0.00149	0.00144	0.00139
-2.8	0.00256	0.00248	0.00240	0.00233	0.00226	0.00219	0.00212	0.00205	0.00199	0.00193
-2.7	0.00347	0.00336	0.00326	0.00317	0.00307	0.00298	0.00289	0.00280	0.00272	0.00264
-2.6	0.00466	0.00453	0.00440	0.00427	0.00415	0.00402	0.00391	0.00379	0.00368	0.00357
-2.5	0.00621	0.00604	0.00587	0.00570	0.00554	0.00539	0.00523	0.00508	0.00494	0.00480
-2.4	0.00820	0.00798	0.00776	0.00755	0.00734	0.00714	0.00695	0.00676	0.00657	0.00639
-2.3	0.01072	0.01044	0.01017	0.00990	0.00964	0.00939	0.00914	0.00889	0.00866	0.00842
-2.2	0.01390	0.01355	0.01321	0.01287	0.01255	0.01222	0.01191	0.01160	0.01130	0.01101
-2.1	0.01786	0.01743	0.01700	0.01659	0.01618	0.01578	0.01539	0.01500	0.01463	0.01426
-2.0	0.02275	0.02222	0.02169	0.02118	0.02068	0.02018	0.01970	0.01923	0.01876	0.01831
-1.9	0.02872	0.02807	0.02743	0.02680	0.02619	0.02559	0.02500	0.02442	0.02385	0.02330
-1.8	0.03593	0.03515	0.03438	0.03362	0.03288	0.03216	0.03144	0.03074	0.03005	0.02938
-1.7	0.04457	0.04363	0.04272	0.04182	0.04093	0.04006	0.03920	0.03836	0.03754	0.03673
-1.6	0.05480	0.05370	0.05262	0.05155	0.05050	0.04947	0.04846	0.04746	0.04648	0.04551
-1.5	0.06681	0.06552	0.06426	0.06301	0.06178	0.06057	0.05938	0.05821	0.05705	0.05592
-1.4	0.08076	0.07927	0.07780	0.07636	0.07493	0.07353	0.07215	0.07078	0.06944	0.06811
-1.3	0.09680	0.09510	0.09342	0.09176	0.09012	0.08851	0.08691	0.08534	0.08379	0.08226
-1.2	0.11507	0.11314	0.11123	0.10935	0.10749	0.10565	0.10383	0.10204	0.10027	0.09853
-1.1	0.13567	0.13350	0.13136	0.12924	0.12714	0.12507	0.12302	0.12100	0.11900	0.11702
-1.0	0.15866	0.15625	0.15386	0.15151	0.14917	0.14686	0.14457	0.14231	0.14007	0.13786
-0.9	0.18406	0.18141	0.17879	0.17619	0.17361	0.17106	0.16853	0.16602	0.16354	0.16109
-0.8	0.21186	0.20897	0.20611	0.20327	0.20045	0.19766	0.19489	0.19215	0.18943	0.18673
-0.7	0.24196	0.23885	0.23576	0.23270	0.22965	0.22663	0.22363	0.22065	0.21770	0.21476
-0.6	0.27425	0.27093	0.26763	0.26435	0.26109	0.25785	0.25463	0.25143	0.24825	0.24510
-0.5	0.30854	0.30503	0.30153	0.29806	0.29460	0.29116	0.28774	0.28434	0.28096	0.27760
-0.4	0.34458	0.34090	0.33724	0.33360	0.32997	0.32636	0.32276	0.31918	0.31561	0.31207
-0.3	0.38209	0.37828	0.37448	0.37070	0.36693	0.36317	0.35942	0.35569	0.35197	0.34827
-0.2	0.42074	0.41683	0.41294	0.40905	0.40517	0.40129	0.39743	0.39358	0.38974	0.38591
-0.1	0.46017	0.45620	0.45224	0.44828	0.44433	0.44038	0.43644	0.43251	0.42858	0.42465
0.0	0.50000	0.49601	0.49202	0.48803	0.48405	0.48006	0.47608	0.47210	0.46812	0.46414

Table S2 – Standard normal distribution. Table values (positive) represent area to the left of the Z-score.

Z	0	0.01	0.02	0.03	0.04	0.05	0.06	0.07	0.08	0.09
0	0.50000	0.50399	0.50798	0.51197	0.51595	0.51994	0.52392	0.52790	0.53188	0.53586
0.1	0.53983	0.54380	0.54776	0.55172	0.55567	0.55962	0.56356	0.56749	0.57142	0.57535
0.2	0.57926	0.58317	0.58706	0.59095	0.59483	0.59871	0.60257	0.60642	0.61026	0.61409
0.3	0.61791	0.62172	0.62552	0.62930	0.63307	0.63683	0.64058	0.64431	0.64803	0.65173
0.4	0.65542	0.65910	0.66276	0.66640	0.67003	0.67364	0.67724	0.68082	0.68439	0.68793
0.5	0.69146	0.69497	0.69847	0.70194	0.70540	0.70884	0.71226	0.71566	0.71904	0.72240
0.6	0.72575	0.72907	0.73237	0.73565	0.73891	0.74215	0.74537	0.74857	0.75175	0.75490
0.7	0.75804	0.76115	0.76424	0.76730	0.77035	0.77337	0.77637	0.77935	0.78230	0.78524
0.8	0.78814	0.79103	0.79389	0.79673	0.79955	0.80234	0.80511	0.80785	0.81057	0.81327
0.9	0.81594	0.81859	0.82121	0.82381	0.82639	0.82894	0.83147	0.83398	0.83646	0.83891
1	0.84134	0.84375	0.84614	0.84849	0.85083	0.85314	0.85543	0.85769	0.85993	0.86214
1.1	0.86433	0.86650	0.86864	0.87076	0.87286	0.87493	0.87698	0.87900	0.88100	0.88298
1.2	0.88493	0.88686	0.88877	0.89065	0.89251	0.89435	0.89617	0.89796	0.89973	0.90147
1.3	0.90320	0.90490	0.90658	0.90824	0.90988	0.91149	0.91309	0.91466	0.91621	0.91774
1.4	0.91924	0.92073	0.92220	0.92364	0.92507	0.92647	0.92785	0.92922	0.93056	0.93189
1.5	0.93319	0.93448	0.93574	0.93699	0.93822	0.93943	0.94062	0.94179	0.94295	0.94408
1.6	0.94520	0.94630	0.94738	0.94845	0.94950	0.95053	0.95154	0.95254	0.95352	0.95449
1.7	0.95543	0.95637	0.95728	0.95818	0.95907	0.95994	0.96080	0.96164	0.96246	0.96327
1.8	0.96407	0.96485	0.96562	0.96638	0.96712	0.96784	0.96856	0.96926	0.96995	0.97062
1.9	0.97128	0.97193	0.97257	0.97320	0.97381	0.97441	0.97500	0.97558	0.97615	0.97670
2	0.97725	0.97778	0.97831	0.97882	0.97932	0.97982	0.98030	0.98077	0.98124	0.98169
2.1	0.98214	0.98257	0.98300	0.98341	0.98382	0.98422	0.98461	0.98500	0.98537	0.98574
2.2	0.98610	0.98645	0.98679	0.98713	0.98745	0.98778	0.98809	0.98840	0.98870	0.98899
2.3	0.98928	0.98956	0.98983	0.99010	0.99036	0.99061	0.99086	0.99111	0.99134	0.99158
2.4	0.99180	0.99202	0.99224	0.99245	0.99266	0.99286	0.99305	0.99324	0.99343	0.99361
2.5	0.99379	0.99396	0.99413	0.99430	0.99446	0.99461	0.99477	0.99492	0.99506	0.99520
2.6	0.99534	0.99547	0.99560	0.99573	0.99585	0.99598	0.99609	0.99621	0.99632	0.99643
2.7	0.99653	0.99664	0.99674	0.99683	0.99693	0.99702	0.99711	0.99720	0.99728	0.99736
2.8	0.99744	0.99752	0.99760	0.99767	0.99774	0.99781	0.99788	0.99795	0.99801	0.99807
2.9	0.99813	0.99819	0.99825	0.99831	0.99836	0.99841	0.99846	0.99851	0.99856	0.99861
3	0.99865	0.99869	0.99874	0.99878	0.99882	0.99886	0.99889	0.99893	0.99896	0.99900
3.1	0.99903	0.99906	0.99910	0.99913	0.99916	0.99918	0.99921	0.99924	0.99926	0.99929
3.2	0.99931	0.99934	0.99936	0.99938	0.99940	0.99942	0.99944	0.99946	0.99948	0.99950
3.3	0.99952	0.99953	0.99955	0.99957	0.99958	0.99960	0.99961	0.99962	0.99964	0.99965
3.4	0.99966	0.99968	0.99969	0.99970	0.99971	0.99972	0.99973	0.99974	0.99975	0.99976
3.5	0.99977	0.99978	0.99978	0.99979	0.99980	0.99981	0.99981	0.99982	0.99983	0.99983
3.6	0.99984	0.99985	0.99985	0.99986	0.99986	0.99987	0.99987	0.99988	0.99988	0.99989
3.7	0.99989	0.99990	0.99990	0.99990	0.99991	0.99991	0.99992	0.99992	0.99992	0.99992
3.8	0.99993	0.99993	0.99993	0.99994	0.99994	0.99994	0.99994	0.99995	0.99995	0.99995
3.9	0.99995	0.99995	0.99996	0.99996	0.99996	0.99996	0.99996	0.99996	0.99997	0.99997
4	0.99997	0.99997	0.99997	0.99997	0.99997	0.99997	0.99998	0.99998	0.99998	0.99998

“If I have seen further it is by standing on the shoulders of giants.”

Sir Isaac Newton, 1675